PRIME MINISTER'S SERVICES
SCIENCE POLICY OFFICE

Wetensschapsstraat 8 rue de la Science
1040 Brussels

D/1989/1191/11

ANTARCTICA

BELGIAN SCIENTIFIC
RESEARCH PROGRAMME
ON ANTARCTICA

**SCIENTIFIC RESULTS
OF PHASE ONE (OCT 85 - JAN 89)**

edited by
S. CASCHETTO

VOLUME III

GLACIOLOGY AND CLIMATOLOGY

This volume presents the scientific results of researches in Glaciology-Climatology that were carried out from October 1985 to January 1989 in the framework of **Phase One** of the **Belgian Scientific Research Programme on Antarctica.**

Studies conducted in other fields addressed by the Programme form the subject of two additional volumes issued by the Science Policy Office (Vol. I: Plankton Ecology and Vol. II: Marine Geochemistry and Marine Geophysics).

The Programme was implemented through the decision of the Council of Ministers of 29 July 1985 with the aim at contributing to the betterment of the knowledge of the functioning of the Antarctic's marine ecosystems and of the role played by Antarctica and the Southern Ocean in global changes.

The studies are being carried on within **Phase Two** of the Programme that will ensure the pursuing and the development until December 1991 of the Belgian research effort.

TABLE OF CONTENTS

I ISOTOPIC COMPOSITION OF ICE FORMED BY WATER FREEZING

R. Souchez, J.L. Tison and R. Lorrain

Co-isotopic composition of ice formed by water freezing: a review 1
Objectives of the Research Program 6
Methods and Analyses 7
Field Work 14
Results and discussion 17
Potential applications 45
General conclusions 47
Acknowledgements 48
References 49

II FLOW SIMULATION IN THE WEDDELL SEA

M. Fettweis, C.-S. Yu and J. Berlamont

Introduction 3
The Weddell Sea 6
Ocean - Ice Models: A Review 10
The Ocean Model 13
Open Boundary Condition for Circulation Models 29
Advection and Diffusion 44
The Weddell Sea Model 50
Conclusion 63
Bibliography 65

III NUMERICAL STUDY OF THE AIR SEA INTERACTIONS IN THE ANTARCTIC COASTAL ZONE AND THEIR IMPLICATIONS ON DEEP SEA FORMATION IN THE CASE OF KATABATIC WIND

H. Gallée, A. Berger, G. Schayes, T. Fichefet, I. Marsiat, C. Tricot and J.P. Van Ypersele

General goals 1
Some characteristics of katabatic winds 1
The atmospheric model 4
Simulation of katabatic winds 12
On air-sea interactions in Antarctic coastal zone 24
Conclusions 32
Applications 34
References 36

IV DYNAMICS OF THE ANTARCTIC ICE CAP

H. Decleir, Ph. Huybrechts, L. De Vos and F. Pattyn

Introduction 1
Development of a 3-dimensional time-dependent numerical model for Antarctica 2
Ice thickness measurements and ice dynamics in the Sør Rondane, Dronning Maud Land, Antarctica 29
References 49

V SIMULATIONS OF THE ANNUAL SEA-ICE COVER IN THE WEDDELL SEA

C. Demuth and J.P. Van Ypersele

Introduction 1
Sea-ice model: thermodynamic component 3
Sea-ice model: dynamic component 8
Geophysical data 10
Numerical aspects 12
Simulations 15
Conclusions 23
Applications 25
References 26
Figures 30

SCIENCE POLICY OFFICE
Research contract
nr ANTAR/01

ISOTOPIC COMPOSITION OF ICE FORMED BY WATER FREEZING

R. Souchez, J.L. Tison and R. Lorrain

LABORATOIRE DE GEOMORPHOLOGIE
UNIVERSITE LIBRE DE BRUXELLES
CP 160
AVENUE F.D. ROOSEVELT, 50
B-1050 BRUXELLES (BELGIUM)

BELGIAN SCIENTIFIC RESEARCH
PROGRAMME ON ANTARCTICA
SCIENTIFIC RESULTS OF PHASE ONE
(OCT 85 - JAN 89)
VOLUME III: GLACIOLOGY AND
CLIMATOLOGY

SUMMARY

This work analyses on the factors involved in apparent isotopic fractionation during water/ice phase changes. Stable isotopes of oxygen and hydrogen have been considered. A combined approach is an originality of this research. Models and computer simulations are used to predict the isotopic distribution in ice formed by water freezing in various environmental settings.

Development of a box diffusion model combined with the boundary layer concept leads to a possibility of determining freezing rates from the isotopic composition of the ice. The model is tested experimentally and the method successfully used in the interpretation of field results. Implications on antarctic glaciology are outlined.

CONTENTS

SUMMARY PAGE

I. CO-ISOTOPIC COMPOSITION OF ICE FORMED BY WATER FREEZING : A REVIEW. 1

II. OBJECTIVES OF THE RESEARCH PROGRAM 6

III. METHODS AND ANALYSES 7

1. Computer simulations 7

2. Cold room laboratory experiments 7

3. Sampling procedures 9

3.1. In the field 9

3.2. In the cold room laboratory 9

3.2.1. Crystallographic vertical profile
3.2.2. Co-isotopic sampling
3.2.3. Chemical sampling
3.2.4. Crystallographic horizontal thin sections

4. Analytical techniques 12

4.1. Crystalline texture and c-axis fabric 12

4.2. Stable isotope analyses 12

4.3. Chemical analyses 13

IV. FIELD WORK 14

1. Lake ice (Brussels) 14

2. First-year sea ice (Breid Bay - East Antarctica) 14

3. Multi-year sea ice (George VI Sound - Palmer Peninsula) 15

4. Basal ice 15

V. **RESULTS AND DISCUSSION** 17

1. Models of the stable isotope distribution in ice formed by water freezing. 17

1.1. The principles 17

1.1.1. Mixing occurs through diffusion and/or convection and homogenizes the whole liquid reservoir at all time (complete mixing)
1.1.2. Mixing occurs through diffusion only and a concentration gradient exists in the liquid reservoir (no convective mixing)
1.1.3. Mixing occurs through diffusion and convection but the latter is limited to the part of the reservoir outside a boundary layer (partial mixing)

1.2. The numerical models 20

1.2.1. The simple diffusion box model
1.2.2. Choice of the variables and adaptations for more complex models

1.3. Results of the simulations 24

1.3.1. Effect of the boundary layer thickness at a given freezing rate
1.3.2. Effect of the freezing rate with a given boundary layer thickness
1.3.3. Damping effect of the ice thickness on the freezing rate
1.3.4. Special case of a semi-infinite reservoir

2. Experimental tests of the model in a finite reservoir 28

2.1. Comparison between data and freezing rate determination in a previous work 28

2.2. Experimental tests in our laboratory 30

3. Investigations on lake ice as a further test 32

4. Growth rates in a first-year sea ice core from Breid Bay (East-Antarctica). 34

4.1. Crystalline structure of the ice cores from Breid Bay and sea ice typology 34

4.2. The deuterium profile 39

4.2.1. Estimation of the boundary layer thickness
4.2.2. Growth rate determination

VI. POTENTIAL APPLICATIONS 45

VII. GENERAL CONCLUSIONS 47

VIII. ACKNOWLEDGMENTS 48

IX. REFERENCES 49

I . CO-ISOTOPIC COMPOSITION OF ICE FORMED BY WATER FREEZING : A REVIEW

Until recently, analysis of stable isotopes (mainly oxygen) in the ice was principally used to deduce paleoclimatic records from ice cores, the fractionation coefficient during condensation processes in the cloud being a function of temperature (Dansgaard, 1964). Such analyses were performed on deep ice cores from the polar ice sheets (Dansgaard et al., 1982 ; Lorius et al., 1985 ; Jouzel et al., 1987). Close to the ice-bedrock interface, debris-rich ice was observed with interbedded debris layers and bubble-free ice layers generally present (Gow et al., 1979). This basal part of the ice sheet is often called the basal ice layer (BIL) in the literature. It has also been described at the margin of several ice caps. Lawson and Kulla (1978) have shown that the oxygen isotopic composition in the basal ice layer can be different from the one in glacier ice above. This fact is, following these authors, related to the fractionation occurring when water refreezes at the ice-bedrock interface. However, the study of only one isotopic ratio ($^{18}O/^{16}O$, in this case) is not relevant to apprehend the complexity of the processes involved.

Co-isotopic studies in ice, both in $^{18}O/^{16}O$ and D/H are not numerous in the literature. A linear relationship between δD and $\delta^{18}O$ for liquid and solid precipitation has been established by Craig et al.(1963) : $\delta D = 8\ \delta^{18}O + d$ with :

$$\delta^{18}O = \frac{^{18}O/^{16}O \text{ sample} - ^{18}O/^{16}O \text{ standard}}{^{18}O/^{16}O \text{ standard}} \times 10^{3}\ ‰$$

and

$$\delta D = \frac{D/H \text{ sample} - D/H \text{ standard}}{D/H \text{ standard}} \times 10^{3}\ ‰$$

The standard is V.S.M.O.W. (Vienna Standard Mean Ocean Water) and d is called the deuterium excess.

Glacier ice follows the same trend which is called the "precipitation effect", the regression line of slope 8 being known as the Meteoric Water Line (MWL).

In collaboration with Dr. J. Jouzel from the "Centre d'Etudes Nucléaires de Saclay", we performed co-isotopic analyses of bulk glacier ice and basal ice samples from polar and alpine environments, using an original analytical method giving the $^{18}O/^{16}O$ and D/H ratios on the same liquid droplet (Hageman and Lohez, 1978). Bulk glacier ice, snow and meltwater samples were invariably aligned on a MWL, whereas basal ice samples were sometimes aligned on another line, thereby revealing original fractionation processes during freezing.

In order to understand this slope due to a freezing effect we designed a model to calculate the isotopic concentration in ice and water at any time during freezing of a finite reservoir (closed system). In this model (Jouzel and Souchez, 1982), it was assumed that no fractionation occurred during melting (Moser and Stichler, 1980) and that freezing took place at a very slow rate, so that the observed apparent fractionation coefficients were always equal to the equilibrium ones (Rayleigh model). The following equation of the freezing slope was obtained :

$$S = \frac{(\alpha-1)}{(\beta-1)} \cdot \frac{(1000 + \delta_o D)}{(1000 + \delta_o {}^{18}O)}$$

in which :

S = freezing slope

α = equilibrium fractionation coefficient for deuterium = 1.0208 (Arnason, 1969)

β = equilibrium fractionation coefficient for oxygen 18 = 1.003 (O'Neil, 1968)

$\delta_o D$ = initial δ value of the water in deuterium

$\delta_o {}^{18}O$ = initial δ value of the water in oxygen 18

Thus the freezing slope only depends on the equilibrium fractionation coefficients and on the isotopic composition of the water before freezing. The more negative being the initial water, the lower is the freezing slope. On the other hand, the model

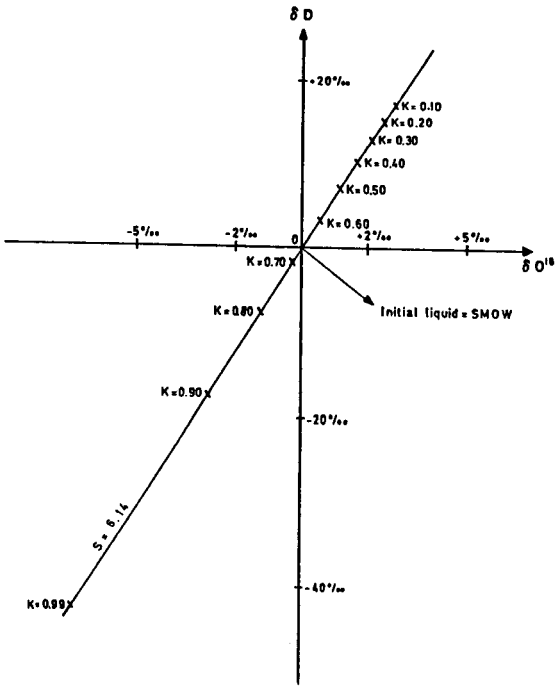

Fig.1. δ values of ten successive fractions of ice formed during the freezing of S.M.O.W. (from Jouzel and Souchez, 1982).

Fig.2. The isotopic composition of water (1 to 6) and ice (7 to 14) during freezing experiments with different initial waters. The straight lines are the calculated slopes from the model. The black dots are the calculated ice values at 95 % freezing. Water samples are denoted by circles, ice samples by crosses (from Souchez and Jouzel, 1984).

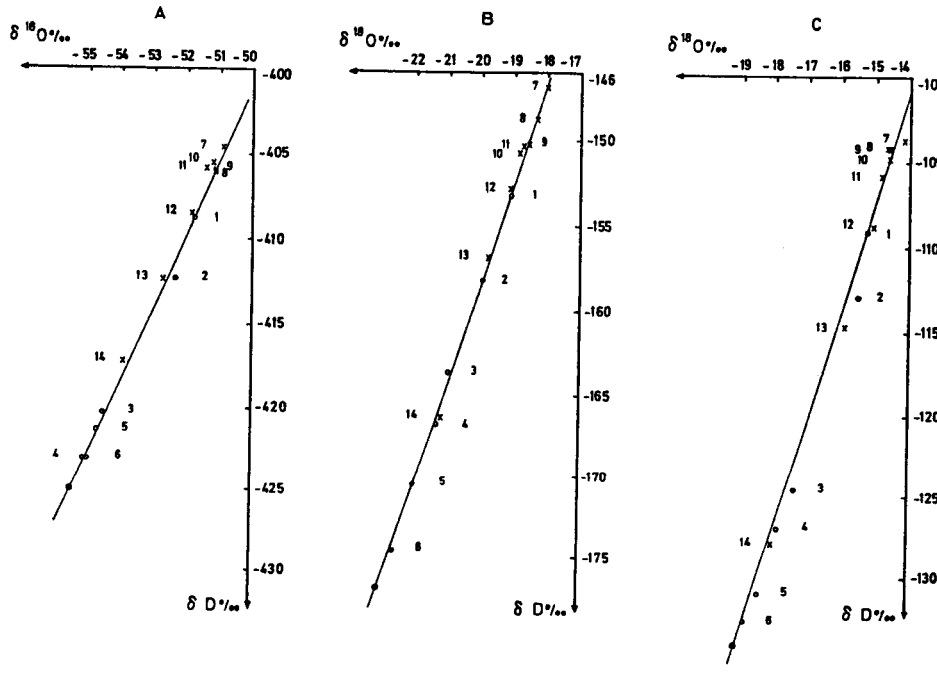

shows that the position of a sample on the line is a function of the percentage of freezing in the reservoir. Figure 1, from Jouzel and Souchez (1982), shows the δ values of ten successive fractions of ice formed during the freezing of S.M.O.W. as it is calculated by the model. The first frozen fractions are enriched in heavy isotopes compared to initial water, whereas the last frozen fractions are depleted in heavy isotopes. It is clear that even in this simple condition, i.e. the freezing of water in a closed system with isotopic equilibrium (allowing the application of the Rayleigh model), ice layers can be either isotopically enriched at the beginning of the process or isotopically impoverished at the end, compared with the initial reservoir. Interpreting a positive shift of 3 ‰ in $\delta^{18}O$ as the signature of a freezing process, a method used previously, could thus not be relevant if the freezing slope is not displayed. On the other hand, if the amount of freezing is important in a closed reservoir, the ice can be impoverished rather than enriched in heavy isotopes. This confirms that the study of only a single isotopic ratio is not sufficient.

The next step was an experimental test of the model, by a controlled freezing of various meltwaters from alpine, arctic and antarctic ice having quite different initial isotopic values (figure 2, from Souchez and Jouzel, 1984). Experimental slopes were in very good agreement with the predictions from the model. However, the distance between points representing the same percentage of freezing and initial water on the line varies from one experience to another, indicating a possible effect of the freezing rate on the apparent fractionation coefficients (which are not in general equal to the equilibrium fractionation coefficients). The same authors have also shown, in this regard, that the freezing rate does not affect the value of the freezing slope.

Further theoretical developments were concerned with an open system model where the isotopic composition and the amount of water in the reservoir varied in the course of freezing (Souchez and Jouzel, 1984). The following equation for S was obtained :

$$S = \frac{\alpha\,(\alpha-1).(1+\delta_O D) \;-\; A/F(\delta_A D-\delta_O D)}{\beta\,(\beta-1).(1+\delta_O{}^{18}O) - A/F(\delta_A{}^{18}O-\delta_O{}^{18}O)}$$

in which :

δ_o = isotopic composition of the initial water
δ_a = isotopic composition of water entering the system
A = water input coefficient
F = freezing coefficient

It follows that :

- The water output coefficient does not affect the freezing slope
- The slope is changed only when the isotopic value of the water entering the system is different from the one of the initial water.

New field observations were explained in this context (Souchez and De Groote, 1985).

II. OBJECTIVES OF THE RESEARCH PROGRAM

The scientific work summarized in this report aimed at studying, both theoretically and experimentally, the factors involved in apparent isotopic fractionation during ice/water phase changes. Models and computer simulations can be used to predict the isotopic distribution in ice formed by water freezing in various environmental settings.

The fundamental role of the freezing rate was planned to be specially investigated in order to know if it is possible to deduce its value from the isotopic distribution.

Ice core sampling in the field was also an objective of the program. This could be particularly important to provide further tests of the models and to give rise to applications in the Antarctic.

It is believed that this approach is of significant interest in the study of the dynamics of ice sheets and in the investigation of the various mechanisms responsible for congelation and frazil sea ice formation in polar regions. A better understanding of these two fields of research is of primordial interest for the global changes model developed nowadays.

III. METHODS AND ANALYSES

1. COMPUTER SIMULATIONS

The numerical models developed in the next section have been written in Fortran IV and run on the Central Computer CDC-CYBER 855 of the University of Brussels. Execution times are dependent on the value of the freezing rate : a typical range for simulations in a closed system with a boundary layer of 0.08 cm is between 500 CP seconds execution time for a freezing rate of 2 cm h^{-1} and 47.000 CP seconds execution time for a freezing rate of 0.1 cm h^{-1}.

2. COLD ROOM LABORATORY EXPERIMENTS

In order to complete experimental tests of the model predictions, several freezing experiments were conducted in the cold room laboratory (temperature range from 0°C to -30°C) using the device shown on figure 3. It ensures the progression of a unidirectional freezing front in a cylindric reservoir filled with the initial water. The cooling system is a cryostat (JULABO FT401) with a temperature range of 0°C to -50°C, and an accuracy of ±0.5°C. The cooling liquid (ethanol) fills the upper reservoir. The heat sink allowing the freezing of the water sample placed in the lower reservoir (8 cm diameter and 10 cm height) occurs through a metallic plate equipped with circular O-rings ensuring the water- and air- tightness. The lower part of the device is connected to an expansion tube, accomodating volume variations due to the progression of the freezing front in the lower reservoir. The whole apparatus is insulated in a foam wall externally plastified to reduce exchanges with the cold room environment so that a macroscopic planar freezing front can be obtained.

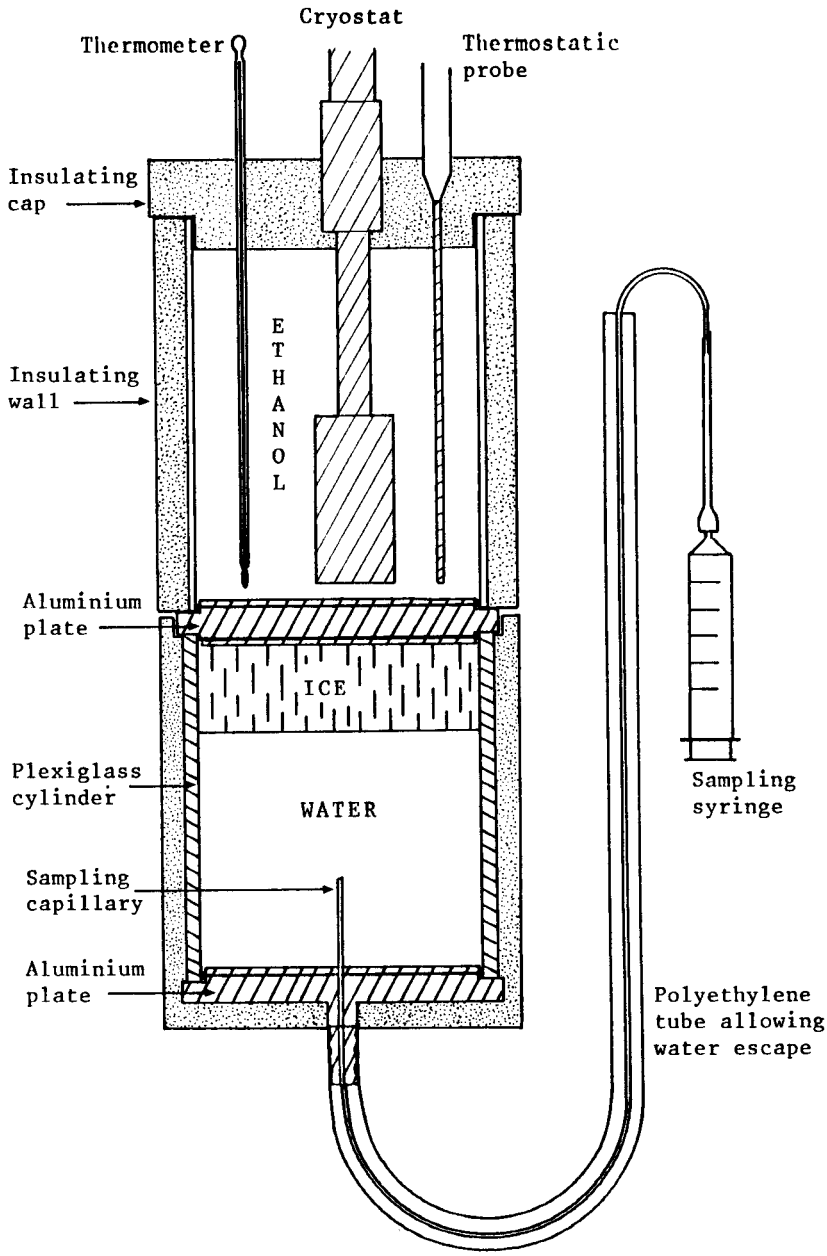

Fig.3. The experimental vessel used for unidirectional freezing of water.

A capillary tube, inserted through the expansion tube into the remaining water present in the cylinder, allows the sampling of water in the course of freezing.

In all the experiments the temperature of the cold room was kept at 0°C. To reach freezing rates compatible with natural growth rates (less than a few mm h^{-1}), the bottom of the upper reservoir is insulated with PVC slices of variable thickness or a thin layer of air is left between the metallic plate and the water sample.

3. SAMPLING PROCEDURES

3.1. In the field

Ice cores were sampled in the field using a S.I.P.R.E and a P.I.C.O ice auger collecting cores of 7.5 cm in diameter and up to 80 cm of individual length during each run. The P.I.C.O.-system is more adequate to use in remote areas, being much lighter to handle.

The samples were immediately transferred in polythene bags to avoid external contaminations and placed in portable freezers below -15°C. This prevented any brine migration and drainage (mainly in sea ice) during transport to our cold laboratory in Brussels. For long distance transportation the polythene bags were inserted in cylindric cardboard containers covered with an aluminium paper-sheet, internally and externally.

3.2. In the cold room laboratory

All the cores were sampled following the same procedure using standard methods to reduce contaminations at the noise level of the measuring apparatus (Fig.4).

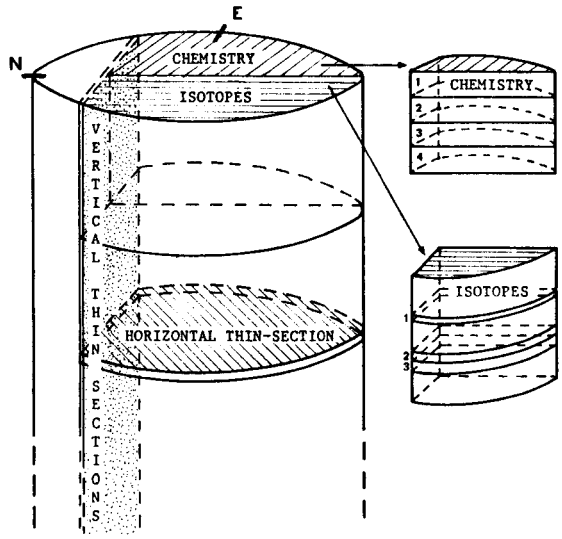

Fig.4. Sampling diagram of the ice-core.

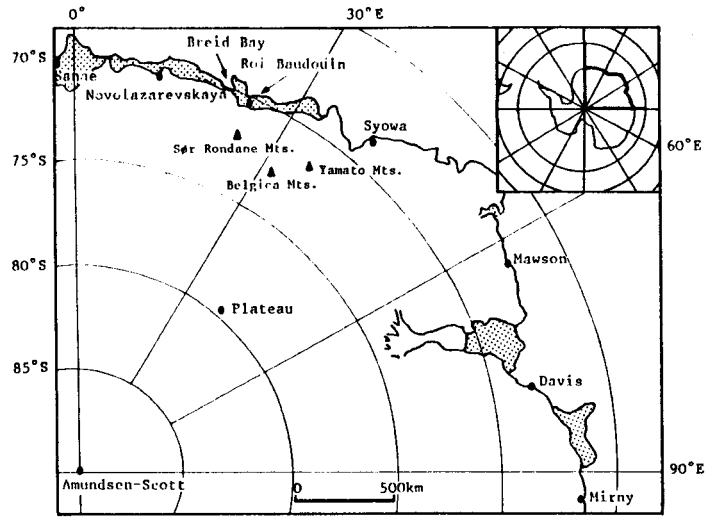

Fig.5. Location of the Breid Bay area in East Antarctica.

3.2.1. Crystallographic vertical profile

A continuous profile of vertical thin sections is always performed on the whole core to provide a decision plan for the isotopic and chemical sampling, on the base of the ice typology. Therefore a lateral cylindric segment is cut on the length of the core and fixed on a 10 cm/10 cm glass plate with a few droplets of water. After reducing the thickness of each sample to about 4 mm with the saw and obtaining a smooth surface using a sliding microtome, the thin section of ice is removed from the glass plate, reversed and placed on another glass plate. It is then reduced to a thickness of 800 to 400µm with the microtome, and viewed between crossed polaroids.

3.2.2. Co-isotopic sampling

One half of the remaining core is sampled in selected spots for co-isotopic analyses in deuterium and oxygen-18. The small amounts of ice necessary for the mass spectrometer measurements (0,3 ml) are also collected with the microtome, allowing a precise location of the samples and the achievement of a detailed profile when required. Usually, a thickness of 150µm (1,5 to 2 ml) is cut in successive runs of 40µm each. The residue of each run is collected with a fine brush in a Petri box. Melting occurs at room temperature and the liquid is immediately transferred in a small test-tube sealed to avoid any significant exchange with the atmosphere that could alter the isotopic composition.

3.2.3. Chemical sampling

The other half of the core is cut in 0.5 cm or 1 cm thick slices with a non-contaminating band-saw. The samples are then conserved in polythene containers, until melted for major cation analyses.

3.2.4. Crystallographic horizontal thin sections

At different levels in the core, horizontal thin sections are performed in a way similar to the one described in section 3.2.1.

4. ANALYTICAL TECHNIQUES

4.1. Crystalline texture and c-axis fabrics

Mean crystal diameter and mean crystal elongation have been measured on vertical thin sections of the cores at regularly spaced intervals and in a few selected horizontal thin sections. The crystal diameter is defined as $d = (L.w)^{1/2}$ where L is the maximum dimension of the crystal and w the value measured at right angles to L (Weeks and Ackley, 1986). The crystal elongation is the L/w ratio. In all cases, measurements were made under a 16x magnification binocular and taken on at least 40 individual crystals to ensure a statistically valid mean value.

Optic axis orientation was performed in horizontal thin sections at regular intervals of approximately 5 cm and in a few vertical thin sections, using a four axis universal stage. A computer program designed by our laboratory automatically plots the optic axes of the ice crystals on the lower Schmidt hemisphere. It calculates the "eigen-vector" and the "best-plane" of the distribution (Franssen and Kummert, 1971) and gives the density diagrams following the method proposed by Kamb (1959). Recent improvements with a more valid statistical method (Dudley et al., 1975) allow discrimination between real clustering of c-axes and fake maxima resulting from the sampling procedure.

4.2. Stable isotope analysis

The samples for co-isotopic analyses were transferred to the Centre d'Etudes Nucléaires de Saclay (Laboratoire de Géochimie Isotopique) in France which is equipped with twin mass-spectrometers specially designed to measure deuterium and oxygen-18 concentrations simultaneously on the same liquid drop. The accuracy of the method is ± 0.5 ‰ on δD and ± 0.1 ‰ on $\delta^{18}O$.

4.3. Chemical analyses

Concentrations in major cations (Na, K, Ca, Mg, Sr) were measured, on special occasions, using a Perkin Elmer atomic absorption flame spectrophotometry apparatus with an accuracy of ± 10 ppb to ± 50 ppb depending on the element considered.

IV. FIELD WORK

1. LAKE ICE

A cold period in Belgium of about 5 weeks during February-March 1986 provided a good opportunity to sample lake ice and so to test the predictions made by some of the models developed in the framework of this program.

Nine cores having a thickness varying between 14 and 20 cm were sampled near Brussels in the Forêt de Soignes. Three of them were treated as described above, and the isotopic profiles compared to the results of the relevant computations and to the meteorological data.

2. FIRST-YEAR SEA ICE

Thanks to professor A. Decleir and M. De Vos, from the Vrije Universiteit Brussel, and to the National Institute of Polar Research from Japan, four sea ice cores were sampled at Breid Bay, during December 1986, as an activity programmed in the JARE 28 Antarctic field season. Breid Bay, close to the japanese station Syowa in East Antarctica, was totally ice free during the previous summer so that the ice cores retrieved are undoubtedly first-year sea ice. The sampling site (70°13'S and 23°47'E) was located in a small bay approximately 30 miles from the ice-shelf border near the old belgian Station Roi Baudouin (fig. 5).

3. MULTI-YEAR SEA ICE

During the Austral summer 1987-1988, Dr. J.-L. Tison has conducted a field program in collaboration with the British Antarctic Survey in the Antarctic Peninsula area (figure 6). Thirteen cores of multi-year sea ice and of surface shelf ice were brought back from the major rifts and from the Eklund Island polynia located in the southern part of George VI ice-shelf (stippled area on figure 6), close to Ronnie Entrance. These cores arrived in Brussels in June 1988 and are now being processed. Removal of salts from the melted samples is required prior to isotopic analyses.

4. BASAL ICE

The sampling of debris-rich basal ice from the Antarctic Peninsula in the surroundings of the summer British base of Fossil Bluffs, was foreseen in the 1987-1988 field program. Unfortunately, due to bad weather conditions and logistical constraints, this work could not be achieved. However, recently (February 1988), in collaboration with the Laboratoire de Glaciologie de Grenoble (Dr. J.-R. Petit) and the Laboratoire de Géochimie Isotopique de Saclay (Dr. J. Jouzel), Dr. R. Souchez sampled basal ice from an antarctic ice core in Terre Adelie. This core was performed in 1987 by the French Antarctic Expeditions and is named C.A.R.O.L.I.N.E. (Coastal Antarctic Record of Last Interglacial Natural Environment). It gives a complete profile through an ice sheet marginal zone, not far from the flow line measured between Dome C and base Dumont d'Urville (IAGP flow line), and reaches the bedrock at 82 m depth. More than 150 samples were collected in the last debris-rich 7 meters of the core and are now being processed.

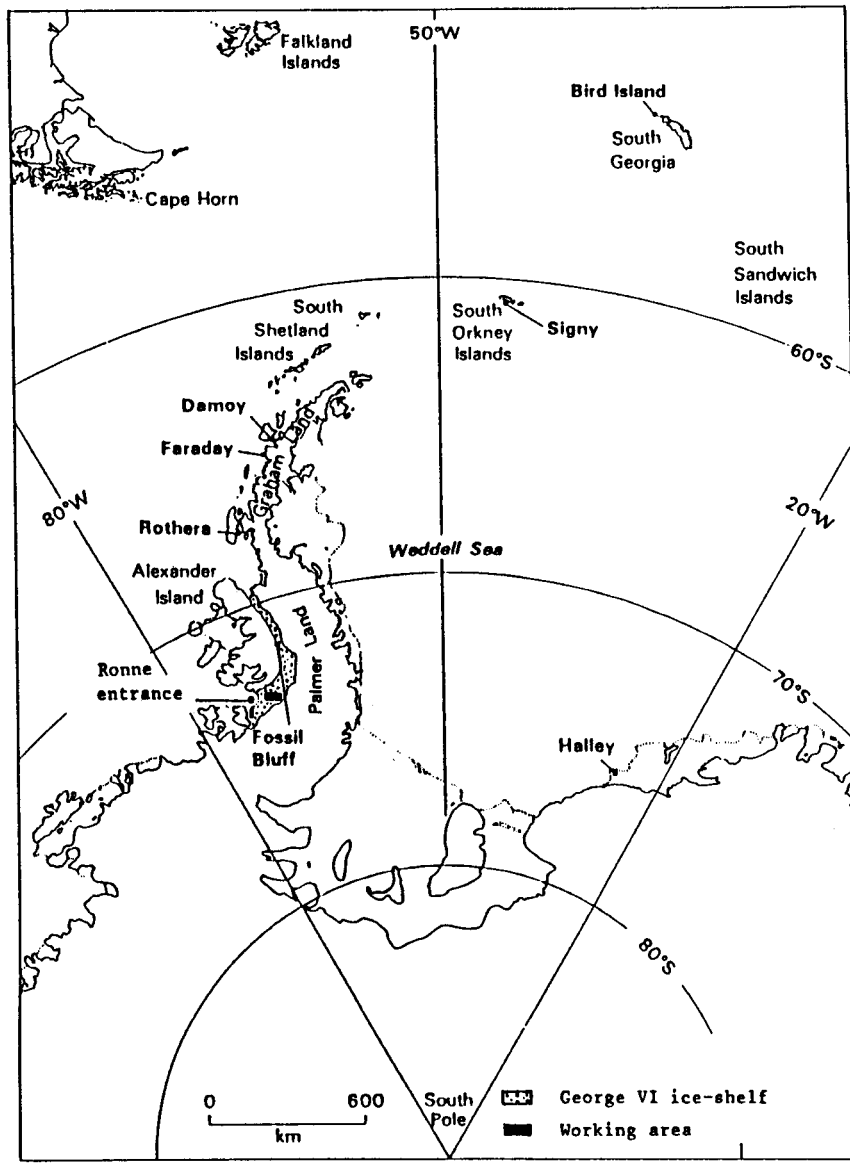

Fig.6. Location of the working area on the George VI ice shelf in the Antarctic Peninsula (from British Antarctic Survey, Annual Report 1984-85, Natural Environment Research Council, 1985.)

V. RESULTS AND DISCUSSION

1. MODELS OF THE STABLE ISOTOPE DISTRIBUTION IN ICE FORMED BY WATER FREEZING

1.1. The principles

Modelling of the redistribution of isotopic species during water freezing is mathematically equivalent to the modelling of the redistribution of a solute during solidification, a problem extensively studied for preparation of materials by zone melting (Tiller et al., 1953).

Distribution of a heavy isotopic species in ice during water freezing is related to the distribution in the liquid immediately adjacent to the freezing front. Since diffusion in the ice is slow ($\approx 10^{-11}$ cm^2 sec^{-1}), the distribution produced in the ice can be obtained from knowledge of the variations in the liquid at the interface. These variations depend on mixing that occurs in the reservoir by diffusion and by convection.

Three main patterns can be observed in a finite reservoir :

1.1.1. Mixing occurs through diffusion and/or convection and homogenizes the whole reservoir at all time (complete mixing) :

A uniform concentration is maintained in the reservoir and a Rayleigh distribution (Dansgaard, 1964) is obtained in the ice (figure 7a):

$$(1+\delta_{ice}) = \alpha(1+\delta_{o})f^{\alpha-1}$$

in which :

$1+\delta_{ice}$ = R_{ice} is the isotopic ratio in ice,

$1+\delta_{o}$ = R_{o} the isotopic ratio in the initial water,

f = the remaining liquid fraction,

α = the equilibrium fractionation coefficient.

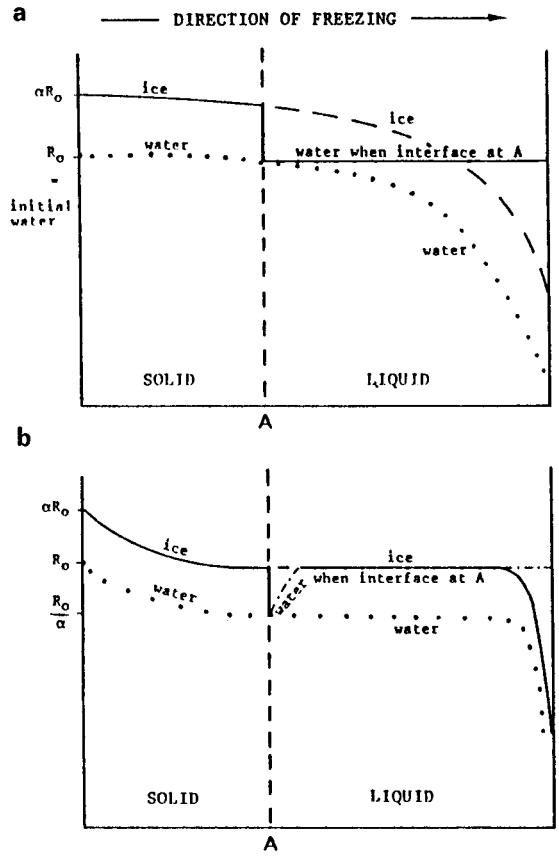

Fig.7.

Isotopic distribution in ice and water during unidirectional water freezing :

a) Complete mixing occurs through diffusion and/or convection and homogenizes the whole reservoir at all time (Rayleigh distribution in the ice).

b) Mixing occurs through diffusion only and a concentration gradient exists in the reservoir ahead of the freezing front.

(from Souchez and Tison, 1987)

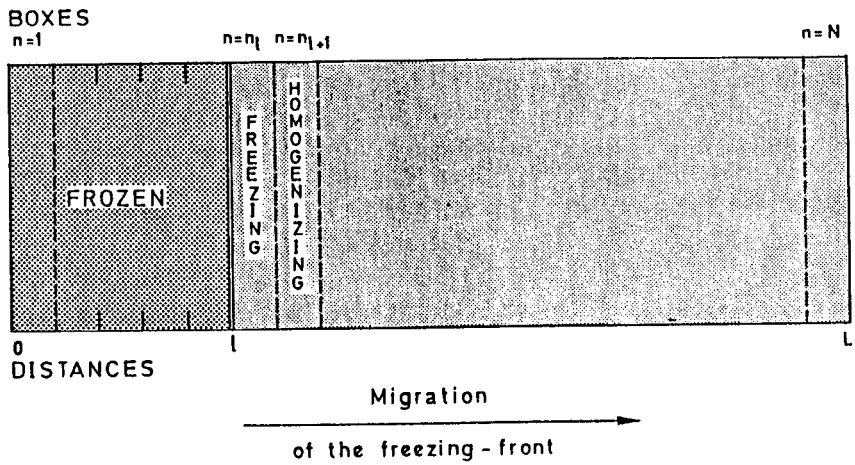

Fig.8. Diagram of the box diffusion model

1.1.2. Mixing occurs through diffusion only and a concentration gradient exists in the reservoir (no convective mixing) :

Ice has an initial isotopic ratio $R_{ice} = \alpha.R_{o}$. Equilibrium fractionation always occurs at the interface. Water at the interface is depleted in the heavy isotope and a concentration gradient is established. Diffusion of the heavy isotope will start from the main body of water. A steady-state may occur in which the input into the diffusion layer is equal to the output into the ice (figure 7b). The initial transient is the region in which the isotopic ratio in ice falls from its initial value of αR_{o} to the steady-state R_{o}. A terminal transient occurs when the ice-water interface approaches the end of the reservoir so that the diffusion necessary to maintain steady-state freezing is no longer possible.

1.1.3. Mixing occurs through diffusion and convection but the latter is limited to the part of the reservoir outside a boundary layer (partial mixing) :

A zone in which transport takes place only by diffusion always exists adjacent to the ice-water interface as a boundary layer of thickness BLT. Because of the existence of this boundary layer, the uniform concentration throughout all the water is not attained, and this will affect the distribution in ice. The thickness of this boundary layer depends upon the amount of mixing present in the liquid. The isotopic distribution in the ice is similar to that for the case of complete mixing (1.1.1.) except for an initial transient. This last pattern is the most probable in natural environments.

The general shape of the curves described above and drawn in figure 7, will be affected by several parameters like the initial water value, the diffusion coefficients, the rate of freezing, the length of the reservoir and the boundary layer thickness (BLT). The effect of these parameters has been studied using the appropriate numerical models, all derived from a simple box diffusion model.

1.2. The numerical models

For the one dimensional case in which growth proceeds by the movement of a plane interface separating liquid and solid, and in the absence of convection, the redistribution of solute during solidification has been analytically calculated by Tiller et al. (1953) and Smith et al. (1955). However, if a boundary layer is introduced, such an approach is quite complex, particularly if the freezing rate varies during the freezing phase. Therefore we preferred to develop a numerical approach using a simple box diffusion model. This diffusion model will first be described, and then the adaptations leading to the derived numerical models taking the other parameters into account.

1.2.1. The simple diffusion box model

Figure 8 shows a sketch of the box model used to simulate unidirectional freezing in a cylindric reservoir. The variables used in the text are also mentioned. The diffusion time step will be noted t and the time for the freezing of one box T. All the developments will be presented in terms of concentrations (C) but are still valid in terms of isotopic ratios (R).

In Nature, the process is a continuum : as soon as freezing starts, the liquid at the interface is depleted in heavy isotopes and diffusion occurs from the bulk reservoir to compensate the deficit. A computer simulation of this process needs a two-stage discretisation :

a) Freezing of the box "n_1" :the box thickness is calculated so that, given the diffusion coefficient and the freezing rate, only the box n_{1+1} homogenizes when the box n_1 freezes (see also 1.2.2.). In that case, the box n_1 freezes in equilibrium with the box n_{1+1} and the concentration in heavy isotopes in the two boxes, after freezing of box n_1, is given by :

$$C_n(\text{ice}) = \alpha\left[\frac{C_{n_1} + C_{n_{1+1}}}{2}\right]$$

$$C_{n_{l+1}}(\text{liquid}) = \left[2 - \alpha\right]\left[\frac{C_{n_l} + C_{n_{l+1}}}{2}\right]$$

b) Box to box diffusion from the end of the reservoir to box n_{l+1}: this diffusion process is controlled by Fick's law, and proceeds during a certain time lapse (a certain number of diffusion time steps), depending on the freezing rate.

The Fick's equation :

$$\frac{\delta C}{\delta t} = D \cdot \frac{\delta^2 C}{\delta x^2}$$

in which : C = concentration
x = distance
D = diffusion coefficient

can be written in a discrete form as :

$$\frac{C_n^{t+1} - C_n^t}{\Delta t} = \frac{D}{\Delta x} \cdot \frac{(C_{n+1}^t - C_n^t) - (C_n^t - C_{n-1}^t)}{\Delta x}$$

or :

$$C_n^{t+1} = C_n^t + B\,(C_{n+1}^t + C_{n-1}^t - 2C_n^t) \qquad (1)$$

with :

$$B = \frac{D\Delta t}{\Delta x^2}$$

For the first liquid box, where there is no diffusion from the left, equation (1) becomes :

$$C_n^{t+1} = C_n^t + B\,(C_{n+1}^t - C_n^t) \qquad (2)$$

and for the last liquid box, where there is no diffusion from the right :

$$C_n^{t+1} = C_n^t + B\,(C_{n-1}^t - C_n^t) \qquad (3)$$

1.2.2. Choice of the variables and adaptations for more complex models :

a) The **diffusion coefficient (D)** is taken in the program as 1.1 x 10^{-5} cm^2 sec^{-1} (Wang et al., 1953).

b) The **isotopic values of the initial water ($\delta_o D$ and $\delta_o {}^{18}O$)** are given as data in the program.

c) The **length of the reservoir (L)** is also fixed in the program. If it is taken one or two orders of magnitude higher than the ice thickness considered, the study of the case of a semi-infinite reservoir becomes possible.

d) The **box thickness (i.e. the number of boxes in the reservoir, N)** : as previously shown, the box thickness must be chosen so that when the box n_1 freezes, only the box n_{1+1} homogenizes. Therefore :

$$C_n^{t+1} = \frac{C_n^t + C_{n+1}^t}{2} = \frac{C_n^t}{2} + \frac{C_{n+1}^t}{2}$$

Applying equation (2) we have :

$$C_n^{t+1} = \frac{C_n^t}{2} + \frac{C_{n+1}^t}{2} = C_n^t + \frac{1}{2}(C_{n+1}^t - C_n^t) = C_n^t + B\,(C_{n+1}^t - C_n^t)$$

it follows that :

$$B = \frac{1}{2} = \frac{D\Delta T}{\Delta x^2}$$

the length of homogenization (length of 1 box) is thus :

$$\Delta x = \sqrt{2D\Delta T} \qquad (4)$$

If V is the freezing rate :

$$\Delta T = \frac{\Delta x}{V}$$

and equation (4) becomes :

$$\Delta x = \frac{2D}{V}$$

N, the number of boxes in the reservoir, is :

$$N = \frac{L}{\Delta x} = \frac{L}{2D/V} = \frac{LV}{2D} \qquad (5)$$

This calculated value of N is a minimum value. Chosing a higher N will slightly improve the accuracy of the results.

e) The diffusion time step (t) is submitted to two constraints :

- the diffusion time step must be smaller than the freezing time of one box. Usually, a value of P = 4 is taken in :

$$\Delta t = \frac{\Delta T}{P}$$

This value is considered as large enough for the solutions of the diffusion equations to converge. P is the number of diffusion steps the computer will achieve after freezing of box n and before freezing of box n+1. One diffusion step consists in using the diffusion equations from box to box throughout the whole liquid reservoir.

- To apply the diffusion equation, B must be less than 1 ; usually it is taken as 0.5.

As :

$$B = \frac{D\Delta t}{\Delta x^2} = \frac{D\Delta T}{\Delta x^2 P} = \frac{D}{PV\Delta x} = \frac{ND}{PLV}$$

We have :

$$P = \frac{ND}{BLV} \qquad (6)$$

If the value obtained for P from (6) is lower than 4, the computer will still consider that P = 4 to satisfy the first constraint.

f) The freezing rate (V) must also be fixed in the program. However, it is most unlikely to remain constant in Nature, due to the increasing thickness of the ice cover with time and to variations of the air temperature. The program is thus adapted to be able to change the freezing rate at any time.

g) The boundary layer thickness (BLT) : to conceive the numerical model simulating partial mixing, a value of the boundary layer thickness must be given to the computer. After each diffusion step, the liquid boxes ahead of the boundary layer are homogenized.

h) **The open or closed nature of the system** : In the case of a closed system, where no water input occurs, a new isotopic value equal to the mean value of all the remaining liquid boxes is affected to each box ahead of the boundary layer, before the next diffusion step occurs.

For an open system, the value resulting from the mixing of initial water with the new water input is placed in all the liquid boxes ahead of the boundary layer, before the next diffusion step occurs.

1.3. Results of the simulations

1.3.1. Effect of the boundary layer thickness at a given freezing rate :

Results of the computing with different values of BLT, for a given freezing rate of 5 mm h^{-1} and a total length L of 10 cm, are shown on figure 9a (from Souchez et al., 1987). If BLT = 0, a Rayleigh distribution is displayed. For BLT $\geq$ 1 cm, the curve is identical to the one obtained by a simple diffusion process. For lower values of BLT, a part of the initial transient exists, followed by a Rayleigh-type distribution with an apparent fractionation coefficient different from the equilibrium value. The part of the initial transient common for all the curves is very well approximated by :

$$\delta_s = \delta_o + (1 + \delta_o)(\alpha - 1)\, e^{-\frac{\alpha V}{D} x} \qquad (7)$$

where x is the frozen thickness. This equation is similar to the one used in solute freezing (Tiller et al., 1953). The difference lies in the fact that selective incorporation of isotopes is considered instead of preferential rejection of solutes.

1.3.2. Effect of the freezing rate with a given boundary layer thickness :

The curves on figure 9b are computed for a fixed BLT of 0.08 cm and freezing rates ranging from 1 to 20 mmh^{-1} (L = 10 cm). The initial transient is different for each curve and it is clearly

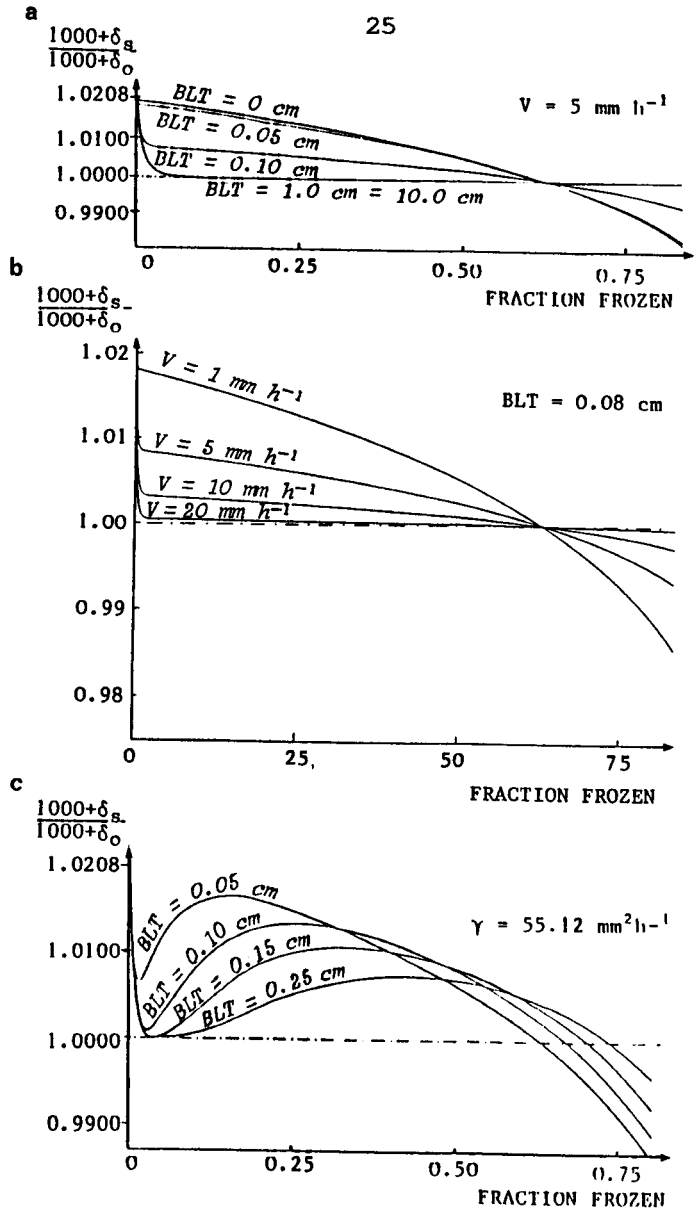

Fig.9. Results from the computer simulations in a finite reservoir :

a) effect of the boundary layer thickness at a given freezing rate (V = 5 mm h^{-1})

b) effect of the freezing rate with a given BLT (0.08 cm)

c) effect of the boundary layer thickness for a decreasing freezing rate with a given γ value

δ_S and δ_O are the isotopic values (deuterium) in the ice and in the initial water respectively.

(partly from Souchez et al., 1987)

seen that for higher freezing rates, diffusion in the boundary layer is less efficient to compensate the depletion of heavy isotopes at the interface, the δ value in the ice being lower at a given distance in the reservoir. Above 20 mm h^{-1}, in this case, a steady state is displayed.

1.3.3. Damping effect of the ice thickness on the freezing rate :

Freezing rates are usually dependent on the thickness of the ice already formed, i.e. the position of the interface at time T. Applying heat transfer theory and experimental work, Terwilliger and Dizio (1970) found that, for a fixed temperature at the cold end, the interface position x at time T is given by $x = (2\gamma T)^{1/2}$ where T is the time elapsed since the beginning of freezing and γ, a constant that can be found from the slope of a linear least squares plot of x versus $T^{1/2}$. The freezing rate is thus related to the increase of the interface position by :

$$V = \frac{\Delta x}{\Delta T} = \frac{\gamma}{x}$$

Introducing these varying freezing rates in our model, a δD distribution curve in ice is obtained for given γ and BLT values (figure 9c, from Souchez et al., 1987). This curve shows an initial drop, a minimum and a reverse gradient before the Rayleigh-type decrease. For increasing values of BLT, the position of the minimum is changed and the reverse gradient decreases. Simulations for various ranges of γ and BLT values occurring in Nature indicate that, unequivocally, one curve corresponds to only one γ-BLT couple. In other words, for a given reservoir, once the position of the minimum and the value of the reverse gradient are determined, γ and BLT are known.

1.3.4. Special case of a semi-infinite reservoir :

When the length of the reservoir is several orders of magnitude higher than the thickness of ice formed one can consider that the δD value of the bulk reservoir remains constant in the course of freezing and equal to the initial water value. Figure 10a is

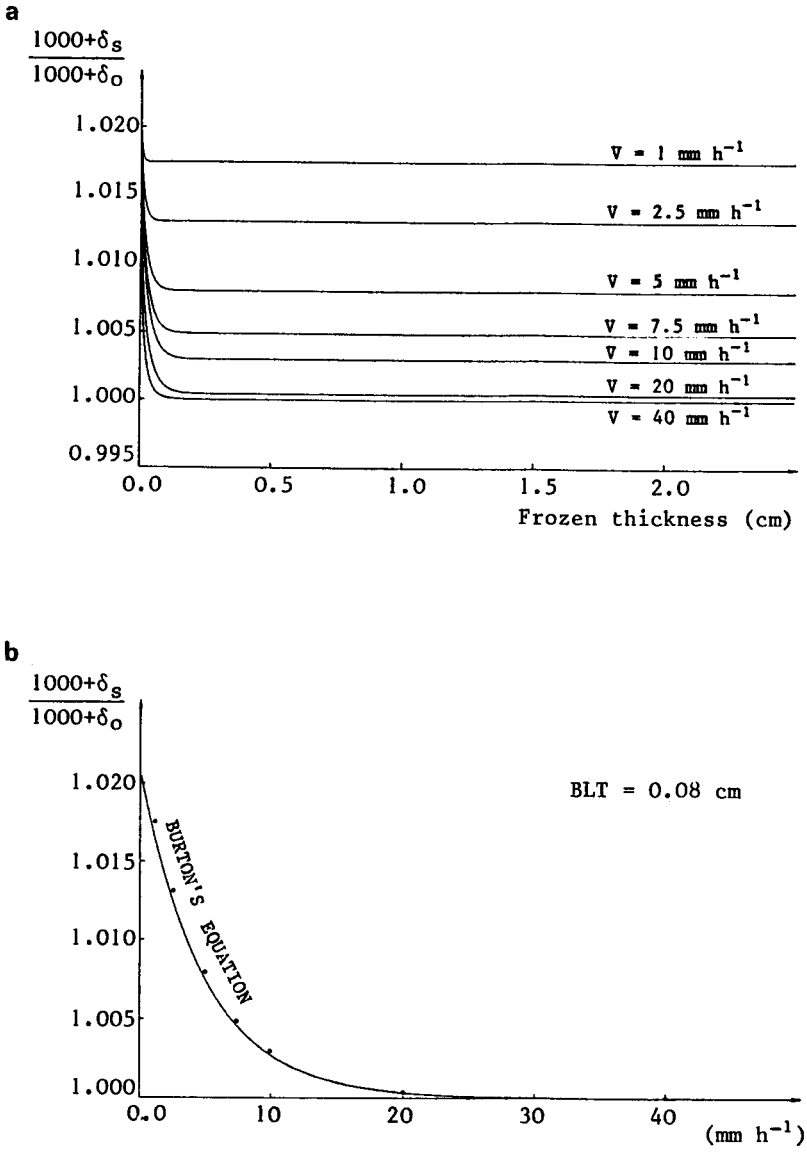

Fig.10. The special case of a semi-infinite reservoir :

a) effect of the freezing rate with a given BLT (0.08 cm). The isotopic distribution displays a steady state at a level depending on the freezing rate.

b) relationship between the freezing rate and the isotopic value of the steady state.The curve represents BURTON's equation, with BLT = 0.08 cm.

δ_s and δ_o are the isotopic values (deuterium) in the ice and in the initial water respectively.

equivalent to figure 9b, but in the case of a semi-infinite reservoir. The initial transient is still present, but the Rayleigh-type distribution is replaced by a steady-state at a given δD value depending on the freezing rate. If the freezing rate changes during the freezing process, a shift will occur towards another steady-state isotopic value in the ice in accordance with the new freezing rate. In this peculiar case, the relationship between the freezing rate and the isotopic composition in the ice can be very well approximated by an equation similar to Burton's equation (Burton et al, 1953) :

$$\frac{1000 + \delta_s}{1000 + \delta_o} = \frac{\alpha}{\alpha - (\alpha-1)e^{-BLT.V/D}}$$

where δ_s is the isotopic δ value in the ice. This equation is drawn on figure 10b (for BLT = 0.08 cm) together with the points representing the steady-state values for the different freezing rates.

2. EXPERIMENTAL TESTS OF THE MODEL IN A FINITE RESERVOIR

2.1. Comparison between data and freezing rate determination in a previous experimental work

In order to estimate an equilibrium value for the fractionation coefficient α for deuterium, Arnason (1969) measured δ values for ice formed in small quantity (a 2 mm thickness) in an experimental device at different freezing rates. Water was stirred during freezing. Ice thickness and stirring rate were the same in all Arnason's experiments. Thus a single x/D ratio in the equation of the initial transient (7) applies to all of them. This ratio can be obtained, from one point of a best fit curve drawn between the measured values, using the equation of the initial transient in its cumulative form. Taking an experiment with V = 1.4 mm h^{-1} (0.000039 cm sec^{-1}), x/D is equal to 980 sec cm^{-1}. Calculated

freezing rates for the other points on the curve using x/D = 980 sec cm^{-1} are compared with the freezing rates observed by Arnason (Table 1, from Souchez et al., 1987). A satisfactory agreement exists between the two. This shows that a prediction of the freezing rate is possible in cases where ice is formed in such small amounts that V can be considered as constant.

$\frac{1+\delta_s}{1+\delta_o}$ on best fit curve	Freezing rates deduced from Arnason	Freezing rates calculated from the equation of the initial transient
1.0204	1.4mm/h (0.000039 cm sec^{-1}) → x/D = 980 sec cm^{-1}	
1.0201	2.0 mm/h	2.4 mm/h
1.0199	4.0 mm/h	3.2 mm/h
1.0194	4.8 mm/h	5.0 mm/h
1.0186	8.6 mm/h	8.2 mm/h
1.0155	24.0 mm/h	22.2 mm/h
1.0116	48.0 mm/h	47.0 mm/h

TABLE 1. Comparison between observed and calculated freezing rates for Arnason's experimental work. (from Souchez et al.,1987)

2.2. Experimental tests in our laboratory :

Three unidirectional freezing experiments, using the experimental device described in section III.2., have been conducted with meltwaters from different antarctic ice cores. The initial water values were respectively :

1. $\delta D = -282.1$ ‰ $\quad \delta^{18}O = -34.65$ ‰
   (Plateau Station PS1)
2. $\delta D = -425.9$ ‰ $\quad \delta^{18}O = -54.20$ ‰
   (Plateau Station PS2)
3. $\delta D = -159.2$ ‰ $\quad \delta^{18}O = -18.30$ ‰
   (Roi Baudouin Station RB1)

The water was not agitated during the freezing experiments. Interface positions in the course of time were measured for each freezing experiment ; results show a linear relationship between the interface position and the square root of time in accordance with the heat transfer model from Terwilliger and Dizio (1970). At a minimum confidence interval of 0.99, the slope of the best fit line is identical in the three experiments and γ can be taken as 55.12 $mm^2\ h^{-1}$. From this, the hyperbolic decrease of the freezing rate can be calculated. Taking this decrease into account in the appropriate numerical model described above, with the appropriate initial water values, a theoretical δD distribution curve in ice can be obtained. Figure 11, (from Souchez et al., 1987) shows this curve for each experiment in solid lines.

The ice cylinder obtained in each experiment was sampled and analysed following the procedures described in sections III.3. and III.4. Results of the isotopic analyses in δD are plotted on figure 11 as open circles. In the three experiments, the minimum and the reverse gradient are observed and, for PS1, where more values were obtained at the onset of freezing, the initial drop is displayed.

A close agreement exists between model and experiment, indicating a possible use of the theory for determining freezing rates in Nature.

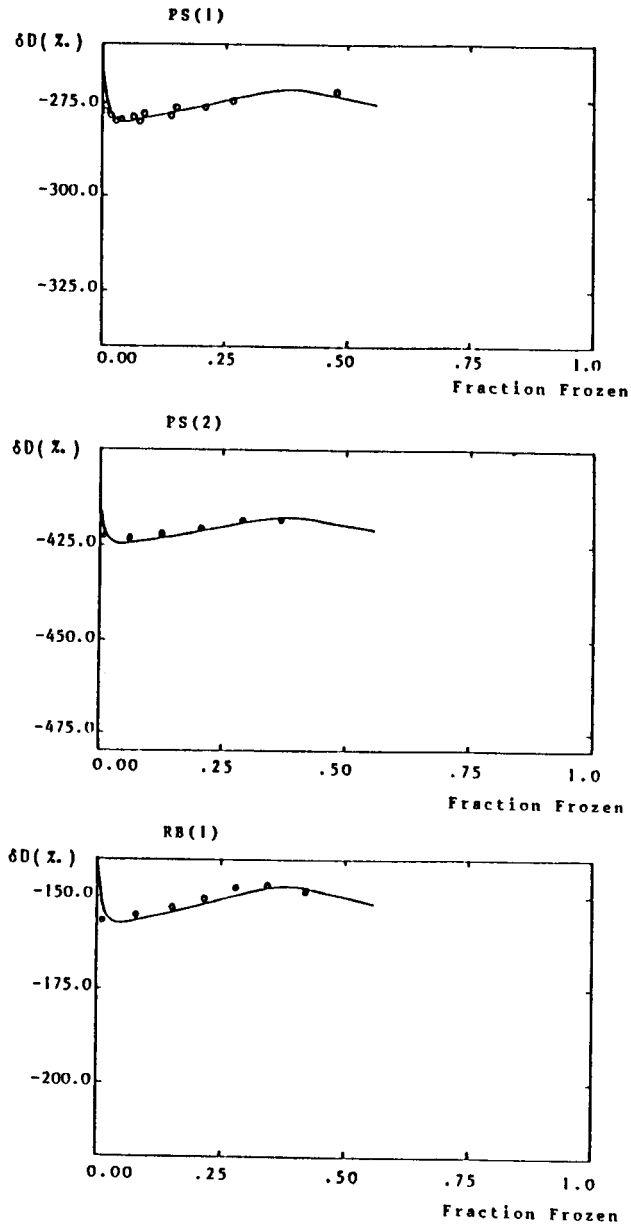

Fig.11. Theoretical curve (solid line) and experimental results (open circles) for the δD distribution in ice in the three experiments. (from Souchez et al., 1987)

3. INVESTIGATION ON LAKE ICE AS A FURTHER TEST :

As mentioned previously, lake ice was sampled in the surroundings of Brussels during the winter 1985-1986. The ice thickness was 2.0 cm on February 3rd and reached 4.4. cm when it was sampled on February 16th. The ice was sampled and analysed following the usual procedure. Eight isotopic values were obtained about 0.5 cm apart. The δD distribution of the points representing these values (open circles in figure 12, from Souchez et al., 1987) exhibits two minima connected with two cold waves present on the recorded ground surface minimum temperature curve. The δD distribution in this lake ice can be very well approached by a twofold simulation with $D = 10^{-5}$ cm^2 sec^{-1} and assuming $\gamma = 1.0$ mm^2 h^{-1} and BLT respectively equal to 3.0 cm and 4.5 cm. The increase in the boundary layer thickness implies a weaker convection. Knowing the value of γ, it is possible from $V = \gamma/x$, to calculate the freezing rate at any point. Integrating with $\gamma = 1$ mm^2 h^{-1}, it requires 239 h and 326 h to form respectively 2.0 cm and 2.4 cm of ice. The two cold waves present on the temperature diagram (figure 12) are separated from each other by a short maximum when the minimum ground surface temperature reaches +0.2°C after 10 freezing days. Thirteen days elapsed for the second cold wave before the sampling occurred. The two periods are thus in close agreement with the ones predicted from the isotopic study.

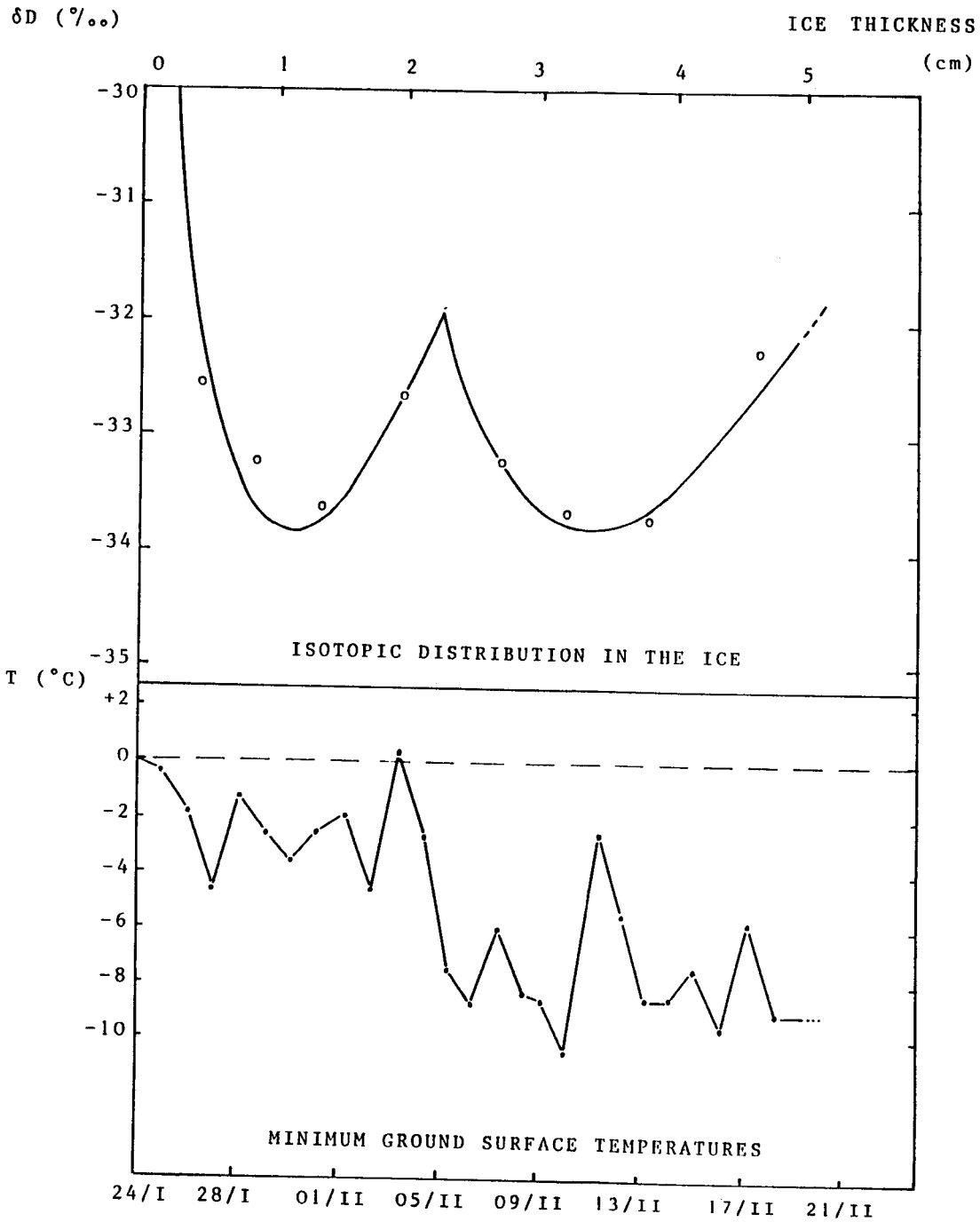

Fig.12. Theoretical curve (solid line) and sample values (open circles) for the δD distribution in the lake ice. The ground surface temperature curve is included. δD of the lake water is -46.5‰. (from Souchez et al., 1987)

4. GROWTH RATES IN A FIRST YEAR SEA ICE CORE FROM BREID BAY (EAST ANTARCTICA) :

Deuterium concentration studies of sea ice are not numerous in the literature. During an investigation of arctic sea ice, Friedman et al.(1961) found that cores collected on Ice Island T3 or on Drift Station Alpha exhibit negative δD values of -2 to -14 ‰. These values are due to the presence of a relatively thin layer of deuterium depleted water on parts of the surface of the Arctic Ocean during the summer. This layer is believed to form by the melting of snow and the mixing of this melt water with sea water. Gow and Epstein (1972) have reported on deuterium concentrations in regard to a special sea ice growth situation in McMurdo Sound, Antarctica.

Chemical analyses of sea ice were undertaken by Weeks and Lofgren (1967), Cox and Weeks (1975) and Nakawo and Sinha (1981) in order to deduce growth rates from the salinity distribution. Our present purpose is to show that the deuterium concentration profile of first-year sea ice can also be used to determine freezing rates. In fact, deuterium concentration is less sensitive to diffusion or drainage than the salinity profile.

4.1. Crystalline structure of the ice cores from Breid Bay and sea ice typology :

Different cores were taken within a few meters distance in the first-year sea ice of the Breid Bay area (see IV.2.). Since they exhibit essentially the same features, the isotopic profile of only one core is given here. The thickness of the ice was about 1.64 m with 0.40 m of dry snow overlying it, so that sea water was reached at a depth of 2.04 m.

A comprehensive sea ice types classification has been developed by Weeks and Ackley (1986) and Gow et al. (1987), among others. Three basic types are commonly described :

a) **Congelation ice** : is formed by direct freezing of sea water to the underside of a preexisting sea ice cover. It shows elongated crystals, both in vertical (columnar shaped crystals) and horizontal thin sections, and exhibits a characteristic substructure of ice plates and brine lamellae within each individual crystal. This substructure results from the dendritic ice growth interface that forms in response to the needs of the constitutional supercooling of sea water, caused by the build-up of brine at the ice/water interface.

b) **Frazil ice** : results from the free nucleation of crystals in the water column. Several processes have been proposed to explain this type of sea ice. Whatever the process in work, the crystals will ascend the water column under buoyancy and freeze together to form frazil ice generally characterized by a fine-grained, equidimensional texture lacking the ice plates and brine lamellae of the congelation ice.

c) **Snow ice** : occurs when snow containing interstitial water (meltwater, rain, sea water) freezes. It is necessarily restricted to the top of the ice cover and exhibits an equidimensional texture generally more bubbly and coarser grained than the frazil ice.

Snow ice and **frazil ice** are both called granular sea ice, due to their equidimensional texture. **Fine grained congelation ice** also occurs in sea ice cores. It shows the typical columnar growth of the congelation ice but at a smaller scale. As the thickness of each individual crystal is of the order of magnitude of the ice plates forming the substructure in coarser congelation ice, this last feature cannot be used to discriminate fine grained congelation ice from frazil ice. Other textural indications will have to be used in this purpose as shown below.

Figure 13 gives the crystalline structure of our selected core from Breid Bay. A major part of the profile consists in a fine-grained sea ice, with a mean crystal diameter ranging from 3 mm near the top to 1 mm at the bottom. This is typical of granular sea ice (Weeks and Ackley, 1986). However, the mean crystal elongation value fluctuating between 1.5 and 2.5 indicates a

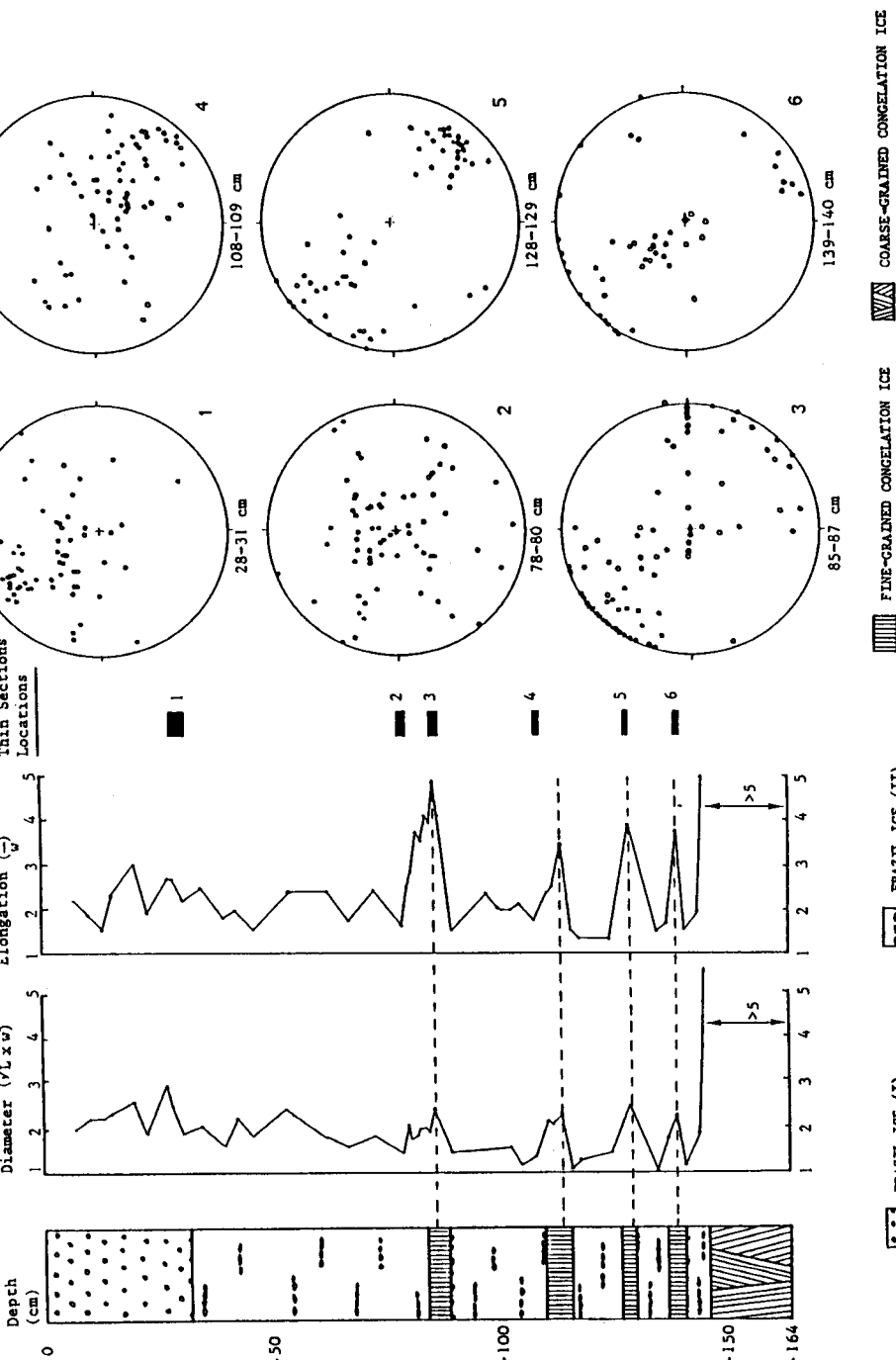

Fig.13. The crystalline structure of the selected first-year sea ice core from Breid Bay (East Antarctica). The mean crystal and the mean elongation parameters are measured in the vertical plane. The fabric diagrams are plotted in the horizontal plane; equigranular crystals are shown with open circles and elongated crystals with black dots.

slight lengthening in the vertical plane (figure 14a). It probably reflects the effect of recrystallisation when individual frazil or soaked snow crystals freeze together under a vertical thermal gradient. Indeed, when measured in the horizontal plane at different heights in the core, the mean crystal elongation is very close to 1 (equidimensional grains, figure 14b). Another reason for this lengthening in the vertical plane could be the tendency for the individual discoids of frazil ice nucleus to be stacked in a vertical position by the movement of slush pancakes against one another, as suggested by Weeks and Ackley (1986). However, this should lead to at least a partial clustering of c-axes in the horizontal plane, which is not observed (thin sections 1 and 2 in figure 13).

The upper 32 cm of the core mainly differ from the lower granular sea ice by a higher bubble content, clearly visible in transmitted light. These closely spaced spherical bubbles, with a diameter ranging between 0,1 and 1,5 mm, do not show any preferential spatial distribution. The higher bubble content and the top position of this 32 cm layer might be the distinctive characteristics of snow ice (Gow et al. 1987). However, the isotopic profile will make this assumption highly improbable.

The lower 18 cm section of the core shows a drastic increase in the mean crystal diameter and elongation corresponding to the typical columnar shaped crystals of the coarse grained congelation ice. Figure 14d clearly illustrates the transition zone between the lower granular sea ice layer and this congelation ice. Crystals of several cm length are often observed and the ice plates and brine lamellae substructure is commonly present in this bottom layer.

At four different levels in the profile, the mean crystal diameter and the mean crystal elongation simultaneously show a marked 2-to 3-fold increase. Although they do not display the typical ice plates/brine lamellae substructures these fine grained elongated crystals can be considered as congelation ice as indicated by their c-axis orientation. Indeed, whereas granular sea ice shows a pattern close to random (thin sections 1, 2 and 4 in

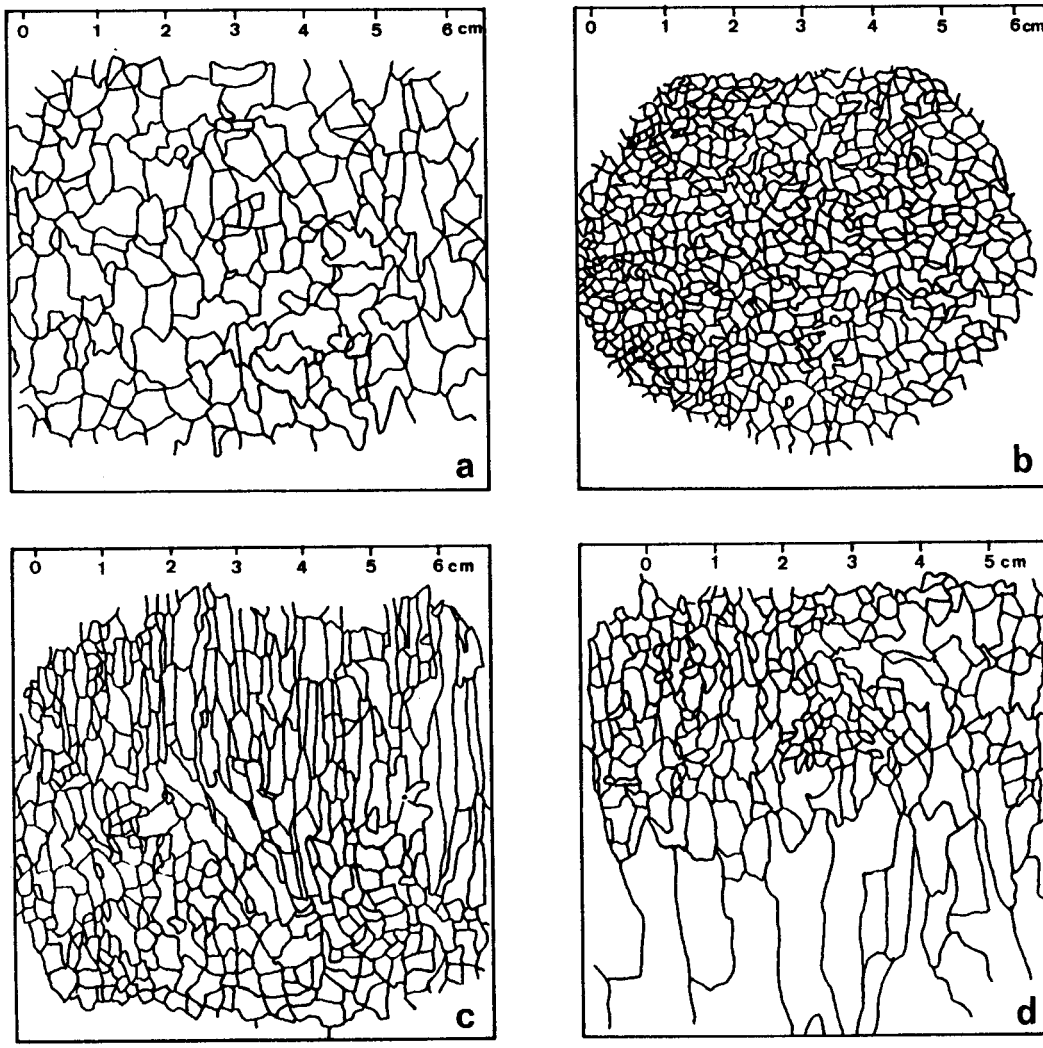

Fig. 14. Thin section drawings from Breid Bay ice core (grid = 1 cm) :

a) top frazil ice in vertical section (cm 32-36). Note the slight elongation in the vertical plane and the W-shaped crystals

b) lower frazil ice in horizontal section (cm 79). Note the equigranular structure and the smaller mean crystal diameter

c) transition zone between fine-grained congelation ice and frazil ice in vertical section (cm 85-90)

d) transition zone between frazil ice and coarse-grained congelation ice in vertical section (cm 144-149)

figure 13), these layers of coarser elongated crystals (black dots in thin sections 3, 5 and 6) show a strong concentration of c-axes close to or in the horizontal plane, a distribution typical of congelation ice. Figure 14c, illustrates the transition zone between fine grained congelation ice (above) and frazil ice (below) between 85 and 92 cm.

Thus, from the crystalline structure data summarized in figures 13 and 14, we can build the vertical section drawn in the left of figure 13 : the core mainly consists of granular frazil ice (77%) ; another 11% consists of coarse grained congelation ice located at the base of the core and the last 12% are fine grained congelation ice layers dispersed in the lower part of the granular frazil ice. This "sandwiching" of frazil between layers of congelation ice has also been described in Weddell Sea floes by Gow et al. (1987).

4.2. The deuterium profile :

Figure 15 shows the δD profile in our selected core from Breid Bay.

There is a general trend towards higher δD values as one proceeds from the top to the bottom of the ice core. Such a trend is understandable if the growth rate diminishes downwards since heavy isotopes are more incorporated in this case (cf. sections V.1.3.2. and V.1.3.4.). Using an equilibrium fractionation coefficient of 1.0208 (Arnason, 1969) and the δD value of -4,8 ‰ of sea water at Breid Bay (estimated from $\delta^{18}O$ and salinity measurements), the δD values at the very bottom closely correspond to the maximum possible shift : $\delta D_{ice} - \delta D_{water} = 20.7$ ‰ instead of 20.8 ‰. This means that the growth rate was nearly zero at the bottom of the core.

A small peak in the δD profile is present at the level of each of the four thin layers of fine grained congelation ice. The δD values are higher than in the surrounding frazil ice and increase as one proceeds from the first thin layer to the fourth one and finally to the coarse-grained congelation ice at the bottom.

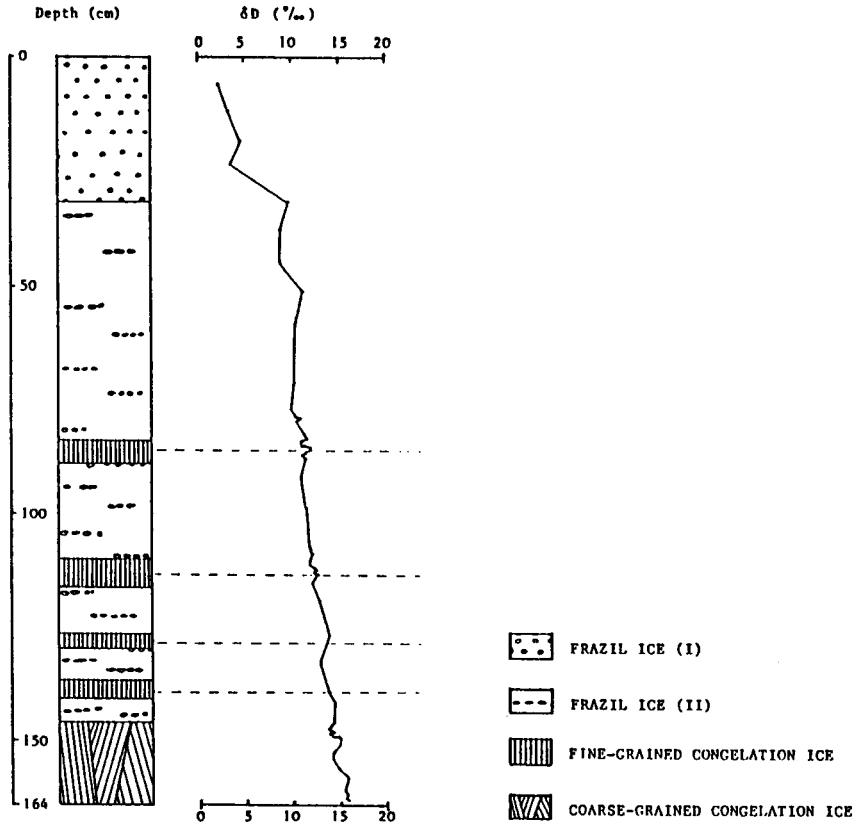

Fig.15. The deuterium profile in the selected core from Breid Bay.

Depth (m)	δD(‰)	Growth Rate (cm/day)	Deduced Surface temperature(°C)
0.86	11.8	2.29	-33.0
1.14	12.4	1.92	-36.5
1.28	13.7	1.16	-25.5
1.40	13.9	1.05	-25.0
1.52	14.2	0.89	-23.0
1.57	14.6	0.67	-18.0
1.61	15.6	0.15	-6.0

TABLE 2. Growth rates and deduced surface temperatures for four samples of fine grained congelation ice (depths : 0.86, 1.14, 1.28, 1.40 m) and three samples of coarse grained congelation ice (depths : 1.52, 1.57, 1.61 m)

We will only pay attention to congelation ice which formed by direct freezing of sea water to the bottom of an existing ice sheet i.e. by the downward progression of a freezing front in sea water, a necessary condition for applying the boundary layer model developed above.

4.2.1. Estimation of the boundary layer thickness :

To be able to deduce the growth rate from the δD value of a congelation ice layer, it is critical to estimate the boundary layer thickness.

In the Cox and Weeks (1975) study, the radioactive isotope ^{22}Na was used as a tracer and the salinity of both the ice and water was determined by sequentially measuring the gamma ray emission from different levels of the sample which was produced by unidirectional freezing. They found a negative linear relationship between $\ln(\frac{1}{k} - 1) - \ln(\frac{1}{k_o} - 1)$ and V, where k_o is the solute distribution coefficient at zero growth rate, k the solute distribution coefficient of the sample and V the growth rate (Weeks and Ackley, 1986). If V is expressed in cm sec^{-1} , the negative slope representing the ratio between the boundary layer thickness and the diffusion coefficient (BLT/D) has the value of 7243 sec cm^{-1} for growth rates higher than 20 10^{-4} cm sec^{-1} (figure 16).

In our sea ice core, local Na concentration measurements were performed in selected spots in order to determine appropriate values for k and k_o. Indeed, k_o can be taken as the ratio between the Na concentration at the bottom of the core - the isotopic value indicating a near-zero growth rate - and the Na concentration in sea water ; this gives $k_o = 0.0437$. For the first thin layer of congelation ice, which is the one formed at the highest growth rate, $k = 0.0524$. Using figure 16 derived from Weeks and Ackley (1986), the deduced freezing rate is higher than 20 10^{-4} cm sec^{-1} so that BLT/D can be taken as 7243 sec cm^{-1}.

A similar procedure can be used for the δD values. The equilibrium fractionation coefficient for deuterium $\alpha = 1.0208$ can be taken as equivalent to k_o. The ratio between the isotopic ratio

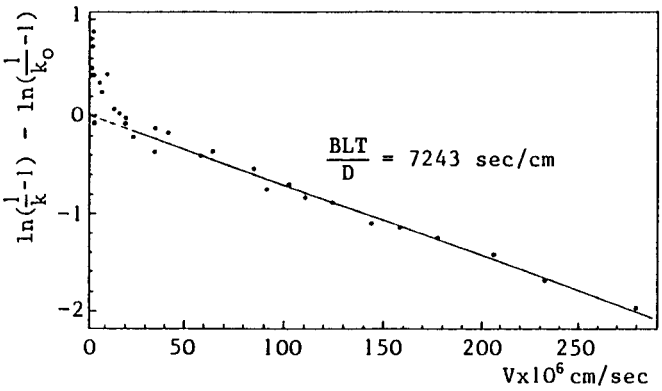

Fig.16. Relationship between distribution coefficient and growth rate (modified after Weeks and Ackley, 1982)

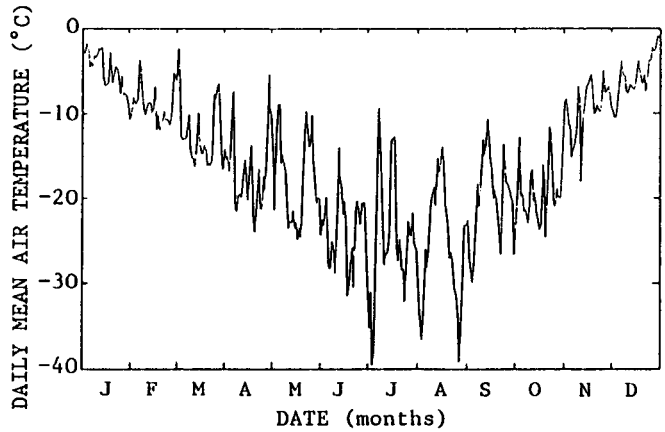

Fig.17. Daily mean air temperatures at Roi Baudouin station in 1966 (data from A.J.Meerburg,1968)

of the first congelation ice layer and that of sea water gives a value of 1.0167 equivalent to k.

Using these values, the two following equations - one for Na (a), the other for δD (b) - can be derived between BLT/D and V :

(a) $\ln(1/0.0524-1)-\ln(1/0.0437-1) = -(BLT/D)_{Na}.V$

(b) $\ln(1-1/1.0167)-\ln(1-1/1.0208) = -(BLT/D)_{\delta D}.V$

As $(BLT/D)_{Na}$ = 7243 sec cm^{-1} and V is the same in the two equations, $(BLT/D)_{\delta D}$ can be known. Since D for deuterium is 1.1 10^{-5} cm^2 sec^{-1} (Wang et al., 1953), BLT is 0.09 cm.

The boundary layer thickness calculated above will be used to determine the freezing rates of the other congelation ice layers in the profile. This is reasonable since the BLT does not depend on the freezing rate.

4.2.2. Growth rate determination :

Using our model with a BLT = 0.09 cm, in a semi-infinite reservoir (V.1.3.4.) where the initial sea water δD value is kept constant in the course of freezing outside the boundary layer, it is possible to deduce growth rates from the δD values of congelation ice samples.

Table 2 gives the results for the four thin layers of fine-grained congelation ice and for three samples of coarse-grained congelation ice. The deduced surface temperatures are also indicated. These deduced surface temperatures are obtained from a simple thermodynamical model similar to the one used by Nakawo and Sinha (1981). It is based on the fact that the energy loss by conduction through the ice is used in changing sea water into sea ice. Thus :

$$-\frac{\lambda.\Delta T.\Delta t}{\Delta x} = \rho.L.x$$

where λ is the thermal conductivity of ice (2.2 W K^{-1} m^{-1}), ρ the volumic mass of ice (0.9 10^3 kg m^{-3}), L the latent heat of fusion (333 kJ kg^{-1}), x the depth from the surface, ΔT the temperature difference and Δt the time interval. It follows that :

$$x.\frac{dx}{dt} = -\frac{\lambda.\Delta T}{\rho.L}$$

Knowing the thickness of the ice already formed and the growth rate, the difference between the surface temperature and the freezing temperature of sea water (-2°C) is obtained.

Figure 17 shows the daily mean air temperature record at Base Roi Baudouin during 1966. Base Roi Baudouin is very close to our sampling site, but continuous temperature recordings in this area were unfortunately only carried out between 1957 and 1966. Although the profile is very similar from one year to another, we will thus only use it on a qualitative ground.

A comparison between values given in table 2 and the daily mean temperature of figure 17 shows a good agreement with the data ; most of the congelation ice being formed after mid-winter.

The results given so far are compatible with those of Nakawo and Sinha (1981) obtained from direct measurements of ice thickness on high arctic sea ice. Slightly higher growth rates for the two first layers of congelation ice are present in our core. Our results are also quite in agreement with Gabison's (1987) thermodynamical model of the formation, growth and decay of first-year sea ice, if the snow cover is considered as a late addition to the ice sheet.

VI. POTENTIAL APPLICATIONS

The concept of the freezing slope on a δD-$\delta^{18}O$ diagram can be applied to distinguish between glacier ice or ice derived from solid precipitation in the area considered and ice resulting either from the congelation of sea ice or from meltwater freezing at the base of an ice sheet. When the range in δD or/and $\delta^{18}O$ is sufficiently important between these two groups, the freezing slope is not a necessary tool to discriminate between different origins. However, in most circumstances, this range is nearly identical so that only the slope is an useful tracer.

Determination of the freezing rate by a co-isotopic study of the ice is an achievement of the program. It allows from the detailed isotopic distribution in the ice to reconstruct the freezing history in favorable circumstances. The method has already been successfully used in the case of a first-year sea ice cover in East Antarctica. It must be further tested in order to estimate its range of application.

In this regard, the three following possibilities exist in the Antarctic :

a) evaluation of sea ice growth rate where the ice cover is mainly congelation ice rather than frazil ice. Such an approach would have important climatological and ecological implications.

b) determination of local accretion rate at the base of antarctic ice shelves by freezing of sea water. This kind of study has some implications in mass balance studies.

c) investigations of basal ice rate of formation in deep antarctic ice cores. Information on freezing rates can produce a refinement of ice sheet flow models that are needed for a paleoclimatic interpretation of deep ice cores.

On a wider range, the methods developed in the program should allow us to study any situation where water is changing from a liquid phase to a solid one. For example :

- Progression of a freezing front in an aggrading permafrost and estimation of the growth rates in segregation ice

- Determination of ice growth rates on superstructures like roads, buildings, bridge piles, harbours and offshore platforms.

VII. GENERAL CONCLUSIONS

Distribution of heavy stable isotopes in ice formed by water freezing is related to the distribution in the liquid immediately adjacent to the freezing front. Since diffusion in the ice is slow, the distribution produced in the ice can be obtained from knowledge of the variations in the liquid at the interface. These variations depend on mixing that occurs by diffusion and by convection. Based on these principles, a method is developed to predict freezing rates from the isotopic distribution in the ice.

Knowing the isotopic values of initial water, the length of the reservoir, the boundary layer thickness and the diffusion coefficients, the freezing rate history of an ice cover can be deduced. The method is successfully applied to experimentally-grown ice cores and to a first-year sea ice cover in East Antarctica.

VIII. ACKNOWLEDGMENTS

Dr. J. Jouzel from the "Centre d'Etudes Nucléaires de Saclay" in France is gratefully acknowledged for allowing co-isotopic analyses to be done in his laboratory and for fruitful discussions.

The authors are much indebted to the British Antarctic Survey for including Dr. J.-L. Tison in their summer antarctic field season 1987-1988 and for their efficient logistic support.

Dr. H. Decleir and M. Devos (V.U.B.) are especially acknowledged for collecting the sea ice cores in Breid Bay. We would also like to thank the National Institute of Polar Research of Japan for their efficiency in taking care of the samples to Tokyo airport and M. Depasse from the Belgian embassy in Tokyo for his cooperation.

This report is a contribution to the Belgian Scientific Research Program on Antarctica (Science Policy Office). The scientific responsibility is assumed by its authors.

IX. REFERENCES

Arnason, B., 1969. The exchange of hydrogen isotopes between ice and water in temperate glaciers. Earth and Planetary Science Letters, Vol.6, No.6, p.423-30.

Burton, J.A., et al., 1953. The distribution of solute in crystal grown from the melt. Part I. Theoretical, by J.A. Burton, R.C. Prim and W.P. Slichter. Journal of Chemical Physics, Vol.21, No.1, p.1987-91.

Cox, G., and Weeks, W., 1975. Brine drainage and initial salt entrapment in sodium chloride ice, C.R.R.E.L. Research Report, 354, p.85.

Craig, H., et al., 1963. Isotopic exchange effects in the evaporation of water, by H. Craig, K.I. Gordon, and Y. Horibe. Journal of Geophysical Research, Vol.68, No.17, p.5079-87.

Dansgaard, W., 1964. Stable isotopes in precipitation. Tellus, 16, p.436-468.

Dansgaard, W., et al., 1982. A new Greenland deep ice core, by W. Dansgaard, H.B. Clausen, N. Gundestrup, C.V. Hammer, S.F. Johnsen, P.M. Kristinsdottir, and N. Reeh. Science, Vol.218, No.4579, p.1273-77.

Dudley et al., 1975. Statistical tests for preferred orientation. Journal of Geology, Vol.83, No.6, p.685-706.

Franssen, L., et Kummert, P., 1971. Présentation d'un programme de traitement des données en géologie structurale. Annales de la Société Géologique de Belgique, T.94, p.39-43.

Friedman, I., et al., 1964. The variation of the deuterium content of natural waters in the hydrologic cycle, by I. Friedman, A.C. Redfield, B. Schoen and J. Harris. Reviews of Geophysics, Vol.23, No.89, p.321-34.

Gabison, R., 1987. A thermodynamic model of the formation, growth and decay of first-year sea ice. Journal of Glaciology, Vol.33, p.105-119.

Gow, A.J., and Epstein, S., 1972. On the use of stable isotopes to trace the origin of ice in a floating ice tongue. Journal of Geophysical Research, Vol.77, No.33, p.6552-57.

Gow, A.J., et al., 1979. On the origin of stratified debris in ice cores from the bottom of the Antarctic Ice Sheet, by A.J. Gow, S. Epstein, and W. Sheely. Journal of Glaciology, Vol.23, No.89, p.185-92.

Gow, A.J., et al., 1987. Physical and structural characteristics of Weddell Sea pack ice, by A.J. Gow, G.F. Ackley, K.R., Buck and K.M. Golden. C.R.R.E.L Report 87-14, p.75.

Hagemann, R. and Lohez, P., 1978. Twin mass spectrometers for simultaneous isotopic analysis of hydrogen and oxygen in water. Advances in Mass Spectrometry, Vol.7, p.504-08.

Jouzel, J., and Souchez, R.A., 1982. Melting-refreezing at the glacier sole and the isotopic composition of the ice. Journal of Glaciology, Vol.28, No.98, p.35-42.

Jouzel, J., et al., 1987. Vostok ice core : a continuous isotope temperature record over the last climatic cycle (160.000 years), by J. Jouzel, C. Lorius, J.R. Petit, C. Genthon, N.I. Barkov, V.M. Kotlyakov and V.M. Petrov. Nature, Vol.329, No.6138, p.403-08.

Kamb, W.B., 1959. Ice petrofabric observations from Blue Glacier, Washington, in relation to theory and experiment. Journal of Geophysical Research, Vol.64, No.11, p.1891-908.

Lawson, D.E., and Kulla, J.B., 1978. An oxygen isotope investigation of the origin of the basal zone of the Matanuska Glacier, Alaska. Journal of Geology, Vol.86, No.6, p.673-85.

Lorius, C., et al., 1985. A 150.000-year climatic record from Antarctic ice, by C. Lorius, J. Jouzel, C. Ritz, L. Merlivat, I. Barkov, Y.S. Korotkevich and V.M. Kotlyakov. Nature, Vol.316, No.6029, p.591-96.

Moser, H. and Stichler, W., 1980. Environmental isotopes in ice and snow, in Fritz, P. and Fontes, J.C., eds. Handbook of environmental isotope geochemistry. New York, Elsevier, Vol.1., p.141-78.

Nakawo, M. and Sinha, N., 1981. Growth rate and salinity profile of first-year sea ice in the High Arctic, Journal of Glaciology, Vol.27, p.315-30.

O'Neil, J.R., 1968. Hydrogen and oxygen isotope fractionation between ice and water. The Journal of Physical Chemistry, Vol.72, No.10, p.3683-84.

Smith, V.G., et al., 1955. A mathematical analysis of solute redistribution during solidification, by V.G. Smith, W.A. Tiller and J.W. Rutter. Canadian Journal of Physics. No.33, p.723-44.

Souchez, R.A., and Jouzel, J., 1984. On the isotopic composition in δD and $\delta^{18}O$ of water and ice during freezing. Journal of Glaciology, Vol.30, No.106, p.369-72.

Souchez, R.A., and De Groote, J.M., 1985. δD-$\delta^{18}O$ relationships in ice formed by subglacial freezing : paleoclimatic implications. Journal of Glaciology, Vol.31, No.109, p.229-32.

Souchez, R., et al., 1987. Freezing rate determination by the isotopic composition of the ice, by R. Souchez, J.-L. Tison and J. Jouzel. Geophysical Research Letters, Vol.14, p.599-602.

Tiller, W.A., et al., 1953. The redistribution of solute atoms during the solidification of metals, by W.A. Tiller, K. Jackson, J. Rutter and B. Chalmers. Acta Metallurgica, Vol.1, p.428-37.

Terwilliger, K.P. and Dizio, S.F., 1970. Salt rejection phenomena in the freezing of saline solutions, Chemical Engineering Science, Vol.25, p.1331-49.

Wang, J., et al., 1953. Self-diffusion and structure of liquid water. III. Measurement of the self-diffusion of liquid water with H^2, H^3 and O^{18} as tracers, by J. Wang, C. Robinson and I. Edelman. Journal of the American Chemical Society, Vol.75, p.466-70.

Weeks, W.F., and Lofgren, G., 1967. The effective solute distribution coefficient during the freezing of NaCl solution, In Physics of snow and ice (H. Oura, ed.), Hokkaido, Vol.1, p.579-97.

Weeks, W.F., and Ackley, S., 1986. The growth, structure and properties of sea ice, in N. Untersteiner Ed. The Geophysics of Sea Ice, Nato ASI Series, Series B, Physics, Vol. 146, p.1196.

SCIENCE POLICY OFFICE
Research contract
nr ANTAR/02

FLOW SIMULATION IN THE WEDDELL SEA

M. Fettweis, C.-S. Yu and J. Berlamont

LABORATORIUM VOOR HYDRAULICA
KATHOLIEKE UNIVERSITEIT TE LEUVEN
DE CROYLAAN, 2
B-3030 HEVERLEE (BELGIUM)

BELGIAN SCIENTIFIC RESEARCH
PROGRAMME ON ANTARCTICA
SCIENTIFIC RESULTS OF PHASE ONE
(OCT 85 - JAN 89)
VOLUME III: GLACIOLOGY AND
CLIMATOLOGY

ABSTRACT

The research carried out concerns the development of a numerical model for hydrodynamics (surface current and water elevation) and thermodynamics (surface temperature) of the Weddell Sea region. The knowledge of currents is necessary to predict the evolution of icefields, which is important for shipping and off–shore works in polar waters.

A 2D numerical model has been used to simulate the currents in the Weddell Sea. The model uses a falsified alternating direction implicit (FADI) scheme. The numerical scheme gives rise to a very efficient computer implementation. The model has been verified by comparing the results of the model for some test cases with known solution. Attention was paid on the development of an appropriate open boundary condition and on the implementation of the advection – diffusion equation.

The boundaries of the Weddell Sea model are situated at 50°S, 80°S, 80°W and 30°E, including the Antarctic Peninsula, the Drake passage and the southern tip of South America. The model has been used to calculate the wind induced and the tidal induced flows.

CONTENTS

1.	Introduction	3
	1.1 Major goal of this study	3
	1.2. Description of the problem	3
	1.3. Procedures and organization of the report	4
2.	The Weddell Sea	6
	2.1. General circulation in the Southern Ocean	6
	2.2. Circulation in the Weddell Sea	7
	2.3. Water masses	7
	2.4. Tides in the Weddell Sea	8
3.	Ocean – Ice Models : A Review	10
	3.1. The geophysical environment	10
	3.2. Thermodynamical models	10
	3.3. Dynamical models	11
	3.4. Dynamical – thermodynamical models	11
4.	The Ocean Model	13
	4.1. Governing equations	13
	4.2. Numerical model	14
	4.2.1. "Falsification"	14
	4.2.2. Finite difference formulation	15
	4.2.3. Discussion of the scheme	18
	4.2.4. Modified scheme	20
	4.3. Applications	21
	4.3.1. Steady flow problem	21
	4.3.2. Unsteady flow problem	25
5.	Open Boundary Condition for Circulation Models	29
	5.1. Introduction	29
	5.2. Review of literature	30

5.3. Numerical implementation and experiments 34
5.3.1. Numerical implementation 34
5.3.2. Numerical experiments 36

6. Advection and Diffusion 44
6.1. Introduction 44
6.2. Approximation of the advective terms 45
6.3. Numerical applications with advection 47
6.3.1. Eddy formation in an idealized channel 47
6.3.2. Practical application for the Weddell Sea model 47
6.4. Approximation of the diffusion terms 47
6.5. The thermo–haline equations 49

7. The Weddell Sea Model 50
7.1. Model area 50
7.1.1. Cartesian grid 50
7.1.2. Spherical grid 53
7.2. Currents due to wind action 53
7.2.1. Atmospheric circulation 53
7.2.2. Model assumptions 54
7.2.3. Results 54
7.2.4. Discussion 59
7.3. Currents due to tidal forcing 60
7.3.1. Boundary condition 60
7.3.2. Results 60

8. Conclusion 63
8.1. Possible applications 63
8.2. General conclusions 64
8.3. Further developments 64

9. Bibliography 65

1. INTRODUCTION

1.1 Major goal of this study

The goal of this study is to develop a numerical model to calculate the ocean circulation in the Weddell Sea. The model should be suitable for real–time applications, such as navigation guidance in polar waters. Therefor special attention was paid on the development of an efficient (i.e. computer implementation, memory space and computation time) numerical scheme. The model is implemented on a PC–AT. The model has to be connected to an ice model in order to simulate the evolution of the marginal ice zone. The results of the simulations done with the Weddell Sea model are compared to those of other models.

1.2. Description of the problem

Antarctic and the surrounding oceans play an important role in the climate system of the earth. Between the oceans and the athmosphere an important transfer of momentum and energy occurs, which is modified in the presence of large ice fields. The upper layer of the ocean is strongly affected by wind forcing. This upper ocean circulation has an impact on the deeper ocean circulation, furthermore the influence of the wind on the ocean circulation is damped in the presence of ice fields. The location of the ice edges and the motion of the ice fields is affected by the wind and the upper ocean circulation.

The ocean circulation can be divided into three parts, i.e. the thermohaline, the wind–driven and the tidal components. The time scale of these components are different.

The thermohaline circulation is due to changes in density of the water caused by weather or climatic changes, it is a seasonal process. When water freezes out, it ejects salt and thus increases the density of the remaining water. The increase in density causes the water to sink, the thermohaline circulation is thus three–dimensional.

Wind–driven currents undergo changes on a much smaller time scale, i.e. a few days or weeks. The wind causes the upper layer of the ocean to be well mixed. It is primarily a horizontal circulation in contrast to the previously mentioned one.

The tides, which are a consequence of the gravitational actions of the moon, the sun and the earth, and the revolution round each other, act on a time scale of a few hours.

The time scale of the model ranges from a few days to a few weeks. For a short period the

influence of the thermohaline circulation is small, the main processes which cause the circulation are the wind and the tides.

1.3. Procedure and organization of the report

The knowledge of ocean currents is necessary to predict the evolution of the ice fields. These currents can be calculated by means of a numerical model. The choice of the model is suggested by the following items :

- the aim of the model
  A choice must be made in function of the desired results. The thickness of an layer of ice is small, the dynamics of it is particularly influenced by surface currents, a 2D phenomenon. The restriction to a 2D model is obtained by integrating the 3D Navier Stokes equations over the depth.
- Solution techniques
  In order to solve the Navier Stokes equations, numerical techniques are necessary. The choice of the numerical scheme determines the accuracy of the solution and the efficiency of the computer implementation (computing time, memory space, computer cost). Three–dimensional models need a lot of computing time and memory space, therefore, they can only be implemented on a big computer. A two–dimensional model, on the other hand, need less computing time and less memory space. With the choise of an efficient numerical scheme such a model can run on a personal computer.

With this in mind, a 2D depth–averaged model has been chosen because the phenomena of interest are two–dimensional (surface currents) and because the computing time is small, which allows the use of the model for operational purposes.

In chapter 2 a short description of the physics in the Weddell Sea and the Southern Ocean is given. In chapter 3 a review of literature of Ocean and Ice models is presented. At the beginning of the contract ANTAR 02, attention was focused on the development of Ice models. This part has been further developed by the MUMM (see Demuth and van Ypersele, 1987) whereas at our laboratory the emphasis of the research was put on the development of an Ocean model.

An existing 2D model (Moelans, 1979) was adapted and improved for applications to the Weddell Sea. This model uses a falsified alternating direction implicit (FADI) scheme, which solves the equations by using the split–operator approach with falsification of the individual stages of the ADI scheme. A modification was implemented in order to get

accurate results for both steady and unsteady flows. The proposed numerical scheme is suitable for the calculation of time–dependent phenomena, such as tidal flows, as well as for the calculation of steady state phenomena (see chapter 4).

The treatment of the open boundaries is an intrinsic and important problem associated with numerical models. The integration domain of the Weddell Sea model is limited by boundaries which have no physical meaning. When integrating the equations for a restricted domain it is necessary to define meaningful conditions at the open sea boundaries. Different ways of approach are discussed in chapter 5.

In order to calculate sea water density a transport model has been developed, which solves the transport equation for temperature and salinity. The transport model has been applied to some test cases (see chapter 6).

In chapter 7 some model results of the Weddell Sea are presented for wind–induced flows and tidal induced flows. The results are compared with those of an 3D model. Finally, the last part is devoted to some possible applications of the research results and to the general conclusions.

2. THE WEDDELL SEA

2.1. General circulation in the Southern Ocean

The area which forms the subject of this study extends from lat. 50° S to 80° S and from long. 80° W to 30° E. It includes the Weddell Sea, the Antarctic Peninsula, the Drake Passage and the Southern tip of South America, (see Fig. 2.1.).

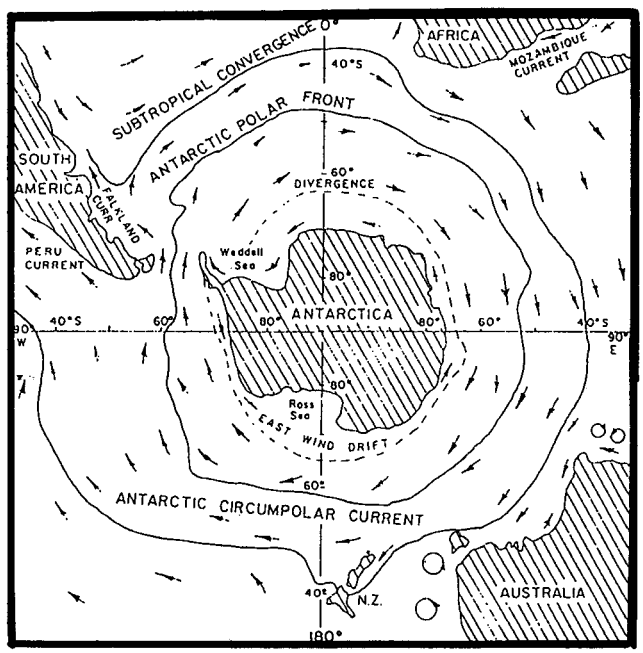

Figure 2.1 : Southern Ocean circulation and mean position for the Antarctic Polar Front and Subtropical Convergence (from Pickard and Emery, 1982)

A special feature of the Southern Ocean, which makes it unique in the world, is that the water is free to move around the continent. No land boundary exists on its north and it is thus continuous with the other oceans. The Southern Ocean can be divided into several zones (Pond and Emery, 1982). The Antarctic Polar Front (Antarctic Convergence) and the Subtropical Convergence divide the surface waters into the Antarctic zone, which extends from the continent to the Antarctic Polar Front and the Subantarctic zone, which is situated between the Antarctic Polar front and the Subtropical Convergence, (see

figure 2.1.). The Antarctic divergence is the transition zone between the east and the west winds, in the Weddell Sea this region lies between 68° and 69° S (Deacon, 1982). The Antarctic Polar Front region is characterized by the strongest average west winds and the maximum northward Ekmandrift (Deacon, 1982).
Around the continent there is a weak westward flowing coastal current. North of 65° S the Southern Ocean Circulation is dominated by an eastward flowing current, which is known as the Antarctic Circumpolar Current. This current is mainly driven by the wind. In general the flow velocities are not very high (Pond and Emery, 1982). The average surface speeds vary from about 4 cm/s in the Antarctic zone to 15 cm/s north of the Polar Front. The volume transport, however, is important because the current is very deep. Average values of water transport through the Drake Passage derived from measurements range from 124 to 139 Sv (Nowlin et.al., 1977; Bryden and Pillsbury, 1977).

2.2. Circulation in the Weddell Sea

The general circulation in the Weddell Sea consists in a large gyre. The water at all depths flows westward along the continental margin, northward along the Antarctic Peninsula and eastward across the Atlantic Ocean. The gyre is closed between 20° E and 30° E by southward movement of the water in the deep and bottom layers (Foster and Carmack, 1976; Deacon, 1979). As pointed out by Taljaard et.al. (1969) this circulation is probably the result of the atmospheric circulation around a nearly permanent low. In the northern part, at least, the gyre is largely baratropic with velocities varying a few cm/s from top to bottom (Foster and Carmack, 1976).

2.3. Water masses

Three main water masses are distinguished in the Southern Ocean (Deacon, 1984; Pond and Emery, 1982) : the Antarctic Surface Water (ASW), the Antarctic Circumpolar Water (ACW), and the Antarctic Bottom Water (ABW).
The ASW, which is found south of the Antarctic Polar Front, has properties which are characterized by ice melting in the summer or by cooling in the winter. This layer is some 100 to 200 m deep, has a low salinity and a low temperature.
Below the ASW and extending to the bottom is the ACW. It has a temperature which is above 0° C and a mean salinity of 34.7 $^{o}/_{oo}$. These features are found all around the

continent, which proves that this water is carried by the Antarctic Circumpolar Current. Gordon (1971) also distinguished Weddell Deep Water (WDW), which composes the bulk of Weddell gyre.

The ABW is formed along the shelf edge, mainly in the Weddell Sea. It is cold and less saline than the Deep Water. The ABW is a mixture of the Deep Water (ACW or WDW) and Shelf Water.

The Shelf Water has a low temperature (–2.0° C) and a salinity of 34.4–34.8 $^{o}/_{oo}$ and a very high density. Probably the formation of these dense waters is due to the sea ice formation near the continental shelf edge.

Carmack and Foster (1975) distinguish between "classical" ABW and Weddell Sea Bottom Water (WBW). The latter is characterized by a lower potential temperature (below –0.7° C) and larger near–bottom temperature gradients. When this water flows away from the region of sinking, it eventually mixes with the warmer deep water above to form ABW (Carmack and Foster, 1975).

2.4. Tides in the Weddell Sea

The Antarctic Ocean has long been considered the region where the tides of the Oceans are generated; this theory is known as Whewell's hypothesis (Whewell, 1833 in Gordeyev et.al., 1975). Numerical experiments in which the Southern Ocean was isolated from the other Oceans, however, did not give substantial differences in the ocean tides in the Atlantic, Indian and Pacific Oceans (Gordeyev et.al., 1975).

Since observational data on tides in the Oceans and especially in the Antarctic Ocean are scarce, our knowledge about ocean tides mainly comes from numerical models. Tidal maps of the World Oceans are compared and discussed in the arcticles by Schwiderski (1980) and Marchuk and Kagan (1984). When looking at the corange map of the M2 tide (Schwiderski, 1980) in the Weddell Sea region, one can see an amphidromic point at about 65° S and 5° W (see figure 2.2.). The location and the number of amphidromic systems in the Atlantic part of the Southern Ocean simulations varies greatly according to the different investigators.

Tiron et.al. (1967) found only one amphidrome, according to Gordeyev et.al. (1973) there are two amphidromic systems and Peeris and Accad (1969), Zahel (1970) and Hendershott (1972) recorded three amphidromes. All the models, however, show an amplification of the M2 tidal wave while it is entering the Weddell Sea; at the continent an tidal elevation of 120 cm is reached, (see figure 2.2.).

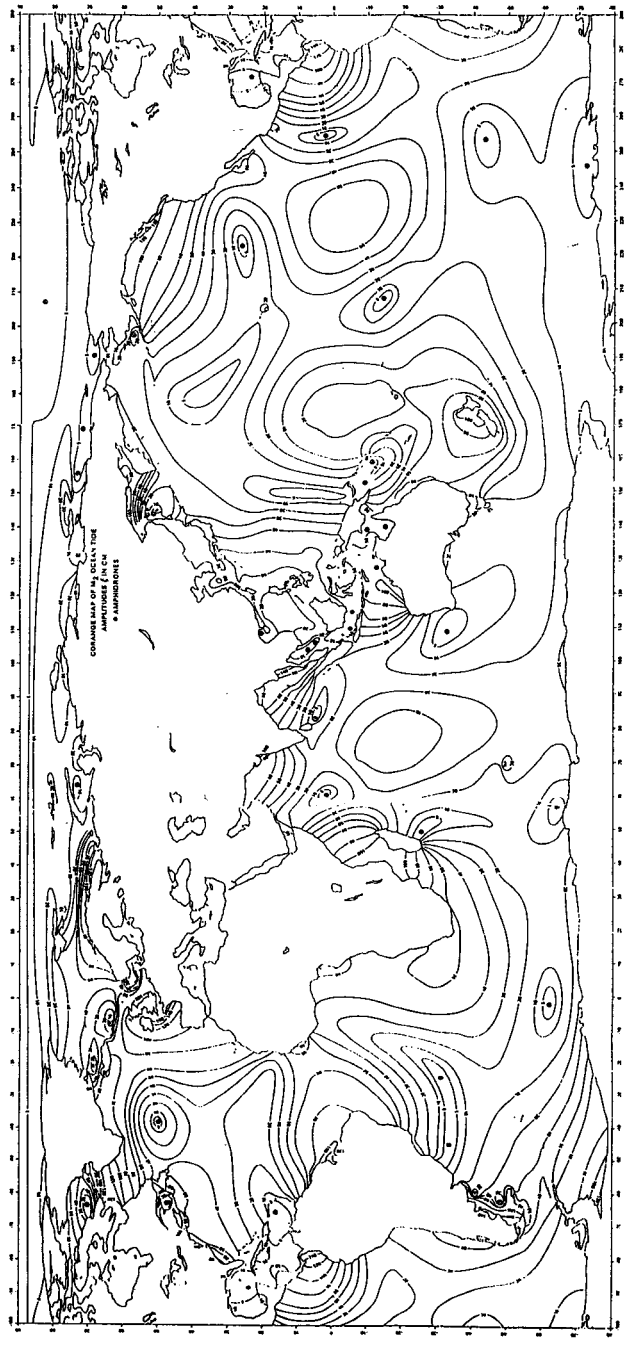

Figure 2.2 : Corange map of M_2 ocean tide, amplitude in cm (from Schwiderski; 1983)

3. OCEAN–ICE MODELS : A REVIEW

3.1. The geophysical environment

The physical system which describes the evolution of the ice is dominated by three mutually connected dynamical processes : the hydrodynamics of the ocean, the thermodynamics of the ocean and the ice dynamics. The atmosphere consists of a time–dependent boundary condition on the surface of each of the three processes. At the surface of the ocean this boundary condition is responsible for exchange of mass (precipitation, evaportion), of motion of water and ice and of heat at the air–water and the air–ice boundaries.

These exchange processes influence the relation between the weather and the surface condition of the ocean. The surface temperature of the ocean and the situation at the ocean surface (currents, waves) together determine the speed of these processes.

The initial growth of the ice is always thermodynamical. Later on the growth can be dynamical due to ridging of the ice fields or to rafting. The ice dynamics is forced by wind, currents, waves, changes in water level and the thermical tensions in the ice.

The thermodynamics play an important role on the dynamical behaviour of ice fields : ice–floes are welded together and new thin ice is formed in the open water during frosty weather. The zones with new thin ice are extremely sensitive to fragmentation and deformation due to the movement of the adjacent older ice–floes. During thaw the ice field is less rigid and thus more sensitive to external forces.

A model of an ice sea has to take into account the three above mentioned processes and their relation between each other. Most of the models, however, take no account of all of these processes. In the following sections some attention will be paid to existing models.

3.2. Thermodynamical models

Miller (1981), Shen and Chiang (1984) and Wake and Rumer (1983) all developed models which only take account of the vertical growth of the ice. This process is achieved by one dimensional heat conduction through the thickness of the ice layer. The heat exchange at the air/ice contact plane is determined by the meteorological data. The temperature of the ocean is responsible for the heat exchange at the ice/water contact plane. The heat

conduction equation is derived from the one–dimensional convection–diffusion equation. These models assume that the ice thickness is different from zero and then are thus not suitable for the reproduction of the initial ice growth.
Miller (1981) assumed that the ocean is not stratified. In this case a two–dimensional current model will do and the temperature distribution of the ocean is accurately enough described by the two–dimensional convection diffusion equation.
Røed (1984) proposed a coupled ice–ocean model for the thermodynamical growth of the marginal ice zone. The model only considers lateral growth and decay of the ice. This is a phenomenon which takes place on a short time scale. The model is purely thermodynamic, advection and diffusion are neglected. The model is forced by the temperature differences between the ocean and the atmosphere. The ice is described in terms of surface concentration and mean ice thickness. This model gives the possibility to simulate the evolution of the marginal ice zone in connection with the dynamics, see e.g. Røed and O'Brien (1983). The model as it was presented by Røed (1984) is, however, too schematic, comparisons with reality are therefore difficult.

3.3. Dynamical models

The mechanical processes which are caused by wind– and water stress stimulate the ice growth (ridging and rafting) and create open water zones where new ice can be formed. During winter, the thermodynamical processes in the great lakes can "only" produce an ice layer 1 m in thickness, whereas ridged ice of 7 to 8 m can occur (Wake and Rumer, 1983). The dynamics can be taken into account when regarding the fragmented ice fields as being a continuum (Chieh and Wake, 1983; Wake and Rumer, 1983).
The equations which are solved for the problem of ice dynamics are the momentum equation of the ice continua, the conservation equation of ice mass and ice surface concentration and the constitutive law of internal ice stresses.
Dynamical models are described by Kollé and Pritchard (1983) and Thorndike et.al. (1975).

3.4. Dynamical–Thermodynamical models

In 1979 Hibler presented a model to simulate the long term evolution of the ice fields in the Arctic. This model is the basis of other modelling work which allows prediction on a shorter time scale (Chieh et.al., 1983; Røed and O'Brien, 1983; Røed, 1984; Rumer, 1983;

Wake and Rumer, 1979 and Wake and Rumer, 1983). The model of Hibler (1979) is similar to the models described in section 3.3. It is important to use a suitable constitutive law of internal ice stresses.

This model is based on the model which was developed during the AIDJEX project (Coon et.al. 1974; Coon et.al. 1976; Pritchard and Colony, 1976 and Thorndike et.al., 1975). Hibler used in his model a simplified version of the thickness distribution function of Thorndike et.al. (1975). Fragmented ice fields can have a different thickness, mainly the new and thin ice is of great importance in the energy balance. It is, more than the thick ice, liable to dynamical and mechanical deformation and to thermodynamical influences. To parameterize the ice, Hibler (1979) uses a distribution function with only two idealized thicknesses (thick and thin).

The Hibler model is suitable for long term climate studies. The grid is, however, too coarse and too many simplifications were carried out to allow accurate short time predictions, as is possible with the AIDJEX model.

4. THE OCEAN MODEL

4.1. Governing equations

The equations which are solved by the model are the 2D shallow water equation (St. Venant hypothesis). The conservation equation of mass can be written as :

$$\frac{\partial z}{\partial t} + \frac{\partial (Hu)}{\partial x} + \frac{\partial (Hv)}{\partial y} = 0 \tag{4.1}$$

and the equations of horizontal motion can be written as :

$$\frac{\partial u}{\partial t} + u\frac{\partial u}{\partial x} + v\frac{\partial u}{\partial y} + g\frac{\partial z}{\partial x} - fv + \frac{1}{\rho H}(\tau_{bx} - \tau_{sx}) = 0 \tag{4.2}$$

$$\frac{\partial v}{\partial t} + u\frac{\partial v}{\partial x} + v\frac{\partial v}{\partial y} + g\frac{\partial z}{\partial y} + fu + \frac{1}{\rho H}(\tau_{by} - \tau_{sy}) = 0 \tag{4.3}$$

where the notation is:

t	:	time (seconds)
x,y	:	horizontal coordinates (m)
z	:	water surface elevation relative to the reference plane (m)
h	:	water depth measured from reference plane (m)
H	:	total water depth (m), H = h + z
u,v	:	vertically averaged velocity components in the x and y directions respectively (m/s)
g	:	gravitational acceleration (m/s^2)
f	:	Coriolis parameter
τ_{bx}, τ_{by}	:	bottom friction components in x and y direction respectively
τ_{sx}, τ_{sy}	:	wind stress components in x and y direction respectively
ρ	:	water density

The bottom friction terms are expressed as follows :

$$\tau_{bx} = \rho\frac{g}{C^2}u\sqrt{u^2 + v^2}, \quad \tau_{by} = \rho\frac{g}{C^2}v\sqrt{u^2 + v^2} \tag{4.4}$$

where C is the Chézy coefficient.
The wind stress terms can be written as

$$\tau_{sx} = \lambda \rho_a W_u \sqrt{W_u^2 + W_v^2}\,, \quad \tau_{sy} = \lambda \rho_a W_v \sqrt{W_u^2 + W_v^2} \tag{4.5}$$

W_u and W_v are the local wind velocity components in X and Y directions respectively, measured 10 meters above the mean sea level, ρ_a is the air density and λ the drag coefficient at the air–water interface.

4.2. Numerical model

In this section the numerical implementation of the equations (4.1.) – (4.3.) is described. The discussion of the implementation of the open boundary is given in chapter 5 and that of the advective terms in chapter 6.

4.2.1. "FALSIFICATION"

The equations (4.1.) – (4.3.) are solved by time integration using the finite difference method. The complete set of equations (4.1.) – (4.3.) is not solved for every time step, because this method is not efficient for the computer implementation. In order to restrict the number of computations, the set of equation (4.1.) – (4.3.) is often expressed in an alternating direction implicit (ADI) manner with three time–level operations executed during each computation cycle (Liu and Leendertse, 1978). At every time step only one momentum equation (4.2.) or (4.3.) is solved implicitly together with the continuity equation (4.1.), the other momentum equation is solved explicitly.
Another possibility consists in skipping the explicit calculations and in solving alternately either (4.1.) and (4.2.), or (4.1.) and (4.3.). This numerical scheme, however, is not unconditonally stable. Unconditional stability can be obtained by falsifying the scheme (Abbott et.al., 1973). The falsified scheme proposed by Moelans and De Bruyn (1986) and Yu et.al., (1988b) is described in this text. The continuity equation is split up into two falsified equations, so that

$$\frac{1}{2}\frac{\partial z}{\partial t} + \frac{\partial (Hu)}{\partial x} = 0, \text{ for odd time steps} \tag{4.6}$$

and

$$\frac{1}{2}\frac{\partial z}{\partial t} + \frac{\partial (Hv)}{\partial y} = 0, \text{ for even time steps} \tag{4.7}$$

The equations (4.6.) and (4.7.), individually, are not consistent with the original differential equation (4.1.). The resultant of two time steps is, however, consistent, as was shown by Yanenko (1971).

4.2.2. FINITE DIFFERENCE FORMULATION

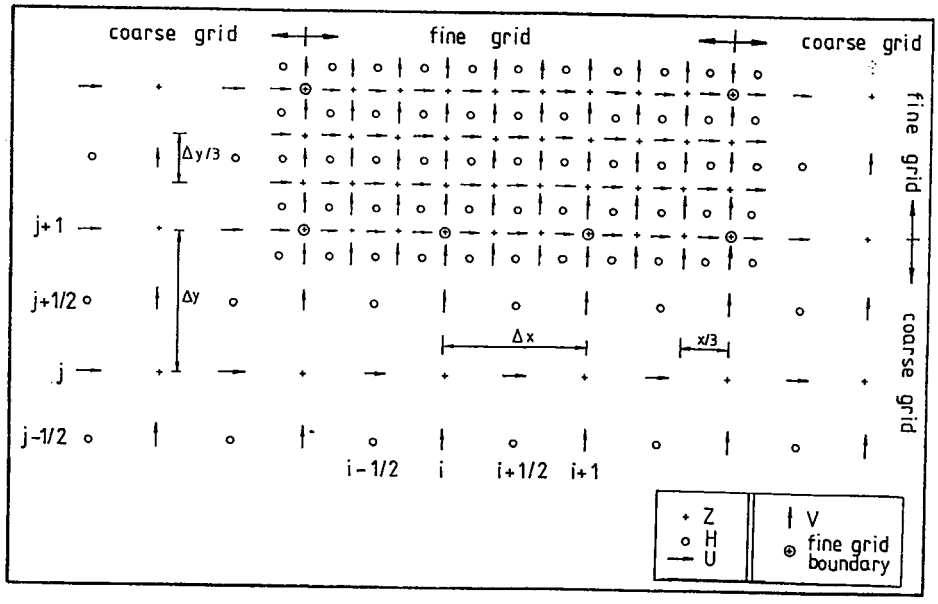

Figure 4.1 : Finite difference staggered grid pattern

The discrete values of the variables u, v and z are described on a space staggered grid, as shown in figure 4.1. At odd time steps and in the x–direction, the falsified equations are expressed as follows :

$$\frac{Z^{n+1}_{i,j} - Z^{n}_{i,j}}{2\Delta t} + \frac{H^{n}_{i+1/2,j} u^{n+1}_{i+1/2,j} - H^{n}_{i-1/2,j} u^{n+1}_{i-1/2,j}}{\Delta x} = 0 \tag{4.8}$$

$$\frac{u^{n+1}_{i+1/2,j} - u^{n}_{i+1/2,j}}{2\Delta t} + g\frac{Z^{n+1}_{i+1,j} - Z^{n+1}_{i,j}}{\Delta x} + f_1(u,v) = 0 \tag{4.9}$$

and

$$\frac{V^{n+1}_{i,j+1/2} - V^{n}_{i,j+1/2}}{2\Delta t} = 0 \tag{4.10}$$

where

$$f_1(u,v) = u^{n+1}_{i+1/2,j} A_x + \bar{v} A_y - f\bar{v} + \frac{1}{\rho H^{n}_{i+1/2,j}}(\tau_{bx} - \tau_{sx}) \tag{4.11}$$

and

$$\bar{v} = \frac{1}{4}\left(v^{n}_{i,j-1/2} + v^{n}_{i,j+1/2} + v^{n}_{i+1,j-1/2} + v^{n}_{i+1,j+1/2}\right) \tag{4.12}$$

$$\tau_{bx} = \frac{\rho g}{C^2} u^{n+1}_{i+1/2,j} \sqrt{(u^{n-1}_{i+1/2,j})^2 + \bar{v}^2} \tag{4.13}$$

A_x and A_y are the second–order upstream differences of the advective terms (see chapter 6 for more details).
The equation (4.10) can be replaced by

$$V^{n+1}_{i,j+1/2} = V^{n}_{i,j+1/2} \tag{4.14}$$

The equation for the even time steps and the y–direction are written as :

$$\frac{Z^{n+2}_{i,j} - Z^{n+1}_{i,j}}{2\Delta t} + \frac{H^{n+1}_{i,j+1/2} V^{n+2}_{i,j+1/2} - H^{n+1}_{i,j+1/2} V^{n+2}_{i,j-1/2}}{\Delta y} = 0 \tag{4.15}$$

$$\frac{u^{n+2}_{i+1/2,j} - u^{n+1}_{i+1/2,j}}{2\Delta t} = 0 \tag{4.16}$$

and

$$\frac{V^{n+2}_{i\,,\,j+1/2} - V^{n+1}_{i\,,\,j+1/2}}{2\Delta t} + g\frac{Z^{n+2}_{i\,,\,j+1} - Z^{n+2}_{i\,,\,j}}{\Delta y} + f_2(u,v) = 0 \tag{4.17}$$

where

$$f_2(u,v) = \bar{u}\,Ax + V^{n+2}_{i\,,\,j+1/2}\,Ay + f\bar{u} + \frac{1}{\rho H^{n+1}_{i\,,\,j+1/2}}(\tau_{by} - \tau_{sx}) \tag{4.18}$$

$\bar{u}$ and τ_{by} can be presented in a similar way as (4.12.) and (4.13.).

Equation (4.16.) can be rewritten for the previous even time step, as :

$$u^{n}_{i+1/2,j} = u^{n-1}_{i+1/2,j} \tag{4.19}$$

The equation (4.14.) and (4.19.) can be combined with the equation (4.17.) and (4.9.) respectively. By doing so, (4.10.) and (4.16.) are superfluous.
The equations

$$\frac{Z^{n+1}_{i\,,\,j} - Z^{n}_{i,j}}{2\Delta t} + \frac{H^{n}_{i+1/2,j}\,u^{n+1}_{i+1/2,j} - H^{n}_{i-1/2,j}\,u^{n+1}_{i-1/2,j}}{\Delta x} = 0 \tag{4.20}$$

$$\frac{u^{n+1}_{i+1/2,j} - u^{n-1}_{i+1/2,j}}{2\Delta t} + g\frac{Z^{n+1}_{i+1,j} - Z^{n+1}_{i\,,\,j}}{\Delta x} + f_1(u,v) = 0 \tag{4.21}$$

are equivalent with (4.8.) – (4.10), and

$$\frac{Z^{n+2}_{i\,,\,j} - Z^{n+1}_{i\,,\,j}}{2\Delta t} + \frac{H^{n+1}_{i\,,\,j+1/2}\,V^{n+2}_{i\,,\,j+1/2} - H^{n+1}_{i\,,\,j-1/2}\,V^{n+2}_{i\,,\,j-1/2}}{\Delta y} = 0 \tag{4.22}$$

$$\frac{V^{n+2}_{i\,,\,j+1/2} - V^{n}_{i,j+1/2}}{2\Delta t} + g\frac{Z^{n+2}_{i\,,\,j+1} - Z^{n+2}_{i\,,\,j}}{\Delta y} + f_2(u,v) = 0 \tag{4.23}$$

are equivalent with (4.15.) – (4.17.).
The model uses equations (4.20.) – (4.23.), which means that formally not the whole set of equations is falsified but only the continuity equation whereas the momentum equations are alternately evaluated every two timesteps. The equations (4.20.), (4.21.), and (4.22.), (4.23) can be written in matrix form and can easily be solved by a double sweep algorithm, see Moelans and De Bruyn (1986).

4.2.3. DISCUSSION OF THE SCHEME

"Falsification" has been introduced to improve the stability of the numerical scheme and to reduce the number of operations. The scheme gives rise to a very efficient computer implementation and the model runs properly on a personal computer (PC–AT).
The accuracy of the scheme is, however, diminished due to the falsification, because the velocity components u– and v are only evaluated every two time steps, see equations (4.10.) and (4.16). The timestep Δt can be seen as a "measure" for the inaccuracy of the u and v calculations. A property of the entire class of ADI methods is that convergence problems occur with large Courant numbers (Benqué et.al., 1982). Although the scheme is unconditionally stable, a high Courant number leads to solutions which are far from reality. Benqué et.al., (1982) performed a numerical experiment in which tidal propagation in a rectangular basin with a S–shaped channel was simulated by using the ADI method of Leendertse, (1970). The computed velocity field with high Courant number (Cr = 95) gave a result which had little physical meaning. An investigation of ADI schemes was also performed by Weare (1976).
The falsified continuity equations (4.20.) and (4.22.) calculate the water elevation z at odd and even time steps. Due to falsification the equations (4.20.) and (4.22.) are not consistent with equation (4.1.) and the calculation of the water elevation is not accurate enough. The resultant of the two time steps is, however consistent, as can be shown after addition of (4.20.) and (4.22) :

$$\frac{Z^{n+2}_{i,j} - Z^{n}_{i,j}}{2\Delta t} + \frac{H^{n}_{i+1/2,j}\, u^{n+1}_{i+1/2,j} - H^{n}_{i-1/2,j}\, u^{n+1}_{i-1/2,j}}{\Delta x} + \frac{H^{n+1}_{i,j+1/2}\, V^{n+2}_{i,j+1/2} - H^{n+1}_{i,j-1/2}\, V^{n+2}_{i,j-1/2}}{\Delta y} = 0 \qquad (4.24)$$

Addition of (4.20.) and (4.22) for another timestep (n−1) gives

$$\frac{Z^{n+1}_{i,j} - Z^{n-1}_{i,j}}{2\Delta t} + \frac{H^{n}_{i+1/2,j}\ u^{n+1}_{i+1/2,j} - H^{n}_{i-1/2,j}\ u^{n+1}_{i-1/2,j}}{\Delta x} + \frac{H^{n-1}_{i,j+1/2}\ V^{n}_{i,j+1/2} - H^{n-1}_{i,j-1/2}\ V^{n}_{i,j-1/2}}{\Delta y} = 0 \tag{4.25}$$

Equation (4.24.) suggests that z taken at even time steps is a good measure for the water elevation, because (4.24.) is consistent with (4.1.), whereas (4.25.) suggests that z taken at the odd time steps is a good measure for the water elevation. There is no argument which allows a choice between the even z or the odd z values. The equations (4.24.) and (4.25.) only show that after two time steps the continuity equation is satisfied, but it is not clear how accurate the water elevation is computed through z. The modeller is now confronted with the "Hamlet" questions about "even"– or "odd" values. An answer will be given in the next section.

In the case of steady state calculations the following equation should hold :

$$\frac{\partial z}{\partial t} = 0 \tag{4.26}$$

The scheme gives, however, the following results :

$$Z^{n+2}_{i,j} = Z^{n}_{i,j} \tag{4.27}$$

$$Z^{n+1}_{i,j} = Z^{n-1}_{i,j} \tag{4.28}$$

and because of (4.20.) and (4.22.) one can see that :

$$Z^{n+1}_{i,j} \neq Z^{n}_{i,j} \tag{4.29}$$

$$Z^{n+2}_{i,j} \neq Z^{n+1}_{i,j} \tag{4.30}$$

The "even" z and "odd" z approaches both satisfy the equation (4.26.) but from (4.29.) and (4.30.) it appears that the "even" and the "odd" values of z are different and consequently that the u– and v– velocity components are inaccurately computed as well.

In figure 4.2. the water elevation is plotted for a steady state problem (the experiment is described in section 4.3.1.). One can see that small oscillation in the calculation of the water elevation occur which are a consequence of (4.29.) and (4.30.).

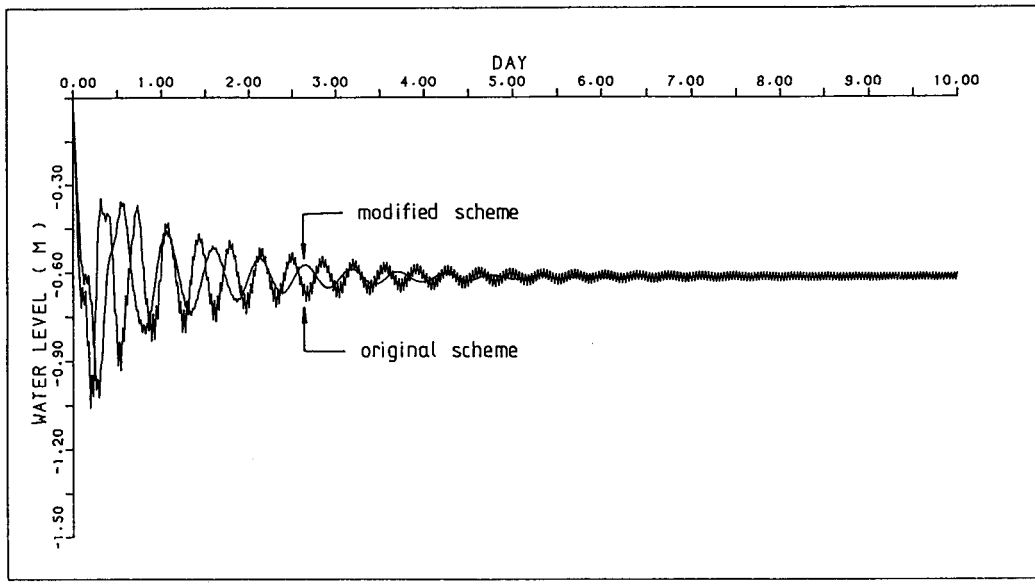

Figure 4.2 : Comparison of calculated water levels between the original and the modified scheme

4.2.4. MODIFIED SCHEME

In order to get accurate results the water elevation has to be time–centered. The u– and v–components are calculated every two time steps, as described in previous sections. The water elevation is now evaluated every time step half–way in between the time of the u and v values. The z variable is still calculated at the same time as the u– and v–variables, but has no physical meaning any more.
The new water elevation, which will be denoted as ζ , is now given by :

$$\zeta = \frac{Z^{odd} + Z^{even}}{2} \tag{4.31}$$

The scheme is formally the same as the one in section 4.2.2. In the momentum equations (4.2.1.) and (4.2.3.) the symbol z has to be replaced by ζ , i.e. the average of the two adjucent z values and the expression of the total water depth (H = h + z) should be replaced by H = h + ζ in every equation it occurs.
In figure 4.2. the results of the original scheme are compared with those of the modified scheme. The accuracy of the modified scheme is higher and the convergence to the steady state is faster.

4.3. Applications

In this section are presented some applications which allow the verification of the model. The model results are compared with the analytical solution of an idealized example and the model is used to calculate the tidal flows in the North Sea. The North Sea has been chosen for the testing of the model, because a lot of measurements are available for this area. Some of these application have already been published, see Moelans and De Bruyn (1986) and Yu et.al. (1988a and 1988b).

4.3.1. STEADY FLOW PROBLEM

A simple–shaped geometry was chosen in order to compare the numerical results with analytical solutions. Sündermann's work (1966) has been reproduced for this case study. The K.U.L. model (presented in this chapter) and the explicit Hansen model (Hansen, 1969), with linear friction term (where τ_b = 2.5 x 10–5 s^{-1} in Eq. (4.2.) and (4.3.)) and with non–linear friction term were used to simulate the hydrodynamic motions in a closed rectangular basin with different wind fields. Experiments were carried out for constant North and Northwest wind. The time interval is 600 sec. The wind–generated flows were approaching steady state after 2880 computation steps or ten days after the constant wind field started acting on the initially still bassin. The results from the K.U.L. model and the Hansen model with linear friction show good agreement with the analytical solution, as shown in tabel 4.1. and tabel 4.2. The Hansen scheme with non–linear friction term does not converge to a stable result, but the K.U.L. model can produce a stable result, (see figure 4.3.).

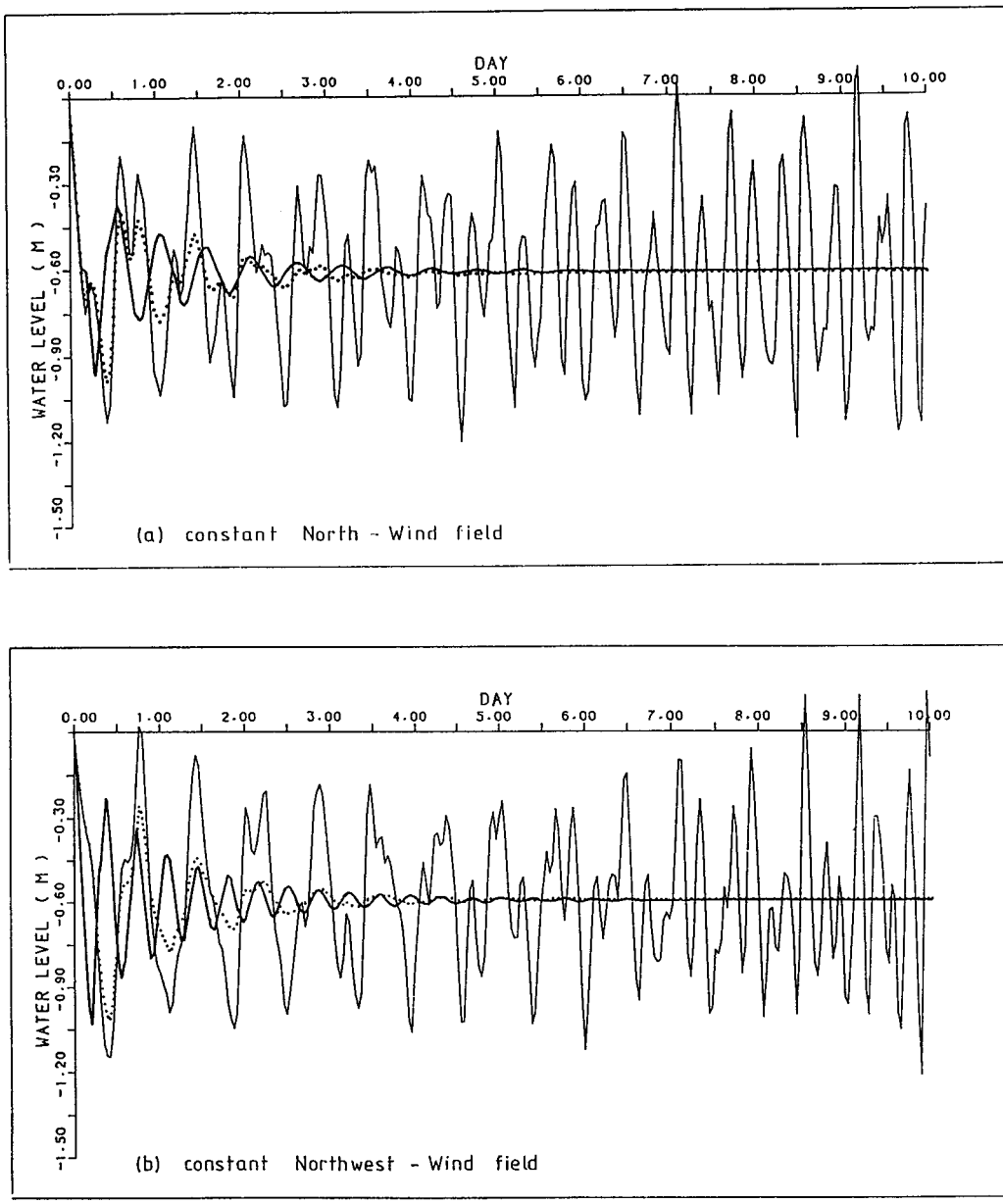

Figure 4.3 : Comparison of calculated water levels between FADI model (_____), Hansen model with linear friction (.....) and Hansen model with non–linear friction (———) from (a) constant North–wind field and (b) constant Northwest–wind field

Table 4.1 : Water level in meters for constant North wind, wind speed = 20m/s, timestep = 2880 (after 10 days)

J \ I	2	3	4	5	6	7	8	9	10	11	†
* 21	-.591	-.591	-.591	-.591	-.591	-.591	-.591	-.591	-.591	-.591	-.620
$	-.590	-.590	-.590	-.590	-.590	-.590	-.590	-.590	-.590	-.590	
20	-.528	-.528	-.528	-.528	-.528	-.528	-.528	-.528	-.528	-.528	-.555
	-.528	-.528	-.528	-.528	-.528	-.528	-.528	-.528	-.528	-.528	
19	-.466	-.466	-.466	-.466	-.466	-.466	-.466	-.466	-.466	-.466	-.489
	-.466	-.466	-.466	-.466	-.466	-.466	-.466	-.466	-.466	-.466	
18	-.404	-.404	-.404	-.404	-.404	-.404	-.404	-.404	-.404	-.404	-.424
	-.403	-.403	-.403	-.403	-.403	-.403	-.403	-.403	-.403	-.403	
17	-.341	-.341	-.341	-.341	-.341	-.341	-.341	-.341	-.341	-.341	-.359
	-.341	-.341	-.341	-.341	-.341	-.341	-.341	-.341	-.341	-.341	
16	-.279	-.279	-.279	-.279	-.279	-.279	-.279	-.279	-.279	-.279	-.294
	-.279	-.279	-.279	-.279	-.279	-.279	-.279	-.279	-.279	-.279	
15	-.217	-.217	-.217	-.217	-.217	-.217	-.217	-.217	-.217	-.217	-.228
	-.217	-.217	-.217	-.217	-.217	-.217	-.217	-.217	-.217	-.217	
14	-.154	-.154	-.154	-.154	-.154	-.154	-.154	-.154	-.154	-.154	-.163
	-.154	-.154	-.154	-.154	-.154	-.154	-.154	-.154	-.154	-.154	
13	-.092	-.092	-.092	-.092	-.092	-.092	-.092	-.092	-.092	-.092	-.098
	-.092	-.092	-.092	-.092	-.092	-.092	-.092	-.092	-.092	-.092	
12	-.030	-.030	-.030	-.030	-.030	-.030	-.030	-.030	-.030	-.030	-.033
	-.030	-.030	-.030	-.030	-.030	-.030	-.030	-.030	-.030	-.030	
11	.032	.032	.032	.032	.032	.032	.032	.032	.032	.032	.033
	.032	.032	.032	.032	.032	.032	.032	.032	.032	.032	
10	.094	.094	.094	.094	.094	.094	.094	.094	.094	.094	.098
	.094	.094	.094	.094	.094	.094	.094	.094	.094	.094	
9	.156	.156	.156	.156	.156	.156	.156	.156	.156	.156	.163
	.156	.156	.156	.156	.156	.156	.156	.156	.156	.156	
8	.218	.218	.218	.218	.218	.218	.218	.218	.218	.218	.228
	.218	.218	.218	.218	.218	.218	.218	.218	.218	.218	
7	.280	.280	.280	.280	.280	.280	.280	.280	.280	.280	.294
	.279	.279	.279	.279	.279	.279	.279	.279	.279	.279	
6	.341	.341	.341	.341	.341	.341	.341	.341	.341	.341	.359
	.341	.341	.341	.341	.341	.341	.341	.341	.341	.341	
5	.403	.403	.403	.403	.403	.403	.403	.403	.403	.403	.424
	.403	.403	.403	.403	.403	.403	.403	.403	.403	.403	
4	.465	.465	.465	.465	.465	.465	.465	.465	.465	.465	.489
	.465	.465	.465	.465	.465	.465	.465	.465	.465	.465	
3	.527	.527	.527	.527	.527	.527	.527	.527	.527	.527	.555
	.526	.526	.526	.526	.526	.526	.526	.526	.526	.526	
2	.588	.588	.588	.588	.588	.588	.588	.588	.588	.588	.620
	.588	.588	.588	.588	.588	.588	.588	.588	.588	.588	

* First line: Numerical results from explicit HANSEN scheme with linear friction term.
$ Second line: Numerical results from KUL model.
†: Analytical solution.

Table 4.2 : Water level in meters for constant Northwest wind, wind speed = 20m/s, timestep = 2880 (after 10 days)

J \ I	2	3	4	5	6	7	8	9	10	11	†
†	-.646	-.600	-.554	-.507	-.461	-.415	-.369	-.323	-.277	-.231	
* 21	-.616	-.572	-.528	-.484	-.439	-.395	-.351	-.307	-.263	-.219	-.231
$	-.616	-.571	-.527	-.483	-.439	-.395	-.351	-.307	-.263	-.219	
20	-.572	-.528	-.484	-.439	-.395	-.351	-.307	-.263	-.219	-.175	-.185
	-.572	-.527	-.483	-.439	-.395	-.351	-.307	-.263	-.219	-.175	
19	-.528	-.484	-.439	-.395	-.351	-.307	-.263	-.219	-.175	-.131	-.138
	-.527	-.483	-.439	-.395	-.351	-.307	-.263	-.219	-.175	-.131	
18	-.484	-.439	-.395	-.351	-.307	-.263	-.219	-.175	-.131	-.087	-.092
	-.483	-.439	-.395	-.351	-.307	-.263	-.219	-.175	-.131	-.087	
17	-.440	-.395	-.351	-.307	-.263	-.219	-.175	-.131	-.087	-.043	-.046
	-.439	-.395	-.351	-.307	-.263	-.219	-.175	-.131	-.087	-.043	
16	-.395	-.351	-.307	-.263	-.219	-.175	-.131	-.087	-.043	.001	.000
	-.395	-.351	-.307	-.263	-.219	-.175	-.131	-.087	-.043	.001	
15	-.351	-.307	-.263	-.219	-.175	-.131	-.087	-.043	.000	.044	.046
	-.351	-.307	-.263	-.219	-.175	-.131	-.087	-.043	.001	.045	
14	-.307	-.263	-.219	-.175	-.131	-.087	-.043	.000	.044	.088	.092
	-.307	-.263	-.219	-.175	-.131	-.087	-.043	.001	.045	.088	
13	-.263	-.219	-.175	-.131	-.087	-.043	.000	.044	.088	.132	.138
	-.263	-.219	-.175	-.131	-.087	-.043	.001	.044	.088	.132	
12	-.219	-.175	-.131	-.087	-.043	.000	.044	.088	.132	.176	.185
	-.219	-.175	-.131	-.087	-.043	.001	.044	.088	.132	.176	
11	-.175	-.131	-.087	-.043	.001	.044	.088	.132	.176	.220	.231
	-.175	-.131	-.087	-.043	.000	.044	.088	.132	.176	.220	
10	-.131	-.087	-.043	.001	.044	.088	.132	.176	.220	.263	.277
	-.131	-.087	-.043	.000	.044	.088	.132	.176	.220	.263	
9	-.087	-.043	.001	.044	.088	.132	.176	.220	.263	.307	.323
	-.087	-.044	.000	.044	.088	.132	.176	.219	.263	.307	
8	-.043	.001	.044	.088	.132	.176	.220	.263	.307	.351	.369
	-.044	.000	.044	.088	.132	.176	.219	.263	.307	.351	
7	.000	.044	.088	.132	.176	.220	.263	.307	.351	.394	.415
	.000	.044	.088	.132	.176	.219	.263	.307	.351	.394	
6	.044	.088	.132	.176	.220	.263	.307	.351	.394	.438	.461
	.044	.088	.132	.176	.219	.263	.307	.350	.394	.438	
5	.088	.132	.176	.220	.263	.307	.351	.394	.438	.482	.507
	.088	.132	.175	.219	.263	.307	.350	.394	.438	.481	
4	.132	.176	.220	.263	.307	.351	.394	.438	.482	.525	.554
	.132	.175	.219	.263	.307	.350	.394	.438	.481	.525	
3	.176	.220	.263	.307	.351	.394	.438	.482	.525	.569	.600
	.175	.219	.263	.307	.350	.394	.438	.481	.525	.568	
2	.220	.263	.307	.351	.394	.438	.482	.525	.569	.612	.646
	.219	.263	.307	.350	.394	.438	.481	.525	.568	.612	

* First line : Numerical results from explicit HANSEN scheme with linear friction term.
$ Second line: Numerical results from implicit KUL model.
†: Analytical solution.

4.3.2. UNSTEADY FLOW PROBLEMS

The model has been used to simulate the tidal flows of the North–West European Continental Shelf. The model represents an area from 12° W to the Baltic Sea, and from 48° N to 61° N. The grid size is 24 x 24 km² for the coarse grid and 8 x 8 km² for the fine grid. The fine grid includes the southern North Sea and the English Channel. The model

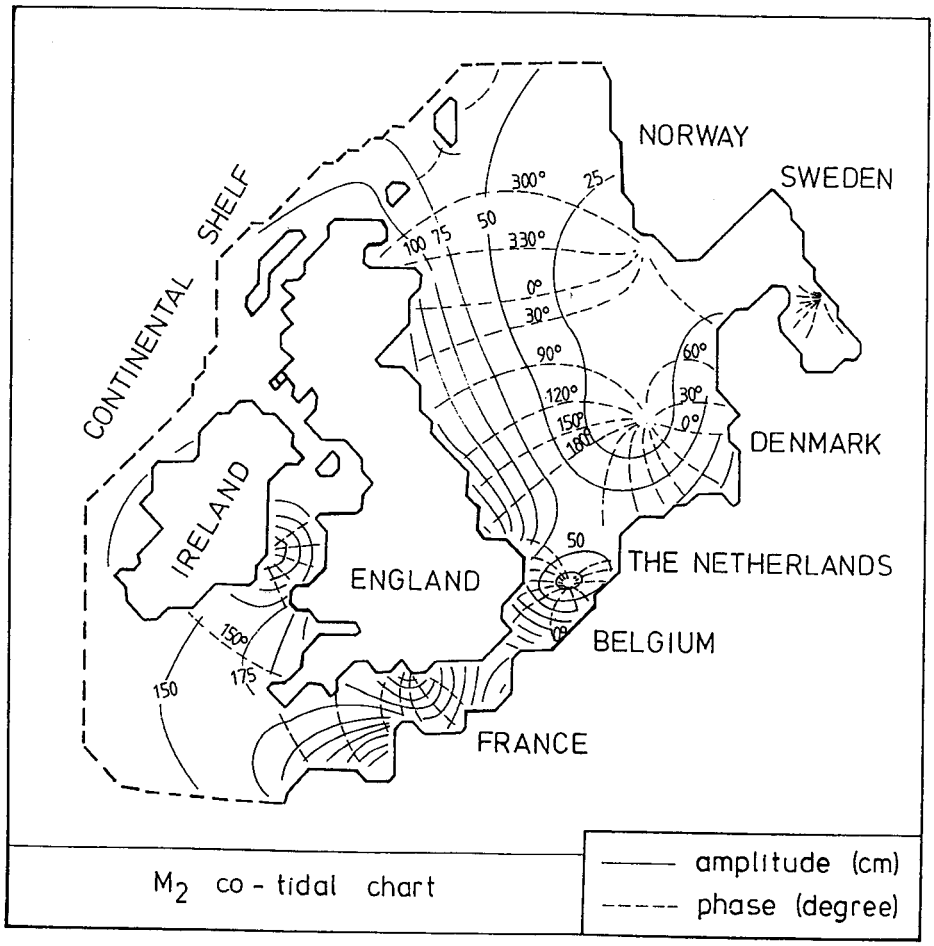

Figure 4.4 : M_2 co–tidal co–range map of the continental shelf model of the North Sea

is forced with 6 tidal constituents (i.e. O1, K1, N2, M2, S2, K2) specified at the open boundaries. The computed co–tidal and co–range map for the M2 tide is illustrated in figure 4.4. The computed tidal currents for the 6 constituents are shown in figure 4.5. The computational results are generally in good agreement compared with those of other models, e.g. see the 3D spectral model of Davies (1987).

In figure 4.6. computed water elevation for different stations situated in the southern North Sea and the English Channel has been compared with measurements. The results have been obtained with a model of the Southern North Sea and the English Channel. The grid and the boundary conditions for this model were given by the organizers of the Tidal Flow Forum (VII Int. Conf. on Computational Methods in Water Resources, MIT, 13–17 June 1988). The aim of this Forum was to compare the results of different models all using the same input data. The conclusion of the experiment was that all the models give about the same performance, the discrepancies between measurements and model results are mainly due to inaccurate input data (boundary conditon, bathymetry, friction parameters ...), see Yu et.al. (1988d). When changing the friction parameter, i.e. using a depth–dependent friction law such as Manning formula, the results are closer to the reference measurements.

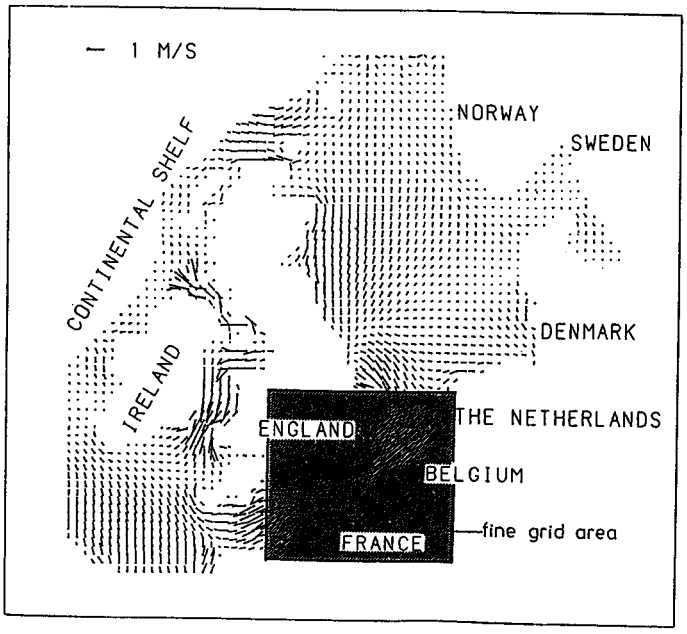

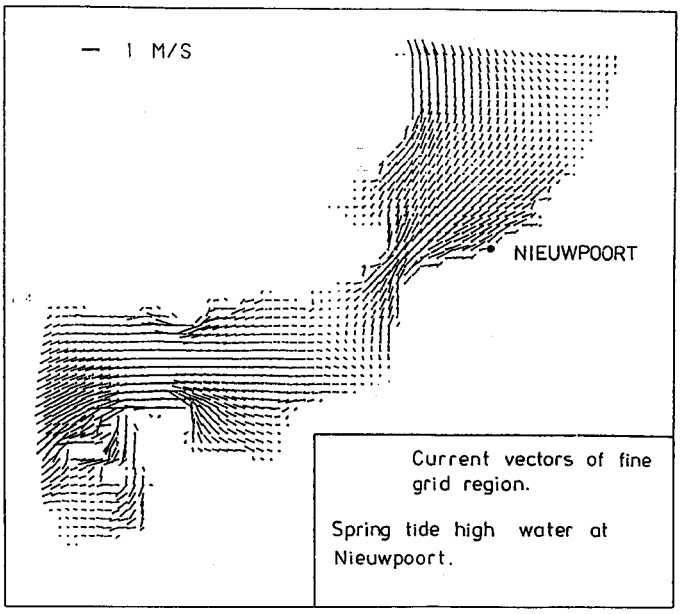

Figure 4.5 : Computed tidal currents (a) coarse grid (b) fine grid, at spring tide high water at Nieuwpoort

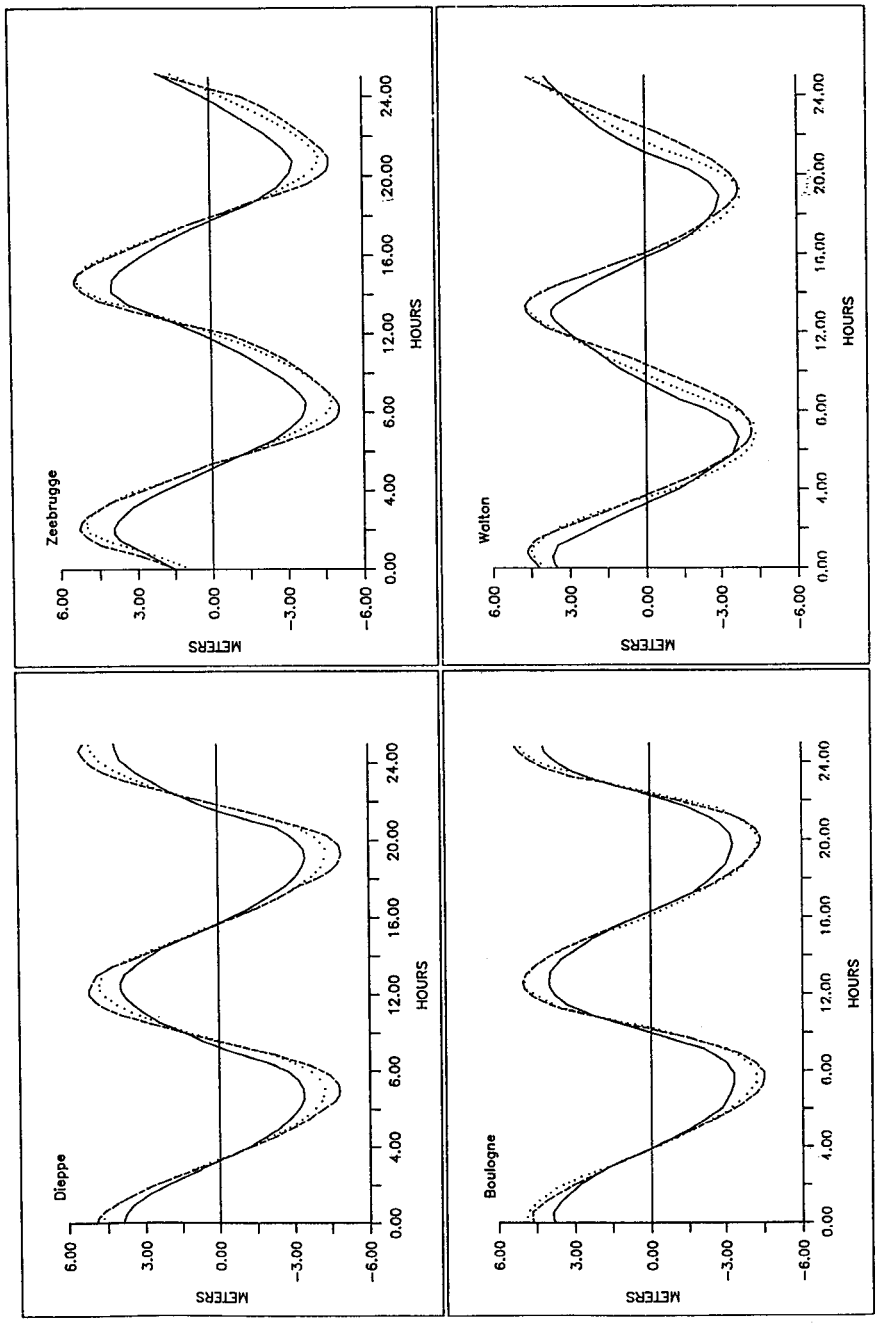

Figure 4.6 : Tidal curves simulated with different friction laws, (———) C=65, (.....) n=0.02 , (– – –) reference

5. OPEN BOUNDARY CONDITION FOR CIRCULATION MODELS

5.1. Introduction

In many numerical models it is necessary to restrict the domain of integration because the computer time (budget) is too big and/or the internal memory of the computer is too small for the whole problem or because the modeller is only interested in local phenomena. The integration domain is in those cases much smaller than the whole ocean basin and one has to introduce boundaries which have no physical meaning. This can lead to a wrong solution of the problem. In order to integrate the equations for a restricted domain it is necessary to define meaningful conditions at the open sea boundaries.

A most common approach is the following one which applies the grid refinement technique : a bigger domain is discretised on a coarse grid and the values of the dependent variables generated at the fine grid/coarse grid boundaries are used as boundary condition for the fine domain. An example of this is given in Yu et.al. (1988c). This technique is in many cases not appropriate because the computer memory needed for the nested model is too big or because the boundary condition for the coarse grid is also unknown.

A second approach consist in the use of an open boundary condition (OBC). The computational boundaries can be subdivided into natural boundaries and artificial boundaries (see Røed and Cooper, 1986). An example of a natural boundary is the closed boundary (continental boundary). According to these authors artificial boundaries can be further subdivided into open boundaries and specified boundaries.

For the latter kind of boundary one or several variables are a priori determined and are independent of the values of the same variables in the interior of the domain. The specified boundary has a great influence on the evolution of the model solution. Examples of this kind of boundary are the tidal models which are forced by specifying the tidal constituents at the boundary (see e.g. Yu et.al., 1988c).

A total different type of boundaries are the open boundaries. Open boundary conditions have to be defined in such a way that the influence of the boundaries is minimal in the interior domain. Røed and Cooper (1986) define an open boundary as "a computational boundary at which disturbances originating in the interior of the computational domain are allowed to leave it without disturbing or deteriorating the interior solution". Unfortunately, perfect open boundaries do not exist (Chapman, 1985), every open boundary condition introduces disturbances in the numerical solution. The choice of an open

boundary condition should therefore be made very carefully. It should be based on the following criteria (Røed and Cooper, 1986) :

- no reflection or generation of disturbances
- the numerical scheme must be stable
- the accuracy should be adequate
- it should be mathematically well posed
- it should be applicable to the numerical model.

In the next section a review of different open boundary conditions is given. In section 5.3. some results with different open boundary condition at the open sea boundary using the model of chapter 4 are considered for some simple cases.

5.2. Review of Literature

The open boundary conditions mentioned in literature can be divided into three types :

- extrapolation formulas (Kreiss, 1966; Chen, 1973)
- formulas based on the Sommerfeld radiation condition
- sponge filters in combination with radiation conditions (Israeli and Orszag, 1981).

All these open boundaries should act in such a way that the variables at the boundary evolve in time coherently with the variables in the interior domain. Radiation condition in combination with a sponge filter uses an absorbing boundary. The sponge is for example a region with increasing bottom friction or with increasing viscosity.

In this section some open boundary conditions are presented which are all based on the Sommerfeld radiation condition which can be written in the form

$$\phi_t \pm C_{\phi x} = 0 \tag{5.1}$$

Where ϕ is the dependent variable which has to be specified at the boundary, C is the phase speed, t is time and x is the coordinate perpendicular to the boundary.

In 1976 Orlanski suggested an implementation of the Sommersfeld radiation condition (5.1.). Following this approach, which has widely been used, the phase speed is not taken as a constant value but is numerically evaluated at each time step from values of ϕ at neighbouring grid points using a leapfrog representation of (5.1.) :

$$C_\phi = -\frac{\Delta x}{2\Delta t}\left(\frac{\phi^n_{B-1} - \phi^{n-2}_{B-1}}{(\phi^n_{B-1} + \phi^{n-2}_{B-1})/2 - \phi^{n-1}_{B-2}}\right) \tag{5.2}$$

where B represents a point at the boundary. If C_ϕ is positive (outflow) it is used in (5.1.) to calculate the boundary value :

$$\phi^{n+1}_B = \frac{\left(1 - \frac{\Delta t}{\Delta x}C_\phi\right)}{\left(1 + \frac{\Delta t}{\Delta x}C_\phi\right)}\phi^{n-1}_B + \frac{2\frac{\Delta t}{\Delta x}C_\phi}{\left(1 + \frac{\Delta t}{\Delta x}C_\phi\right)}\phi^n_{B-1} \tag{5.3}$$

when C_ϕ is greater than $\Delta x/\Delta t$ the boundary value is :

$$\phi^{n+1}_B = \phi^{n-1}_B \tag{5.4}$$

If the phase speed is negative (inflow) the boundary value is either specified or unchanged. Camerlengo and O'Brien (1980) simplified the Orlanski method, they proposed to use only the extreme phase speed values. This method seems to yield better results when simulating the outflow of Kelvin waves for a free wave experiment, but does not have the long–time stability a perfect open boundary condition should have (Camerlengo and O'Brien, 1980). It should be mentioned here that unfortunately no numerical implementation of an open boundary condition is perfect for general models. Numerical treatments of open boundaries are thus only an approximation of the problem but are at present the most reasonable approach (Chapman, 1985).

Miller and Thorpe (1981) tested different numerical formulations of the Sommerfeld radiation condition. They showed that the Orlanski (1976) formulation can be made more accurate when using the upstream method instead of the leapfrog method. A finite difference formulation of (5.1.) using the upstream method is given by

$$\phi^{n+1}_b = \phi^n_b\left(1 - \frac{C_\phi \Delta t}{\Delta x}\right) - C_\phi \frac{\Delta t}{\Delta x}\left(\phi^n_b - \phi^n_{b-1}\right) \tag{5.5}$$

The phase speed is calculated by use of (5.5.) :

$$C_\phi = \frac{\Delta x}{\Delta t} \frac{\phi_{B-1}^{n} - \phi_{B-1}^{n-1}}{\phi_{B-2}^{n-1} - \phi_{B-1}^{n-1}} \tag{5.6}$$

and is then substituted into (5.5.) to get the boundary value. Miller and Thorpe (1984) also performed a truncation error analysis and concluded that a higher accuracy is obtained when

$$C_\phi = \frac{\Delta x}{\Delta t} \left(\frac{\phi_{B-1}^{n+1} - \phi_{B-1}^{n}}{\phi_{B-2}^{n} - \phi_{B-1}^{n}} + \frac{\phi_{B}^{n} - \phi_{B}^{n-1}}{\phi_{B-1}^{n-1} - \phi_{B}^{n-1}} - \frac{\phi_{B-1}^{n} - \phi_{B-1}^{n-1}}{\phi_{B-2}^{n-1} - \phi_{B-1}^{n-1}} \right) \tag{5.7}$$

The different methods described here have all the drawback that the phase speed in the direction perpendicular to the boundary is unrealistic because a ϕ that is multi dimensional is substituted in a formula that only allows advection in one direction (Raymond and Kuo, 1984). They proposed to use different radiation condition for the different directions. For a two–dimensional model the radiation conditions are :

$$\phi_t \pm C_x \phi_x = 0 \tag{5.8}$$

$$\phi_t \pm C_y \phi_y = 0 \tag{5.9}$$

Where c_x and c_y are the phase velocities in x and y directions, respectively.

The vector phase speed C does not satisfy the rules of vector decomposition, so cx and cy are not the projections of the vector phase speed C. When adding (5.8.) and (5.9.), one obtains

$$\phi_t = -\alpha_x C_x \phi_x - \alpha_y C_y \phi_y \tag{5.10}$$

where αx and αy are weighing factors, so that $\alpha x + \alpha y = 1$.
Instead of (5.10.) one can also write :

$$\phi_t = \overline{C}_x \phi_y + \overline{C}_y \phi_y \tag{5.11}$$

where $\overline{C}_x$ and $\overline{C}_y$ are the projections of c in the x and y direction respectively. When relating (5.10.) and (5.11.) one obtains formulations for αx and αy.

$$\alpha_x = \phi_x^2/(\phi_x^2 + \phi_y^2) \tag{5.12}$$

$$\alpha_y = \phi_y^2/(\phi_y^2 + \phi_x^2) \tag{5.13}$$

$\bar{c}_x$ and $\bar{c}_y$ or equivalently cx and cy are written as :

$$\overline{C}_x = -\phi_t\phi_x/(\phi_x^2 + \phi_y^2) \tag{5.14}$$

$$\overline{C}_y = -\phi_t\phi_y/(\phi_x^2 + \phi_y^2) \tag{5.15}$$

A similar formulation as by Orlanski (1976) can now be derived for each coordinate direction.

The formula (5.1.) only holds without forcing at the boundary. In the case of forcing the right–hand side of (5.1.) is non–zero. In order to allow forcing at the boundary, the radiation condition has to be modified.

Røed and Smedstad (1984) suggested splitting the dependent variables into two modes, one mode which contains the local contribution including e.g. the local forcing by wind and one which contains the non–local contribution. Only for the latter part is a boundary condition needed. Røed and Smedstad (1984) used the Camerlengo and O'Brien (1980) method as boundary condition. In the next section are presented some experiments which give a comparison between the behaviour of the Orlanski and the Camerlengo–O'Brien condition. It seems that the latter is better in the case of long dispersive edge waves.

Another approach which incorporates external forcing at the boundary was proposed by Blumberg and Kantha (1985). They developed a "damped" Sommerfeld radiation condition which can be used for tidal or meteorological forcing :

$$\zeta_t + C\zeta_x = \frac{1}{T_f}(\zeta - \zeta_k) \tag{5.16}$$

where ζ is the elevation above MSL, ζ_k can contain tidal elevation or pressure gradient. The phase velocity C is equal to $\sqrt{gh}$ and is thus fixed in time. "The term on the right

represents damping which tends to force the value of ζ at the boundary to some known value ζ_k with a time scale of order T_f" (Blumberg and Kantha, 1985).

In an article by Bills and Noye (1987) is presented an investigation of open boundary condition for tidal models. They concluded that the Blumberg and Kantha (1985) method is not an appropriate condition to be used in the case of pure tidal forcing. They proposed a modified Blumberg and Kantha (1985) condition, which uses the Orlanski (1976) calculation of phase speed. This condition gives better performance but "seems unnecessarily complicated in comparison to the Orlanski (1976) condition" (Bills and Noye, 1987). They recommend the Orlanski (1976) condition for tidal models if a radiation condition is required. The success of this condition is mainly due to its separation of tidal motion into ingoing and outgoing flows. The more accurate difference form of C proposed by Miller and Thorpe (1981), see eq (5.7.), is not used by Bill and Noye (1987) because "it is not likely that C will significantly alter over a distance $2\Delta x$ in the time interval $\Delta t/2$ for the tidal disturbance".

5.3. Numerical implementation and experiments

5.3.1. NUMERICAL IMPLEMENTATION

The Orlanski and the Camerlengo and O'Brien condition have been used as open boundary condition.

Re–arranging (5.1.), the phase velocity is calculated as :

$$C = -\frac{\partial\phi}{\partial t} \Big/ \frac{\partial\phi}{\partial x} \tag{5.17}$$

The following difference equation is used to obtain the value of the phase velocity c :

$$C = -\frac{4\Delta x}{\Delta t}\left(\frac{\phi^{n}_{B-1} - \phi^{n-2}_{B-1}}{\phi^{n}_{B-1} + \phi^{n-2}_{B-1} - 2\phi^{n-2}_{B-2}}\right) \tag{5.18}$$

the value of c for the next (even) time–step is :

$$C = -\frac{4\Delta x}{\Delta t}\left(\frac{\phi_{B-1}^{n+1} - \phi_{B-1}^{n-1}}{\phi_{B-1}^{n+1} + \phi_{B-1}^{n-1} - 2\phi_{B-2}^{n}}\right) \tag{5.19}$$

if $C \leq 0$ the flow is ingoing, if $C > 0$ the flow is outgoing. Orlanski restricted the value of C so that :

if $C \leq 0$ then C is set to zero,

if $0 < C \leq 2\Delta x/\Delta t$ then C keeps the calculated value, and

if $C > 2\Delta x/\Delta t$ then C is set to $2\Delta x/\Delta t$.

As has already been mentioned in the previous section, Camerlengo and O'Brien took only the extreme phase velocity values :

if $C \leq 0$ then C is set to zero, and

if $C > 0$ then C is set to $2\Delta x/\Delta t$.

The value of C is put in (5.1.) to calculate the value at the boundary. The difference form of (5.1.) is given by :

$$\phi_B^{n+1} = \frac{\phi_B^{n-1}\left(1 - \frac{C\Delta t}{4\Delta x}\right) + \phi_{B-1}^{n}\,\frac{C\Delta t}{2\Delta x}}{1 + \frac{C\Delta t}{4\Delta x}} \tag{5.20}$$

and

$$\phi_B^{n+2} = \frac{\phi_B^{n}\left(1 - \frac{C\Delta t}{4\Delta x}\right) + \phi_{B-1}^{n+1}\,\frac{C\Delta t}{2\Delta x}}{1 + \frac{C\Delta t}{4\Delta x}} \tag{5.21}$$

For an ingoing wave, i.e. $C = 0$, both the Orlanski and the Camerlengo and O'Brien scheme are reduced to

$$\phi_B^{n+1} = \phi_B^{n-1} \; ; \; \phi_B^{n+2} = \phi_B^{n} \tag{5.22}$$

The open boundary condition is applied to the sea surface elevation. The calculation of the velocity values needs a special treatment. It is more accurate to calculate the velocity by extrapolation using interior values than by using the mor[illegible]quation. By doing so, the stability of the scheme and the accuracy of the results are higher (Bills and Noye, 1987).

5.3.2. NUMERICAL EXPERIMENTS

To examine the effect of the open boundary conditions in the model, described by (4.1.) – (4.3.), three numerical experiments have been carried out :

- baratropic relaxation
- alongshelf wind stress
- forced waves at the open boundary.

A long channel (600 x 1200 km) with a simple bathymetry was chosen as a test basin in order to keep the interpretation of the results simple. The dimension of the basin, the value of the different parameters and the set up of the experiments were adapted from Røed and Smedstad (1984). For more information see their article.

a. Barotropic relaxation

In this simulation no forcing is applied. The fluid is initially at rest with the sea surface elevated 10 cm in the middle of the computational domain. The upper and the lower boundary are open. This experiment allows the investigation of the wave reflection properties of the open boundary condition. Adjustment takes place by dispersive Poincaré waves and non–dispersive Kelvin waves (Gill, 1976 in Røed and Smedstad, 1984). The channel has a constant depth of 160 m. In figure 5.1. the deviation of the surface elevation is shown for different time steps. After 16 hours most of the waves have passsed the open boundaries. Hardly any differences exist between the Camerlengo and O'Brien (1980), and the Orlanski (1976) condition. This experiment shows that the open boundary conditions are good implemented. In figure 5.2.(a) is presented a longitudinal section through the channel at different times. In this case the initial jump is a sinus wave centered at the middle of the domain. In figure 5.2.(b) the total energy at a cross section close to the northern boundary is plotted versus time. The disturbances have disappeared after about 30 hours.

b. Alongshelf wind stress

The channel has now a shelf region with a water depth of 160 m and a width of one–third of the channel from the right–hand wall, the rest of the channel consists of

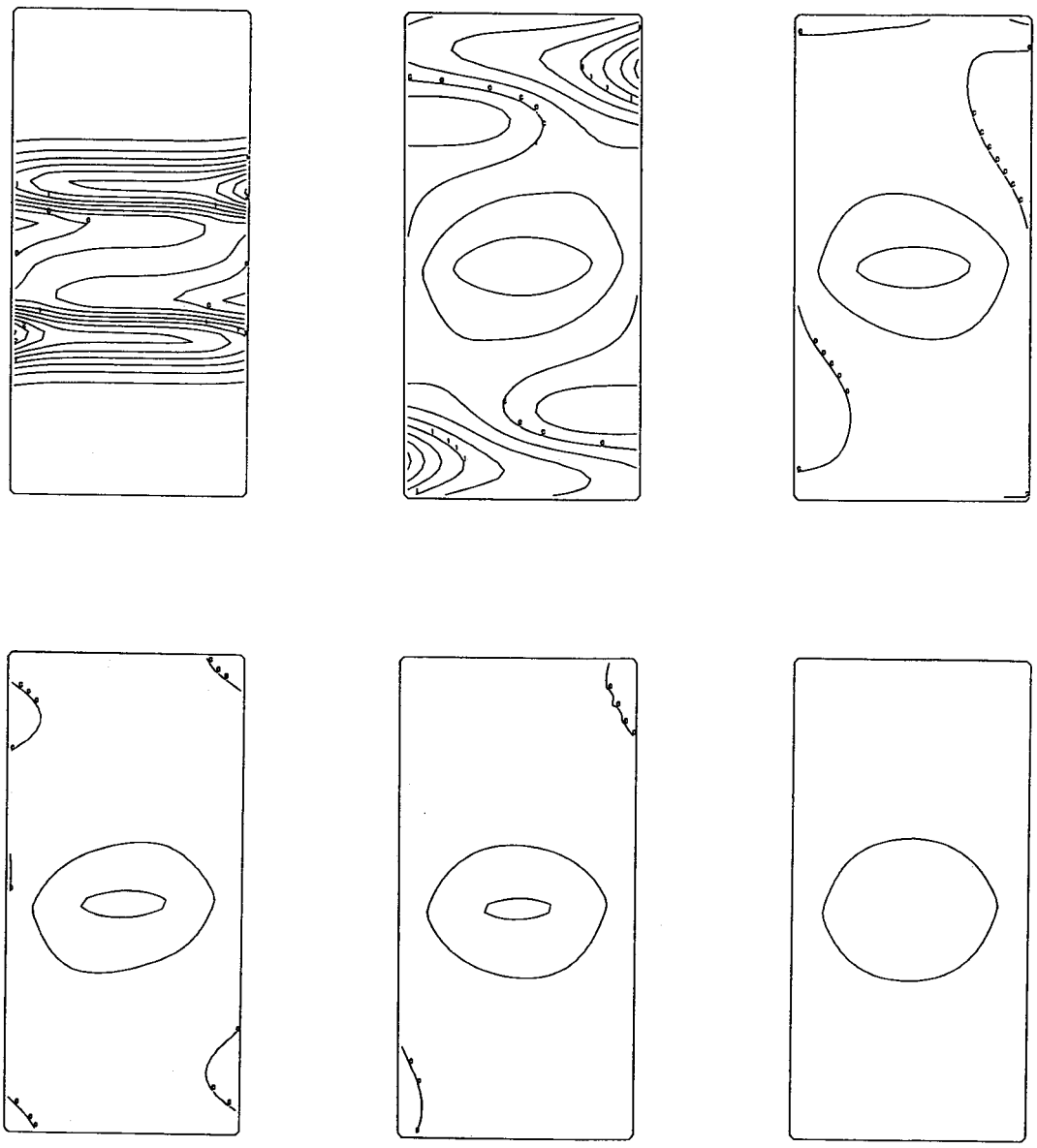

Figure 5.1 : Surface elevation in cm (contour interval = 0.25cm) for the barotropic relaxation experiment. The northern and the southern boundary are open. The solution is shown after 2, 5, 8, 11, 16 and 32 hours

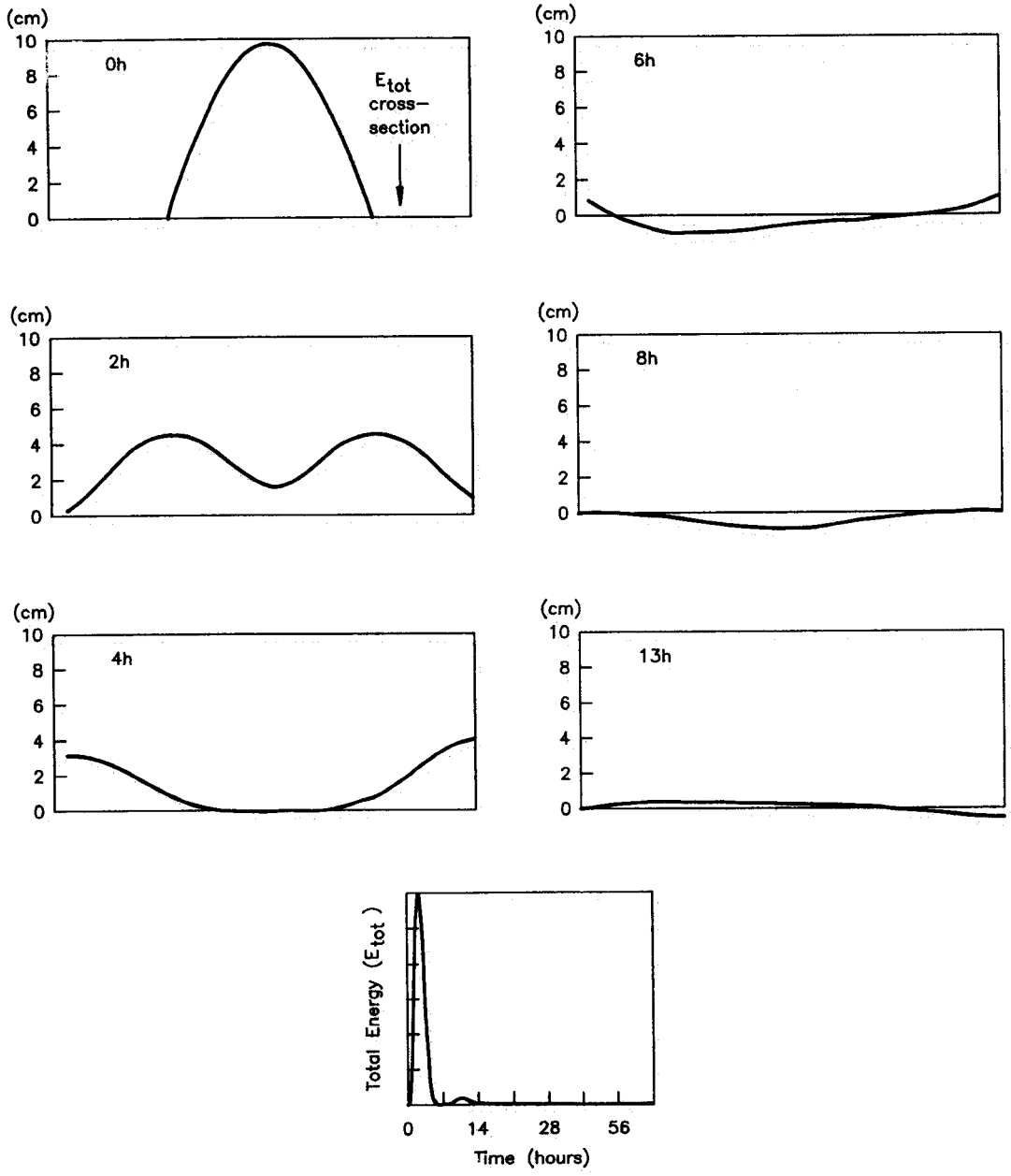

Figure 5.2 : (a) Surface elevation in a longitudinal section through the channel for the barotropic relaxation experiment (sinus wave). The solution is shown after 0, 2, 4, 6, 8 and 32 hours. (b) Total energy (E_{tot}) at a cross section close to the northern boundary (see figure at 0 hours for the exact position)

a deep ocean (h = 1600 m). Only the upper boundary is open. Wind stress is applied along the channel axis in the lower half of the channel and is turned on for 8 hours and then set to zero.

In consequence of the wind action different kinds of waves are formed : the topography generates dispersive shelf waves and when the wind is turned on a non–dispersive Kelvin wave is generated. The sequence of events is illustrated in figure 5.3. for the Orlanski condition and in figure 5.4. for the Camerlengo and O'Brien condition. The results are compared with those of Røed and Smedstad (1984) which were obtained in a closed channel with such a length that the fastest wave and its reflection did not disturb the solution within the region of interest during the computation. The agreement is good. Small differences occur between the solutions obtained with the Orlanski and the Camerlengo and O'Brien condition. After 32 hours of simulation the shelf waves have left the computation domain in case the Orlanski condition is used. Compared with the solution of Røed and Smedstad, the Camerlengo and O'Brien condition gives better performance than the Orlanski condition.

c. Forced waves at the open boundary

This experiment was set up in order to check at the response of the water to wind forcing. The basin has the same dimensions as in the previous experiments. The depth is constant (160 m) as in experimentent (b) and the wind is blowing in the lower half of the channel. The southern boundary is forced whereas the northern is unforced. After an adjustement time a steady state sea surface elevation sets up and generates an alongshelf geostrophic current. The adjustment time is a function of the water depth and the friction coefficient (see Chapman, 1985).

After 8 hours, the wind is turned off and a geostrophic flow is developed, except for some oscillations (see figs 5.5. and 5.6.). Both, the Camerlengo and O'Brien and the Orlanski open boundary condition do not give such a good performance as the open boundary condition proposed by Røed and Smedstad (1984).

In our case, a geostrophic flow is formed after a longer period (±24 h v. ±16 h). This is to be expected, since until now, open boundary with forcing is not implemented.

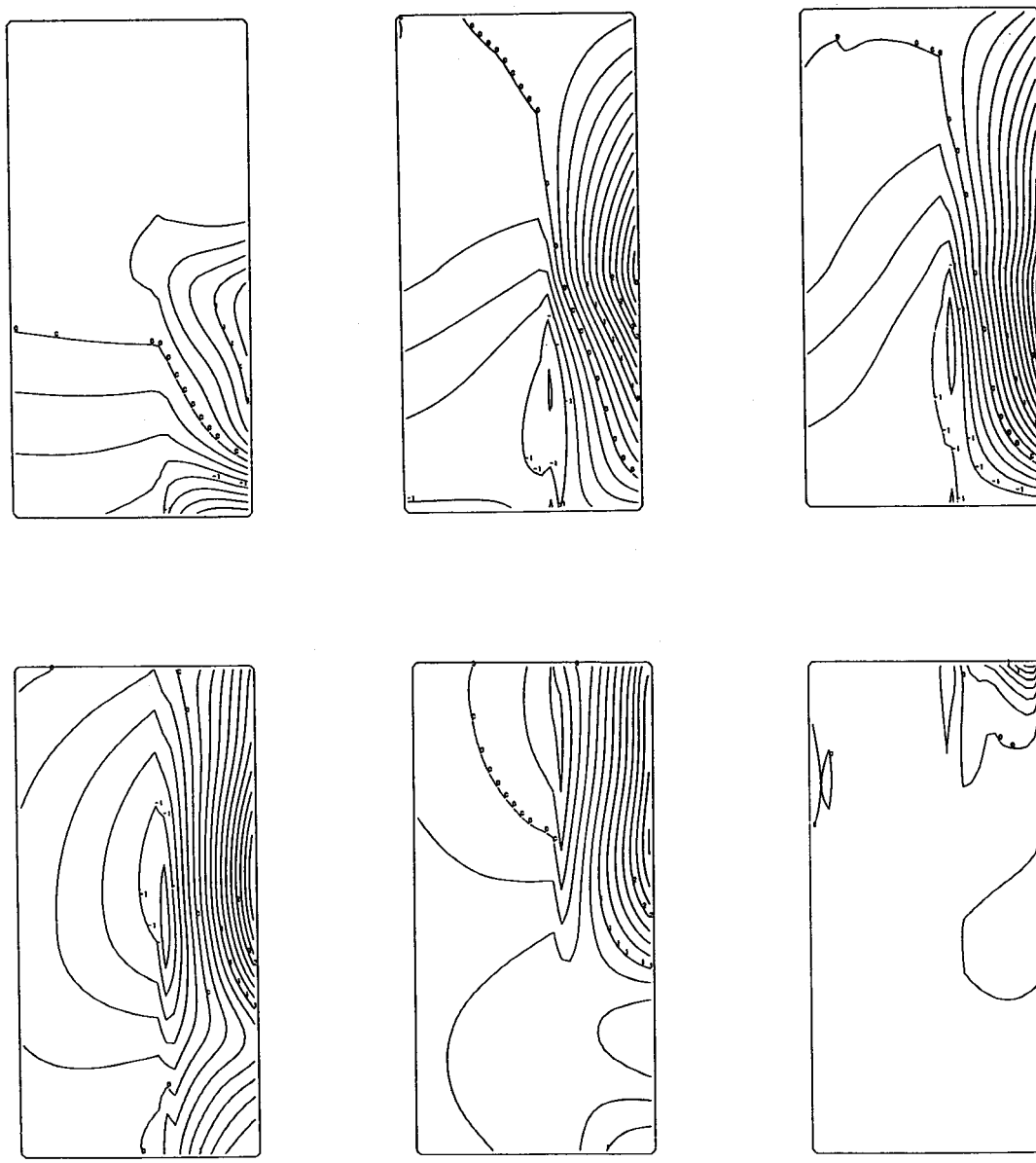

Figure 5.3 : Surface elevation in dm (contour interval is 2.5cm) for the alongshelf wind stress experiment. Only the northern boundary is open. The Orlanski open boundary condition has been used. The solution is presented after 2, 6, 8, 11, 17 and 32 hours

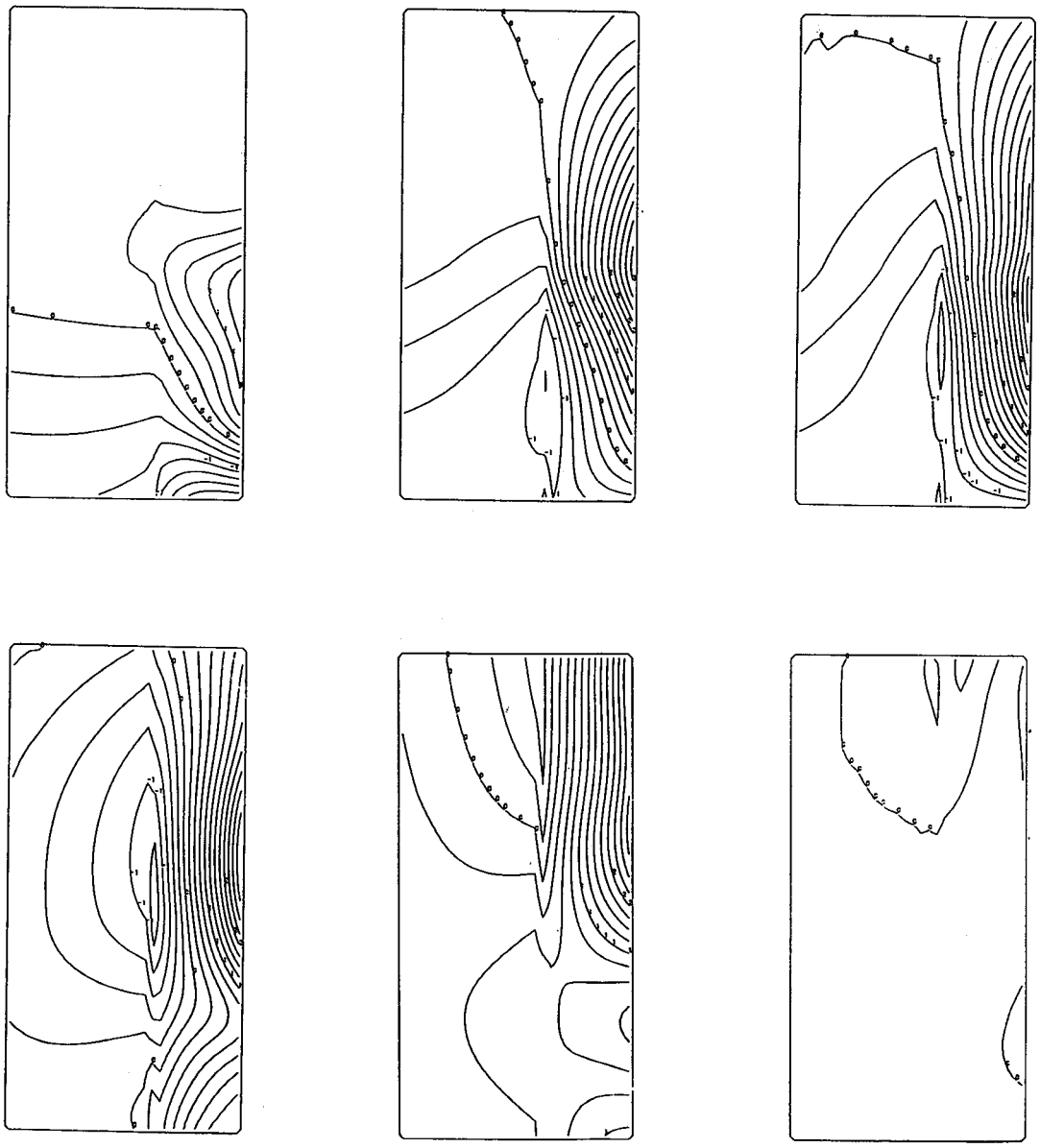

Figure 5.4 : idem 5.3 except that the Camerlengo and O'Brien open boundary condition has been used

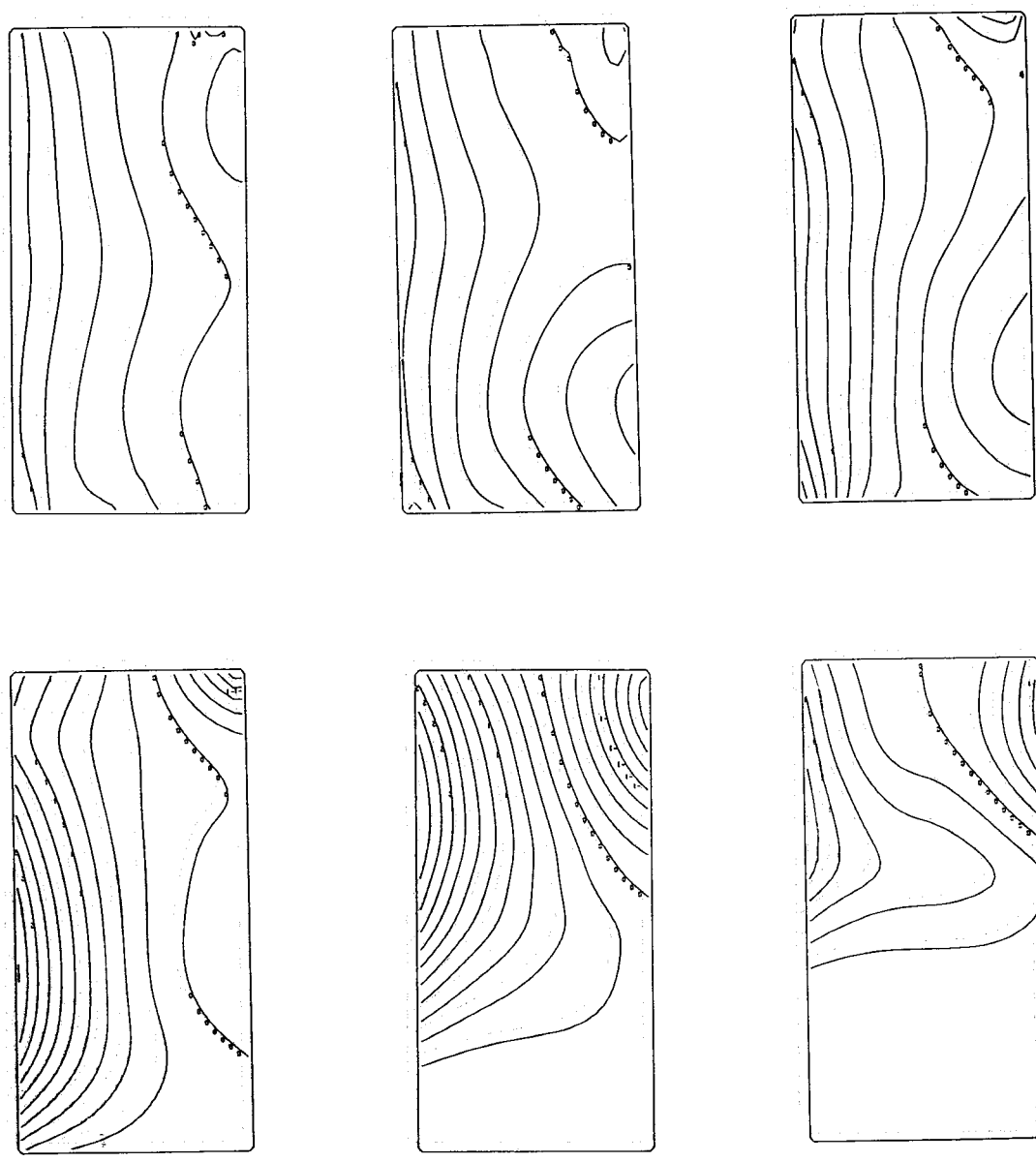

Figure 5.5 : Surface elevation in dm (contour interval is 5cm, the numbers have to be multiplied by 2 to get the elevation in dm) for the forced wave experiment. The northern and the southern boundary is open. The Orlanski open boundary condition has been used. The solution is presented after 3, 6, 8, 16, 24 and 32 hours

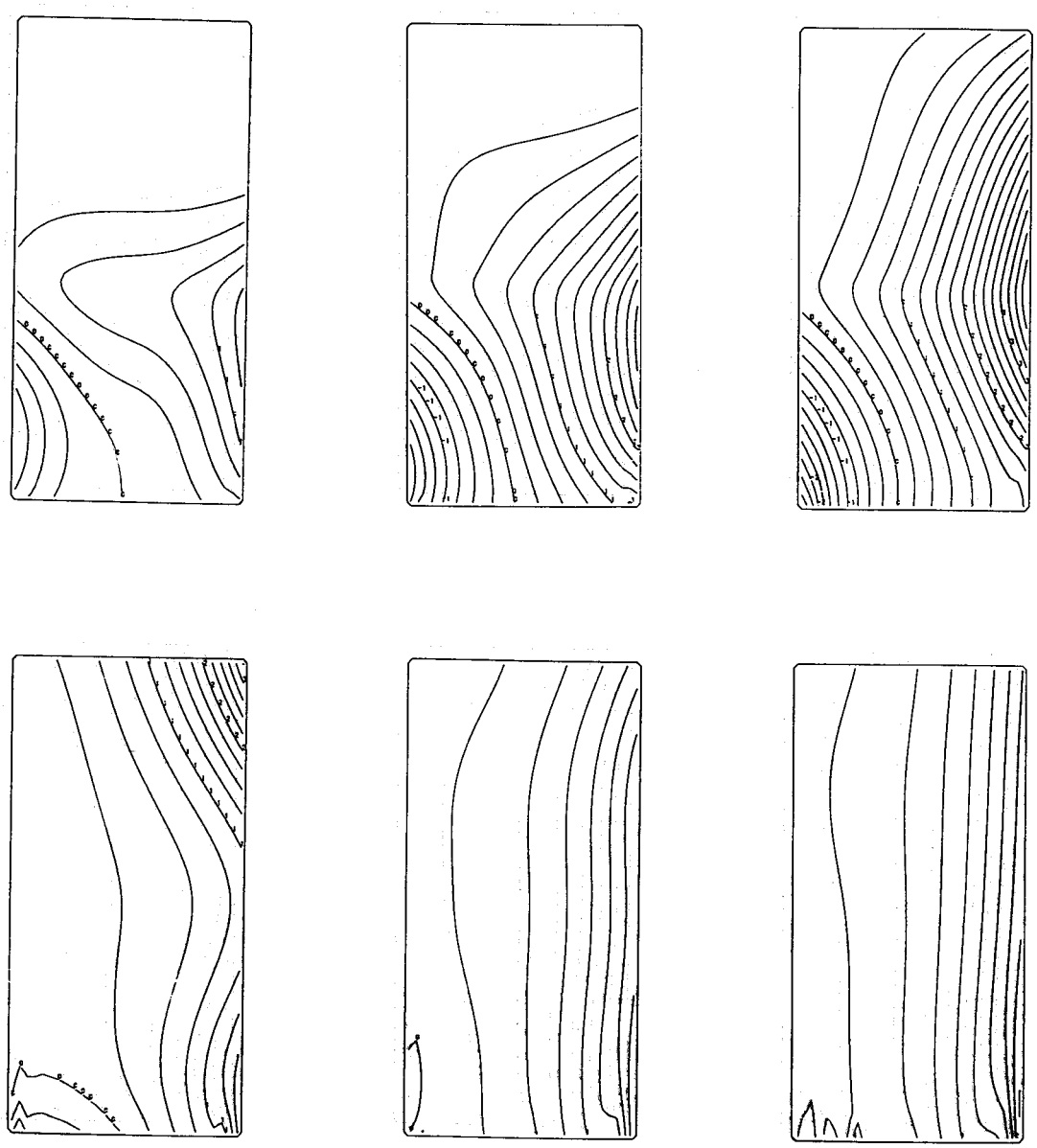

Figure 5.6 : idem 5.5 except that the Camerlengo and O'Brien open boundary condition has been used

6. ADVECTION AND DIFFUSION

6.1. Introduction

In chapter 4 the finite difference scheme for the quasi–linear equations of the tidal motion in the sea has been dealt with. The expression quasi–linear refers to the approximation of the quadratic friction laws in the momentum equations.
In the deeper parts of the sea it is usually permitted to leave the convective terms out of consideration. Sea modelling is mainly carried out by the applications of the quasi–linear equations.
For the flows near a coast, however, the convective terms gain importance. The increasing importance of these terms is mainly due to the depth variation and the shape of the coastline.
The convective terms determine the circulation according to the following hyperbolic equations :

$$\frac{\partial u}{\partial t} + u\frac{\partial u}{\partial x} + v\frac{\partial u}{\partial y} = 0 \text{ in x direction} \tag{6.1}$$

$$\frac{\partial v}{\partial t} + u\frac{\partial v}{\partial x} + v\frac{\partial v}{\partial y} = 0 \text{ in y direction} \tag{6.2}$$

Many methods for the integration of these equations are mentioned in literature. According to the way in which they are constructed, these methods can be classified as follows :

- methods based upon separate approximation of each derivative by finite differences
- methods by characteristic interpolation (Benqué et.al., 1982)
- characteristic methods (Abbott, 1979)
- finite element methods (Morton, 1980)
- spectral methods (Gottlieb and Orzag, 1977).

Since the previous chapters all deal with the finite difference integration method for the shallow water equations defined on a fixed equidistant grid, only the first method will be discussed in this chapter.
To introduce the advective terms into the equations (4.2.) – (4.3.), the following items must be paid attention to:

- the approximation of the finite difference operator should be chosen carefully, since

the finite difference representation of the convective terms and the solution of the difference equations may give complications with respect to the accuracy of the solution and the possibility of induced instabilities (Weare, 1976).

- the boundary conditions are more complicated because the vertical tide and the velocity vectors must be known at the open sea boundary. Often the measurement of the velocity vectors is a difficult affair from a practical point of view. It is recommended to choosing the boundary in the sea, where the convective terms have a relatively small value.

6.2. Approximation of the advective terms

Stelling (1984) discussed several numerical methods for the advective equations. He suggested that the reduced phase error split scheme can show excellent results, both for time dependent and steady state problems. Some other operators may adequately approximate the advective terms. They are introduced using the notation, shown in figure 4.1. as follows :

(a) first–order upstream scheme

$$\left.\frac{\partial u}{\partial x}\right|_{i-1/2,j} = \begin{cases} \dfrac{u_{i-1/2,j} - u_{i-3/2,j}}{\Delta x} + \tau_c, \text{ for } u > 0 \\ \dfrac{u_{i+1/2,j} - u_{i-1/2,j}}{\Delta x} + \tau_c, \text{ for } u \leq 0 \end{cases} \tag{6.3}$$

τ_c represents the truncational error which is inherent when replacing the advective terms by the finite difference approximation.

(b) second–order central difference scheme

$$\left.\frac{\partial u}{\partial x}\right|_{i-1/2,j} = \frac{u_{i+1/2,j} - u_{i-3/2,j}}{2\Delta x} + \tau_c \tag{6.4}$$

(c) second–order upstream scheme

$$\left.\frac{\partial u}{\partial x}\right|_{i-1/2,j} = \begin{cases} \dfrac{1}{2\Delta x}\left(3u_{i-1/2,j} - 4u_{i-3/2,j} + u_{i-5/2,j}\right) + \tau_c, \text{ for } u > 0 \\ \dfrac{1}{2\Delta x}\left(-u_{i+3/2,j} + 4u_{i+1/2,j} - 3u_{i+5/2,j}\right) + \tau_c, \text{ for } u \leq 0 \end{cases} \tag{6.5}$$

(d) QUICK scheme

$$\left.\frac{\partial u}{\partial x}\right|_{i-1/2,j} = \begin{cases} \frac{1}{\Delta x}\left(\frac{3}{8}u_{i+1/2,j} + \frac{3}{8}u_{i-1/2,j} - \frac{7}{8}u_{i-3/2,j} + \frac{1}{8}u_{i-5/2,j}\right) + \tau_c, \text{ for } u > 0 \\ \frac{1}{\Delta x}\left(-\frac{1}{8}u_{i+3/2,j} + \frac{7}{8}u_{i+1/2,j} - \frac{3}{8}u_{i-1/2,j} - \frac{3}{8}u_{i-3/2,j}\right) + \tau_c, \text{ for } u \leq 0 \end{cases} \quad (6.6)$$

Besides these there are other higher–order schemes which are more accurate but, compared with the computational effort of a second–order scheme, less interesting.

Shyy (1983) investigated the accuracy of the above described approximations for the advective–dominated flows in case of steady state. This is the most difficult case to prevent instabilities. The second order central difference operator is the commanly used algorithm. It can easily be adapted in implicit schemes especially when the double sweep method to solve the tri–diagonal matrix is applied. Bella (1970) found that the central difference operator may give rise to oscillating results when the advective dominated flows are not in a certain direction, e.g. back water effects in one dimensional problems or recirculating flows in two–dimensional problems. The QUICK scheme was first developed by Leonard (1979). It involves the use of a quadratic interpolation to estimate the solute concentration on a space staggered grid. The QUICK scheme is quite commonly used in one dimensional contaminant transport models, because it gives better prediction accuracy and less oscillation in unidirectional flow problems. The upwind scheme was claimed by Falconer and Liu (1988) and Backhaus (1983). Their results contain much numerical dispersions and a strong damping of the peak values occurs. An advantage of this scheme is that no phase lag occurs for pure convective flows and that it is oscillation free along the computational directions, because the operators are dependent on the local velocity.

The orders of accuracy are dependent on the user's decision, for small area models second– or higher– order schems can be necessary, whereas for polar modelling first–order approximation of the advective terms is accurate enough. Besides the large amount of assumption needed at the boundaries, which may diminish the accuracy, the higher–order schemes also require a greater computational effort.

In the next section the second–order upwind scheme is applied to a test problem. The first–order upwind scheme has been used for the Weddell Sea model.

6.3. Numerical applications with advection

6.3.1. EDDY FORMATION IN AN IDEALIZED BASIN

A second–order upwind scheme has been applied to approximate the advective terms in the non–linear shallow water equations. In figure 6.1. the dimension and the geometry of the

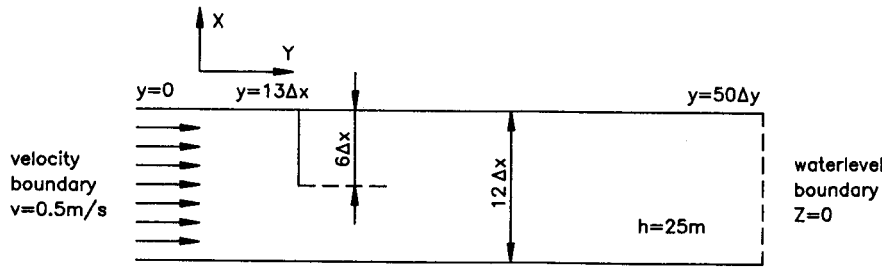

Figure 6.1 : The test basin $\Delta x=\Delta y=25m$, $\Delta t=20s$

basin is described. The aim of this application is to investigate the eddy formation and the stability of the scheme. The flow is assumed to be in steady state, although it is initially a time dependent problem. The Courant number Cf = 18, this is an extreme case to test the stability of the scheme. Benqué et.al. (1982) tested the scheme up to Cf = 96. The accuracy of the result, however, was questioned by them and by Stelling (1984). The flow pattern of the eddy formation is shown in figure 6.2.

6.3.2. PRACTICAL APPLICATION TO THE WEDDELL SEA MODEL

A first order upwind operator has been introduced to the spherical coded model for the flow simulation in the Weddell Sea. The results will be presented in the next chapter.

6.4. The approximation of the diffusion terms

The diffusion terms can be written as

$$\frac{\partial u}{\partial t} + E\left(\frac{\partial^2 u}{\partial x^2} + \frac{\partial^2 u}{\partial y^2}\right) = 0 \qquad (6.7)$$

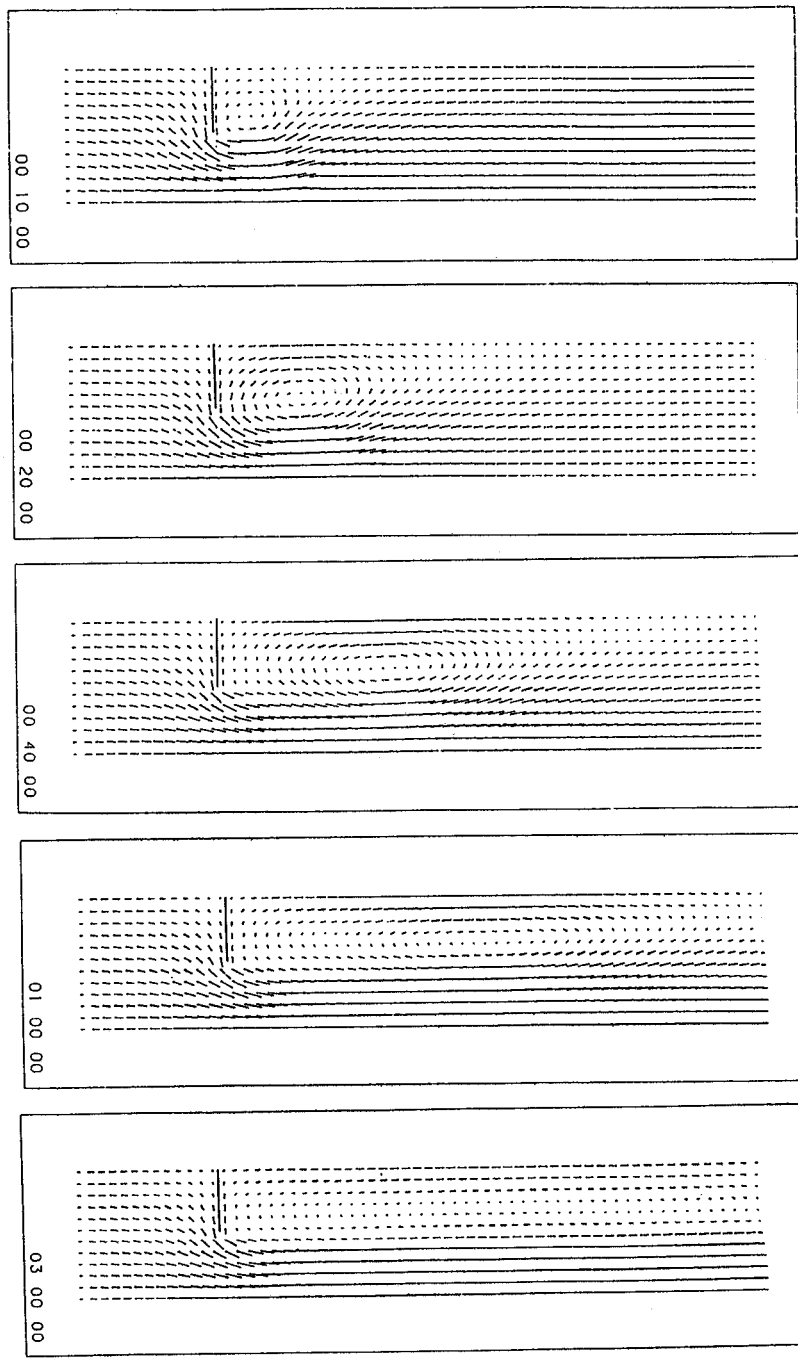

Figure 6.2 : Eddy formation in an idealized basin. Time in hours, minutes, seconds

$$\frac{\partial v}{\partial t} + E\left(\frac{\partial^2 v}{\partial x^2} + \frac{\partial^2 v}{\partial y^2}\right) = 0 \tag{6.8}$$

they can be easily approximated by a second order central difference operator presented as follows (the notation is shown in figure 4.1.).

$$\left.\frac{\partial^2 u}{\partial x^2}\right|_{i-1/2,j} = \frac{u_{i+1/2,j} - 2u_{i-1/2,j} + u_{i-3/2,j}}{\Delta x^2} + T_\alpha \tag{6.9}$$

Where T_α is the truncational error term of the Taylor expansion. The difficulty in the application of the diffusion terms consists in the determination of the eddy viscosity (E in (6.7.) and (6.8.)).

6.5. The thermo–haline equations

The differential equation for salinity and temperature prediction can be written as

$$\frac{\partial s}{\partial t} + u\frac{\partial s}{\partial x} + v\frac{\partial s}{\partial y} + E\left(\frac{\partial^2 s}{\partial x^2} + \frac{\partial^2 s}{\partial y^2}\right) = 0 \tag{6.10}$$

and

$$\frac{\partial T}{\partial t} + u\frac{\partial T}{\partial x} + v\frac{\partial T}{\partial y} + E\left(\frac{\partial^2 T}{\partial x^2} + \frac{\partial^2 T}{\partial y^2}\right) = Q_T \tag{6.11}$$

where S is salinity, T is temperature, E is eddy viscosity and Q_T is a source term which represents effects such as solar radiation. We have now added equations for S and T, so we have 5 equations (4.1. – 4.3., 6.9., 6.10.) for 6 unknowns since ρ must also be regarded as unknown. It can be obtained from S and T through the equation of state of sea water, (see e.g. Pond and Pickard, 1983).

7. THE WEDDELL SEA MODEL

7.1. Model area

The boundaries of the model are situated at lat. 50° S and 80° S and long. 80° W and 30° E, including the Antarctic peninsula, the Southern tip of South America and the Drake passage, (see figure 7.1.). The region is discretised on a Cartesian– and a spherical grid.

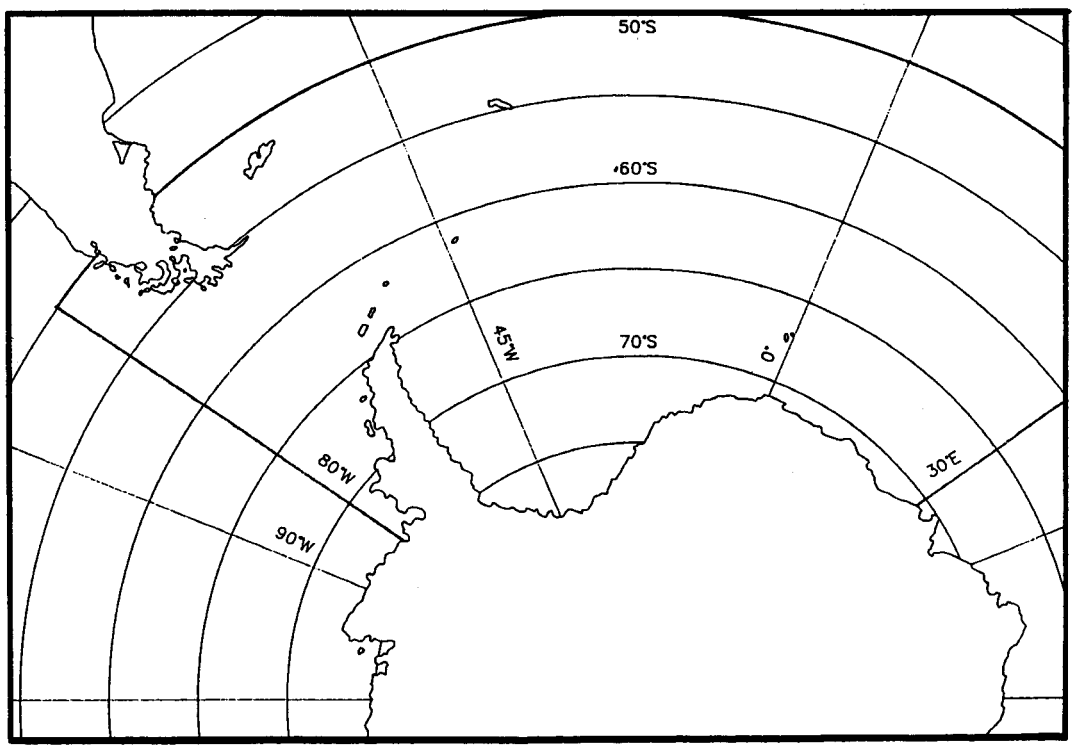

Figure 7.1 : The model area

7.1.1. CARTESIAN GRID

The model area is resolved by a 111 x 111 km² horizontal grid. The geometry is taken from the Admiralty Charts Nos 3170, 3175, 3176 and 3200. In figure 7.2. the Cartesian grid is presented.

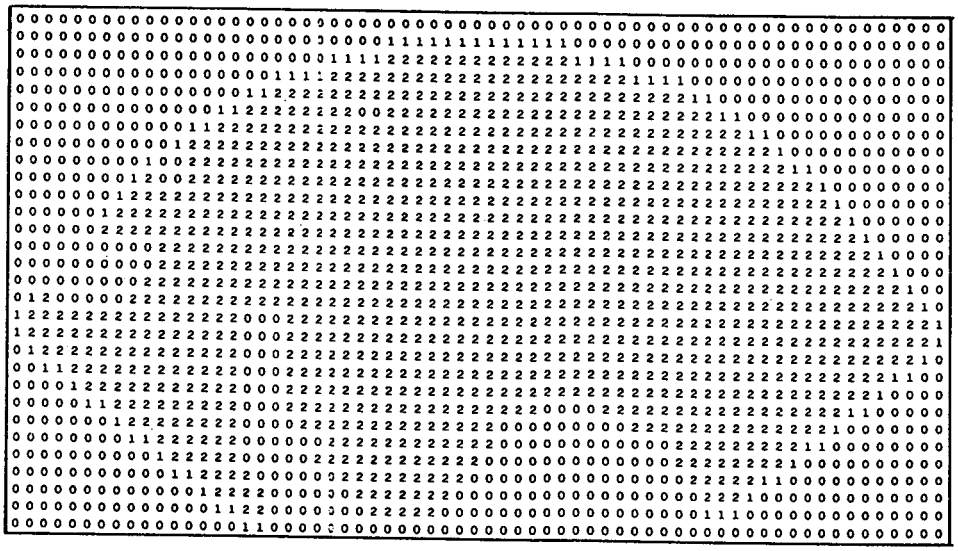

Figure 7.2 : Cartesian grid 2 = water point, 1 = open boundary, 0 = land point or point outside the computational grid

The surface of the earth is curved, but the numerical scheme uses (horizontal) x, y coordinates. The curved surface of the earth has to be projected on a horizontal plane, which introduces distortions. In order to minimize deformation a stereographic projection has been used. The coordinates of the grid have been calculated with respect to a "new" pole situated at 65°S25°W, this is in the middle of the model area. A plane tangent on the earth in this point has been constructed and the geometry of the region has been projected on it. The geographical coordinates of the grid points can be calculated as follows (see figure 7.3.) :

(i) Calculation of the spherical coordinates of the cartesian grid with respect to the "new" pole 65°S25°W :

$$\phi' = 90^\circ - \sqrt{I^2 + J^2} \qquad (7.1)$$

Where ϕ' is the latitude with respect to 65°S25°W and I, J are the indexes of the Cartesian grid.

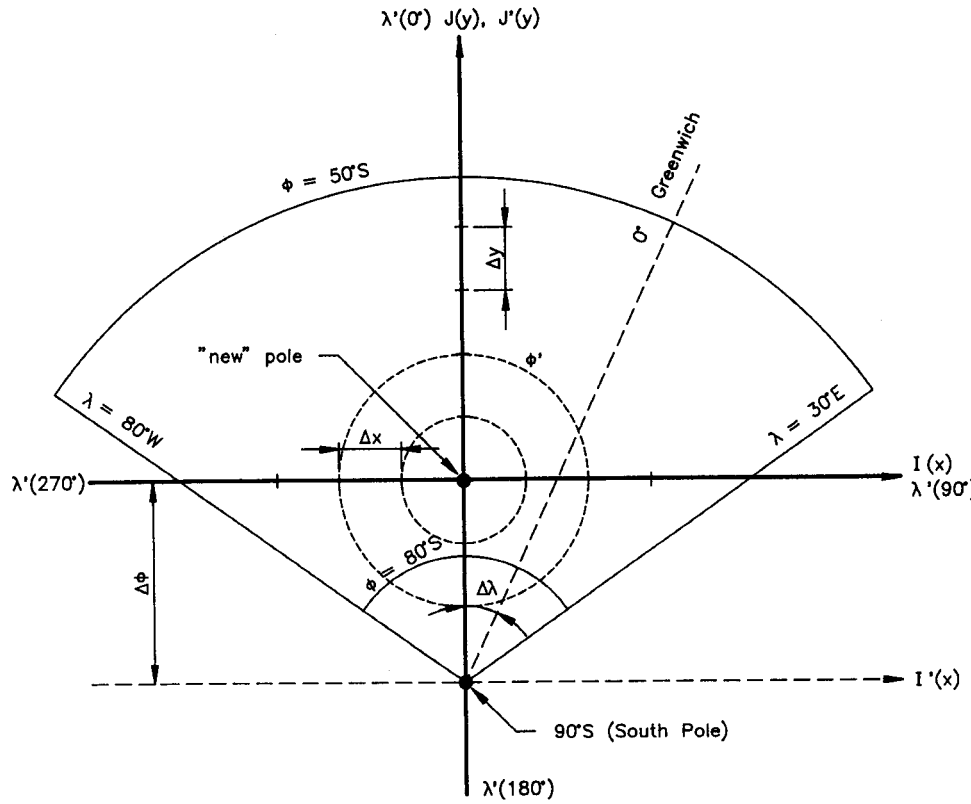

Figure 7.3 : Construction of the grid points for the Cartesian grid by means of a stereographic projection

The longitude (λ') with respect to 65°S25°W can be obtained by

$$\lambda' = \arctan(I/J) \tag{7.2}$$

(ii) Calculation of the geographical coordinates (ϕ,λ) can be done by a translation of 25° ($= \Delta\phi$) and a rotation of 25° ($= \Delta\lambda$).

$$\phi = 90° - \sqrt{(90 - \phi')^2 + \Delta\phi^2 - 2(90 - \phi)\Delta\phi\cos\lambda'} \tag{7.3}$$

$$\lambda = \arctan\left(\frac{(90 - \phi').\sin\lambda'}{\Delta\phi + (90 - \phi')\cos\lambda'}\right) - \Delta\lambda \tag{7.4}$$

7.1.2. SPHERICAL GRID

A drawback of the Cartesian grid is that the lateral boundaries are not straight lines; zig–zag boundaries complicate the implementation of open boundary conditions and furthermore can give erronous velocity results close to the boundary (Holsters, 1985). The model equation has therefore been expressed in a spherical way. The grid is the same as the one used by van Ypersele (1986). The grid distance is 2° in longitude and 1° in latitude (see figure 7.4.).

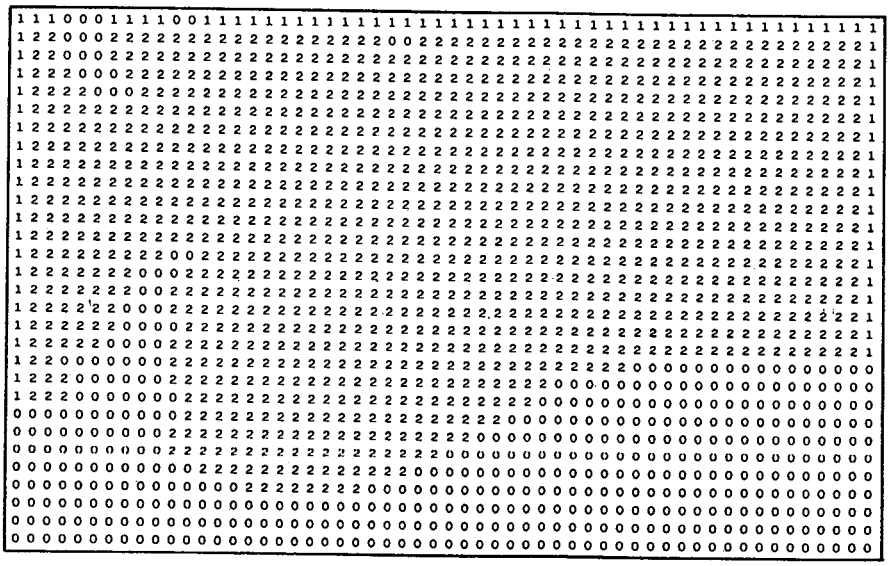

Figure 7.4 : Spherical grid. See figure 7.2 for the explanation of the code

7.2. Currents due to wind action

7.2.1. ATMOSPHERIC CIRCULATION

The ocean currents in the model area are primarily driven by the wind. In the Weddell Sea the ocean circulation consists in a large gyre. As was mentioned by Taljaard et.al. (1969) this circulation is probably the result of the atmospheric circulation around a nearly permanent low. In the northern part of the model area, i.e. between 50°S and 60°S, the

wind is eastward with average velocities of 10 m/s. In the Drake passage the average speed reaches 15 m/s.
In the Weddell Sea exists a clockwise circulation. The wind blows from the east along the coast–line and northwards along the Antarctic Penisula. The wind speeds in the Weddell Sea are lower than in the northern part of the model area, they reach average values of .
6 m/s. The climatological April and October mean surface wind fields are shown for the model domain in figure 7.5. and 7.6. The wind data are derived from the data of Taljaard et.al. (1969).

7.2.2. MODEL ASSUMPTIONS

The two–dimensional model from chapter 4 has been used to describe the currents. Two–dimensional depth averaged models have been widely applied for the simulation of continental shelf seas. In this study it is shown that they are also suitable for the simulation of surface currents outside the shelf area. The model of the Weddell Sea, presented in this text, has not a realistic bathymetry. The water depth is reduced so that the "bottom"of the model lies in the water and thus only the upper layer of the ocean is simulated, the deeper layers are considered invariable. This approach is permitted as the surface layer of the ocean differs from the underlying layer and the momentum exchange between the surface layer and the lower layer is small. The depth of the model corresponds to the mixed layer of the ocean and to the depth of the photic layer. In the next section are presented some results of the model.

7.2.3. RESULTS

The model is forced by monthly averaged wind fields as described in 7.2.1. Different runs have been carried out in order to test the sensitivity of the model to some parameters. The influence of the coordinate system, of the "water depth" and of the friction coefficient has been investigated. In figure 7.7. is shown the circulation when the lateral boundaries are considered to be closed. It is clear that the boundaries have an enornous influence on the circulation, the currents are only realistically simulated in the centre of the domain.
In figure 7.8. the circulation is shown for the months April and October when an open boundary condition is applied at the lateral boundaries (see chapter 5.).

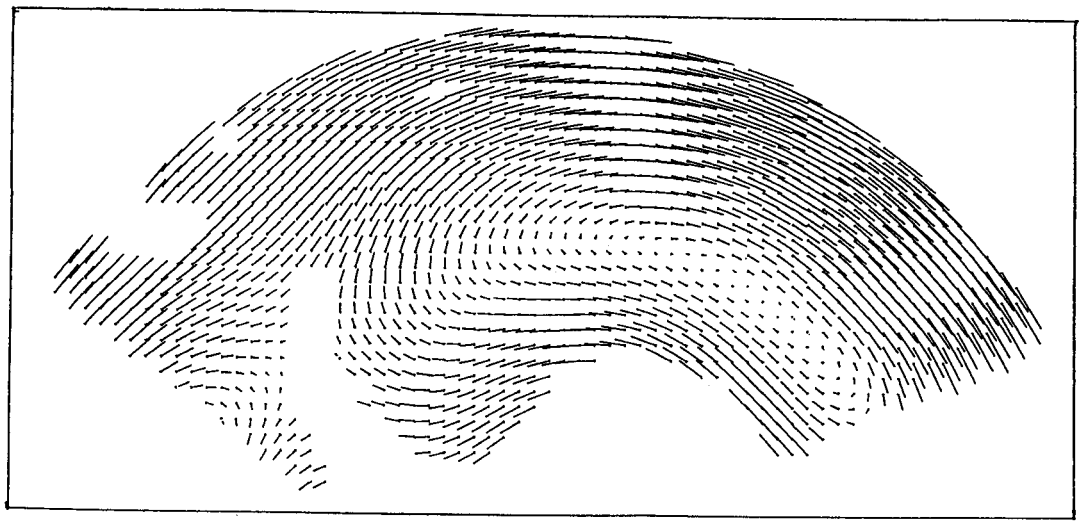

Figure 7.5 : Mean surface wind field of April (from Taljaard et.al., 1969), Cartesian grid

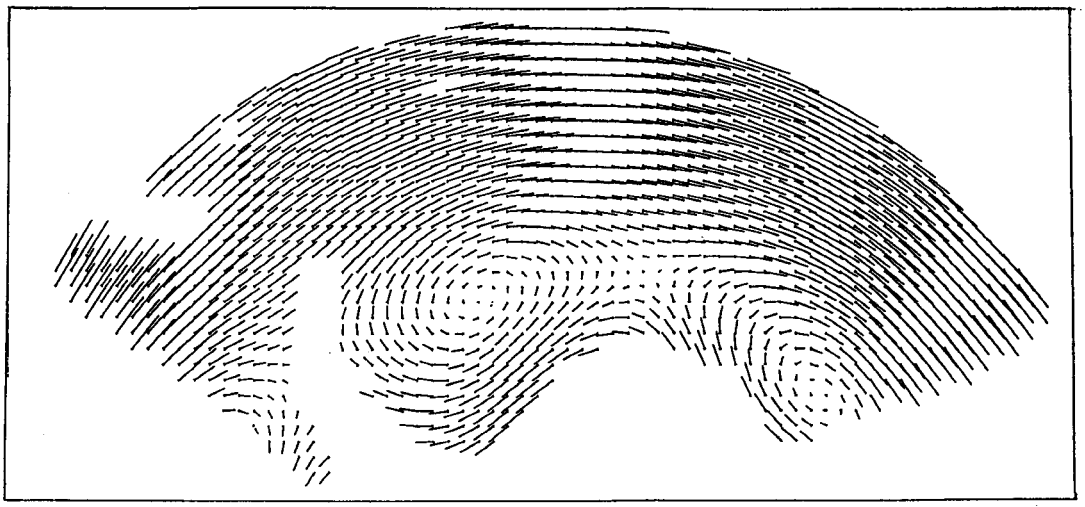

Figure 7.6 : Mean surface wind field of October (from Taljaard et.al., 1969), Cartesian grid

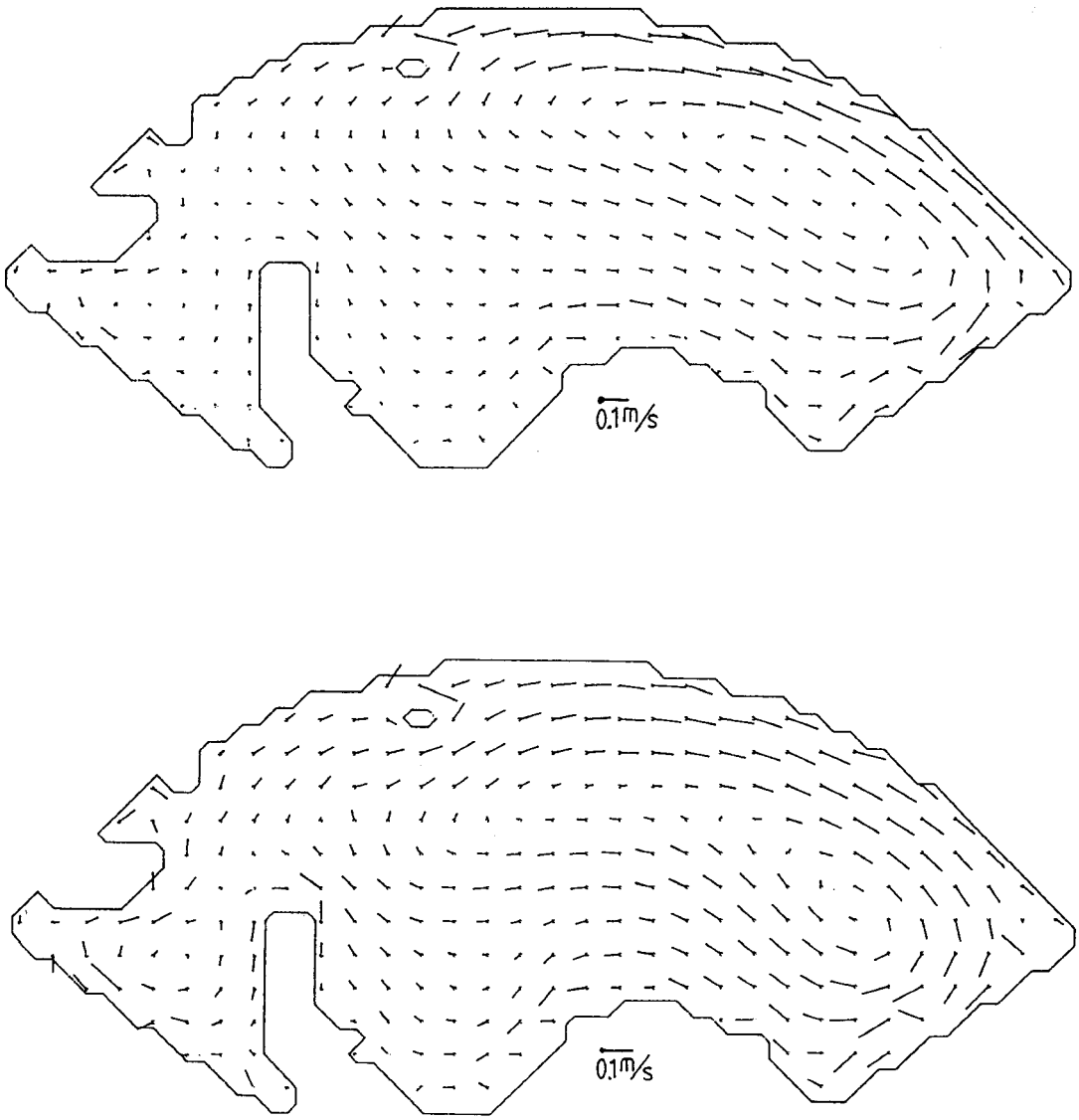

Figure 7.7 : Current vectors calculated for (a) April and (b) October, Cartesian grid (closed boundary). Plotting distance is $2\Delta x$, $2\Delta y$.

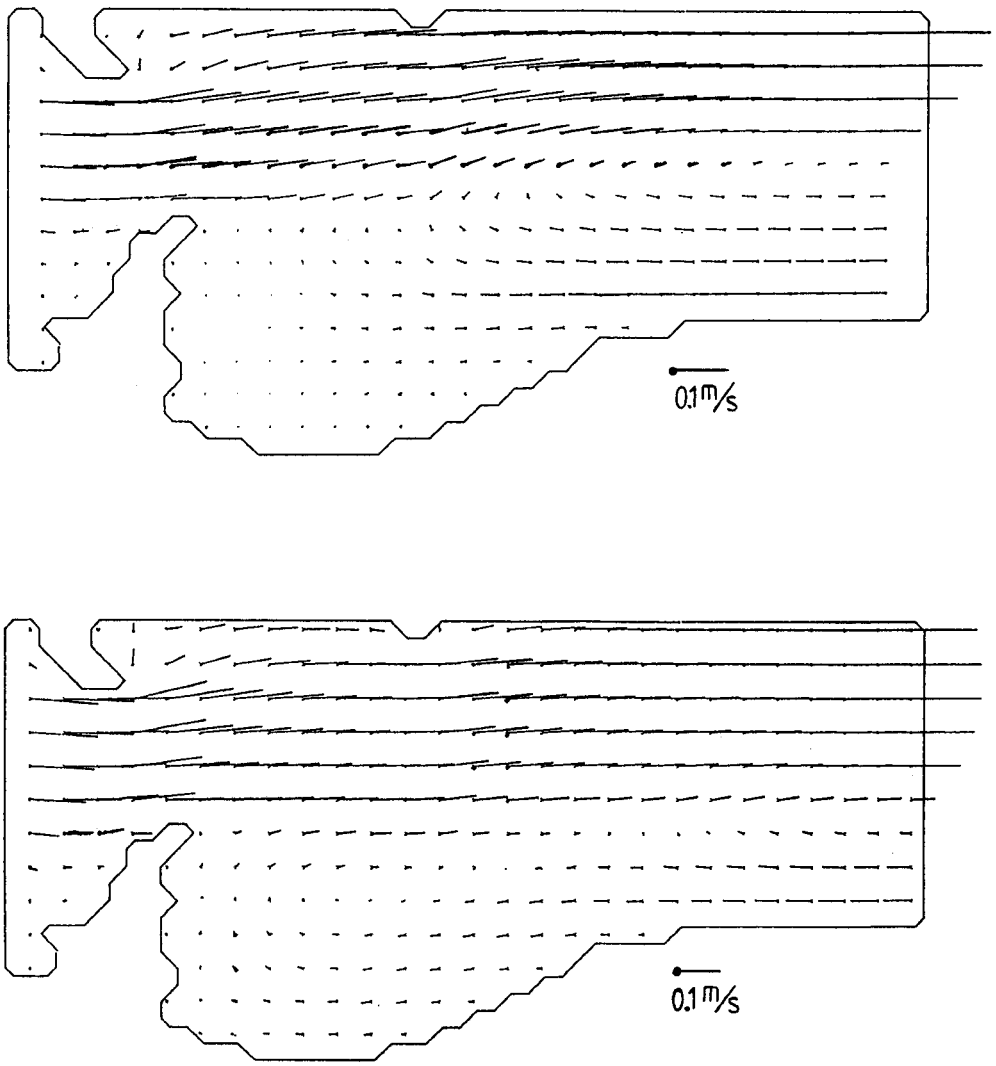

Figure 7.8 : Current vectors calculated for (a) April and (b) October, Spherical grid (open boundary). Plotting distance is $2\Delta x$, $2\Delta y$.

The flow is realistic in magnitude and the features of the currents are well simulated : the strong flow through the Drake passage, the westward currents near the coast and the Weddell Sea gyre are reproduced.

In table 7.1. the results with different friction coefficient are compared with van Ypersele's results : it appears that the currents are qualitatively and quantitatively of the same order of magnitude. It should be pointed out here that besides the fact that the number of dimension in the two models is different (2D vs 3D) the boundary condition at the lateral boundary is different too. In the model of van Ypersele (1986) the eastern and western boundaries are connected in such a way that the water which flows out at one boundary enters at the other one and vice versa. This approach is permitted since the currents in the region are circumpolar and thus similar at the eastern and western sides. However, the values close to the boundary should be interpreted with caution. This periodic boundary condition has also been applied to the model presented here (see Fettweis et.al., 1987); it leads, however, to numerical instabilities, probably because of the required extrapolation.

Table 7.1 : (a) U–velocity in cm/s at lat 60°S for April

Run \ Longit	72°W	60°W	48°W	36°W	24°W	12°W	0°	12°E	24°E
C=∞	27.3	22.0	13.6	11.3	6.7	2.7	0.6	−0.9	−0.8
C^2=6000	17.3	15.1	11.0	8.9	5.9	2.5	2.9	−2.5	−0.8
C^2=3000	14.0	12.2	9.1	7.6	5.2	2.3	3.1	−0.8	0.9
Van Ypersele	13.69	5.40	3.23	3.41	6.16	3.2	4.46	−0.06	2.46

(b) V–velocity in cm/s at lat 60°S for April

Run \ Longit	72°W	60°W	48°W	36°W	24°W	12°W	0°	12°E	24°E
C=∞	2.5	1.6	3.1	3.3	4.3	2.1	0.7	0.4	−0.4
C^2=6000	0.2	2.0	3.9	3.6	4.7	2.9	1.7	0.8	0.1
C^2=3000	0.3	1.2	2.2	1.5	2.2	1.3	0.5	0.2	0.0
Van Ypersele	7.71	5.36	2.79	9.75	8.53	4.05	7.98	5.08	−1.03

7.2.4. DISCUSSION

Every model which describes a physical phenomenon gives rise to inaccuracies, because reality cannot perfectly be approximated by the hypotheses used. A first possible origin of discrepancies between model results and observation may be found in the fact that the input data (wind velocities or tidal forcing at the boundary) are inaccurate.
In this case calibration of the model is necessary in order to get results which are close to observations. For the Weddell Sea model, this would mean turning the parameters such as friction or water depth. We have not attempted, however, to calibrate the model since we do not have at our disposal the observation which could serve for this purpose. What has been carried out is a sensivity study of these parameters. By doing so, the influence of changing friction or water depth values on the results can be observed. This makes it possible to evaluate the model : when the model is e.g. insensitive to the value of the friction coefficient, calibration will be difficult and hence the applicability of the model as well. Another problem which is related to the operational character of the model, is that the quality of the model results are dependent on the quality of the input data (wind velocities). These data are predicted ones (in the case of a forecast model) and are partly responsible for the discrepancies when the predictions are not accurate.
Except for the above–mentioned possible reasons of discrepancies between model results and reference data, the formulation of the model and the hypotheses used may account for the differences. (The model uses a hypotheses which is a simplification of reality, see 7.2.2.). As can be seen, the results of the model differ from those of the 3D model (van Ypersele, 1986). A 3D model should be more complete than a depth–averaged 2D model but the computational effort is many times greater. The results of the 2D Weddell Sea model are, however, satisfactory, as they simulate the main features in this area. The model runs on a PC–AT, the computational costprice is thus very low. As has already been mentioned previously it is not possible as yet to evaluate the model due to a lack of observation. The model results have been compared with those of the 3D model of van Ypersele and the agreement is satisfactory (it could be improved by calibration but this is not our goal).

7.3. Currents due to tidal forcing

7.3.1. BOUNDARY CONDITION

Along the eastern, western and northern boundary the tide has been regarded as the external forcing. The open boundary data have been reconstructed from 9 constituents (i.e. Q_1, O_1, P_1, K_1, N_2, M_2, S_2, K_2, M_f). These constituents are descended from Schwiderski's (1983) global ocean tidal simulation.

7.3.2. RESULTS

The bathymetry was taken from van Ypersele (1986). The time step is 447 seconds. The water elevation and the momentum of the model was started from rest. After a few tidal cycles the sea surfaces reaches a stable condition. The calculation of one M_2 cycle (= 100 time steps) takes about 10min on a HP–Vectra. In figure 7.9 the computed tidal currents for the M_2 tide are presented and in figure 7.10 those for the 9 constituents. The results are generally in good agreement compared to the few observations and the results of other models. In figure 7.11 the tidal elevation at 75° S 46° W is shown. It is clear from this figure that the tides in the Weddell Sea are of the "mixed" type, i.e. both the diurnal and the semi–diurnal constituents are important. The "form ratio" F of the major diurnal to the semi–diurnal constituents is equal to 0.4.

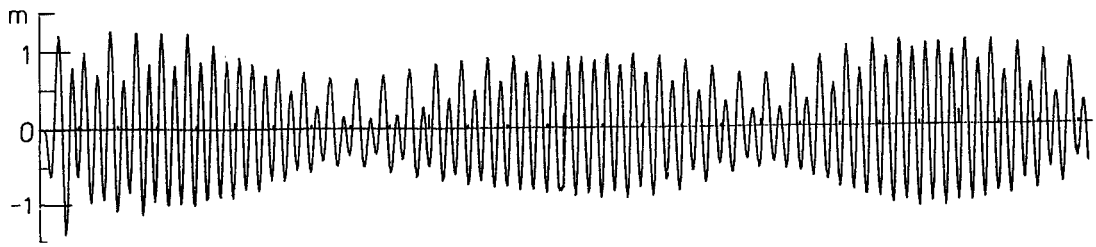

Figure 7.11 : Tidal elevation at 75° S 46° W

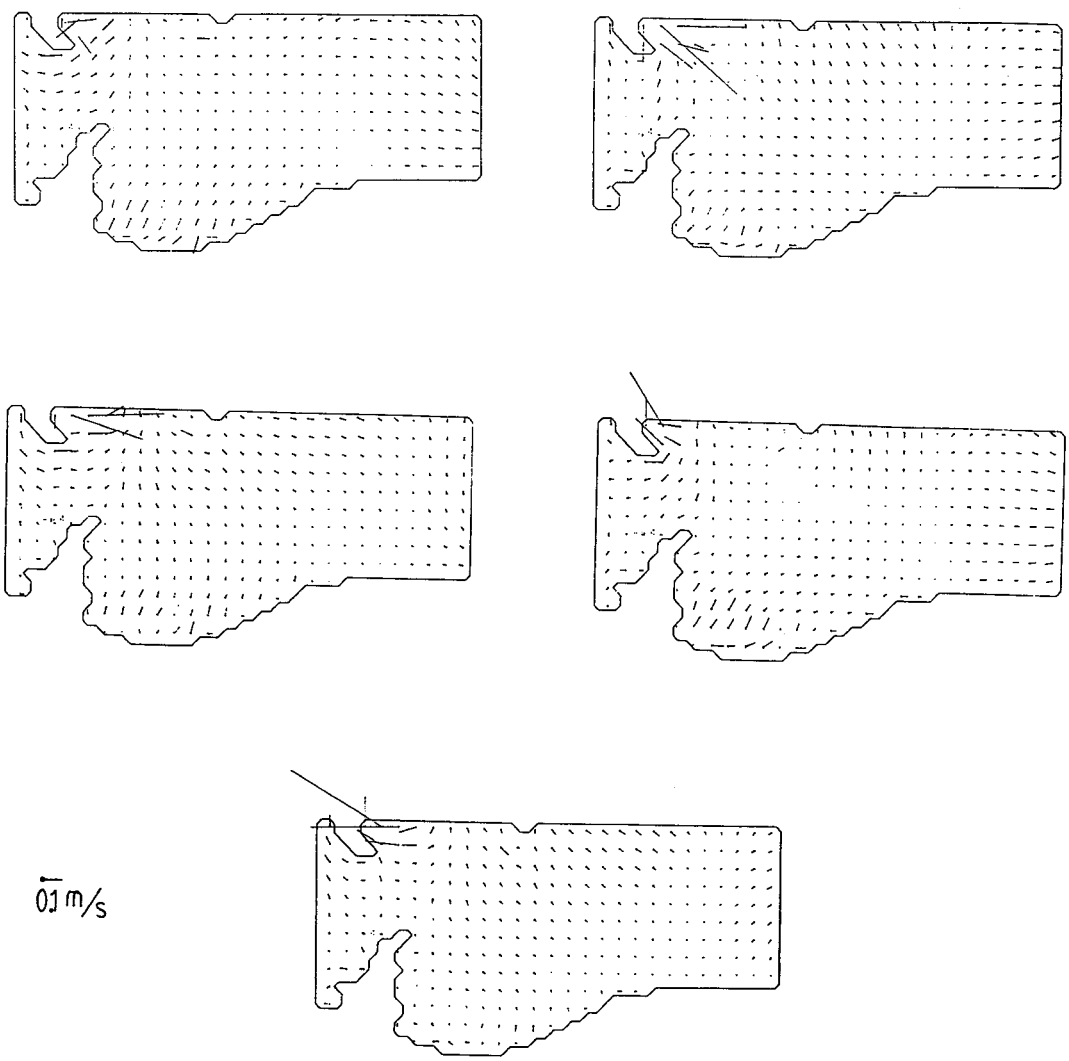

Figure 7.9 : M_2 current vectors. The time between two drawings is 2,5 hours.
Plotting distance is $2\Delta x$, $2\Delta y$.

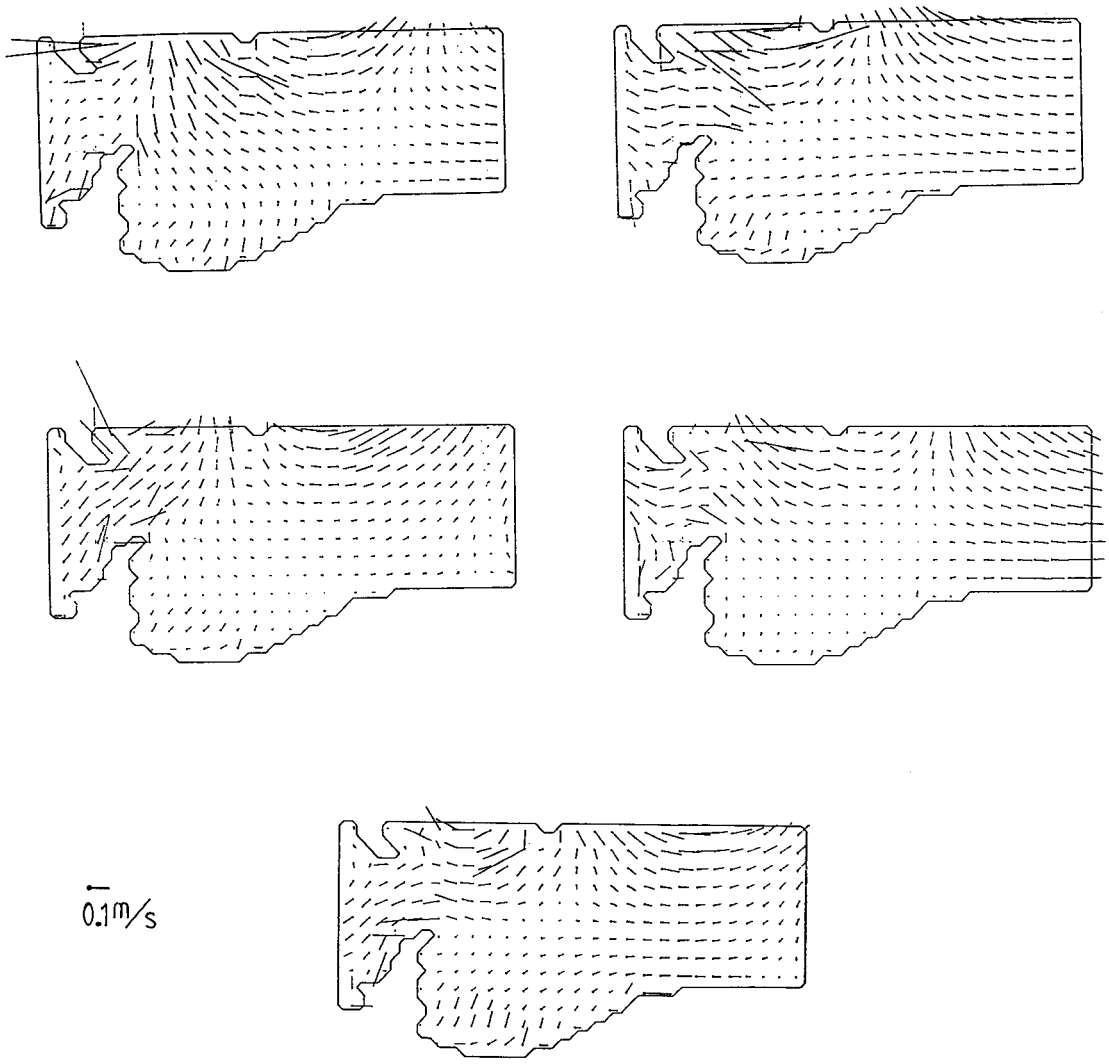

Figure 7.10 : Tidal cuurent vectors (9 constituents).
The time between two drawings is 5 hours.
Plotting distance is $2\Delta x$, $2\Delta y$.

8. CONCLUSION

8.1. Possible applications

The research carried out at the Laboratory of Hydraulics under the "ANTAR 02" contract has been focused on the development of a numerical model to calculate currents and tidal elevations. Special attention was paid to the efficiency of the algorithm for memory space and computation time. The model runs properly on a PC–AT and is suitable for operational purposes. The possibility of knowing tidal elevation or currents for a certain place or area is important in different kind of applications :

- the currents in the Weddell Sea, calculated with the model, can serve as input data for an ice–model, which takes into account the dynamics of the ice fields. By doing so, predictions can be made concerning the periodic melting and growing of the ice fields.
- all physical and biological advective phenomena, e.g. transport of plancton, transport of pollutants, require the knowledge of the currents to predict their displacement in an ocean. The transport model developed can be used to simulate the behaviour of these phenomena.
- when dealing with wind forcing in a numerical ocean model open boundaries have to be transparant for disturbances generated in the domain of computation. Appropriate open boundary conditions have been implemented in the model. Possible applications are the simulation of storm surges and the simulation of wind induced flows (see Weddell Sea model).

The model has been constructed in such a way that it can easily be adapted to an arbritrary area :

- the model has been applied to the North Sea. For this area a lot of measurements are available and many modelling work has been performed. The North Sea application has allowed the validation of the model, i.e. the comparison of the results with measurements and with the results of other numerical models. A tidal model of the North Sea and especially the southern part offers, of course, a lot of applications which are of great importance for purposes such as navigation guidance, management of dredging works, prediction of storm surges, transport of pollutants,

depth measurements in the sea, erosion problems ... along the Belgian coast and the Scheldt estuary.

8.2. General conclusions

In chapter 4 a numerical model is presented which solves the 2D depth averaged shallow water equations. The model has been successfully applied to some test cases : simulation of the response of a simple–shaped closed basin to wind forcing, (chapter 4.3.1.); simulation of the tidal currents in the North West European continental shelf area and in the Southern North Sea and English Channel region, (chapter 4.3.2.). The implementation of the advective and the diffusion terms is presented in chapter 6; a test case has been set up in order to investigate the eddy formation and the stability of the scheme (chapter 6.3.1.). In chapter 5 the implementation of an open boundary condition based on the Sommerfeld radiation condition is described. Some simple numerical tests have been carried out in order to check the applicability of the condition (chapter 5.3.2.). Chapter 7 is devoted to the Weddell Sea application. The model has been successfully used to simulate the wind induced currents (chapter 7.2.) and the tidal currents (chapter 7.3.) in this area. The results have been compared with those of a 3D model and the similarity is qualitatively and quantitatively satisfactory. No measurement data were availaible to test the model results on reality.

8.3. Further developments

The ocean model, presented in this report, takes into account the third dimension by means of the friction coefficient at the "bottom" of the model. It can thus be regarded as the upper layer of a multilayer model. The value of the friction coefficient has to be known in order to make quantitative calculations. This parameter can be obtained by a model which takes into account the vertical plane e.g., a multilayer model. It would be interesting to compare the results of a more sophisticated model with the 2D model. The friction coefficient of the 2D model can be calculated with a multilayer model. By doing, so the 2D model can come up to the level of a 3D model but with a much higher efficiency of computer implementation.

9. BIBLIOGRAPHY

Abbott M.B., Damsgard A. and Rodenhuis G.S. 1973. System 21, "Jupiter" (A Design System for Two–Dimensional Nearly–Horizontal Flows). J. of Hydraulic Res. Vol 11. No 1. 1–28.

Abbott M.B. 1979. Computational Hydraulics, Elements of the Theory of Free Surface Flows. Pitman Advanced Publishing Program. Boston London Melbourne. 326p.

Backhaus J.O. 1983. A Semi–Implicit Scheme for the Shallow– Water Equations for Application to Shelf Sea Modelling. Cont. Shelf Res. Vol 2. No 4. 243–254.

Bella D.A. and Grenney W.J. 1970. Finite–Difference Convection Errors. J.Sanitary Eng. ASCE. SA6. Vol 96.

Benqué J.P., Cunge J.A., Feuillet J., Hauguel A. and Holly F.M. 1982. New Method for Tidal Current Computation. J. of the Waterway, Port, Coastal and Ocean Division. Proc. ASCE. Vol 188. No WW3. 396–417.

Bills P. and Noye J. 1987. An Investigation of Open Boundary Conditions for Tidal Models of Shallow Seas. In: Numerical Modelling: Applications to Marine Systems. Noye J. (Ed.). Elsevier Science Publishers B.V. (North Holland).159–194.

Blumberg A.F. and Kantha L.H. 1985. Open Boundary Conditions for Circulation Models. J.Hydr.Eng. ASCE. Vol 111. No 2. 237–255.

Bryden H.L. and Pillsbury R.D. 1977. Variability of Deep Flow in the Drake Passage from Year–Long Current Measurements. J.Phys.Oceanogr. vol 7. 803–810.

Camerlengo A.L. and O'Brien J.J. 1980. Open Boundary Condition in Rotating Fluids. J.Comp.Phys. Vol 35. 12–35.

Carmack E.C. and Foster T.D. 1975. On the Flow of Water Out of the Weddell Sea. Deep–Sea Res. Vol 22. 711–724.

Chapman D.C. 1985. Numerical Treatment of Cross–Shelf Open Boundaries in a Barotropic Coastal Ocean Model. J.Phys. Oceanogr. Vol 15. 1060–1074.

Chen J.H. 1973. Numerical Boundary Conditions and Computational Modes. J.Comp.Phys. Vol 13. 522–535.

Chieh S.H., Wake A. and Rumer R.R. 1983. Ice Forecasting Model for Lake Erie. J. Waterway, Port, Coastal and Ocean Eng. Vol 109. No 4. 392–415.

Coon M.D., Maykut S.A., Pritchard R.S., Rothrock D.A. and Thorndike A.S. 1974. Modelling the Pack–Ice as an Elastic Plastic Material. AIDJEX Bulletin. 24. 1–105.

Coon M.D., Colony R., Pritchard R.S. and Rothrock D.A. 1974. Calculation to Test a Pack–Ice Model. In : Numerical Methods in Geomechanics. ASCE. Desai C. (Ed.). 1210–1227.

Davies A.M. 1987. Numerical Modelling of Marine Systems. In: Numerical Modelling: Applications to Marine Systems. J.Noye (Ed). Elsevier Science Publishers B.V. (North Holland). 1–24.

Deacon G.E.R. 1982. Physical and Biological Zonation in the Southern Ocean. Deep–Sea Res. Vol 29. No 1A. 1–15.

Deacon G.E.R. 1982. Polar Oceanography. Paper presented at Challenger Society meeting on 'Physical Oceanography 1984', Menai Bridge, 16–21 Sep 1984.

Demuth C. and van Ypersele de Strihou J. 1987. Sea–Ice Simulation in the Weddell Sea. Proc. of the Belgian National Colloquium on Antarctic Research, Brussels, Oct 20, 1987. Prime Minister's Services – Science Policy Office. 195–212.

Dronkers J.J. 1975. Tidal Theory and Computation. In: Advances in Hydrosciences. Chow V.T. (Ed.). Vol 10. 145–230.

Falconer R.A. and Liu S. 1988. Modelling Solute Transport using QUICK Scheme. J.Env.Eng. ASCE. Vol 114. No 1. 3–20.

Fettweis M., Berlamont J. and Hermans I. 1987. 2D Simulation of Weddell Sea Circulation. Proc. of the Belgian National Colloquium on Antarctic Research. Brussels, 20 Oct 1987. Prime Minister's Services – Science Policy Office. 177–194

Foster T.D. and Carmack E.C. 1976. Temperature and Salinity Structure in the Weddell Sea. J.Phys.Oceanogr. Vol 6. 36–44.

Gordeyev R.G., Kagan B.A. and Rivkind V.Ja. 1973. Numerical Solution of the Equation of Tidal Dynamics in the World Ocean. Dokl. AN SSSR. Vol 209. 340–343.

Gordeyev R.G., Kagan B.A. and Rivkind V.Ja. 1975. Numerical Experiments on Tidal Dynamics in the World Ocean. Izv. Akad. Nauk SSSR. Fizika atmosfery i okeana. Vol II. No 2. 162–174.

Gordon A.L. 1971. Oceanography of Antarctic water. Antarctic Oceanology 1, Antarctic Res. Series. Vol 15. J.L.Reid (Ed). American Geophysical Union. Washington DC. 169–203.

Gottlieb D. and Orszag S.A. 1977. Numerical Analysis of Spectral Methods, Theory and Application. Society for Industrial and Applied Mathematics. Philadelphia.

Hansen W. 1969. A Two–Dimensional Numerical Sea Model. Phil. Trans. Roy. Soc. London. Vol 265. 93–137.

Hendershott M.C. 1972. The Effects of Solid Earth Deformation on Global Ocean Tides. Geoph. J. Roy. Astron. Soc. Vol 29. 389–402.e

Hibler III W.D. 1979. A Dynamic Thermodynamic Sea Ice Model. J. Phys. Oceanogr. Vol 9. 815–846.

Israeli M. and Orszag S.A. 1981. Approximation of Radiation Boundary Conditions. J.Comp.Phys. Vol 41. 115–135.

Kollé J.J. and Pritcard R.S. 1983. A Comparison of Two Sea Ice Trajectory Models with AIDJEX Observations. Transaction of the ASME. Vol 105. 346–351.

Kreiss H–O. 1970. Initial Boundary Value Problems for Hyperbolic Systems. Communications on Pure and Applied Mathematics. Vol XXIII. 277–298.

Leendertse J.J. 1970. A Water Quality Model for Well–Mixed Estuaries and Coastal Seas. Principles of Computation, Rand Corporation Memorandum. Vol 1. RM–6230–RC.

Liu S.K. and Leendertse J.J. 1978. Multidimensional Numerical Modeling of Estuaries and Coastal Seas. Adv. in Hydroscience. Vol 11. 99–104.

Marchuk G.I. and Kagan B.A. 1984. Ocean Tides Mathematical Models and Numerical Experiments. Pergamon Press. Oxford New York Toronto Sydney Paris Frankfurt. 292p.

Miller J.D. 1981. A Simple Model of Seasonal Sea Ice Growth. Transaction of the ASME. Vol 103. 212–218.

Miller M.J. and Thorpe A.J. 1981. Radiation Condition for the Lateral Boundaries of Limited–Area Numerical Models. Quart.J.R.Met.Soc. Vol 107. 615–628.

Moelans D. 1979 Tweedimensionaal Numeriek Model van de Noordzee m.i.v. het Windeffect. Internal report KUL 04–HY–4. Leuven. 18p.

Moelans D. and De Bruyn R. 1986. Stromingsmodel van het Continentaal Plat van de Noordzee. Internal report Kul. 28–HY–10. Leuven. 62p.

Morton K.W. 1980. Petrow Garlekin Methods for Non–Selfadjoint Problems. In: Proc. of the 8th Biannel Conference on Numerical Analysis. Springer Verlag. Dundee.

Nowlin Jr. W.D., Whitworth III T. and Pillsbury R.D. 1977. Structure and Transport of the Antarctic Circumpolar Current at Drake Passage from Short–Term Measurements. J.Phys. Oceanogr. Vol 7. 788–802.

Orlanski J. 1976. A Simple Radiation Boundary Condition. J. Comp.Phys. Vol 21. 251–269.

Pekeris C.L. and Accad Y. 1969. Solution of Laplace's Equations for the M2–Tide in the World Ocean. Philos. Trans. Roy. Soc. London. Vol A 265. 413–436.

Pickard G.L. and Emery W.J. 1982. Descriptive Physical Oceanography, An Introduction. Pergamon Press, Oxford New York Toronto Sydney Frankfurt. 249p.

Pond S. and Pickard G.L. 1983. Introductory Dynamical Oceanography. 2nd edition. Pergamon Press. Oxford New York Toronto Sydney Frankfurt. 329p.

Pritchard R.S. and Colony R. 1976. A Difference Scheme for the AIDJEX Sea–Ice Model. In: Numerical Methods in Geomechanics. ASCE. Desai C.(Ed.). 1194–1209.

Raymond W.H. and Kuo H.L. 1984. A Radiation Boundary Condition for Multi–Dimensional Flows. Quart.J.R.Met.Soc. Vol 110. 535–551

Røed L.P. and O'Brien J.J. 1983. A Coupled Ice–Ocean Model of Upwelling in the Marginal Ice Zone. J. Geoph. Res. Vol 38. 2863–2872.

Røed L.P. 1984. A Thermodynamic Coupled Ice–Ocean Model of the Marginal Ice Zone. J. Phys. Oceanogr. Vol 14. 1921–1929.

Røed L.P. and Smedstad O.M. 1984. Open Boundary Conditions for Forced Waves in a Rotating Fluid. SIAM J.Sci.Stat.Comp. Vol 5. 414–426.

Røed L.P. and Cooper C.K. 1986. Open Boundary Conditions in Numerical Ocean Models. In: Advanced Physical Oceanographic Numerical Modelling. O'Brien J.J. (Ed.) D.Reidel Publishing Company Dordrecht. 411–436.

Rumer R.R. 1983. Simulation of Lake Ice Dynamics. In: Frontiers of Hydraulic. Engeneering. ASCE. Shen E.T. (Ed.). MIT Cambridge. 9–12 Aug.

Schwiderski E.W. 1980. On Charting Global Ocean Tides. Reviews of Geophysics and Space Physics. Vol 18. No 1. 243–268.

Schwiderski E.W. 1983. Atlas of Ocean Tidal Charts and Maps. Marine Geodesy.

Shen H.T. and Chiang L.A. 1984. Simulation of Growth and Decay of River Ice Cover. J. Hydr. Div. ASCE. Vol 110. 958–971.

Shyy W. 1983. Study of Finite Difference Approximatios to Steady–State, Convection–Dominated Flow Problems. General Electric Report No 83CRD184. 22p.

Stelling G.S. 1984. On the Construction of Computational Methods for Shallow Water Flow Problems. Rijkswaterstaat Communications No35/1984. La Hague. 226p.

Sündermann J. 1966. Ein Vergleich zwischen der Analytischen und der Numerischen Berechnung winderzeugter Strömungen und Wasserstände in einem Modellmeer mit Anwendung auf die Nordsee. Ph. D. of the Univ. Hamburg. 77p.

Taljaard J.J., Van Loon H., Crutcher H.L. and Jenne R.L. 1969. Climate of the Upper Air I, Southern Hemisphere, Vol.1, Temperatures, Dew Points and Heights at Selected Pressure Levels. NAVAIR 50–1C–55. US Naval Weather Service, Washington DC. 135p.

Thorndike A.S., Rothrock D.A., Maykut G.A. and Colony R. 1975. The Thickness Distribution of Sea Ice. J. Geoph. Res. Vol 80. 4501–4513.

Tiron K.D., Sergeev Yu.N. and Michurin A.N. 1967. The Tidal Chart of the Pacific, Atlantic and Indian Oceans. Vestnik LGU. No 24. 123–135.

van Ypersele de Strihou J. 1986. A Numerical Study of the Response of the Southern Ocean and its Sea Ice to a CO Induced Atmospheric Warming. Cooperative Thesis NCAR CT99 Universite Catholique de Louvain, Belgium and National Center for Atmospheric Research, U.S.A. 135p.

Wake A. and Rumer R.R. 1979. Modelling Ice Regime of Lake Erie. J Hydr. Eng. ASCE. Vol 105. 827–844.

Wake A. and Rumer R.R. 1983. Great Lakes Ice Dynamics Simulation. J. Waterway, Port, Coastal and Ocean Eng. ASCE. Vol 109. 86–102.

Weare T.J. 1976. Instability in Tidal Flow Computational Schemes, J of the Hydraulic Division, Proc. ASCE. Vol 102.
HY5. 569 580.

Whewell W. 1833. Essay Towards a First Approximation to a Map of Cotidal Lines. Trans. Roy. Soc. 147.

Yanenko N.N. 1971 The Method of Fractional Steps. Springer Verlag Berlin Heidelberg New York. 160p.

Yu C.S., Fettweis M., De Bruyn R. and Berlamont J. 1988a. A 2D Model for Steady and Unsteady Flows. In: Computer Methods and Water Resources, 1st Int. Conf., Morocco 1988, Vol 2 Computational Hydraulics. Ouazar D., Brebbia C.A. and Barthet H. (Eds.). Computational Mechanics Publication and Springer–Verlag. 403–414.

Yu C.S., Fettweis M. and Berlamont J. 1988b. A 2D Model for Tidal Flow Computations. In: Computational Methods in Water Resources Vol 1 Modeling Surface and Sub–Surface flows. Proc. VII Int. Conf. MIT, USA, June 1988. Celia M.A. et.al. (Eds.). Elsevier and Computational Mechanics Publication. 281–286.

Yu C.S., Fettweis M., Berlamont J., Decroo D. and Blomme E. 1988c. Tidal Currents along the West–Belgian Coast. To be published in the Proc. of the Int. Conf. on Computer Modelling in Ocean Engeneering. Venice. 19–23 Sep. 1988.

Yu C.S., Fettweis M., Hermans I. and Berlamont J. 1988d. Tidal Flow Simulation in the English Channel and Southern North Sea. (to be published).

Zahel W. 1970. Die Reproduktion gezeitenbedingter Bewegungs–vorgange im Weltozean mittels des Hydrodynamisch–Numerischen Verfahrens. Mitteil. Inst. Meereskunde Univ. Hamburg. No 17. 1–50.

SCIENCE POLICY OFFICE
Research contract
nr ANTAR/03

NUMERICAL STUDY OF THE AIR SEA INTERACTIONS IN THE ANTARCTIC COASTAL ZONE AND THEIR IMPLICATIONS ON DEEP SEA FORMATION IN THE CASE OF KATABATIC WIND

H. Gallée, A. Berger, G. Schayes,
T. Fichefet, I. Marsiat, C. Tricot
and J.P. van Ypersele

INSTITUT D'ASTRONOMIE ET DE
GEOPHYSIQUE G. LEMAITRE
UNIVERSITE CATHOLIQUE DE LOUVAIN
CHEMIN DU CYCLOTRON, 2
B-1348 LOUVAIN-LA-NEUVE (BELGIUM)

BELGIAN SCIENTIFIC RESEARCH
PROGRAMME ON ANTARCTICA
SCIENTIFIC RESULTS OF PHASE ONE
(OCT 85 - JAN 89)
VOLUME III: GLACIOLOGY AND
CLIMATOLOGY

Contents

1 General goals 1

2 Some characteristics of katabatic winds 1

3 The atmospheric model 4

3.1 Equations of the atmospheric model 4

3.2 Filtering 6

3.3 Upper and lower boundary conditions 7

3.4 Lateral boundary conditions 8

3.5 Parameterization of turbulent fluxes 8

3.5.1 Vertical turbulent diffusion above the surface layer 8

3.5.2 Vertical turbulent diffusion in the surface layer 9

3.6 The grid and the numerical scheme of the model 10

3.7 The surface model 11

4 Simulation of katabatic winds 12

4.1 Control run 17

4.2 Run C1 23

4.3 Run P1 23

5 On air-sea interactions in Antarctic coastal zone 24

5.1 Introduction 24

5.2 Development of a time dependant model of a coastal polynia 26

5.3 Air-Sea interaction between katabatic flow and ocean 29

6 Conclusions 32

7 Applications 34

8 References 36

Keywords Katabatic Wind - Air Sea Interactions - Mesoscale - Deep Sea Formation - Antarctica

Abstract :

Antarctica plays an important and particular role in the climate system. Its location (South Pole) is responsible of the formation of an ice sheet which covers entirely the continent. Because of the intense infrared radiative heat losses, cold dense air forms near the surface and flows down to the coast where its daily average speed reaches 200 km/hour at some places. Katabatic flow can thwart the synoptic weather situation and can maintain coastal water areas free of ice. In these ice free zones, strong heat exchanges occur between the cold atmosphere and the relatively warm ocean, with enhanced sea ice formation and salt rejection in the water column. This mechanism plays an important role in the deep sea water formation and, because the ocean is an important reservoir of heat and CO_2, it can affect the climate over long time scales.

The purpose of the present work is the study of the ocean - atmosphere interactions in the Antarctic coastal zone under polar night conditions which are particularly favorable to katabatic winds development. The spatial evolution of katabatic winds along idealized and realistic slopes representative of Antarctic terrain is investigated using an atmospheric two-dimensional primitive equation model written in terrain following σ-coordinate and with high resolution. The surface heat balance of snow (which is assumed to recover sea ice and continental ice) is computed using a simple soil model.

Three first simulations are done with the ocean being recovered by sea ice. The slope is either constant, either realistic (Adélie Land topography

is then chosen). Much of the flow evolution is completed by 15 *h integration period. Then a downslope momentum forces analysis of the katabatic flow is made, emphasizing on physical mechanisms in the coastal zone. The importance of the reversal of the pressure gradient force in the coastal zone, causing the sudden decay of katabatic winds and the onset of a "sea ice breeze" flow, is discussed. It is shown that the cause of this phenomenon is the pilling up of cold katabatic air in the coastal region.*

Second the consequences of the absence of sea ice cover on the whole ocean or in a small coastal polynia, are examined. The terrain profile is that of Adélie Land. It is seen that a small water area free of ice does not influence the atmospheric circulation significantly. On the contrary, the heating of the air by an underlaying completely ice free ocean is such that the "sea ice breeze flow" in the coastal zone is weakened.

Finally a polynia model is forced by the output of the atmospheric model in the case of an ocean free of ice. The computed salt fluxes in the polynia are sufficient so that deep sea water can form if the atmospheric circulation is maintained during 2 month.

1 General goals

One purpose of the climate studies done at the Institut d'Astronomie et de Géophysique G. Lemaître is the simulation of long term climatic changes. This study requires to consider the mechanisms driving the climatic system over long time scales, i.e. from a century to a few thousand years. One of these mechanisms, among the most important, is the deep oceanic circulation because it involves large amounts of heat exchanged between the equator and the poles and because the deep ocean is an important reservoir of CO_2. The source of the deep oceanic circulation is localized in ice-free polar oceans. In these zones important heat transfers occur from ocean to atmosphere. This leads to dense water formation either by the cooling of salty water, either by sea ice formation and salt rejection in the water column. Near the Antarctic coast, the second mechanism occurs in wind driven open water areas (polynias). If, particularly during the whole Antarctic winter, the wind is sufficiently strong to advect the new sea ice out of the coastal polynia, the ocean - atmosphere heat exchanges occuring in the polynia are sufficient to explain the formation of coastal dense water which can ultimately contributes to the Antarctic bottom water formation.

The aim of the present research is to study such interactions in the Antarctic coastal zone. In particular the heat exchanges between the atmosphere and ice-free ocean will be quantified under strong wind and cold air temperature conditions. Such conditions are observed in Antarctica when either a katabatic wind blows down along the slope of the ice sheet, or cyclonic activity generates easterly storms along the coast, or both. This study will be restricted to the case of pure katabatic wind events.

2 Some characteristics of katabatic winds

Katabatic wind is a gravity driven atmospheric current which is forced by the cooling

of air adjacent to a sloped surface. It is observed all around the world and called glacier or valley wind (Mather and Miller, 1967). It is generally classified as a mesoscale phenomenon. The most remarkable exception to this rule arises when the length scale of the slope becomes as large as the scale of a continent and when the surface cooling conditions required for the production of a strong sloped inversion are satisfied. This is the case at least for Greenland and Antarctica, especially during the long polar night. For such situation the downslope induced surface wind reaches a stormy character and is perhaps the most remarkable climatic feature which has already been observed on polar ice caps (Parish and Bromwich, 1987).

Observations and previous studies have shown that the Antarctic surface winds are anomalous compared to the well-understood mid-latitude flows. Katabatic winds in the coastal region of Adélie Land, Antarctica, are responsible for probably the most intense daily mean wind speed observed near the sea level (Schwerdtfeger, 1984). Parish and Bromwich (1987) point out that typical katabatic regimes in the Terra Nova Bay region are comparable to the Adélie Land winds. Important characteristics of katabatic winds are their persistence and directional constancy (ratio of the vector resultant wind to the mean wind speed). It appears that the srongest winds occur over the steep coastal perimeter where slopes exceed 10^{-2} within the first 150 km inland and that they blow almost directly downslope. Observations also clearly reveal the sensitivity of katabatic flow to topographic confluence zones. It is believed that a confluence channel with a correspondingly large cold air supply is the fundamental cause on the anomalously intense katabatic regime along the Adélie Land coast and in the Terra Nova Bay region (Parish and Bromwich, 1987).

An remarkable feature characterizing strong katabatic storms is the important amount of suspended snow particles in the air (Kodama et al.,1985). Snow drift can accelerate or decelerate the boundary flow. The following influences are possible : (i) increase in density by entrainment, (ii) decrease in temperature by sublimation of snow particles, and (iii) increase in surface friction.

Antarctic surface flow represents an enormeous mass and sensible heat transport between Antarctica and northern latitudes and may represent a significant component in the Earth-atmosphere global energy budget (Parish, 1988). There appears to be a need for better understanding not only of the Antarctic winds but also of the interaction between katabatic winds and large-scale atmospheric circulation features of the southern hemisphere.

Strong katabatic winds which blow offshore from the continent can therefore maintain coastal water areas free of ice, especially during the winter season (Kurtz and Bromwich, 1985, Zwally and Comiso, 1985). In these ice free zones, a large amount of heat is exchanged between the cold atmosphere and the relatively warm ocean, with enhanced sea ice formation and salt rejection in the water column (Zwally and Comiso, 1985). Up to now there are not enough available information which confirm that the katabatic winds maintain their identity for some distance seaward from the coast, except perhaps for the Terra Nova Bay polynia. Moreover observations at some places along the coast of Adélie Land reveal that the katabatic winds undergo hydraulic jump with a sudden diminution of the wind force (André, 1987), and the maintenance of open water areas at other places, suggesting the persistance of strong winds at substantial distance offshore from the glaciers.

The purpose of this report is first to examine the evolution of the katabatic wind in the coastal area and to give some ideas about the kind of physical mechanisms that are responsible for the persistance or the weakening of katabatic wind when it passes the coastline. The atmospheric model which is used for this study is described in section 3. In section 4 the results of three katabatic winds simulations are presented. In the first two experiments the slope of the ice sheet is assumed to be constant respectively at 5 % and 1 %. In the third experiment the terrain profile is taken to be representative of the fall-line of Adélie Land.

Second the implications of katabatic winds on sea air interactions in the Antarctic coastal zone are examined, especially when ocean is free of sea ice. To pursuit this goal,

a polynia model is developped in section 5 and forced by the momentum and heat fluxes computed by the atmospheric model. Finally the salt rejection in the water column over the whole polynia is quantified for polynia length reaching steady state. The implication on deep sea formation is presented.

Conclusions are drawn in section 6.

3 The atmospheric model

3.1 Equations of the atmospheric model

The atmosphere is simulated with a hydrostatic mesoscale primitive equations model, assuming homogeneity of the dependant variables along the coast (2-dimensional approximation). To express the surface boundary conditions in a way as easiest as possible, σ-coordinate is used :

$$\sigma = \frac{p - p_t}{p_\star} \tag{1}$$

where p is pressure, p_t refers to the pressure at the top of the model, (set equal to 50 kPa), p_s is the surface pressure and $p_\star = p_s - p_t$

The averaged forms of the horizontal equations for momentum are therefore :

$$\frac{\partial u}{\partial t} = -u\frac{\partial u}{\partial x} - \dot{\sigma}\frac{\partial u}{\partial \sigma} + f(v - v_g) - \frac{\partial \phi}{\partial x}\mid_p + F_x \tag{2}$$

$$\frac{\partial v}{\partial t} = -u\frac{\partial v}{\partial x} - \dot{\sigma}\frac{\partial v}{\partial \sigma} - f(u - u_g) + F_y \tag{3}$$

where x is the horizontal offshore (positive southward) axis, y is the horizontal onshore (positive eastward) axis, t is time, u, v and $\dot{\sigma}$ are respectively the southward, eastward and σ components of the wind , f is the Coriolis parameter, $\vec{V_g} = (u_g, v_g)$ is the geostrophic wind, R_a is the perfect gas constant for dry air, T is air temperature, $\phi = gz$ is the geopotential, g is gravity, z is altitude, $\mid_p$ means that the pressure gradient force $-\frac{\partial \phi}{\partial x}$ is calculated on an isobaric surface. This avoids its development into the sum $-\frac{R_a T}{p_s + \frac{p_t}{\sigma}}\frac{\partial p_s}{\partial x} - \frac{\partial \phi}{\partial x}\mid_\sigma$ which

leads to severe truncation errors on steep topography (Alpert et al, 1982). F_x and F_y are the subgrid correlation terms which are approximated by the divergences of the vertical turbulent momentum fluxes (see appendix for more details) :

$$F_x = -\frac{\partial}{\partial\sigma}(\overline{u'\dot{\sigma}'}) \tag{4}$$

$$F_y = -\frac{\partial}{\partial\sigma}(\overline{v'\dot{\sigma}'}) \tag{5}$$

where the overbar indicates time average. It must be pointed out that to preserve simplicity overbar is avoided except for the turbulent fluxes.

The vertical momentum equation is approximated by the hydrostatic equilibrium and after some algebra one gets :

$$\frac{\partial\phi}{\partial(\frac{T}{\theta})} = -C_p\theta(1+.608q) \tag{6}$$

where

$$\theta = T(\frac{p_0}{p})^\kappa \tag{7}$$

is the definition of potential temperature, $p_0 = 1000\ hPa$, $\kappa = \frac{R_a}{C_p}$, C_p is the specific heat at constant pressure for dry air and q is the specific humidity.

The equation of state for humid air as a perfect gas is given by :

$$p = \rho R_a T(1+.608q) \tag{8}$$

The continuity equation is expressed through the time tendency equation for p_* :

$$\frac{\partial p_*}{\partial t} = -\int_0^1 \frac{\partial(p_* u)}{\partial x} d\sigma \tag{9}$$

from which $\dot{\sigma}$ can be computed,

$$\dot{\sigma} = \frac{1}{p_*}[\sigma\int_0^1 \frac{\partial}{\partial x}(p_* u)d\sigma - \int_0^\sigma \frac{\partial}{\partial x}(p_* u)d\sigma] \tag{10}$$

The averaged form of the thermodynamic energy conservation is :

$$\frac{\partial\theta}{\partial t} = -u\frac{\partial\theta}{\partial x} - \dot{\sigma}\frac{\partial\theta}{\partial\sigma} + \frac{\partial R_{IR}}{\partial\sigma} + F_\theta \tag{11}$$

where R_{IR} is the infrared radiative heat flux (Sasamori, 1968) and

$$F_\theta = -\frac{\partial}{\partial \sigma}(\overline{\theta' \dot{\sigma}'}) \tag{12}$$

is the divergence of the turbulent heat flux.

The averaged form of the specific humidity conservation is expressed by :

$$\frac{\partial q}{\partial t} = -u\frac{\partial q}{\partial x} - \dot{\sigma}\frac{\partial q}{\partial \sigma} + F_q \tag{13}$$

where

$$F_q = -\frac{\partial}{\partial \sigma}(\overline{q' \dot{\sigma}'}) \tag{14}$$

is the divergence of the turbulent moisture flux.

Equations (2), (3), (6), (8)-(11) and (13) form a system of 8 equations for 8 unknows u, v, $\dot{\sigma}$, ϕ, p_*, ρ, θ and q. The variables p and T can be obtained from the definitions (1) and (7) of σ and θ respectively, and the turbulent fluxes introduced in (4), (5), (12) and (14) will be parameterized.

3.2 Filtering

In the presence of the stable Antarctic atmosphere, especially near the surface, the katabatic flow will generate gravity waves propagating parallelly to the surface. The energy of these waves is expected to cascade to smaller length scales but this cannot occur because the smallest feature that can be resolved by the model has a wavelength of two times the grid spacing (Pielke, 1984).

A first method to remove these waves would be the use of a physical parameterization of the horizontal subgrid scale correlation terms so that energy is extracted from the equations in a manner consistent with reality. But the horizontal subgrid mixing in mesoscale models is not well known, and it is usually parameterized by a first order closure scheme (horizontal diffusivity) which is arbitrarily adjusted until $2 \triangle x$ wavelengths do not appear

to degrade the solutions significantly (numerical tuning). Moreover, when horizontal subgrid mixing is considered in the model, the expression of $\dot{\sigma}'$ by an appropriate expression that involves w' results in the appearance of a term involving the σ-derivative of $\tan\alpha\ \overline{u'u'}$ for the x-component of the turbulent frictional force and $\tan\alpha\ \overline{u'v'}$ for the y-component, where α is the slope angle of the σ surface (Alpert and Neumann, 1984). Finally the parameterization of the horizontal correlation terms in the terrain following coordinate σ system leads to a vertical contribution of the numerical tuning which destroy the physical solution of the model. It was found during the preliminary experiments of the model that the contribution of the horizontal diffusion coefficient to the vertical diffusion was much greater than the vertical one with as consequence an unrealistic simulated vertical wind profile (see appendix).

A second method to remove the spurious waves consists in the use of a spatial smoother (or filter) which removes the shortest waves, but leaves the longer ones relatively unaffected. The selective low-pass filter which is used is analysed by Alpert (1981). It is corrected to take into account the variation of the slope and has the following form :

$$(1-\delta)\overline{\psi}_{j-1} + 2(1+\delta)\overline{\psi}_j + (1-\delta)\overline{\psi}_{j+1} = \psi_{j-1} + 2\psi_j + \psi_{j+1} + \delta R_c \qquad (15)$$

where $j \pm 1 \rightarrow (j \pm 1)\ \triangle x$, ψ is the field to be smoothed and $\overline{\psi}$ is the smoothed field. δ is an arbitrarily chosen weighting parameter for the smoothed values and $R_c \simeq -\frac{\partial \psi}{\partial x}\mid_{j+1}$ $(\tan\alpha\mid_{j+1} - \tan\alpha\mid_j)\ \triangle x$ is the correction term (see appendix).

3.3 Upper and lower boundary conditions

The boundary conditions at the top of the model, where $p = p_t$ $(\sigma = 0)$, are :

$$\dot{\sigma} = 0 \qquad (16)$$

$$\frac{\partial u}{\partial \sigma} = \frac{\partial v}{\partial \sigma} = 0 \qquad (17)$$

$$\frac{\partial \theta}{\partial \sigma} = 0 \tag{18}$$

$$q = q_{observed} \tag{19}$$

The boundary conditions at the surface ($\sigma = 1$) are :

$$u, v = 0 \tag{20}$$

$$T = T_s(t) \tag{21}$$

$$q = q_s(T_s) \tag{22}$$

where T_s is the predicted air surface temperature in function of time t (see below), and q_s is the saturation specific humidity corresponding to the air surface temperature T_s.

3.4 Lateral boundary conditions

To help suppress spurious boundary reflections, the following radiation condition are used :

$$\frac{\partial f}{\partial t} + c\frac{\partial f}{\partial x} = 0 \tag{23}$$

where $f = u, v, \theta$ or q and c is the wave velocity. This scheme has been introduced by Orlanski (1976) and discussed later by Miller and Thorpe (1981).

3.5 Parameterization of turbulent fluxes

3.5.1 Vertical turbulent diffusion above the surface layer

Parameterization of turbulence above the surface layer is done by expressing the double covariance term of (4), (5), (12) and (14) by the classical Austausch exchange formulation (see appendix) :

$$F_x = +\frac{g^2}{p_*^2}\frac{\partial}{\partial \sigma}(\rho^2 K_z \frac{\partial \overline{u}}{\partial \sigma}) \tag{24}$$

$$F_y = +\frac{g^2}{p_*^2}\frac{\partial}{\partial \sigma}(\rho^2 K_z \frac{\partial \overline{v}}{\partial \sigma}) \tag{25}$$

$$F_\theta = +\frac{g^2}{p_*^2}\frac{\partial}{\partial\sigma}(\rho^2 K_{zh}\frac{\partial\overline{\theta}}{\partial\sigma}) \tag{26}$$

$$F_q = +\frac{g^2}{p_*^2}\frac{\partial}{\partial\sigma}(\rho^2 K_{zh}\frac{\partial\overline{q}}{\partial\sigma}) \tag{27}$$

where K_z and K_{zh} are the vertical turbulent diffusion coefficients respectively for momentum and heat. They are expressed as follows :

$$K_z = l^2 \mid \frac{\triangle\overline{V}}{\triangle z} \mid F(R_i) \tag{28}$$

$$K_{zh} = l^2 \mid \frac{\triangle\overline{V}}{\triangle z} \mid F_h(R_i) \tag{29}$$

where

$$l = \frac{kz}{l + \frac{kz}{\lambda}}$$

$$\frac{\triangle\overline{V}}{\triangle z} = [(\frac{\partial\overline{u}}{\partial z})^2 + (\frac{\partial\overline{v}}{\partial z})^2]^{\frac{1}{2}}$$

$$R_i = \frac{g}{\overline{\theta}}\frac{\frac{\partial\overline{\theta}}{\partial z}}{(\frac{\triangle\overline{V}}{\triangle z})^2}$$

are the mixing length, the wind shear and the Richardson number respectively. The functions $F(R_i)$ and $F_h(R_i)$ of the Richardson number are given by Louis (1979). The value of λ is chosen to be 40 m, which is representative of the limit mixing length for katabatic winds.

3.5.2 Vertical turbulent diffusion in the surface layer

The parameterization of turbulence will be different for the surface layer. Because the turbulent fluxes in the surface layer may be assumed constant, it is possible to get from the observations a good parameterization of thenn, although it is computationally expensive. On the other hand, the upper part of the planetary boundary layer is less known but the parameterization of K used in this model is simpler.

The formulation is given by Businger (1973), who use the friction variables u_*, θ_*, q_* and the Monin-Obukhov length L :

$$u_*^2 = -\overline{V'w'} \tag{30}$$

$$-\overline{u'w'} = \frac{\overline{u}}{\overline{V}} u_*^2 \tag{31}$$

$$-\overline{v'w'} = \frac{\overline{v}}{\overline{V}} u_*^2 \tag{32}$$

$$-\overline{\theta'w'} = u_*\theta_* \tag{33}$$

$$-\overline{q'w'} = u_* q_* \tag{34}$$

$$L = -\frac{\overline{\theta} u_*^2}{kg\theta_*} \tag{35}$$

where $k = .4$ is the Von Karman constant, w is the vertical velocity in z coordinates and $V = (u^2+v^2)^{\frac{1}{2}}$. Using universal functions, and taking into account the roughness length z_0 of the surface, the friction variables are obtained through the values of the corresponding variables at 10 m height, Businger (1973) providing the relationships between $u_{10\ m}$ and u_*, $\triangle q = q_{10\ m} - q_s(T_s)$ and q_*, $\triangle\theta = \theta_{10\ m} - \theta_s$ and θ_*, where θ_s is the potential temperature at the surface. It is therefore possible to use these relations and (28)-(33) in order to determine the contribution of the turbulent diffusions F_x, F_y, F_θ and F_q in the surface layer.

3.6 The grid and the numerical scheme of the model

Horizontal grid spacing is regular : $\triangle x = 2\ km$, with 53 or 250 grid intervals. Vertical discretization is irregular to get more σ-levels close to the surface. The initial height of the σ-levels are $z = 10,\ 25,\ 55,\ 125,\ 295,\ 680,\ 1550$ and $3500\ m$. The time step is such that the Courant-Friedrich-Levy criterion is satisfied for fast gravity waves. Hence $\triangle t = 4\ s$ was adopted. The numerical scheme is based on splitting techniques (Marchuck, 1974, Bornstein, 1975 and Gadd, 1978). The contribution of the pressure gradient to the first

horizontal momentum equation is achieved with a leap frog scheme. For the turbulent flux contributions a semi-implicit scheme is used and for advection a semi-lagrangian scheme.

3.7 The surface model

Ground surface temperature is predicted from the force restore slab model of Blackadar (1978), modified by Deardorff (1978) :

$$\frac{\partial T_s}{\partial t} = -C_1 \frac{H_A}{\rho_s c_s d_1} - C_2 \frac{T_s - T_2}{\tau_1} \tag{36}$$

with $C_1 = 3.72$, $C_2 = 7.4$, H_A (positive upward) is the sum of the heat fluxes coming from the atmosphere and absorbed at the ice sheet surface : the net infrared radiative fluxes, the sensible and latent heat turbulent fluxes. The surface parameters are those of the snow, which is assumed to cover the sea ice and the continental ice during the Antarctic winter : the specific mass : $\rho_s = 330\ kg\ m^{-3}$, the heat capacity : $c_s = 2\ 10^3\ J\ kg^{-1}\ K^{-1}$, the thermal diffusivity : $\kappa_s = .27\ 10^{-6}\ m^2\ s^{-1}$, the depth reached by the diurnal temperature wave : $d_1 = (\kappa_s \tau_1)^{\frac{1}{2}} = .15\ m$, with the length of the day : $\tau_1 = 86400\ sec.$ Finally T_2 is the mean temperature of the ice and is assumed to be the average of T_s over the previous 24 *hours*.

Table I: Initial atmospheric profiles for the katabatic winds simulations

altitude z (m)	pressure p (mb)	temperature T (K)	relative humidity U (%)
0.0	1000.0	250.0	63.
709.2	907.6	250.0	83.
1182.0	850.8	250.0	97.
2046.0	756.0	250.0	86.
2622.0	698.6	250.0	78.
3100.6	654.2	247.3	80.
5015.0	499.0	236.5	86.
8371.0	299.8	213.6	13.
10849.0	200.3	206.4	23.
15067.0	99.0	202.5	20.

4 Simulation of katabatic winds

The purpose of the experiments is to describe the spatial evolution of katabatic flows over different types of steep slope characterizing the coastal zone of the Antarctic continent, with a particular attention given to the physical processes driving the pressure gradient force for such circulation.

First, two model integrations were performed with ice terrain having constant slopes :

control run	$z_{surf} = 0.$	-34 km	$< x < 0$ km
(5 % *slope*)	$z_{surf} = 0.05$ x	0 km	$< x < 50$ km
	$z_{surf} = 2.5$ km	50 km	$< x < 70$ km
run C1	$z_{surf} = 0.$	-34 km	$< x < 0$ km
(1 % *slope*)	$z_{surf} = 0.01$ x	0 km	$< x < 50$ km
	$z_{surf} = 0.5$ km	50 km	$< x < 70$ km

where $x = 0$ is the coastline. The 5 % ice slope chosen for control run is fairly typical of katabatic flows occuring in Antarctica near the coast and the slope of run C1 is typical for the Antarctic ice sheet $\sim 50\ km$ far from the coast.

The third integration (run P1) is achieved with a realistic ice terrain profile which is representative of the slope of Adélie land (fig.1).

In all runs the initial temperature and humidity structures are given in table I. They are obtained by modifying the zonally averaged mean winter observed conditions at $67^o\ South$ (see Oort, 1983), to get an isothermal profile from the level $T = 250\ K$ to the surface. This correction is more appropriate for typical polar night conditions on the Antarctic continent (Schwerdtfeger,1984 and Parish, 1984). Geostrophic wind vector is chosen to be $\vec{V_g} = (0,0)$ for all simulations. Each simulation consists of a 15-h model time integration starting from conditions of rest. At the end of the integration period, it can be assumed that the model variables are not far from steady state (Parish and Waight, 1987). Only these results are discussed here.

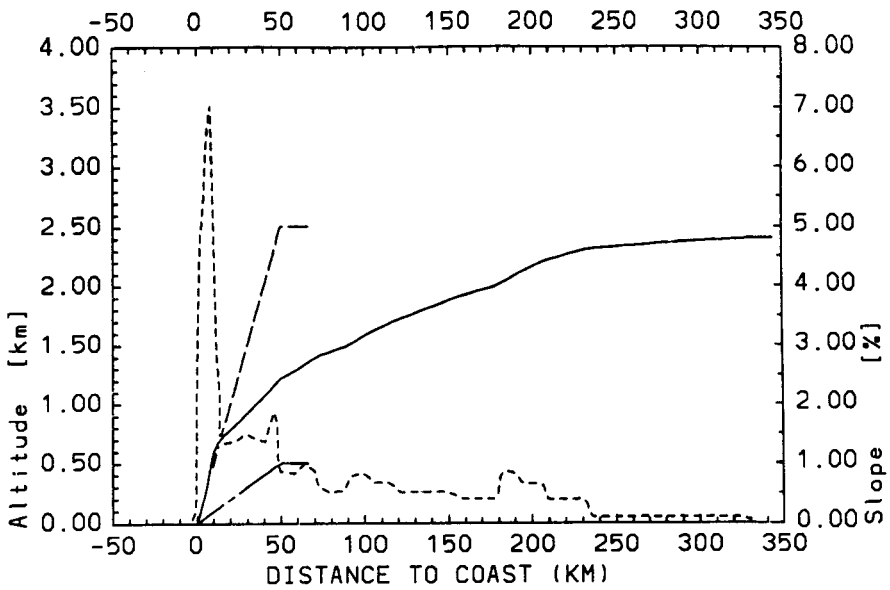

Figure 1: *Terrain profile for Antarctic katabatic winds simulations :*

— — — — — : Control run terrain profile
— - — - — : Run C1 terrain profile
- - - - - - - : Adélie Land terrain slope
——————— : Adélie Land terrain profile

The total pressure gradient force can be written as follows (Mahrt and Larsen, 1982) :

$$PGF \simeq g\frac{\delta\theta}{\theta_0}\sin\alpha - \cos\alpha\frac{g}{\theta_0}h\frac{\partial\bar{\theta}}{\partial x} - \cos\alpha\frac{g}{\theta_0}\bar{\theta}\frac{\partial h}{\partial x} - \frac{1}{\rho}\frac{\partial p}{\partial x} \tag{37}$$

where α is the slope angle, z the height above the ice surface, h is the top of the inversion layer, taken as the height at which potential temperature profile is significantly different from the upper levels potential temperature profile. The mean potential temperature of the katabatic layer from z to h is :

$$\bar{\theta} = \frac{1}{h}\int_z^h \delta\theta dz \tag{38}$$

$\delta\theta = \theta - \theta_0$, where $\theta(z)$ and $\theta_0(z)$ are respectively the potential temperature and the basic state potential temperature representative of the potential temperature outside the katabatic layer. $\bar{\theta}(z \longrightarrow 0)$ is the vertically averaged deficit of potential temperature. Integrating the pressure gradient force from the surface to $z = h$, with the large scale

contribution being equal to zero and assuming constant θ_0 in the inversion layer, it follows :

$$\overline{PGF} \simeq g\frac{\bar{\theta}}{\theta_0}\sin\alpha - \cos\alpha\frac{g}{\theta_0}h\frac{\partial\bar{\bar{\theta}}}{\partial x} - \cos\alpha\frac{g}{\theta_0}\bar{\bar{\theta}}\frac{\partial h}{\partial x} \tag{39}$$

where

$$\bar{\bar{\theta}} = \frac{1}{h}\int_0^h \bar{\theta}dz \tag{40}$$

As in Kodama and Wendler (1986), the first term of the right hand side is the pressure gradient force due to the inversion (buoyancy term, referenced hereafter as B). The second term is the pressure gradient force due to the change in the temperature profile in the inversion layer, and to the surface potential temperature change along the slope (temperature gradient term, referenced hereafter as TG). The third term is the pressure gradient force due to the change in the depth of the inversion layer (depth change term, referenced hereafter as DC).

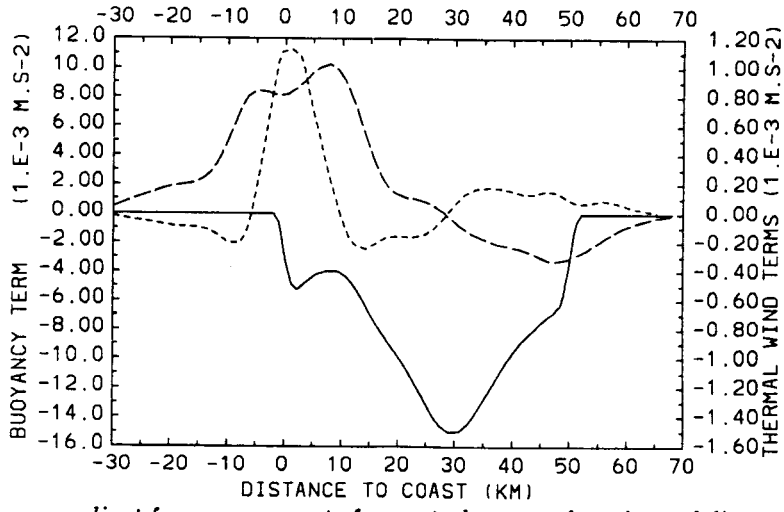

Figure 2: *Total pressure gradient force components for control run, as functions of distance to the coast (positive distances on the continent)*

———— : Buoyancy term (B)
- - - - - - - : Temperature gradient term (TG)
— — — — — : Depth change term (DC)

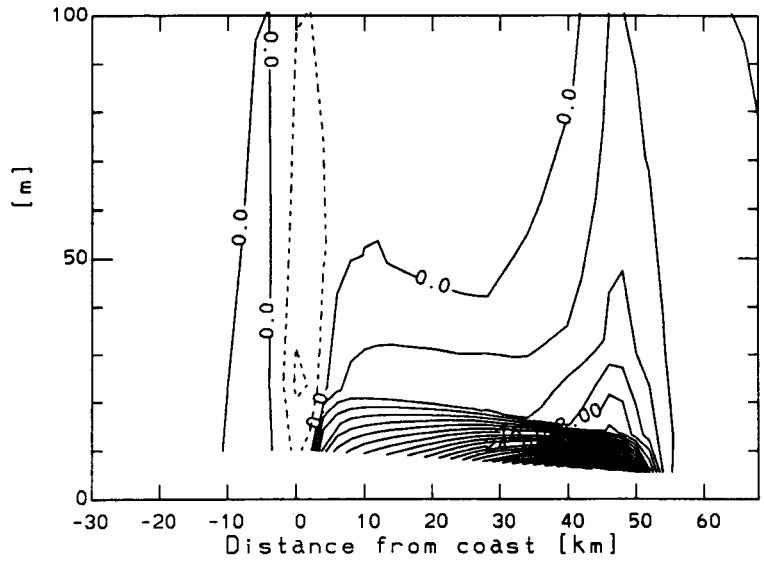

Figure 3: *Total pressure gradient force, as a function of distance to coast and height above surface, for control run. Full lines indicate that force is downslope. Contour interval of* $2.10^{-3}\ m.s^{-2}$

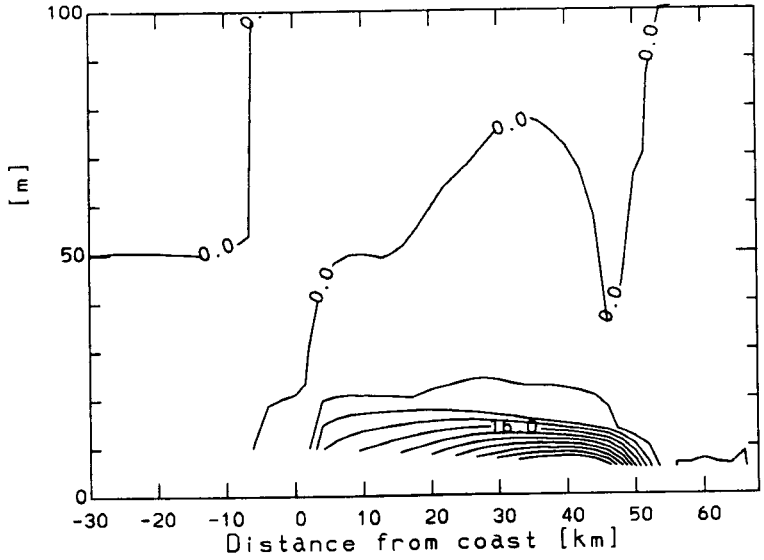

Figure 4: *Stress divergence, as a function of distance to coast and height above surface, for control run. Full lines indicate that stress divergence is upslope. Contour interval of* $4.10^{-3}\ m.s^{-2}$

4.1 Control run

The x dependance of B, TG and DC is shown on fig.2 for the control run (5 % slope). The x, z dependance of the total pressure gradient force and the stress divergence are displayed on fig.3 and 4 respectively. It can be seen that at the beginning of the slope (between 50 km and 30 km inland), the important potential temperature deficit due to radiational cooling of the ground and the surface air layer on the plateau causes B to be driving force of the katabatic wind. Moreover, the onset of katabatic wind causes the flow to lose more heat by turbulent heat exchange with the cold underlaying surface, and B further increases. As it can be seen from fig.5, $\mid u \mid$ reaches rapidly its maximum. This is the phase of the "advective-gravity flow" defined by Mahrt (1982). On this part of the slope, the decrease of h seems to be due mainly to the acceleration of the katabatic layer, because of the mass transport conservation constraint. The value of the local Froude number, defined as

$$F^* = \frac{U^2}{(g\bar{\bar{\theta}}/\theta_0)h} \tag{41}$$

with U the vertical average of u from $z = 0$ to $z = h$, is greater than unity (shooting flow). With an integral model Lalaurette and André (1985) predicted shooting flow for such slope. After the first 20 km of slope, TG is negative and DC is positive : this reflect the effect of downslope advection in a stable atmosphere and the entrainment of upper warm ambient air into the katabatic layer, with as consequense a decrease of B. Force analysis of the downslope momentum (cfr. fig.3 and 4) show that this regime results from a close balance between pressure gradient force and stress divergence ("equilibrium flow", following Mahrt,1982). The role of the Coriolis force is negligible, as also found by Parish and Waight (1987). Similar stationary flows were simulated with integral models by Manins and Sawford (1979), and Lalaurette and André (1985), who show the importance of the turbulent entrainment of upper warm air into the katabatic layer, when ambient stratification is stable. The importance of the entrainment mechanism in Antarctica was

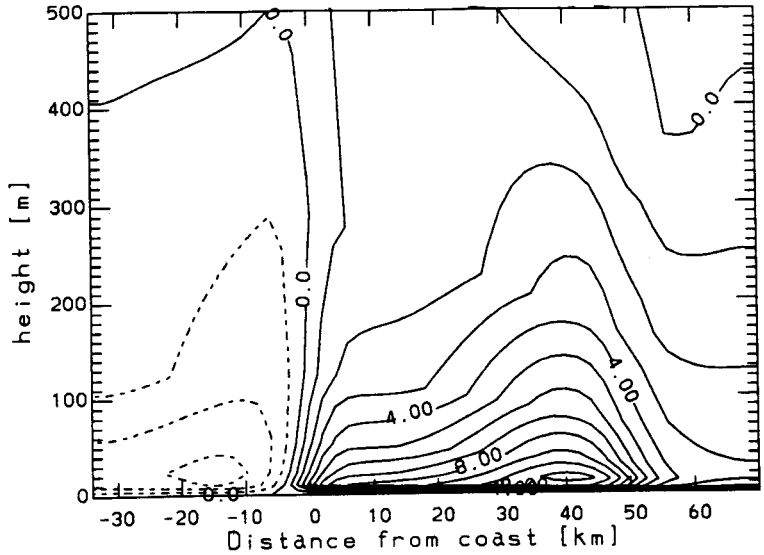

Figure 5: *u, as a function of distance to coast and height above surface, for control run. Full lines indicate downslope wind. Contour interval of* $1.m.s^{-1}$

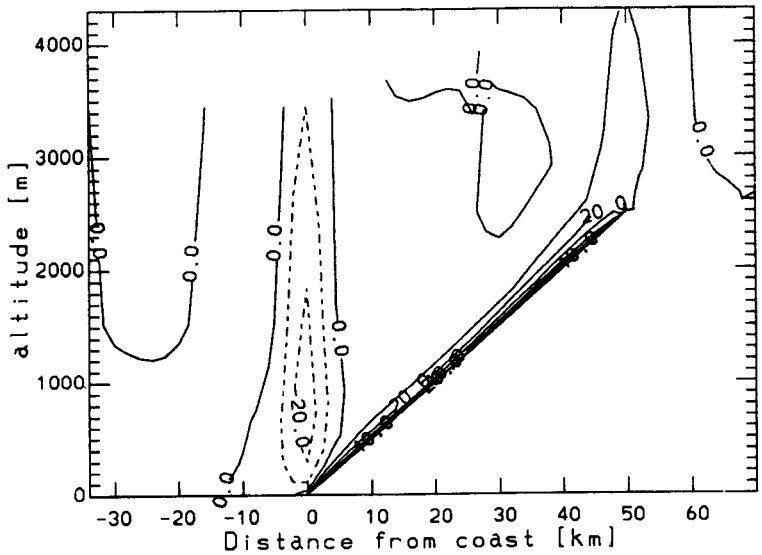

Figure 6: *w, as a function of distance to coast and altitude, for control run. Full lines indicate downward motion. Contour interval of* $10.cm.s^{-1}$.

also suggested by Wendler and Kodama (1986) but the lack of direct observations prevented thenn to quantify this hypothesis. In the present model, turbulent entrainment is taken into account through internal mixing, but its effects are difficult to determine since the transition between the katabatic flow and overlying flow can be thick and the katabatic flow is not necessarily fully turbulent. On the other hand, the entrainment due to mass divergence in the katabatic stream is taken into account. Nevertheless, the simulated DC is relatively smaller when compared with the integral models previously mentioned. This can be explained by the effect of the vertical stability which inhibits turbulent entrainment, as also found by Nappo and Rao (1987), who demonstrate the dependance of entrainment on ambient stratification.

The "equilibrium flow" is maintained down to the coast, where there is a rapid transition to a flow in the opposite direction ("sea ice breeze flow"). The vertical component w of the wind is shown in fig.6. Strong upward motion arises at the coast line. These simulated features are consistant with the building up of a thick cold air layer further on the sea, when the buoyancy force completely disappear at the coast line. Such mechanism can also been understood as a strong positive feedback initiated by the residual positive (directed from sea to land) thermal wind force (TG + DC) and leading to a further increase of DC. This could explain why the model simulates there a short transition from the katabatic flow towards a "sea ice breeze flow". A coastal jumplike phenomenon was also observed during the IAGO-Katabatic Programme[1] (André, Wendler and Zéphoris, 1986) and André (1987), where the transition zone from katabatic flow to "sea ice breeze flow" was very sharp, with a surface pressure increase on sea and probably stronger vertical winds and turbulent mixing. Of course the use of the hydrostatic assumption in the present model precludes the simulation of such small scale features.

[1] Interaction Atmosphère Glace Océan

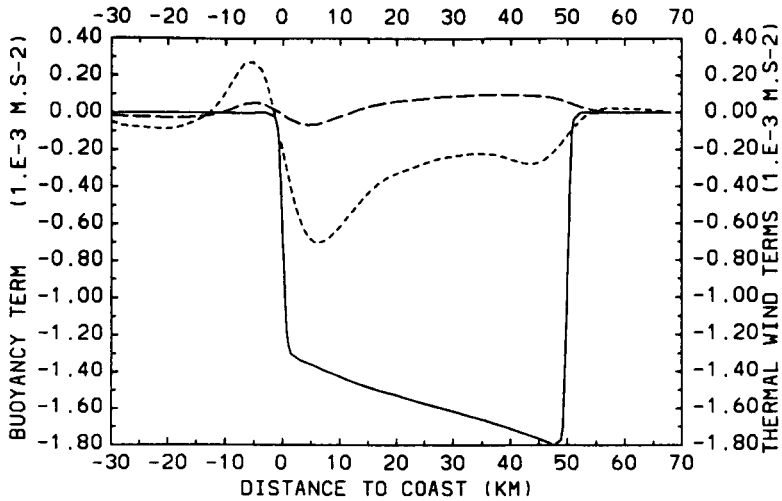

Figure 7: *Total pressure gradient force components for run C1, as functions of distance to the coast (positive distances are on the continent)*

——— : Buoyancy term (B)
- - - - - - - : Temperature gradient term (TG)
— — — — — : Depth change term (DC)

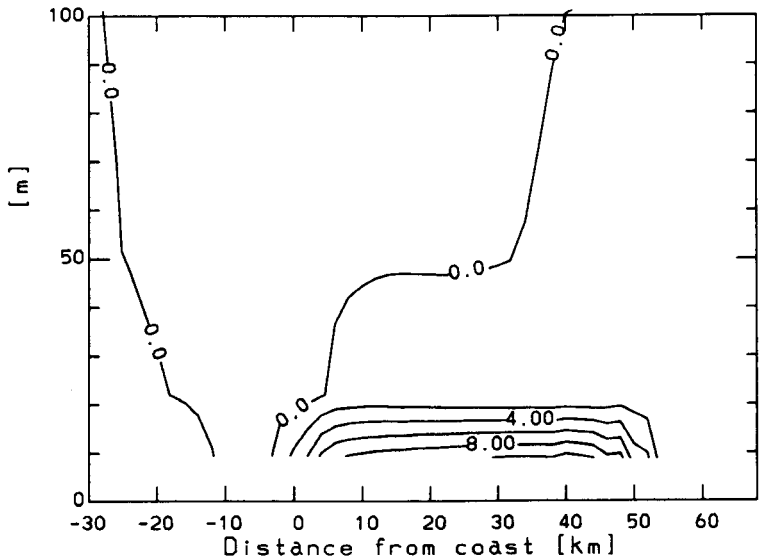

Figure 8: *Total pressure gradient force, as a function of distance to coast and height above surface, for run C1. Negative values (i.e. directed downslope) represented by full lines. Contour interval of* $2.10^{-3}\ m.s^{-2}$.

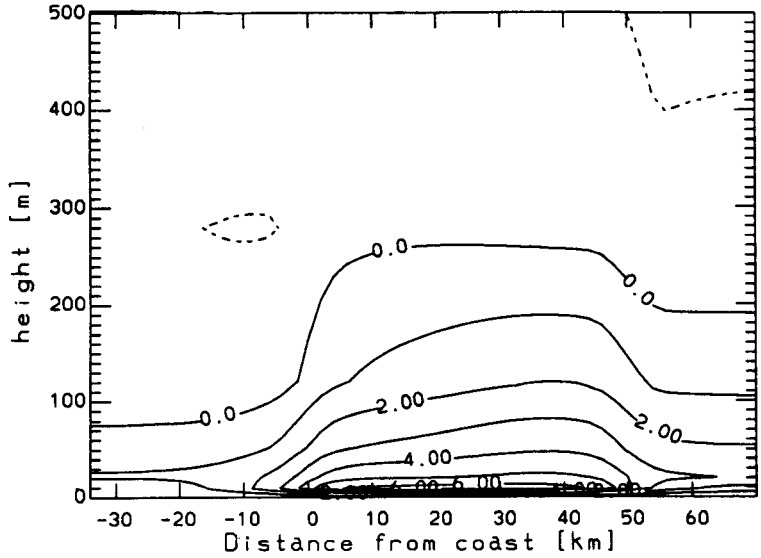

Figure 9: *u, as a function of distance to coast and height above the surface, for run C1. Full lines indicate downslope wind. Contour interval of* $1.m.s^{-1}$.

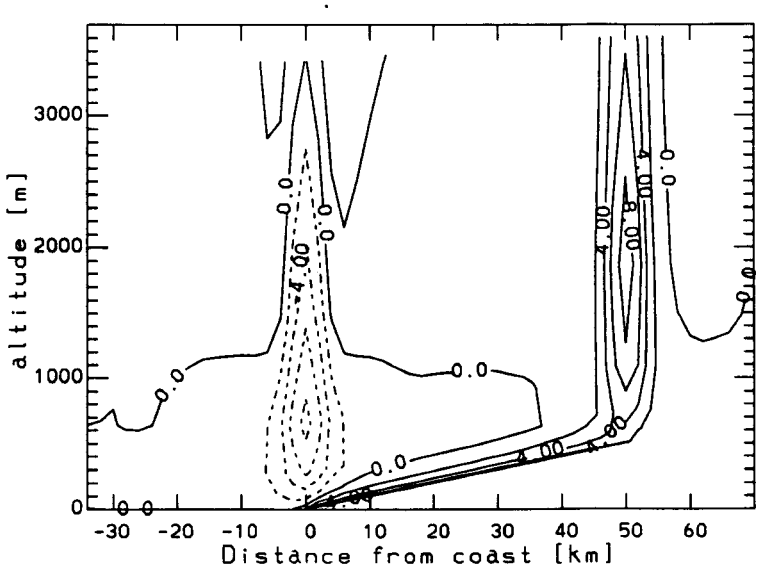

Figure 10: *w, as a function of distance to coast and altitude, for run C1. Full lines indicate downward motion. Contour interval of* $2.cm.s^{-1}$.

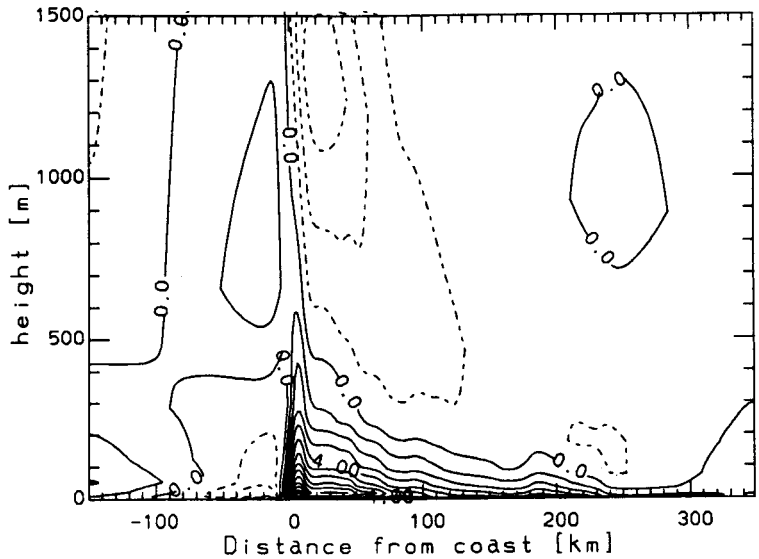

Figure 11: *u, as a function of distance to coast and height above the surface, for run P1. Full lines indicate downslope wind. Contour interval of* $1.m.s^{-1}$.

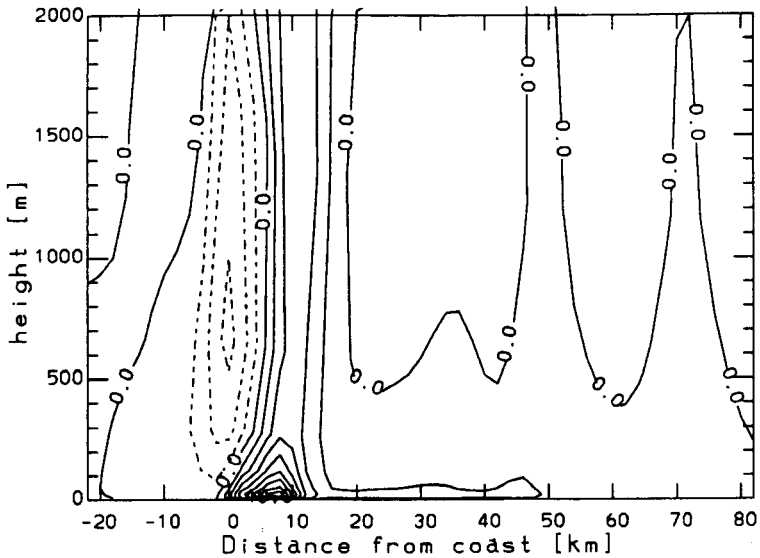

Figure 12: *w, as a function of distance to coast and altitude, for run P1. Full lines indicate downward motion. Contour interval of* $10.cm.s^{-1}$.

4.2 Run C1

Changing the ice slope modify the buoyancy force and maybe the wind regime in the coastal zone. The purpose of run C1 is to evaluate the response of katabatic flow to a lowering of the slope from 5 % to 1 %.

The x dependance of B,TG and DC is shown on fig.7 and the x, z dependance of the total pressure gradient force on fig.8, the latter being in close equilibrium with the stress divergence. The fields of u and w can be found on fig.9 and 10 respectively. As expected, B is less important than in run C1 and the simulated katabatic flow is slower. Since the beginning of the slope, the surface temperature increases downslope and it seems that this contribution to TG dominates. Two others noticeable features are found :

i) the greater homogeneity of the u and PGF fields and the smaller weakening of B all along the slope for run C1 and

ii) the absence of a "sea ice breeze flow" on sea near the surface. The relative constancy of B along the slope suggests that the destruction of the temperature deficit by downslope warming is less important than for control run. Moreover the absence of any important positive DC, indicates that entrainment is less important with a smaller slope. In the coastal area DC becomes slightly positive. This is correlated with a near zero total pressure gradient force on sea, a smaller amplitude of the inertial force and a smaller amplitude of w at the coast (three times less than for control run). Finally the positive TG in the marine coastal zone may be due to the weakening of the wind and the turbulent mixing, with a smaller downward sensible heat flux, so that radiational cooling becomes the dominant contribution to the sea ice surface thermodynamic energy balance.

4.3 Run P1

When the model is simulated over the more realistic Adélie land terrain profile (see fig.1), the slope is everywhere less than 1 %, excepted in the coastal area where it exceed

5 % . The magnitude and vertical profile of the simulated u field (fig.11) are representative of soundings shown in Schwerdtfeger (1984, his fig.3.10) and in Adachi (1979), for the East Antarctic coastal zone. On the other hand, the x, z dependance of u and w fields in the coastal zone (see fig.11 and 12 respectively), is comparable with the situation of control run. This reflects a similar downslope momentum balance in this area.

5 On air-sea interactions in Antarctic coastal zone

5.1 Introduction

Observations and model studies reveal that katabatic wind is very strong on the steepest slopes of the Antarctic ice sheet. When katabatic flow passes the coastline, it is found (André, 1987, Kurtz and Bromwich, 1985, Gallée and Schayes, 1988) that the winds weaken rapidly offshore. Althought the simulated katabatic wind speed is less important than the observed one in some places of Antarctica (Adélie Land, Terra Nova Bay,...), it is obvious from recent studies (Pease, 1987, Ou, 1988) that an offshore wind $u = 10\ m.s^{-1}$ is sufficient to maintain in the coastal zone a water area free of ice (polynia).

In this section the importance of the air-sea interactions in the coastal zone is investigated. Three cases are considered : (i) the Antarctic ocean is covered by sea ice, (ii) the Antarctic ocean is free of sea ice, and (iii) a small polynia is localized near the coast.

The first situation was already analysed (Gallée and Schayes, 1988) : the downslope momentum forces analysis which is made of simulated steady state katabatic flow, shows the importance of the reversal of the pressure gradient force in the coastal zone, causing the sudden decay of katabatic winds when they pass the coastline. The development of the reversal pressure gradient force occurs in areas where the slope becomes very small. The slope decay causes the katabatic wind to be less strong, with then the pilling up of the cold air and a dramatic local increase of the depth of the flow, generating the reversal

pressure gradient force.

The second situation can occur in some places in Antarctica at the end of austral summer. For such ideal case, it is expected that strong heat exchanges will occur between the relatively warm ocean and the very cold katabatic air. This is important for the atmospheric circulation and the sea ice formation. It is expected that the heating of the cold katabatic air by the warm ocean could influence the pressure field in the coastal zone and possibly destroy the reversal pressure gradient force. The heat exchanges also affect strongly the open ocean, because the temperature of the sea water column in the Antarctic coastal zone is no far from the freezing point (Zwally and Comiso, 1985). The consequence of it is that the heat losses cause a hight amount of small ice crystals (frazil) to form on the water surface. Then the wind-generated sea water circulation herds the frazil crystals together into long plumes of grease ice running parallel to the surface winds (Cavalieri and Martin, 1985). The frazil is thus advected downwind and is solidified farer seawards, with as result the maintenance of an open water area near the coast. This open water area is called a polynia[2]. Since the total frazil production is area dependant, the polynia must reach a size at which it is producing enough ice to maintain a steady state balance with the seaward advection of the solidified ice. To simulate the polynia evolution, a time dependant model of a wind-driven coastal polynia is developped. Then this model is forced with the output of the atmospheric model.

Many polynias are present along the Antarctic coast (Cavalieri and Martin, 1985). The purpose of the third run of the atmospheric model is the simulation of this frequent case. For this run, the fixed open water width is chosen to be consistent with the results of the simulation of the polynia model.

The polynia model is presented in the next subsection and some comments about the simulations are made in subsection 3.

[2]The shape of a polynia, which may be approximated by a rectangle or an ellipse, is in contrast to the long, broken linear shape of a lead.

5.2 Development of a time dependant model of a coastal polynia

The horizontal one-dimensional polynia model which is developped in the present section is similar to the time-dependant model of Ou (1988) and is improved to take into account the spatial variations of the atmospheric variables over the polynia. Let be u_A the component of the wind directed perpendicular to the coastline from land to sea. For the purpose of coupling between the polynia model and the atmospheric model, u_A is taken as the u component of the wind at 10 m height. The heat loss to the atmosphere from the open ocean causes production of the frazil ice (at a rate P), which is "herderd" downwind at a surface drift speed u_W. In the mean time, the consolidated ice is advected offshore at the ice drift speed u_I. For simplicity, assume that (Ou, 1988) :

$$u_I \simeq .02\overline{u_A}$$

$$u_W(x) \simeq .035 u_A(x)$$

where $\overline{u_A} = \int_l^{l+l_I} u_A(x)dx$, with l_I the characteristic length scale behond which internal ice stress can be neglected. The value $l_I = 40\ km$ seems reasonable. The coordinate $x = l$ (measured from the coast) specifies the position of the ice edge. Let be h the amount of grease ice contained in a water parcel (of unit surface area). The conservation equation of h in the polynia can be written :

$$\frac{\partial h}{\partial t} = P(x) - u_W(x)\frac{\partial h}{\partial x} \tag{42}$$

where the ice production rate P is computed as follows :

$$P = \frac{H_A - H_W}{L_{fi}}$$

with H_A the total heat flux towards the atmosphere. H_W is the heat flux which must be loss by the ocean until the sea water temperature reaches the freezing point :

$$H_W = -h_W \frac{\partial}{\partial t}(\rho_W C_W T_{fi})$$

Indeed when sea ice forms, the increasing water salinity due to salt rejection in the water column h_W modifies the sea water characteristics :

(i) the freezing temperature T_{fi} of sea water decreases (Danard et al., 1984) :

$$T_{fi} = 273.16 - 10^{-3}(3 + 53.75 S_W + 0.04 S_W^2 + 0.00004 S_W^3)$$

where S_W $[g.kg^{-1}]$ is the sea water salininity.

(ii) The density of sea water increases (Mamayev, 1975) :

$$\rho_W = 1028.52 - 0.0735\ T - 0.00469\ T^2 + (0.802 - 0.002\ T)(S_W - 35)[kg.m^{-3}]$$

Let remark that ρ_W is also a function of the sea water temperature $T[^oC]$.

(iii) The specific heat of sea water decreases (Fofonoff, 1962) :

$$C_W = C_W^0(T') - 5.075\ S_W - 1.4\ 10^{-2}\ S_W^2 [J.kg^{-1}.K^{-1}]$$

with $T' = T + 0.7\ S_W + 0.0175\ S_W^2$

and $C_W^0(T') = 4178.4 + (8.46 + 26.19\ e^{-0.048\ T'})\ 10^{-3}(T' - 33.67)$.

The latent heat of freezing of sea water is also a function of salinity :

$$L_{fi} = 333.9(1. - 0.001\ S_I - \frac{S_I}{S_W}(1 - 0.001\ S_W)$$

where S_I is the sea ice salinity. For frazil ice grown in salt water of salinity $S_W = 34\ g.kg^{-1}$, $S_I = 10\ g.kg^{-1}$ is a mean value (Cavalieri and Martin, 1985).

To derive the flux balance at the ice edge, consider a control volume (the dashed box in the fig.13) encompassing the ice edge where active collection and solidification of frazil occur. The flux balance, viewed from the moving frame affixed to the ice edge, states that

$$h_I(u_I(l) - \frac{dl}{dt}) = h(l)(u_W(l) - \frac{dl}{dt}) \tag{43}$$

where h_I is the thickness of the consolidated ice exiting from the control volume. Parameterization of h_I requires some understanding of the frazil collection process at the ice edge.

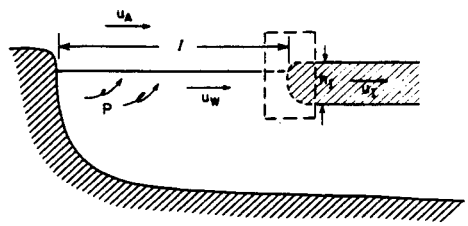

Figure 13: *A schematic of a coastal polynia driven by an offshore wind (u_A). The frazil ice is produced in the open ocean at a rate P and herderd downwind at the surface drift speed u_W while the consolidated ice is advected offshore at the ice drift speed u_I. The dashed box indicates the control volume encompassing the ice edge which has a coordinate l (measured from the coast). h_I is the thickness of the consolidated ice eziting the control volume (from Ou, 1988)*

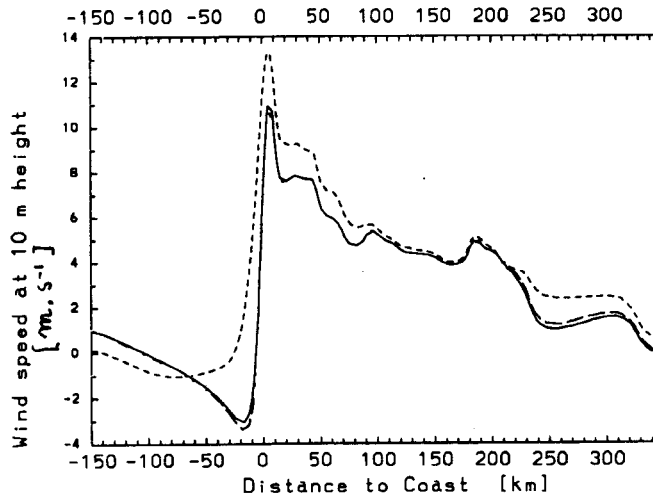

Figure 14: *u (positive seaward), at 10 m above the surface, as a function of distance to coast.*

——— : Ocean covered by sea ice
- - - - - - - : Ocean free of sea ice
— — — — — : Presence of a polynia (4 *km* width)

Although there have been laboratory experiments (Martin and Kauffman, 1981) and model studies (Bauer and Martin, 1983) of the grease ice growth in small leads, their results are not directly applicable to polynia where the collection process seems to be quite different (Ou, 1988). Consequently, the frazil collection thickness is taken to be constant. A reasonable value of $h_I = .1\ m$ is chosen for the present study (Pease, 1987). The horizontal discretization of the model is $\triangle x = 200\ m$ and the time step $\triangle t = 360\ s$ is such that the Courant-Friedrich-Levy criterion is satisfayed. The model is tested for a simple situation (i.e. u_A, P are constant) for which the simulated regime is in fairly good agreement with previous studies (Pease, 1987; Ou,1988).

5.3 Air-Sea interaction between katabatic flow and ocean

For the purpose of this study, katabatic winds are simulated over a realistic terrain profile in Adélie Land (Antarctica) extending from the sea level to 2400 m height 350 km inland. The oceanic domain extend over 150 km and is covered by sea ice (simulation $P1$), or free of sea ice (simulation $P2$), or covered by sea ice excepted in a small coastal polynia (size : 4 km), (simulation $P3$). The horizontal grid spacing is $\triangle x = 2\ km$ and the time step $\triangle t = 4\ s$ for each run. The results presented here are obtained after the model reaches steady state (i.e., after 15 hour simulation). The wind speed at 10 m above the surface is displayed on fig.14. for the three simulations, over continent and ocean.

Table II gives a comparaison between simulation $P1$,$P2$ and $P3$ for the heat fluxes in the surface layer for the coastal grid point. When ocean is free of ice, the sensible heat transfer from the ocean to the atmosphere is large. This is due to the strength of the wind ($V_{10m} = 6.9$ and $11.7\ m.s^{-1}$ for simulations $P1$ and $P2$ respectively) and to the temperature difference between the cold air and the warm ocean. The latent heat flux increase from simulation $P1$ to $P2$ is less important than the sensible heat flux increase because of the low saturated water vapor pressure in Antarctica. The total heat loss per

Table II: Vertical heat fluxes in the coastal surface layer (positive upward)

$W.m^{-2}$	simulation $P1$	simulation $P2$	simulation $P3$
net I.R.	65.	133.	145
sensible	-52.	308.	307
latent	0.	124.	84
total	13.	565.	536

unit area from the coastal open ocean is 565 $W\ m^{-2}$. Thus the large differences in the wind regime between simulation $P1$ and $P2$ can be explained by the destruction of the wall of cold katabatic air by the heating from the relatively warm sea water over the whole oceanic domain.

On the other hand, there are no significant differences between simulation $P1$ and $P3$ because the open water area is too small to allow a sufficient heating of the cold air coming from the continent, so that the decay of the katabatic wind is comparable for both situations. On fig.15 are shown for simulation $P2$ the wind speed u_A, the ice production rate P and the ratio $\frac{P}{u_A}$, as a function of the distance from the coast. It can be seen that the ratio of $\frac{P}{u_A}$ is independant of x, excepted where $\mid u_A \mid \simeq 0$ so that it is primarily a function of air temperature when the wind speed is not too small. The output of the atmospheric model for simulation $P2$ is then used to force the polynia model. The initialization of the polynia model is done by observing that the polynia width must be bounded by the offshore extent of the katabatic wind. At initial time it is assumed that the polynia is free of grease ice ($h(x) = 0$), and that $S_W = 34\ g.kg^{-1}$, which is a typical value for the Antarctic summer shelf water (Cavalieri and Martin, 1985). Assuming no variation in the atmospheric variables[3], the evolution of the polynia width l, the ice drift u_I and the amount of ice contained in a water parcel arriving at the ice edge $h(l)$ are shown on fig.16.

[3]For the present study, the strength of the sea ice breeze flow increases when the ocean becomes recovered

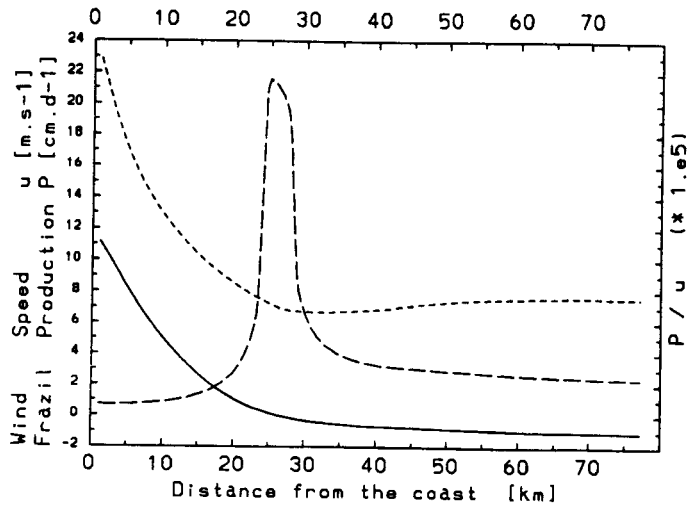

Figure 15: *Simulated characteristics of the forcing of open ocean by the atmosphere, as a function of distance to coast :*

——— : u_A (positive seaward)
- - - - - - - : Frazil production rate P
— — — — — : ratio $\frac{P}{|u_A|}$

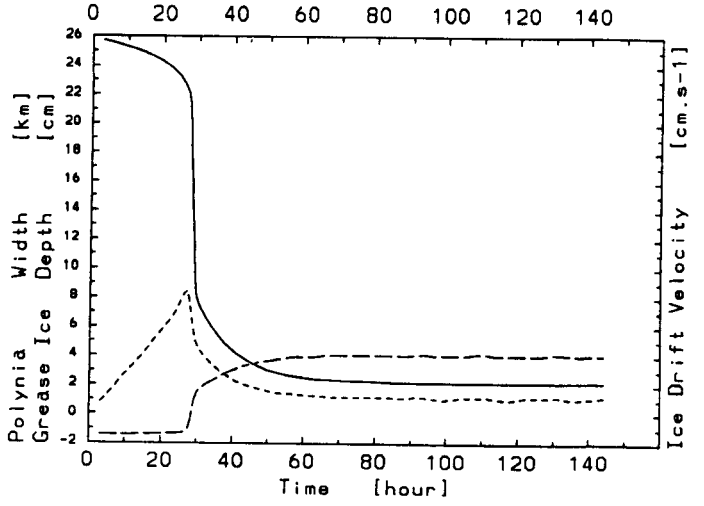

Figure 16: *Simulated characteristics of the polynia evolution, as a function of time :*

——— : polynia width l
- - - - - - - : amount $h(l)$ of ice contained in a water parcel arriving at the ice edge
— — — — — : ice drift velocity u_I

It can be seen that during the first day, $h(l)$ increases but is not important enought so that the polynia width depends mainly on the sea ice drift which is directed towards the coast. After this first stage an important reduction of the polynia area is simulated. This second stage happens when the grease ice thickness reaches the critical value $h \simeq h_I$. During the second stage, the solidified ice comes closer to the coast and is thus influenced by the katabatic wind, so that the ice drift becomes directed from land to ocean. Finally the regime result from the balance between grease ice production and ice drift. During the regime stage, the polynia width is 2.2 km. The salinity variation computed by the polynia model and averaged over the polynia area is $\frac{\partial S_W}{\partial t} = 0.0109\ g.kg^{-1}.day^{-1}$. Following Cavalieri and Martin, the shelf water salinity must be greater than $S_W = 34.63\ g.kg^{-1}$ for bottom water formation to occur. The present polynia simulation indicates that it would require 2 $month$.

6 Conclusions

Katabatic wind is a noticeable atmospheric phenomenon, especially in Antarctica, where the conditions required for its onset are present during the most part of the year. Its impact on the atmosphere-ocean interactions in the polar regions of the Southern Hemisphere must be emphasized, because the strength of the wind is sufficient to maintain open water area at some places near the coast. The aim of the present work was to provide a first approach to the study of these processes.

The dynamics of katabatic winds were first studied and a primitive equation model was simulated in the conditions of the Antarctic coastal zone. The results give indications

by sea ice, so that the polynia cannot maintain. Nevertheless, the observations in Terra Nova Bay support strong evidence of the presence of a polynia forced by katabatic winds during the whole Antarctic winter, so that the present assumption of no variation of the atmospheric variables gives a first guess of what are the effects of sea air interactions for this case

about the physical mechanisms which are responsible of the sudden variations of katabatic wind at the end of the ice sheet slope. It is shown that the variations of the depth of the katabatic layer just before the coastline play a key role for the persistance of the wind speed and direction. The evolution of the depth of the katabatic layer is governed mainly by the rate of entrainment of upper relatively warmer air, on acceleration leading to a shallower katabatic layer and on deceleration causing the accumulation of katabatic air. When the increase of the flow depth is sufficient, a positive feedback occurs at the coastline, with a further dramatic increase and the onset of a counter flow on sea. Although the hydrostatic assumption was used, it is not surprising to simulate such phenomenon, because the cause and consequense of it can be understood as hydrostatic mechanisms. On the other hand, the sharp transition which is observed between upwind and downwind conditions is non hydrostatic, and further work must be done to give a complete description of it. It must be also emphasized the ideal conditions of such circulation :

(i) its two-dimensional character precludes the simulation of the confluence zones and thus a realistic simulation of the extraordinary katabatic winds which are observed at least in some places of Adélie Land and in Terra Nova Bay.

(ii) The influence of embedded drift snow is not taken into account. As already shown by Kodama et al (1985), the effect of blowing snow is to increase the downslope pressure gradient force by an additional contribution due to the density of the snow and the sublimation of snow particles. Nevertheless this effect becomes important only for strong winds (i.e. wind speed greater than $\simeq 12\ m.s^{-1}$).

Second, sea air interactions in the Adélie Land coastal zone were simulated in the case of katabatic winds simulated by the atmospheric model. A polynia model was developped. It was simulated with as input the momentum and heat fluxes computed by the atmospheric model, for which an ocean free of see ice was chosen as surface boundary condition. When the forcing is taken to be constant, results show that the polynia remains open and that salt rejection in the water column is sufficient to form deep sea water there. Nevertheless, when

the polynia is again forced by the atmospheric model with consistent surface boundary conditions, sea ice is drifted further to the coastline. This is explained by the strengthening of the sea ice breeze when sea ice cover increases. It is possible that such situation occurs in some places of Antarctica, where no polynia is observed, even when katabatic wind is blowing.

But it must also be pointed out that the sea ice dynamics are crudely estimated : the time lag between the wind forcing and the sea ice response is neglected and the internal ice stress is not included. An other simplification is that the effects of oceanic currents are neglected. This can be important for the polynia evolution because sea ice advection is also constrained by the water stress at the ice-ocean interface and sea ice advection is one of the two basic forcings which determine the position of the sea ice edge. One must also point out that the fresh water advection by the oceanic current in the area of large salt rejections also could delay the onset of deep sea water formation.

7 Applications

Although the present study seems to be restricted to a very particular zone of Antarctica, its implications in other domains of interest may not be neglected.

A first consequence of it is the development of a numerical tool particularly easy to handle and which allows a better understanding of model parameters which must be used in Antarctic katabatic winds simulations. This is interesting for the development of more complex mesoscale atmospheric models which are much more difficult to implement (i.e. because of their computational time costs and mainly because of the enormeous time they require to analyse the results). This is also the case for atmospheric general circulation models (AGCM) for which the simulation of Antarctic present climate is quite difficult. This is due to the fact that katabatic winds must be considered as subgrid scale phenomena in AGCM so that they must be parameterized. The development of such paramaterization

for AGCM could be easely tested with mesoscale models.

But a better knowlegde of the modeling of slope winds in the atmosphere could also give some indications of how to simulate similar circulations in the ocean, especially the density currents along the continental shelf. This is particularly true for the deep sea water formation in the Antarctic coastal zone.

An other consequence of the development of a mesoscale model for the purpose of study of Antarctic katabatic winds is a better understanding of the meteorological conditions during the Antarctic polar night. Meteorological observations are difficult to do because of the extreme cold conditions and a mesoscale model could be a valuable tool to fulfill the severe lack of observations. The present knowledge also allows a more efficient study of other frequent mesoscale circulations in Antarctica, especially the mountain barrier winds, which blow for example in the Weddel Sea along the Antarctic peninsula.

Acknowledgments

The authors wish to thank Prof. J.Neumann and Prof. P.Alpert (Tel Aviv University) for providing us with an initial version of the mesoscale atmospheric model, and for stimulating comments and suggestions during their visits to the Institut d'Astronomie et de Géophysique G. Lemaître in Louvain-la-Neuve. We also thank Dr. J.Cl.André and Dr. P.Pettré for useful discussions at the Centre National de la Recherche Météorologique, Toulouse, France. Valuable comments and suggestions on this work were received from Prof. V.Ramanathan (University of Chicago). This research is sponsored by the Belgian Program "Scientific research on the Antarctic" (Services of the Prime Minister - Science Policy Office) under contract ANTAR03.

8 References

Adachi T.: 1979, 'Numerical Simulation of Katabatic Wind Profile at Syowa Station, Antarctica' *Antarctic Record* **67**, 64-74.

Alpert P., Cohen A. and Neumann J.: 1980, 'On the Sigma Coordinate System', *Contrib. 80-5 to the Hebrew University of Jerusalem, Dept. of Atmosph. Sci.*, 25 pp.

Alpert P.: 1981, 'Implicit Filtering in Conjonction with Explicit Filtering', *J Computational Phys* **44**, 212-219.

Alpert P., Cohen A., Neumann J. and Doron E.: 1982, 'A Model Simulation of the Summer Circulation from the Eastern Mediterranean Past Lake Kinneret in the Jordan Valley', *Mon Wea Rev* **110**, 994-1006.

Alpert P. and Neumann J.: 1984, 'On the Enhanced Smoothing over Topography in some Mesometeorological Models', *Boundary Layer Meteorol.* **30**, 293-312.

André J.-Cl., Wendler G. and Zéphoris M.: 1986, 'The "IAGO- Katabatic" Programme.', *Antarctic Climate Research* **1**, 17-18.

André J.-Cl.: 1987, 'Des chercheurs dans le vent : vous avez dit blizzard ?', *La Recherche* **18**, 1254-1256.

Bornstein R.D.: 1975, 'The Two-Dimensional URBMET Urban Boundary Layer Model', *J Appl Meteor* **14**, 1459-1477.

Cavalieri D.J. and Martin S.: 1985, 'A Passive Microwave Study of Polynias Along the Antarctic Wilkes Land Coast', *Oceanology of the Antarctic Continental Shelf, Antarctic Research Series* **43**, 227-251.

Danard M., Gray M. and Lyv G.: 1984, 'A Model for Predicting Ice Accretion and Ablation in Water Bodies', *Mon Wea Rev* **112**, 1160-1169

Deardorff J.W.: 1978, 'Efficient Prediction of Ground Surface Temperature and Moisture with Inclusion of a Layer of Vegetation', *J Geophys Res* **83**, 1889-1903.

Fofonoff N.P.: 1962, 'Physical Properties of Sea-Water', *The Sea* **1**, John Wiley & Sons, 3-30.

Gadd A.J.: 1978, 'A Split Explicit Integration Scheme for Numerical Weather Prediction', *Quart.J.R.Met.Soc.* **104**, 569-582.

Gallée H.: 1985, 'Application to the Belgian Coast of a 2- Dimensional Primitive Equation Model Using σ-Coordinate', *Air Pollution Modeling and its application IV*, De Wispelaere C. (Ed.) Plenum Press, 359-374.

Gallée H., Berger A., Marsiat I., Fichefet T., Schayes G. and Tricot C.: 1987, 'A Study of Antarctic Katabatic Winds, Scientific Report of the Institut d'Astronomie et de Géophysique G. Lemaître: 1987/3, 41 p.

Gallée H., Schayes G., Tricot C. and Berger A.,: 1988, 'A Simulation of Katabatic Winds in the Antarctic Coastal Zone', *Proceedings of the Belgian National Colloquium on Antarctic Research*, Prime Minister's Services - Science Policy Office (Ed.), 241-260.

Gallée H. and Schayes G.: 1988, 'Dynamical Aspects of the Katabatic Winds Evolution', submitted to *Boundary Layer Meteorol.*

Holton J.R.,: 1972, 'An Introduction to Dynamic Meteorology', *Acad Press*, 319 pp.

Kodama Y., Wendler G. and Gosink J.,: 1985, 'The Effect of Blowing Snow on Katabatic Winds in Antarctica', *Annals of Glaciology* **6**, 59-62.

Kodama Y. and Wendler G.: 1986, 'Wind and Temperature Regime Along the Slope of Adélie Land, Antarctica', *J Geophys Res* **91**, 6735-6741.

Kurtz D.D. and Bromwich D.H.: 1985, 'A Recurring, Atmospherically Forced Polynia in Terra Nova Bay', *Oceanology of the Antarctic Continental Shelf, Antarctic Research Series* **43**, 177-201.

Lalaurette F. and André J.Cl: 1985, 'On the Integral Modelling of Katabatic Flows', *Boundary Layer Meteorology* **33**, 135-149.

Louis J.-F.: 1979, 'A Parametric Model of Vertical Eddy Fluxes in the Atmosphere', *Boundary Layer Meteorology* **17**, 187-202.

Manins P.C. and Sawford, B.L.: 1979, 'A Model of Katabatic Winds', *J.Atmos.Sci.* **36**, 619-630

Mahrt L.: 1982, 'Momentum Balance of Gravity Flows' *J.Atmos.Sci.* **39**, 2701-2711.

Mahrt, L. and Larsen, S.: 1982, 'Small Scale Drainage Front', *Tellus* **34**, 579-587.

Mamayev O.I.: 1975, 'Temperature-Salinity Analysis of World Ocean Waters', *Elsevier Oceanology Series* **11**, Elsevier, 39-44

Mather K.B. and Miller G.S.: 1967, 'Notes on Topographic Factors Affecting the Surface Wind in Antarctica, with Special Reference to Katabatic Winds, and Bibliography', *Technical Report of the University of Alaska*, 63 pp.

Miller M.J. and Thorpe A.J.: 1981, 'Radiation Conditions for the Lateral Boundaries of Limited Area Numerical Models', *Quart.J.R.Met.Soc.* **107**, 615-628.

Nappo C.J. and K.S. Rao: 1987, 'A Model Study of Pure Katabatic Flows', *Tellus* **39A**, 61-71.

Oort A.H.,: 1983, 'Global Atmospheric Circulation Statistics: 1958-1973', *NOAA professionnal paper* **14**, 180 pp.

Orlanski I.: 1976, 'A Simple Boundary Condition for Unbounded Hyperbolic Flows', *J Computational Phys* **21**, 251-269.

Ou H.W.: 1988, 'A Time-Dependant Model of a Coastal Polynia', *J Phys Ocean* **18**, 584-590

Parish T.R.: 1984, 'A Numerical Study of Strong Katabatic Winds over Antarctica', *Mon Wea Rev* **112**, 545-554.

Parish T.R. and Waight K.T.: 1987, 'The Forcing of Antarctic Katabatic Winds', *Mon Wea Rev* **115**, 2214-2226

Pease C.H.: 1987, 'The Size of Wind-Driven Coastal Polynias', *J Geophys Res* **92**, 7049-7059

Pielke R.A.: 1984, 'Mesoscale Meteorological Modeling', *Acad Press*, 612 pp.

Sasamori T.: 1968, 'The Radiative Calculation for Application to General Circulation Experiments', *J Appl Meteorol* **7**, 721-729

Schwerdtfeger W.: 1984, 'Weather and Climate of the Antarctic', *Developments in Atmospheric Sciences* **15**, Elsevier, 261 pp.

Zwally H.J., Comiso J.C. and Gordon A.L.: 1985, 'Antarctic Offshore Leads and Polynias and Oceanographic Effects', *Oceanology of the Antarctic Continental Shelf, Antarctic Research Series* **43**, 203-226.

Appendix : On the Parameterization of the Subgrid Scale Terms in a Terrain Following Coordinate Mesoscale Model

.1 The parameterization of subgrid Scale Fluxes

.1.1 Development of an expression for the divergence of the subgrid scale fluxes

In the σ system, the conservation equations of momentum can be written, neglecting molecular viscosity effects and assuming homogeneity in the y-direction[1] :

$$\frac{\partial u}{\partial t} = -u\frac{\partial u}{\partial x} - \dot{\sigma}\frac{\partial u}{\partial \sigma} + f(v - v_g) - \frac{\partial \phi}{\partial x}\,|_p \tag{1}$$

$$\frac{\partial v}{\partial t} = -u\frac{\partial v}{\partial x} - \dot{\sigma}\frac{\partial v}{\partial \sigma} - f(u - u_g) \tag{2}$$

where

$$\sigma = \frac{p - p_t}{p_*}$$

p is the pressure, p_t refers to the pressure at the top of the model, p_s is the surface pressure and $p_* = p_s - p_t$

x is the horizontal offshore (positive southward) axis, y is the horizontal onshore (positive eastward) axis, t is time, u, v and $\dot{\sigma}$ are respectively the southward, eastward and σ components of the wind , f is the Coriolis parameter, $\vec{V_g} = (u_g, v_g)$ is the geostrophic wind, $\phi = gz$ is the geopotential, g is gravity, z is altitude, $|_p$ means that the pressure gradient force $-\frac{\partial \phi}{\partial x}$ is calculated on an isobaric surface. This avoids its development into the sum $-\frac{R_a T}{p_* + \frac{p_t}{\sigma}}\frac{\partial p_*}{\partial x} - \frac{\partial \phi}{\partial x}\,|_\sigma$ which leads to severe truncation errors on steep topography (Alpert et al, 1982). Note that the molecular viscosity effects have been neglected.

[1] It is easy to generalize the following developments when there is no homogeneity in the y-direction

Numerical resolution of these equations on computer system requires, of course, to discretize the integration domain over specified time step and grid intervals. It is thus necessary to average the conservation equations over these intervals. In performing this averaging, it is convenient to perform the following decomposition on the dependant variables (Pielke, 1984) :

$$\psi = \overline{\psi} + \psi' \tag{3}$$

where $\overline{\psi}$ represents the average of ψ over a finite time increment $\triangle t$ and space intervals $\triangle x$, $\triangle y$, $\triangle \sigma$. The variable ψ' is the deviation of ψ from the average and is often called a subgrid scale perturbation. Performing[2] the averaging process yields (Alpert et al., 1980) :

$$\frac{\partial \overline{u}}{\partial t} = -\overline{u}\frac{\partial \overline{u}}{\partial x} - \overline{u'\frac{\partial u'}{\partial x}} - \dot{\overline{\sigma}}\frac{\partial \overline{u}}{\partial \sigma} - \overline{\dot{\sigma}'\frac{\partial u'}{\partial \sigma}} + f(\overline{v} - v_g) - \frac{\partial \overline{\phi}}{\partial x}\,|_p \tag{4}$$

$$\frac{\partial \overline{v}}{\partial t} = -\overline{u}\frac{\partial \overline{v}}{\partial x} - \overline{u'\frac{\partial v'}{\partial x}} - \dot{\overline{\sigma}}\frac{\partial \overline{v}}{\partial \sigma} - \overline{\dot{\sigma}'\frac{\partial v'}{\partial \sigma}} - f(\overline{u} - u_g) \tag{5}$$

The subgrid scale terms $-\overline{u'\frac{\partial u'}{\partial x}}$, $-\overline{\dot{\sigma}'\frac{\partial u'}{\partial \sigma}}$, $-\overline{u'\frac{\partial v'}{\partial x}}$ and $-\overline{\dot{\sigma}'\frac{\partial v'}{\partial \sigma}}$ are unknown and must be parameterized in terms of known quantities. In the rectangular coordinate system x, y, z the decomposition of the subgrid scale terms into vertical and horizontal components is necessitated for major reasons :

i) the horizontal grid spacing $\triangle x$ is much larger than the vertical spacing $\triangle z$, so that the parameterizations of subgrid scale mixing in the horizontal and vertical directions would be expected to be different and

ii) much more is known about the functional form of the vertical subgrid scale fluxes than of horizontal subgrid scale fluxes : the first one can be parameterized on the physical basis of vertical turbulence but the parameterization of the latter needs to take into account other subgrid scale processes than horizontal turbulence and can be constrained by numerical stability criteria.

[2]The following developments must also be made for the thermodynamic energy and specific humidity conservation equations.

In the terrain-following coordinate σ system when

$$\frac{\partial \sigma}{\partial x} |_z \ll \frac{\partial \sigma}{\partial z} |_z$$

it should be desirable to retain this separation into vertical and horizontal components. This will now be done for the momentum conservation in the x direction. To pursuit this goal, it is customary to write the subgrid scale terms in the flux form of the momentum equation. This is obtained first by multiplying the equation of mass conservation by u and averaging to get :

$$\overline{u}\frac{\partial \overline{p}_\star}{\partial t} = -\overline{u\frac{\partial p_\star u}{\partial x}} - \overline{u\frac{\partial p_\star \dot{\sigma}}{\partial \sigma}} = 0. \tag{6}$$

Then multiplying the momentum equation by $p_\star$, averaging and summing both equations :

$$\frac{\partial \overline{p}_\star \overline{u}}{\partial t} = -\frac{\partial \overline{p}_\star \overline{u}\overline{u}}{\partial x} - \frac{\partial \overline{p}_\star \overline{u'u'}}{\partial x} - \frac{\partial \overline{p}_\star \overline{\dot{\sigma}}\overline{u}}{\partial \sigma} - \frac{\partial \overline{p}_\star \overline{\dot{\sigma}'u'}}{\partial \sigma} + \overline{p}_\star f(\overline{v} - v_g) - \overline{p}_\star \frac{\partial \overline{\phi}}{\partial x} |_p = 0. \tag{7}$$

where it is taken into account that $p_\star \simeq \overline{p}_\star$ and $\phi \simeq \overline{\phi}$ (Alpert et al.,1980). This last equation is called the flux form equation and $-\overline{p}_\star \overline{u'u'}$ and $-\overline{p}_\star \overline{\dot{\sigma}'u'}$ are called the subgrid scale fluxes. Multiplying the averaged form of the mass conservation equation by $\overline{u}$ and substracting the result from the flux form equation one gets :

$$\frac{\partial \overline{u}}{\partial t} = -\overline{u}\frac{\partial \overline{u}}{\partial x} - \frac{1}{\overline{p}_\star}\frac{\partial \overline{p}_\star \overline{u'u'}}{\partial x} - \overline{\dot{\sigma}}\frac{\partial \overline{u}}{\partial \sigma} - \frac{1}{\overline{p}_\star}\frac{\partial \overline{p}_\star \overline{\dot{\sigma}'u'}}{\partial \sigma} + f(\overline{v} - v_g) - \frac{\partial \overline{\phi}}{\partial x} |_p = 0. \tag{8}$$

where

$$F_x = -\frac{1}{\overline{p}_\star}\frac{\partial \overline{p}_\star \overline{u'u'}}{\partial x} - \frac{1}{\overline{p}_\star}\frac{\partial \overline{p}_\star \overline{\dot{\sigma}'u'}}{\partial \sigma} \tag{9}$$

is the divergence of the subgrid scale fluxes. It must now be noted that the vertical subgrid scale fluxes contain the expression $\overline{u'\dot{\sigma}'}$ and not $\overline{u'w'}$. It is of interest to find relationships between these quantities. First note that in the σ system, if the terrain slope is not too large (Pielke, 1984, his p.120) :

$$|\frac{\partial \sigma}{\partial x}| \ll |\frac{\partial \sigma}{\partial z}|$$

Then the expression of the hydrostatic assumption is very simple[3] and

$$w = \frac{dz}{dt} = \frac{1}{g}\frac{d\phi}{dt} = \frac{1}{g}(\frac{\partial\phi}{\partial t} + u\frac{\partial\phi}{\partial x} - \frac{p_*\dot{\sigma}}{\rho g}) \tag{10}$$

In order to obtain simple relationships between vertical subgrid scale fluxes in the rectangular coordinate system and in the σ system, the two following approximations have been made (Alpert and Neumann, 1984) :

(i) Taking that the local variation of the geopotential is small :

$$w \simeq \frac{1}{g}u\frac{\partial\phi}{\partial x} - \frac{p_*\dot{\sigma}}{\rho g} \tag{11}$$

(ii) Performing the same decomposition of the dependant variables as previously, it is presumed that in regions of topography the term $|\ \frac{\partial\overline{\phi}}{\partial x}\ |$ is larger than $|\ \frac{\partial\phi'}{\partial x}\ |$. And one gets :

$$\overline{u'\dot{\sigma}'} = \frac{\rho g}{p_*}[-\overline{u'w'} + \overline{u'u'}\frac{\partial\overline{z}}{\partial x}] \tag{12}$$

where the Austausch formulation yields :

$$\overline{u'w'} = -K_v\frac{\partial\overline{u}}{\partial z} \tag{13}$$

A convenient way for the expression of the "horizontal" subgrid scale flux in the x direction is the use of an eddy exchange coefficient. This is done in the rectanglar coordinate system (because $\tilde{u} = u$)[4] and then transformed into the σ system[5] :

$$\overline{u'u'} = -K_H\frac{\partial\overline{u}}{\partial x}\ |_z = -K_H(\frac{\partial\overline{u}}{\partial x}\ |_\sigma + \frac{\partial\sigma}{\partial x}\frac{\partial\overline{u}}{\partial\sigma}) \tag{14}$$

---

[3] $|\ \frac{\partial\sigma}{\partial x}\ | \ll |\ \frac{\partial\sigma}{\partial z}\ | \Longrightarrow |\ \frac{\partial p}{\partial x}\ | \leq |\ \frac{\partial p}{\partial\sigma}\ | \Longrightarrow \frac{\partial\phi}{\partial\sigma} \simeq -\frac{p_*}{\rho}$

[4] The notation $\tilde{u}$, if it used, refers to the σ system. The notation u compared to the notation $\tilde{u}$ then refers to the rectangular coordinate system or z system

[5] An other way to proceed is to express directly $\overline{u'u'}$ in the σ system by

$$\overline{u'u'} = -\tilde{K}_H\overline{u}_{;x} = -\tilde{K}_H(\frac{\partial\overline{u}}{\partial x} + \Gamma^1_{x,i}\overline{u}_i) = -\tilde{K}_H(\frac{\partial\overline{u}}{\partial x})$$

where subscript i refers to the x, y and σ direction, $u_i = u, v, \dot{\sigma}$. $\Gamma^1_{x,i}$ is the Christoffel symbol. Repeated indices are summed (Pielke, 1984)

Finally after some algebra one gets :

$$F_x = \underbrace{\frac{1}{\overline{p}_\star}\frac{\partial}{\partial x}(\overline{p}_\star K_H \frac{\partial \overline{u}}{\partial x})}_{\text{A}} + \underbrace{\frac{g}{\overline{p}_\star^2}\frac{\partial}{\partial x}(\rho\alpha K_H \frac{\partial \overline{u}}{\partial \sigma})}_{\text{B}} + \underbrace{\frac{g}{\overline{p}_\star^2}\frac{\partial}{\partial \sigma}(\rho\alpha K_H \frac{\partial \overline{u}}{\partial x})}_{\text{C}}$$

$$+ \underbrace{\frac{\partial}{\partial \sigma}((\frac{\rho g}{\overline{p}_\star}\alpha)^2 K_H \frac{\partial \overline{u}}{\partial \sigma})}_{\text{D}} + \underbrace{\frac{\partial}{\partial \sigma}((\frac{\rho g}{\overline{p}_\star})^2 K_v)\frac{\partial \overline{u}}{\partial \sigma})}_{\text{E}} \qquad (15)$$

where $\alpha = \frac{\partial z}{\partial x}$. Term A is the horizontal diffusion on σ surfaces. Term E is the divergence of the vertical turbulent flux. Term B,C and D are correction terms.

.1.2 Discussion

As already pointed out, there is not up to now a satisfactory parameterization of the horizontal subgrid scale mixing in mesoscale models, so that the simplest classical Austausch formulation is chosen. Even with this formulation, it must be pointed out that the knowledge of the horizontal diffusion coefficient is very poor : because the horizontal grid distance is at least an order of magnitude larger than the vertical grid distance, not only turbulence but other physical processes and scales of motion would be involved in the grid scale transports, and this should be reflected in the magnitude of the horizontal diffusion coefficient. Moreover because of numerical stability constraints on the σ surfaces, the horizontal diffusion coefficient K_H is tuned until spurious waves do not degrade the numerical solution significantly (Pielke, 1984). The value of K_H needed by the numerical constraint is much more important than that approximated only on the basis of physical arguments. The consequence of this is that the use of a correction procedure involving the numerical tuning of K_H could leed to the destruction of the solution in the vertical. So the less bad solution to numerical stability constraint should be to work with a numerical smoother working on the σ surfaces. Nevertheless it is interesting to test the effect when realistic values of the horizontal diffusion coefficient are used (i.e. K_H ranging from 5 10^3 to 5 10^4 $m^2.s^{-1}$).

.1.3 Numerical resolution of the diffusion term when correction terms are included

A very stable semi-implicit scheme has been used here for the numerical resolution of the expression of the turbulent frictional force. The finite difference expression equivalent to the contribution of F_x to u takes the following form :

$$\frac{u_{i,k}^{n+1} - u_{i,k}^{n}}{\triangle t} = aF_{x,i,k}^{n} + bF_{x,i,k}^{n+1} \tag{16}$$

where subscript $i = 1, m$ refers to i^{th} horizontal grid point and the subscript $k = 1, l$ refers to k^{th} vertical level, with l the 10 m level and $l + 1$ the surface. n refers to the current time step and $n + 1$ to the next one. This means that in $F_{x,i,k}^{n+1}$ the values of $u_{i,k}^{n+1}$ are used and in $F_{x,i,k}^{n}$ the values of $u_{i,k}^{n}$ are used. The constant a and b are chosen such that

$$a + b = 1.$$

Developping and rearranging, one gets after a few algebra the following matrix system :

$$A_i U_{i-1} + B_i U_i + C_i U_{i+1} = D_i \tag{17}$$

with $i = 2, m - 1$ and where the form of the matrix D_i and U_i is :

$$D_i, U_i = \begin{pmatrix} d_{i,1}^{n} \\ d_{i,2}^{n} \\ \cdots \\ d_{i,k}^{n} \\ \cdots \\ d_{i,l}^{n} \end{pmatrix}, \begin{pmatrix} u_{i,1}^{n+1} \\ u_{i,2}^{n+1} \\ \cdots \\ u_{i,k}^{n+1} \\ \cdots \\ u_{i,l}^{n+1} \end{pmatrix} \tag{18}$$

A_i,B_i and C_i are tridiagonal matrix which form is :

$$A_i = \begin{pmatrix} a_{i,1,1} & a_{i,1,2} & 0 & 0 & 0 & 0 \\ a_{i,2,1} & a_{i,2,2} & a_{i,2,3} & 0 & 0 & 0 \\ 0 & a_{i,3,2} & a_{i,3,3} & a_{i,3,4} & 0 & 0 \\ \cdots & & & & & \\ 0 & 0 & 0 & 0 & a_{i,l,l-1} & a_{i,l,l} \end{pmatrix} \tag{19}$$

where the elements have the following form :

$$A_{i,k,k-1} = \frac{b \triangle t}{2 \triangle x} \frac{g(r_{i-1,k} + r_{i,k-1})}{p_{\star,i}(\sigma_{k+1} - \sigma_{k-1})}$$

$$A_{i,k,k} = \frac{b \triangle t}{\triangle x^2} \frac{p_{\star,i-\frac{1}{2}} K_{H,i-\frac{1}{2},k}}{p_{\star,i}}$$

$$A_{i,k,k+1} = -\frac{b \triangle t}{2 \triangle x} \frac{g(r_{i-1,k} + r_{i,k+1})}{p_{\star,i}(\sigma_{k+1} - \sigma_{k-1})}$$

$$B_{i,k,k-1} = b \triangle t \frac{1}{\sigma_{k+\frac{1}{2}} - \sigma_{k-\frac{1}{2}}} d_{i,k-\frac{1}{2}} \frac{1}{\sigma_k - \sigma_{k-1}}$$

$$B_{i,k,k} = -1 - \frac{b \triangle t}{\triangle x^2} \left(\frac{p_{\star,i+\frac{1}{2}} K_{H,i+\frac{1}{2},k}}{p_{\star,i}} + \frac{p_{\star,i-\frac{1}{2}} K_{H,i-\frac{1}{2},k}}{p_{\star,i}} \right) - \frac{b \triangle t}{\sigma_{k+\frac{1}{2}} - \sigma_{k-\frac{1}{2}}} \left(\frac{d_{i,k+\frac{1}{2}}}{\sigma_{k+1} - \sigma_k} + \frac{d_{i,k-\frac{1}{2}}}{\sigma_k - \sigma_{k-1}} \right)$$

$$B_{i,k,k+1} = b \triangle t \frac{1}{\sigma_{k+\frac{1}{2}} - \sigma_{k-\frac{1}{2}}} d_{i,k+\frac{1}{2}} \frac{1}{\sigma_{k+1} - \sigma_k}$$

$$C_{i,k,k-1} = -\frac{b \triangle t}{2 \triangle x} \frac{g(r_{i+1,k} + r_{i,k-1})}{p_{\star,i}(\sigma_{k+1} - \sigma_{k-1})}$$

$$C_{i,k,k} = \frac{b \triangle t}{\triangle x^2} \frac{p_{\star,i+\frac{1}{2}} K_{H,i+\frac{1}{2},k}}{p_{\star,i}}$$

$$C_{i,k,k+1} = \frac{b \triangle t}{2 \triangle x} \frac{g(r_{i+1,k} + r_{i,k+1})}{p_{\star,i}(\sigma_{k+1} - \sigma_{k-1})}$$

where

$$r_{i,k} = \rho_{i,k} \alpha_{i,k} K_{H,i,k}$$

$$d_{i,k} = \frac{g \rho_{i,k}}{p_{\star,i}} (\alpha_{i,k}^2 K_{H,i,k} + K_{v,i,k})$$

The elements of matrix D_i can be written :

$$D_{i,k} = -(1+\frac{a}{b})u_{i,k} - \frac{a}{b}(A_{i,k,k-1}u^n_{i-1,k-1} + A_{i,k,k}u^n_{i-1,k} + A_{i,k,k+1}u^n_{i-1,k+1}$$

$$+B_{i,k,k-1}u^n_{i,k-1} + B_{i,k,k}u^n_{i,k} + B_{i,k,k+1}u^n_{i,k+1}$$

$$+C_{i,k,k-1}u^n_{i+1,k-1} + C_{i,k,k}u^n_{i+1,k} + C_{i,k,k+1}u^n_{i+1,k+1})$$

The boundary conditions (i.e. $\frac{\partial \overline{u}}{\partial x} = -c\frac{\partial \overline{u}}{\partial t}$ for the lateral boundaries, $\frac{\partial \overline{u}}{\partial z} = 0$ for the top boundary $\sigma = 0$ and $u = u_0 = 0$ with $\overline{u'w'} = u^2_*$ for the surface boundary $\sigma = 1$) are introduced in the development. For example the lateral boundary condition $u_{1,k} = u_{2,k} - c\frac{\Delta x}{\Delta t}$ leeds to the corrections $B^{corr.}_{2,k,j} = A_{2,k,j} + B_{2,k,j}$, with $j = k-1, k$ or $k+1$ and $D^{corr.}_{2,k} = D_{2,k} - A_{2,k,k}c\frac{\Delta x}{\Delta t}$. A similar correction may be developped for the top boundary condition with $c = 0$. For the surface boundary condition, it is customary to replace the contribution

$$(\frac{\rho_{i,l+\frac{1}{2}}g}{p_{*,i}})^2 \frac{K_v}{\sigma_{l+1} - \sigma_l}(a(u_{0,i} - u^n_{i,l}) + b(u_{0,i} - u^{n+1}_{i,l}))$$

by

$$-\frac{\rho_{i,l+\frac{1}{2}}g}{p_{*,i}}\frac{u_{i,l}}{V_{i,l}}u^2_{*,i}$$

in the development of $F_{x,i,l}$. This leads to the correction :

$$D^{corr.}_{i,l} = D_{i,l} + \frac{\Delta t}{\sigma_{l+\frac{1}{2}} - \sigma_{l-\frac{1}{2}}}\frac{\rho_{i,l+\frac{1}{2}}g}{p_{*,i}}\frac{u_{i,l}}{V_{i,l}}u^2_{*,i}$$

The solution of this fully implicit scheme both in the $x-$ and $\sigma-$ direction involves a set of $(m-2) \times l$ algebraic simultaneous equations and it could be obtained by using an overrelaxation technique. But the convergence of the method may be slow or leeds to some errors, and the programmation of it on vectorized fast computers is not efficient. On the other hand the solution of the system by a matrix inversion technique, although it needs more algebraic operations, is solved exactly and in only one iteration. Moreover the vectorization of the code is very efficient, so that this technique is chosen for the present study.

Resolution of the matrix system : The matrix system which must be solved is thus :

$$A_i U_{i-1} + B_i U_i + C_i U_{i+1} = D_i$$

with for $i = 2$:

$$B_2 U_2 + C_2 U_3 = D_2$$

and for $i = m - 1$:

$$A_{m-1} U_{m-2} + B_{m-1} U_{m-1} = D_{m-1}$$

First compute

$$G_{m-1} = -(B_{m-1})^{-1} A_{m-1}$$

$$H_{m-1} = -(B_{m-1})^{-1} D_{m-1}$$

with $(B_{m-1})^{-1}$ the matrix inverse of B_{m-1}. Then

$$G_i = -Y_i A_i$$

$$H_i = -Y_i (D_i - C_i H_{i+1})$$

with

$$Y_i = (B_i + C_i G_{i+1})^{-1}$$

from $i = m - 2$ to $i = 2$, and finally

$$U_2 = H_2$$

$$U_i = H_i + G_i U_{i-1}$$

from $i = 3$ to $i = m - 1$.

.1.4 The numerical smoother

In the presence of the stable Antarctic atmosphere, especially near the surface, the katabatic flow will generate gravity waves propagating parallelly to the surface. On the other hand, the energy of the circulation on large scale waves is expected to cascade to

smaller length scales but this cascade is interrupted in the model because the smallest feature that can be resolved has a wavelength of two times the grid spacing (Pielke, 1984).

Expression of the "horizontal" subgrid scale correlation terms, if it is developped on a well known physical basis, must be sufficient to preclude the propagation of spurious waves. Nevertheless horizontal subgrid scale mixing is up to now poorly understood and its parameterization by a diffusive formulation in a mesoscale hydrostatic model for the purpose of Antarctic katabatic winds simulations seems non appropriate : to get simulations comparable with the observations, horizontal diffusion coefficient must be tuned behond its range of uncertainty.

A second method to remove the spurious waves consists in the use of a spatial smoother which removes the shortest waves, but leaves the longer ones relatively unaffected. The selective low-pass filter which is used is analysed by Alpert (1981). Its form is the following :

$$(1-\delta)\overline{\psi}_{i-1} + 2(1+\delta)\overline{\psi}_i + (1-\delta)\overline{\psi}_{i+1} = \psi_{i-1} + 2\psi_i + \psi_{i+1} \qquad (20)$$

where $i \pm 1 \rightarrow (i \pm 1) \triangle x$, ψ is the field to be smoothed and $\overline{\psi}$ is the smoothed field. δ is an arbitrarily chosen weighting parameter for the smoothed values.

The filter is corrected for the smoothing of p_* to take into account the variation of the slope and has the following form :

$$(1-\delta)\overline{p}_{*,i-1} + 2(1+\delta)\overline{p}_{*,i} + (1-\delta)\overline{p}_{*,i+1} = p_{*,i-1} + 2p_{*,i} + p_{*,i+1} + \delta R_c \qquad (21)$$

where $R_c \simeq -\frac{\partial p_*}{\partial z} \mid_{j+1} (\tan\alpha \mid_{i+1} - \tan\alpha \mid_i) \triangle x$ is the correction term and α is the slope angle. The correction can be easely understood with the help of the following example. Let $\psi = z_{surf} + h$ where h is a constant height above the surface. Suppose that a slope variation occurs at point i so that

$$z_{surf,i+1} = z_{surf,i} + \triangle x(\tan\alpha \mid_{i+1} - \tan\alpha \mid_i)$$

For the shake of simplicity take $\tan\alpha \mid_i = 0$, (i.e. $z_{surf,i-1} = z_{surf,i}$). Applying the filter

with $\delta = 1$ (i.e. explicit filter) will give :

$$\overline{\psi_i} = \frac{1}{4}(\psi_{i-1} + 2\psi_i + \psi_{i+1})$$

so that the new value of h is h_i :

$$\overline{h_i} = \frac{1}{4}(\psi_{i-1} + 2\psi_i + \psi_{i+1}) - z_{surf,i} = h + \frac{1}{4} \triangle x(\tan\alpha\,|_{i+1} - \tan\alpha\,|_i)$$

It can be easely understood from this example that a correction $-\triangle x(\tan\alpha\,|_{i+1} - \tan\alpha\,|_i)$ must be added to $\overline{\psi_{i+1}}$ and ψ_{i+1} in the expression of the filter.

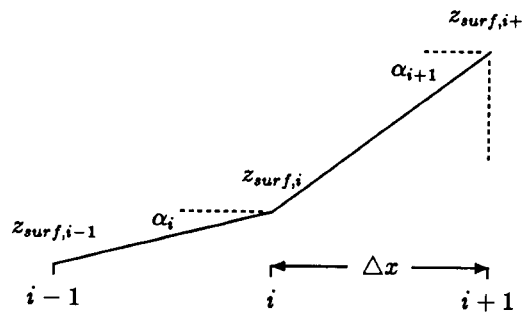

One may reasonably assume that the variation of other dependant variables (i.e. $\psi = u, v, \theta$ and q) along the slope is small, so that the correction term R_c may be neglected.

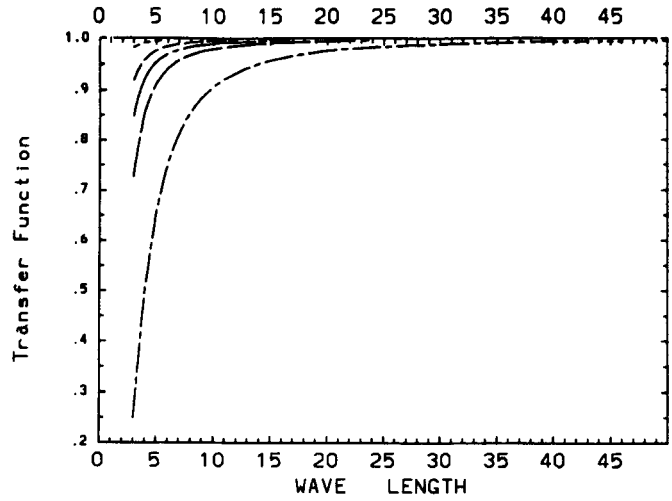

Figure 1: *The transfer function of the filter displayed as a function of wave length L for a few values of filter parameter δ. Units of L are △x increments*

– – – – $\delta = 0.05$ — - — - — - — - $\delta = 1.$
- - - - - - $\delta = 0.01$ —— —— —— —— $\delta = .2$
———— $\delta = .002$ ———— - ———— - $\delta = .1$

Numerical effects of the selective filter : The transfer function of the selective filter, when $R_e = 0$ can be written :

$$R = \frac{\overline{\psi}}{\psi} = \frac{1}{1 + \delta \tan^2 \frac{k\triangle x}{2}} \tag{22}$$

where $k = \frac{2\pi}{L}$ and L is the wave length. Smoothing is infinite for wave length $L \leq 2 \triangle x$. It should be interesting to compare the effect of diffusion and filtering on σ surfaces. For this purpose one computes the value of K_H which for a particular wave length gives the same smoothing as the filter. For the diffusion equation on the σ surface :

$$\frac{\partial u}{\partial t} = K_H \frac{\partial^2 u}{\partial x^2}$$

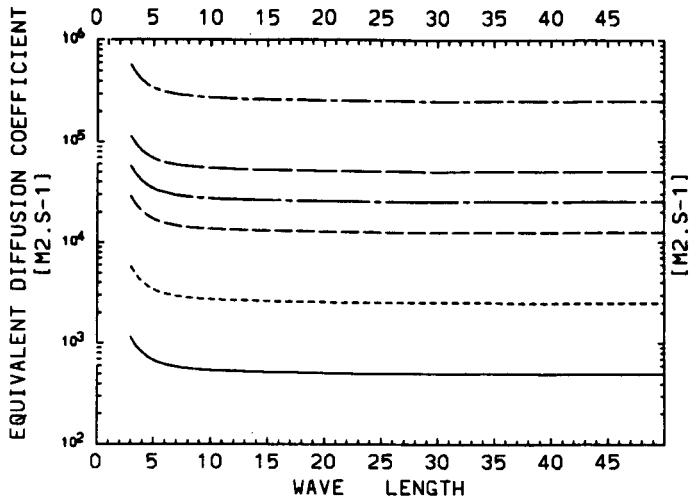

Figure 2: *Diffusion coefficient giving the same smoothing as the filter, as a function of wave length L (units : $\triangle x$) and filter parameter δ.*

$\delta = 0.05$ $\delta = 1.$
$\delta = 0.01$ $\delta = .2$
$\delta = .002$ $\delta = .1$

Using the semi-implicit numerical scheme :

$$\frac{u_i^{n+1} - u_i^{n+1}}{\triangle t} = K_H(a\frac{u_{i+1}^n - 2u_i^n + u_{i-1}^n}{\triangle x^2} + b\frac{u_{i+1}^{n+1} - 2u_i^{n+1} + u_{i-1}^{n+1}}{\triangle x^2}$$

where $a + b = 1$. The smooting can be written :

$$G = \frac{1 + 2ar(\cos(k \triangle x) - 1)}{1 + 2br(\cos(k \triangle x) - 1)}$$

where $r = \frac{K_H \triangle t}{\triangle x^2}$. Equating R and G gives :

$$K_H = \frac{\triangle x^2}{\triangle t} \frac{\delta}{4(\cos^2(\frac{\pi \triangle x}{L}) + a \sin^2(\frac{\pi \triangle x}{L}))} \tag{23}$$

So for a particular wave length, how more the filter is used (i.e. for smaller $\triangle t$), how more the smoothing is efficient and how more the equivalent horizontal diffusion is increased.

The previous expression also states that the filter must be more selective (i.e. δ smaller) for poor resolution (i.e. when $\triangle x$ is larger)

.2 Simulations

In the present section the model solutions in the case of Antarctic katabatic winds are discussed. The horizontal grid spacing is $\triangle x = 2\ km$ and the time step is $\triangle t = 4\ s$. For all the simulations, the terrain profile is the following :

slope	z_{surf}		
0 %	0.	-34 km	< x < 0 km
5 %	0.05 x	0 km	< x < 50 km
0 %	2.5 km	50 km	< x < 70 km

where $x = 0$ is the coastline.

The smoothing due to the filter is displayed on fig.1 as a function of wave length L for a few values of filter parameter δ. The equivalent K_H for the semi-implicit scheme (i.e. $a = 0.25$) is represented on fig.2. It can be seen that $\delta = .2$ gives a value of $K_H = 5.10^4\ m^2 s^{-1}$ for long waves, which seems realistic. This value is chosen as a reference value for the present discretization.

The numerical effects of the filter in the model can be analyzed by comparing the following simulations :

(i) only the divergence of vertical turbulence (term E in the development of F_z)[6] and the numerical smoothing ($\delta = .2$) on the σ surfaces are taken into account (control run). The simulated K_v range from the molecular diffusion value towards a maximum $K_{v\ max} \simeq 10\ m^2 s^{-1}$. Simulations for which $\delta < .1$ are such that external gravity waves propagate in the model. For $\delta \simeq 0.05$, the model blows up. A reasonable value for the filter parameter is $\delta = .2$ when $\triangle x = 2\ km$ and $\triangle t = 4\ s$.

[6]Similarly for the conservation equations for v, θ and q

(ii) The divergence of vertical turbulence (term E), the diffusion on the σ surfaces (term A) and numerical smoothing are taken into account. For this simulation the values of the parameters are $K_H = 5.10^4\ m^2 s^{-1}$ and $\delta = .002$. Results after 15 *hour* simulation show that numerical effects of the diffusion on σ surfaces and the filter are added and that no differences with the control run are found.

(iii) The divergence of vertical turbulence (term E), the correction due to the horizontal subgrid scale diffusion induced in the vertical (terms C and D), the horizontal diffusion (term A plus the correction term B) and the numerical smoothing are taken into account. Two simulations are done and are presented here. For both $\delta = 0.002$ but the value of K_H are different. For the first (referred here as D1), $K_H = 5.10^3\ m^2 s^{-1}$ and for the second (D2), $K_H = 5.10^4\ m^2 s^{-1}$. Let remark that for the 5 % slope the correction due the D term on K_v range then from $\alpha^2 K_H = 12.5$ to 125 $m^2 s^{-1}$. It is thus expected strong mixing in the vertical.

The results which are shown are those obtained after 15 *hour* simulation, for which it can be reasonably estimated that the dependant variables have reached the steady state. Because they are representative of the simulation, the following fields are displayed :

(i) the field of the u-component of the wind field and (ii) the field of the potential temperature deficit $\delta\theta = \theta - \theta_0$, where $\theta(z)$ and $\theta(z)_0$ are respectively the potential temperature and the basic state potential temperature representative of the potential temperature outside the katabatic layer.

u and $\delta\theta$ are respectively displayed on fig.3 and 4 for the control run, on fig.5 and 6. for run D1 and on fig.7 and 8. for run D2.

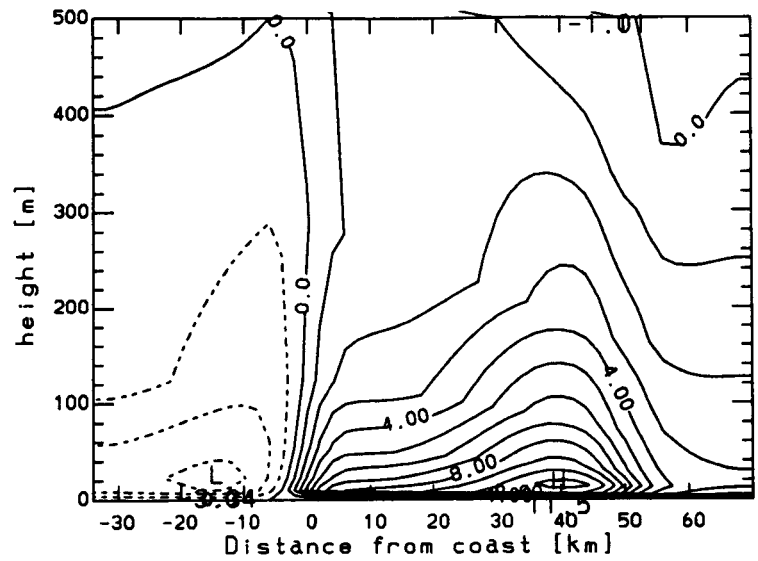

Figure 3: *u, as a function of distance to coast and height above surface, for control run ($\delta = .2$). Full lines for downslope wind. Contour interval of* 1 $m.s^{-1}$

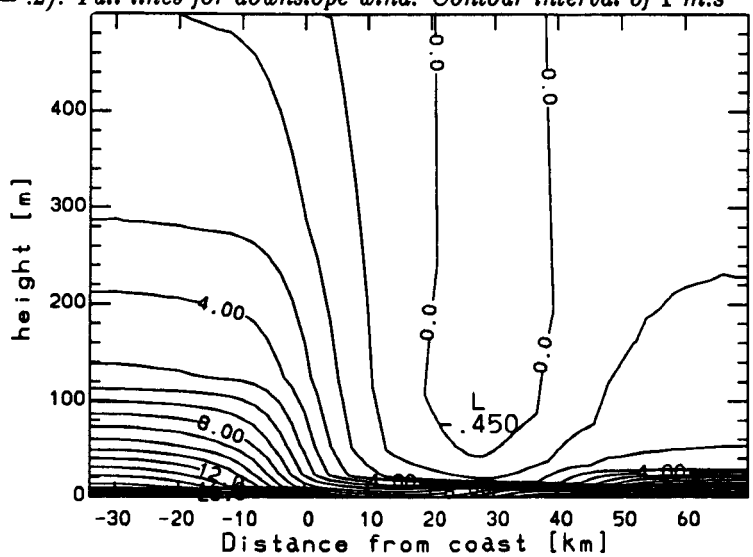

Figure 4: *$\delta\theta$, as function of distance to coast and height above surface, for control run ($\delta = .2$). Full lines for positive values . Contour interval of* $1°C$

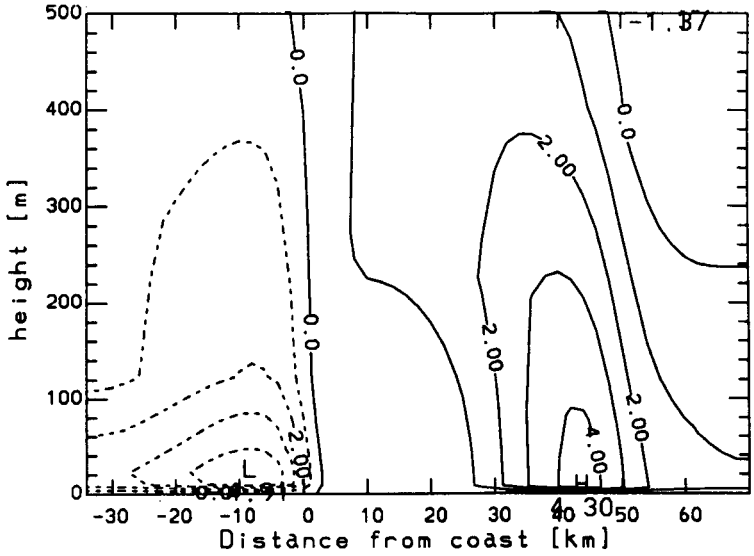

Figure 5: *u, as a function of distance to coast and height above surface, for run D1 (δ = .002 and $K_H = 5.10^3\ m^2 s^{-1}$). Full lines for downslope wind. Contour interval of 1 $m.s^{-1}$*

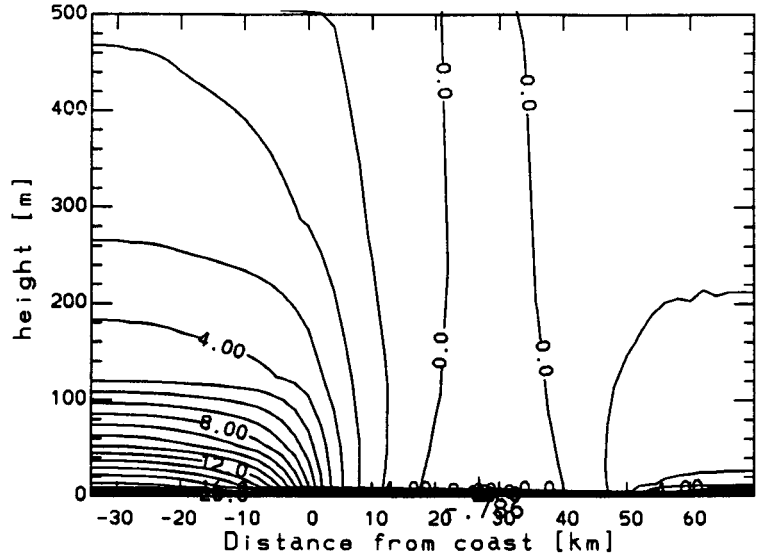

Figure 6: *$\delta\theta$, as function of distance to coast and height above surface, for run D1 (δ = .002 and $K_H = 5.10^3\ m^2 s^{-1}$). Full lines for positive values . Contour interval of 1°C*

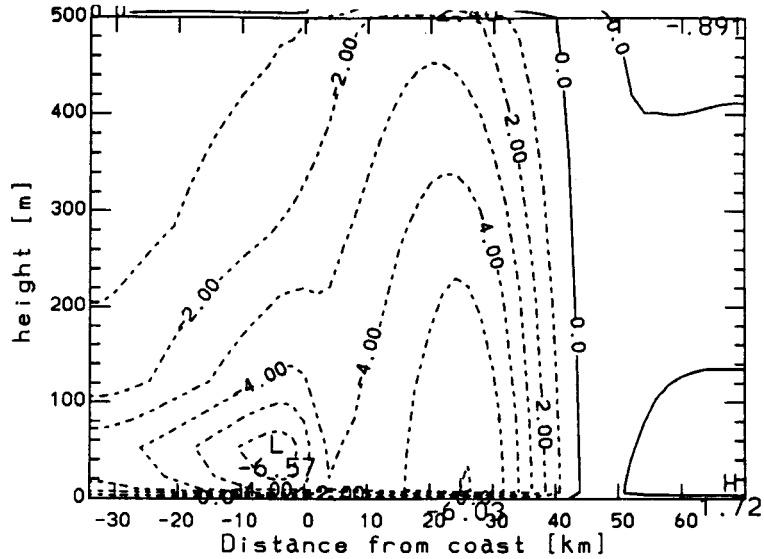

Figure 7: *u, as a function of distance to coast and height above surface, for run D2 (δ = .002 and $K_H = 5.10^4\ m^2s^{-1}$). Full lines for downslope wind. Contour interval of 1 $m.s^{-1}$*

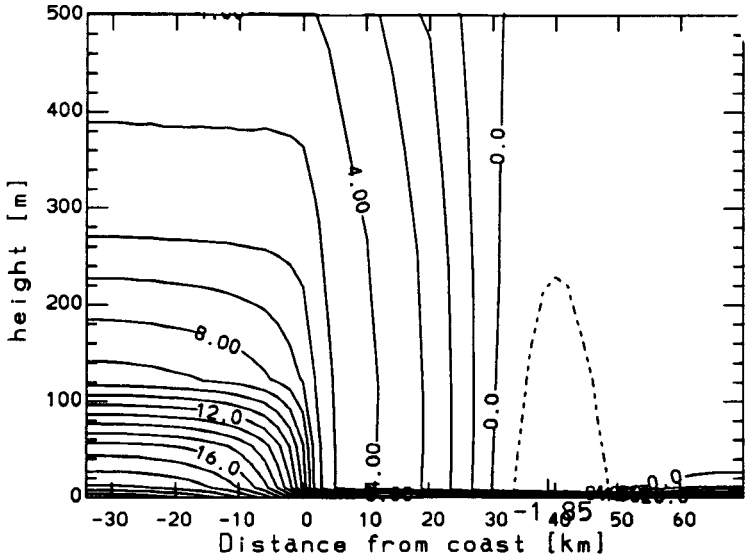

Figure 8: *$\delta\theta$, as function of distance to coast and height above surface, for run D2 (δ = .002 and $K_H = 5.10^4\ m^2s^{-1}$). Full lines for positive values . Contour interval of 1°C*

It is found that vertical mixing of heat is so enhanced that the potential temperature

deficit in the katabatic layer is destroyed, with as consequence no katabatic force. In conclusion it is found during these experiments that the contribution of the horizontal diffusion coefficient to the vertical diffusion is much greater than the vertical one with as consequence some unrealistic solution of the model.

Finally the simulations for which the filter is not used need to choose too hight values for K_H to avoid spurious wave propagation so that the model is computationally unstable. This reflects the importance of the cascade of the energy of the katabatic circulation towards $2 \triangle x$ waves and the necessity to remove these waves absolutely.

.3 Conclusion

Horizontal subgrid scale mixing in mesoscale models for which horizontal grid spacing is greater than vertical grid spacing is up to now not well known. When terrain following coordinates (i.e. σ system) are used, even the vertical subgrid scale terms appearing from the average operation of the conservation equations are not directly expressible in terms of vertical turbulence. Nevertheless it is possible to go back to an expression of the vertical subgrid scale term in the rectangular coordinate system (i.e. z system), with the addition of correction terms including the effect of the horizontal subgrid scale mixing induced in the vertical by the slope.

If the nature of horizontal subgrid scale mixing can be considered as essentially turbulent (i.e., when the horizontal grid spacing is small), the effect of the correction terms can be important and must be carefully parameterized. This can be done in nonhydrostatic models (Gross, 1986).

On the contrary, it seems reasonable that in hydrostatic models operating with the σ system, distinction must be done between vertical turbulence and horizontal subgrid scale mixing, so that the correction terms must contain the effect of horizontal turbulence only. If the slope of the σ surfaces is not too important (i.e. < 10 %), with the hypothesis

that horizontal turbulence is of the same order of magnitude as the vertical one, it is easely understood that the contribution of the former in the vertical can be neglected when compared to the later. On the other hand, the interruption of the energy cascade on the smallest resolvable wave length of the model (i.e. the $2 \triangle x$ wave) occurs on the σ surfaces and must be eliminated on these surfaces.

This is especially illustrated for flows which properties (i.e. $u, v, \theta, q, ...$) are roughly constant following terrain slope, such as katabatic flow. Such atmospheric circulation can be considered as a strong disturbance and generates an important amount of energy on the $2 \triangle x$ wave but also on gravity waves which travel parallely to the surface in the model. Various experiments with the present model show that the best solution to remove these waves is the use of a selective low-pass filter operating on σ surfaces and corrected to take into account the slope variation.

References

Alpert P., Cohen A. and Neumann J.: 1980, 'On the Sigma Coordinate System', *Contrib. 80-5 to the Hebrew University of Jerusalem, Dept. of Atmosph. Sci.*, 25 pp.

Alpert P.: 1981, 'Implicit Filtering in Conjonction with Explicit Filtering', *J Computational Phys* **44**, 212-219.

Alpert P., Cohen A., Neumann J. and Doron E.: 1982, 'A Model Simulation of the Summer Circulation from the Eastern Mediterranean Past Lake Kinneret in the Jordan Valley', *Mon Wea Rev* **110**, 994-1006.

Alpert P. and Neumann J.: 1984, 'On the Enhanced Smoothing over Topography in some Mesometeorological Models', *Boundary Layer Meteorol.* **30**, 293-312.

Gross G.: 1986, 'A Numerical Study of the Land and Sea Breeze Including Cloud Formation', *Beitr. Phys. Atmosph.* **59**, 97-114.

Holton J.R.,: 1972, 'An Introduction to Dynamic Meteorology', *Acad Press*, 319 pp.

Pielke R.A.: 1984, 'Mesoscale Meteorological Modeling', *Acad Press*, 612 pp.

SCIENCE POLICY OFFICE
Research contract
nr ANTAR/04

DYNAMICS OF THE ANTARCTIC ICE CAP

H. Decleir, Ph. Huybrechts, L. De Vos
and F. Pattyn

GEOGRAFISCH INSTITUUT
VRIJE UNIVERSITEIT BRUSSEL
PLEINLAAN, 2
B-1050 BRUSSEL (BELGIUM)

BELGIAN SCIENTIFIC RESEARCH
PROGRAMME ON ANTARCTICA
SCIENTIFIC RESULTS OF PHASE ONE
(OCT 85 - JAN 89)
VOLUME III: GLACIOLOGY AND
CLIMATOLOGY

CONTENTS

INTRODUCTION : General research goals 1

CHAPTER 1 : Development of a 3-dimensional time-dependent numerical model for Antarctica 2

1. Specific research goals 2
2. Model equations 6
2.1. Ice flow 6
2.1.1. Grounded ice 7
2.1.2. Ice shelf 9
2.1.3. Grounding zone 12
2.2. Thermodynamics 15
2.3. Bed adjustment 16
3. Data sets 18
4. First results : a diagnostic simulation 22
5. Summary and conclusions 27

CHAPTER 2 : Ice thickness measurements and ice dynamics in the Sør Rondane, Dronning Maud Land, Antarctica 29

1. Specific research goals 29
2. Ice thickness measurements, instruments and methods 31
2.1. Instruments 31
2.2. Gravimeter survey 33
2.3. Interpretation of gravimeter ice thickness measurements 33
3. Comparison of radio echo sounding and gravimeter ice thickness results 36
4. Subglacial relief in the Sør Rondane 38
5. Dynamics of the ice sheet 42
6. Summary and conlusions 47

REFERENCES 49

SUMMARY

The Antarctic Ice Sheet plays an important role in the glacio-climatic sysem of the earth. The ice cap and the marginal mountain areas in Antarctica contain a fascinating archive of past environmental changes. Modelling these changes and predicting future behaviour is a major task for those concerned with the global environment.

In view of this, the development of a 3-D thermo-mechanical model of the Antarctic Ice Sheet was undertaken. In a first stage, a 2-D flowline version has been extensively tested and used to investigate the reaction of the East Antarctic Ice Sheet with respect to a full glacial cycle. These studies have, among other things brought to light that i) creep instability is unlikely to occur and initate surging of the East Antarctic Ice Sheet ii) the evolution of ice thickness following a glacial-interglacial climatic shift is strongly controlled by the different heat transfer mechanisms and related time scales and iii) that due to the diffusive heat time scale operating on 10^4 years, a steady state cannot possibly be reached. As the flow and temperature fields were shown to encompass a number of counteracting effects, typical elevation changes in central East Antarctica may not have exeeded 100 m, implying that the palaeotemperature record recovered at Vostok Station is primarily of climatic origin.

The complete 3-D model covering the entire Antarctic Ice Sheet has been implemented on a CRAY-2 super computer and experiments with this model are still in progress. First results of some diagnostic runs seem to indicate that i) the model yields stable solutions ii) the diagnostic flow field cannot possibly in accordance with staedy state requirements iii) basal ice at pressure melting is confined to West Antarctica, the Antarctic Peninsula, outlet glaciers and the thick interior ice areas of East Antarctica. However, it appears that for a good evaluation of the present state of the ice cap a long time integration over the 160,000 year long Vostok signal is necessary.

Interpreting the glacier variations as observed in the marginal mountain areas and explaining the role of those changes in the dynamics of the ice sheet was the second objective of this Research Program. During the Austral summer 1986-87 an expedition to the Sør Rondane Mountains, Dronning Maud Land, was carried out in collaboration with the Japanese Antarctic Research Expedition (JARE 28). The subglacial relief of the mountains in the central part of the area was mapped, using a gravimeter survey, extending to the previous glaciological work carried out by fromer Belgian Expeditions. A comparison with radar echo sounding lines allowed to test the new modelling procedure and the gravimetric method in general as compared to the radar technique (within 10%). The results indicate a subglacial fiordlandscape with overdeepened glacial valleys. One-dimensional flow line models were developed to simulate the glacier behaviour. It shows that some glaciers are in the process of being cut off from the main ice supply and confirms their

present local character. As for explaining the glacier expansion in the past, it was shown that a 500 m increase in ice thickness can be obtained by an advance of the grounding line towards the edge of the continental shelf. A possible scenario might be a lowering of the sea level with 150 m and a temperature drop of 11K.

INTRODUCTION

GENERAL RESEARCH GOALS

The Antarctic Ice Sheet plays an important role in the study of climate and climatic change. Since the ice sheet contains around 90% of the earth's fresh water resources, it is of considerable importance to get more insight in the reaction of the ice sheet due to environmental changes. If the ice sheet would completely melt away, the resulting rise in global sea level would amount to around 70 m. It is clear from this figure, that even relatively small changes in its grounded volume may have far reaching consequences.

On the other hand, the ice contains a unique archive on the history of our climate. Physio-chemical analyses on deep ice cores reveal a continuous record of variables as temperature, atmospheric CO_2, dust content and so on, on time scales well into the previous glacial period. The interpretation of this archive requires a knowledge of the dynamics of the ice sheet in response to environmental conditions. In particular, particle trajectories and age-depth profiles have to be constructed.

Another archive regarding the past environment lies hidden in the glacial till and landscape forms of the marginal mountains surrounding Antarctica. Here, also modelling the glacial flow through the damming mountains, proves necessary for accurate interpretation of the geological and geomorphological findings.

The interpretation of glacial dynamics in the mountain areas requires however detailed knowledge of the subglacial relief which is seldom available. These data can only be obtained by means of additional and new field measurements.

In short, the aims of the present research work on the ice dynamics can be summarized as follows : (i) development of a three-dimensional time-dependent numerical model for Antarctica capable of providing the necessary information of change in ice volume pertinent to climatic change studies (ii) ice dynamics within a marginal mountain area. In the latter part of the study it is hoped to combine field work, modelling and remote sensing in order to understand observed glacier fluctuations and to relate them properly to climatic change.

CHAPTER 1

DEVELOPMENT OF A 3-DIMENSIONAL TIME-DEPENDENT NUMERICAL MODEL FOR ANTARCTICA

1. SPECIFIC RESEARCH GOALS

The Antarctic Ice Sheet essentially interacts with its environment in three ways, all of them interrelated in a complex way : i) by changes in the extent of its grounded domain ii) by changes in its nourishment or mass balance and iii) by changes in its flow properties, in particular ice temperature. With respect to (i) changes in the free water depth, as a result of global sea level variations and local isostatic bed adjustment may be of crucial importance. The accumulation rate depends on such factors as temperature of snow formation, distance to moisture source, surface orientation with respect to prevailing winds, surface gradient (orography) and general atmospheric circulation. This essentially requires a parameterisation of the accumulation rate in terms of these factors. Ablation (which is of minor importance in the present ice sheet) may eventually be dealt with in a similar fashion. Regarding point (iii) this essentially means that the heat equation has to be solved simultaneously with the equations governing ice flow. Changes in the flow properties of ice due to crystal fabric are disregarded, simply because there is no quantitative information available as how to deal with these effects. It may be assumed, however, that these effects are of less importance than changes in ice stiffness due to temperature.

So, in order to be able to deal with the problems mentioned above, a three dimensional thermo-dynamic ice sheet / ice shelf model with geodynamics (the bed response) has been developed for the Antarctic. This model computes the fully coupled velocity and temperature fields (coupled by means of the Arrhenius equation, relating the flow parameter to temperature), as well as the free surface elevation in a time dependent mode. Furthermore, in order to allow for a changing domain, the model has been coupled with an ice shelf model and the crucial problem of grounding zone dynamics has been dealt with in a pragmatic way, though containing, we believe, the relevant physics.

Isostatic bed adjustment, due to changing ice or water loading and unloading has been modelled following the concept of a viscous astenosphere, with the lithosphere deflection calculated taking into account the flexural rigidity or stiffness of the crust.

The mass balance parameterisation, relating the accumulation pattern in essence to geometric parameters, has been developed by Paul Fortuin (Instituut voor Meteorologie en Oceanografie, Rijksuniversiteit Utrecht), and will allow an estimate to be made of accumulation rates with respect to changing climatic and ice sheet boundary conditions.

The model equations are then solved on a 3-D grid with high resolution in the lower layers, where the vertical cartesian coordinate is mapped onto a new coordinate, scaled to local ice thickness. This approach, although involving a complex coordinate transformation, has the advantage that the lower and upper ice boundaries will always coincide with a gridpoint, thereby avoiding boundary problems and/or complicated interpolation techniques. We opted for a finite difference approach to solve the equations and employed the Alternating-Direction-Implicit method to integrate the continuity equation forward in time. The problem then reverts to simultaneous solving sets of tridiagonal systems along rows parallel to the x- and y-axes respectively. This approach ensures computational stability for time steps at least an order of magnitude larger than the conventional explicit time-stepping methods, while producing realistic solutions and avoiding spurious effects.

To our knowledge, this is the first time that an ice sheet model with a complete degree of complexity and sophistication has been developed. A first attempt in this direction was made by Jenssen (1977), who tried to solve the full set of thermo-mechanical equations for 'shallow ice flow'. However, when applying the model to the Greenland Ice Sheet, numerical instabilities occured, so that a long time integration could not be carried out. Furthermore, available computer resources at that time limited the horizontal resolution to a coarse 200 km grid. In more recent papers on the solution of the thermo-mechanical equation for cold ice flow, it appears that numerical problems are still encountered (Hutter et al., 1986; Hindmarsh and Hutter, 1988). Other studies along the lines drawn by Jenssen include Antarctic models developed by Kvasov and Verbitsky (1981) and Herterich (1988). In these models however, changes in the extent of the grounded ice sheet and a coupled ice shelf are not considered constraining their applicability to a steady state East Antarctic Ice Sheet. Another class of ice sheet models deals explicitly with changes in the horizontal and vertical extent of ice sheets, but excludes thermodynamics (Mahaffy, 1976; Oerlemans, 1982). In the latter model, a diagnostic description of ice shelves was included. However, in the work of Oerlemans the need was recognized to deal with ice shelves and grounding line dynamics in a much more refined way.

In the present ice sheet model, several of the handicaps and shortcomings of the above mentioned studies seem to have been overcome : thermodynamics are included, a stable and efficient numerical scheme is made use of as well as a high resolution grid. Also ice shelf dynamics are accounted for explicitly and the full stress equilibrium is considered at the grounding zone, where the transition from grounded to floating ice takes place.

As mentioned previously, our model also contains full time-dependence. Regarding the long time scales connected with the thermodynamic evolution, still enhanced by complex interaction with the ice flow field and geometric (ice thickness) parameters, it is very probable that the present temperature distribution is far from steady state. In effect, the ice temperature constitutes some sort of memory of the system and is no doubt still reacting to past changes in boundary conditions (surface temperature, accumulation, basal temperature gradient). This means, that modelling the present ice sheet as a steady state ice sheet is at most a good approximation. In other words, to say something meaningful about the present state, one should take into account the past history of the ice sheet and model at least a full glacial - interglacial cycle. More speculatively, this approach may provide an alternative view on the balance problem, as the present 'background' evolution of the ice sheet will come out of the model at time zero. Of course, one should keep in mind that boundary conditions on these time scales are at best known in a rather schematic fashion. We take the Vostok surface temperature record (dated back to around 160000 years BP, Jouzel et al., 1987) as prime variable and relate accumulation to the saturated vapour pressure with respect to the temperature above the surface inversion layer, and sea-level variations to the ice volume evolution on the Northern Hemisphere continents. There may be a problem connected with using the surface temperature record, as this record also includes a contribution due to local changes in surface elevation, that are unlikely to be representative for the whole ice sheet. However in a recent paper (Huybrechts and Oerlemans, 1988) typical elevation changes at this location were estimated to be of the order of around 100 m, implying that the bias introduced is an order of magnitude smaller than the main signal contrast (glacial - interglacial change of 10°C) and at most of similar magnitude than uncertainties introduced by other factors (background ocean δ^{18} value, laboratory accuracy, atmospheric lapse rate, etc...).

At present, Philippe Huybrechts is a guest at the Alfred Wegener Institute for Polar Research, Bremerhaven, where the model has been implemented on a remotely linked CRAY-2 computer in Stuttgart. Numerical experiments are currently on the way that aim at better understanding the response of the ice sheet with respect to environmental parameters (accumulation, ice surface temperature, sea level) and the role therein of the transient thermal regime. This research involves a sensitivity study of the ice sheet with respect to a steady state glacial and interglacial state, and the study of transient response of the ice sheet due to the glacial-interglacial transition that constitutes the main element of change on time scales of the order 10^4-10^5 years, our main interest.

It is anticipated that this research may throw more light on questions such as its flow and thermal regime, the impact of bed temperature conduction on the areal distribution of basal melting areas with time, timing of grounding and ungrounding processes, magnitude and direction of the areal distribution of local ice thickness imbalance, crucial controls on domain changes etc..., and of

course, also basic shortcomings in the present state of the art in ice sheet modelling and insufficient data coverage.

In this report a short overview will be presented of the equations governing the model, the constructed data sets and results of a first diagnostic model run that primarily aims at producing a steady state interglacial temperature field input for the forthcoming prognostic model runs.

2. MODEL EQUATIONS

The full thermodynamic Antarctic ice flow model contains a description of i) deformation of grounded ice ii) grounding zone dynamics iii) ice shelf flow iv) grounded ice temperature evolution v) bedrock temperature (by vertical diffusion only) and vi) bed adjustment. The inputs of the model are the mass balance distribution, temperature- dependent flow-law coefficients, thermal parameters, ice surface 10m-temperature, geothermal heat flux, sea level stand, bedrock elevation and rheological parameters for the underlying bedrock. It essentially outputs the 3-D velocity and temperature fields, as well as the geographical distribution of mass (ice thickness and horizontal ice sheet extent).

Here only a very brief outline of the model equations will be presented. For a more comprehensive overview of the model equations and the numerical procedures involved, one is referred to Huybrechts (1986) : A three-dimensional time-dependent numerical model for polar ice sheets : some basic testing with a stable and efficient finite difference scheme, VUB Geografisch Instituut, Report 86-1.

2.1 Ice flow

The fundamental equation to be solved is a continuity equation for ice thickness H:

$$\frac{\partial H}{\partial t} = - \nabla (\vec{v} H) + M - S \qquad (1)$$

where $\vec{v}$ is the vertically integrated velocity vector, M the local mass balance and S the basal melting rate in m/years.

Deriving the velocity field in terms of ice thickness and/or its gradient then leads to a parabolic partial differential equation, that may be regarded as a diffusion equation in one unknown H. The remainder of this section will be essentially devoted to a derivation of the velocity field in the respective parts of the ice sheet.

2.1.1 Grounded ice

Ice deformation is assumed to result from shear strain, with the shear stress distribution in the model given by :

$$\tau_{xz}(z) = \tau'_{xz}(z) = -\rho\, g\, (H + h - z)\, \frac{\partial(H+h)}{\partial x} \qquad (2)$$

$$\tau_{yz}(z) = \tau'_{yz}(z) = -\rho\, g\, (H + h - z)\, \frac{\partial(H+h)}{\partial y} \qquad (3)$$

where τ_{xz}, τ_{yz} are shear stress components in a horizontal plane in the usual cartesian coordinate system (x,y,z), h bed elevation, ρ ice density and g acceleration of gravity.

The velocity field then follows from a Glen-type flow law governing the creep of polycrystalline ice, that relates deformation to stress :

$$\dot{\varepsilon}_{ij} = A(T^*)\, \tau_*^{n-1}\, \tau'_{ij} \qquad i,j = x,y,z \qquad (4)$$

In this expression $\dot{\varepsilon}_{ij}$ [a^{-1}] are the strain rate components related to velocity gradients by definition, τ_* the effective stress defined in terms of all the stress deviator components, n the flow law exponent (taken to be 3), and A [$Pa^{-n}\, a^{-1}$] the flow law coefficient. A[T*] introduces the temperature dependence of ice deformation and obeys an Arrhenius relationship :

$$A[T^*] = m\, .\, a\, \exp\left[\frac{-Q}{R\, T^*}\right] \qquad (5)$$

where R is the universal gas constant, Q the activation energy for creep, and T* absolute temperature corrected for the dependence of the melting point on pressure.

Integrating (4) twice over ice thickness then yields an expression for the depth averaged horizontal velocity vector :

$$\vec{v}\,H = -2(\rho g)^n \left[\nabla (H+h).\nabla (H+h) \right]^{\frac{n-1}{2}} \nabla (H+h) \int_h^{H+h} \int_h^z A(T^*)(H+h-z)^n \, dz \, dz' \qquad (6)$$

The vertical velocity component then follows from the incompressibility condition, yielding:

$$w(z) - w(h) = -\int_h^z \nabla . \vec{v}(z) \, dz \qquad (7)$$

with kinematic boundary condition at the lower ice boundary :

$$w(h) = \frac{\partial h}{\partial t} + \vec{v}(h) . \nabla h \qquad (8)$$

The solution of the continuity equation then proceeds as follows : (6) is substituted in (1), that may be written then as a diffusion equation for ice thickness :

$$\frac{\partial H}{\partial t} = -\nabla D \nabla (H+h) + M - S \qquad (9)$$

where D is a strongly nonlinear diffusion coefficient, depending on ice thickness to the fourth power and surface elevation gradient to the fifth power. Evaluating the diffusivity at the old time step (in effect linearizing the problem), an implicit ADI time stepping method is then applied. This shifts the problem to solving simultaneous sets of tridiagonal systems, that is effected by a simple and straightforward Gaussian elemination.

2.1.2 Ice shelf

In ice shelves the floating criterion applies :

$$H + h = \left[1 - \frac{\rho_i}{\rho_w} \right] H \qquad (10)$$

where ρ_i en ρ_w are ice and water density respectively.

In contrast with grounded ice dynamics, where the pressure gradient force is roughly balanced by basal shear stresses, in ice shelves there is a balance between the pressure gradient force and normal stress gradients. Equations describing the velocity distribution in ice shelves may be derived from general principles as follows.

The basic stress equation reads :

$$\frac{\partial \tau_{ii}}{\partial r_i} + \frac{\partial \tau_{ij}}{\partial r_j} + \frac{\partial \tau_{ik}}{\partial r_k} = \rho\, g_i$$

$$i,j,k = x,y,z \qquad (11)$$

Assuming local hydrostatic equilibrium in the vertical and introducing the stress deviator, the following expressions hold :

$$\tau_{zz}(z) = -\rho\, g\, (H+h-z) \qquad (12)$$

$$\tau'_{ij} = \tau_{ij} - \frac{\delta_{ij}\, \tau_{kk}}{3} \qquad i,j,k = x,y,z \qquad (13)$$

$$\tau'_{ii} = 0 \qquad (14)$$

After some algebraic manipulation the basic stress equations (11) may then be rewritten as a set of coupled equations, expressing a balance between gradients in stress deviators and the pressure gradient force, divided by ice thickness :

$$2\frac{\partial}{\partial x}\tau'_{xx} + \frac{\partial}{\partial x}\tau'_{yy} + \frac{\partial}{\partial y}\tau_{xy} = \rho\, g\frac{\partial(H+h)}{\partial x} \qquad (15)$$

$$2\frac{\partial}{\partial y}\tau'_{yy} + \frac{\partial}{\partial y}\tau'_{xx} + \frac{\partial}{\partial x}\tau_{xy} = \rho\, g\frac{\partial(H+h)}{\partial y} \qquad (16)$$

where the horizontal shear stresses $\tau_{xz} = \tau_{yz} = 0$.

Equations for the velocity in the ice shelf are then obtained by introducing the flow law :

$$\dot{\varepsilon}_{ij} = A(T)\,\tau^{n-1}\,\tau'_{ij} \qquad (17)$$

$$\text{where } \tau^2 = \frac{1}{2}\left[\tau'^2_{ii} + 2\left[\tau^2_{xz} + \tau^2_{xy} + \tau^2_{yz}\right]\right] \qquad (18)$$

$$\text{and } \dot{\varepsilon}_{ij} = \frac{1}{2}\left[\frac{\partial u_i}{\partial x_j} + \frac{\partial u_j}{\partial x_i}\right] \qquad (19)$$

$$\text{also } \dot{\varepsilon} = A(T)\,\tau^n \qquad (20)$$

$$\text{from (17) : } \tau'_{ij} = \dot{\varepsilon}_{ij}\,A^{-1}\,\tau^{1-n}$$

$$\text{from (19) : } \tau^n = \dot{\varepsilon}A^{-1}$$

$$\text{and thus : } \tau'_{ij} = \dot{\varepsilon}_{ij}\,A^{-1/n}\,\dot{\varepsilon}^{1/n-1} \qquad (21)$$

$$\text{moreover : } \dot{\varepsilon}^2 = \frac{1}{2}\left[\dot{\varepsilon}^2_{ii} + 2\left[\dot{\varepsilon}^2_{xy} + \dot{\varepsilon}^2_{yz} + \dot{\varepsilon}^2_{xz}\right]\right]$$

in the absence of horizontal shear strain rates leading to :

$$\dot{\varepsilon}^2 = \dot{\varepsilon}_{xx}^2 + \dot{\varepsilon}_{yy}^2 + \dot{\varepsilon}_{xx}\,\dot{\varepsilon}_{yy} + \dot{\varepsilon}_{xy}^2 \qquad (22)$$

Substituting all these equations in (15), (16) then leads to the final set of equations:

$$2\frac{\partial}{\partial x}\left[f\frac{\partial u}{\partial x}\right] + \frac{\partial}{\partial x}\left[f\frac{\partial v}{\partial y}\right] + \frac{1}{2}\frac{\partial}{\partial y} f\left[\frac{\partial u}{\partial y} + \frac{\partial v}{\partial x}\right] =$$

$$\rho\, g\, A^{1/n}\, \frac{\partial (H+h)}{\partial x} \qquad (23)$$

$$2\frac{\partial}{\partial y}\left[f\frac{\partial v}{\partial y}\right] + \frac{\partial}{\partial y}\left[f\frac{\partial u}{\partial x}\right] + \frac{1}{2}\frac{\partial}{\partial x} f\left[\frac{\partial u}{\partial y} + \frac{\partial v}{\partial x}\right] =$$

$$\rho\, g\, A^{1/n}\, \frac{\partial (H+h)}{\partial y} \qquad (24)$$

$$\text{with } f = \left[\left(\frac{\partial u}{\partial x}\right)^2 + \left(\frac{\partial v}{\partial y}\right)^2 + \left(\frac{\partial u}{\partial x}\right)\left(\frac{\partial v}{\partial y}\right) + \left[\frac{1}{2}\left(\frac{\partial u}{\partial y} + \frac{\partial v}{\partial x}\right)\right]^2 \right]^{\frac{1-n}{2n}}$$

Equations (23), (24) are of elliptic type and are solved by point relaxation. With this straightforward technique an initial velocity distribution (u,v) is introduced and the residual computed at every gridpoint. This residual is then made zero locally and the process is repeated iteratively until the maximum error on the grid is below a certain level, in our case 1 m/year. In general, convergence is achieved with a number of iterations below 100.

In the model the ice sheet actually extends to the edge of the numerical grid, simply because there is not an easy way at all to predict where the ice shelf will calve and hence, the ice cliff front will be situated. This should not present a problem, as in an ice shelf a balance between the forward force (i.e. essentially the longitudinal stress deviators integrated over ice thickness) and the opposing force due to hydrostatic pressure at the ice front should hold at any place. Also, calculations pointed out that the velocity field is hardly affected by conditions further downstream, so that the calculations can be cut off at any place without basically influencing the flow conditions upstream. So, (23), (24) are solved subject to boundary conditions applying to unconfined, freely

floating ice shelves at the edge :

$$\dot{\varepsilon}_{xx} = \frac{\partial u}{\partial x} = A(T)\left[3^{1/2} \tau'_{xx} \right]^{n-1} \tau'_{xx} \qquad (25)$$

$$\dot{\varepsilon}_{yy} = \frac{\partial v}{\partial y} = A(T)\left[3^{1/2} \tau'_{yy} \right]^{n-1} \tau'_{yy} \qquad (26)$$

where the longitudinal stress deviators are found from the aforementioned force balance at the ice shelf front :

$$\tau'_{xx} = \frac{1}{6} \rho_i g H \left[1 - \frac{\rho_i}{\rho_w} \right] \qquad (27)$$

$$\tau'_{yy} = \frac{1}{6} \rho_i g H \left[1 - \frac{\rho_i}{\rho_w} \right] \qquad (28)$$

and lateral shear is assumed to be zero, yielding an equation that may be used to find the second velocity component :

$$\frac{\partial u}{\partial y} + \frac{\partial v}{\partial x} = 0 \qquad (29)$$

At the grounding zone, the boundary conditions on velocity are not velocity gradients, but the vertically integrated velocity components.

2.1.3 Grounding zone

Between the grounded ice zone, where the pressure gradient force is balanced by basal shearing and the ice shelf, where basal shearing is non-existent and normal stress gradients are dominating, there must be a transition zone where all the stress components are important. It has

been shown by several authors in one-dimensional studies (Herterich, 1987 ; Van der Veen, 1987) that this transition zone is quite small, and as far as the profile is concerned, smaller than typical gridsizes in numerical models (40 km in our case). Moreover, according to Van der Veen (1987), the normal stress gradients at the grounding zone can also be neglected, so that stress deviators only contribute in the effective stress at the grounding zone.

The inclusion of the normal stress deviators τ'_{xx} and τ'_{yy} and the lateral shear stress τ'_{xy} then apparently soften the ice at the grounding zone only. Extending these concepts to two dimensions, the equation for the vertically integrated velocity then reads :

$$\bar{v} = -\frac{2}{5} A H \left[\tau_{xz}^2 + \tau_{yz}^2 + \frac{5}{3} \left(\tau'^2_{xx} + \tau'^2_{yy} + \tau'_{xx} \tau'_{yy} + \tau'^2_{xy} \right) \right] .$$

$$\rho \, g \, H \, \nabla \, (H+h) \qquad (30)$$

where τ'_{xx}, τ'_{yy} and τ'_{xy} still have to be found.

In three dimensions there is no straightforward way to derive these stress deviator components. To circumvent this difficulty the following strategy is followed. The velocity field is calculated first in the ice shelf and grounded ice zone separately according to their respective physics. This leads to velocity gradients or strain rates over the grounding zone, where the flow law is now applied in the inverse direction. Considering a vertically integrated situation, the flow law components of (17) and (19) now read :

$$\frac{\partial \bar{u}}{\partial x} = A(\bar{T}) \, \overline{\tau^2} \, \overline{\tau'_{xx}} \qquad (31)$$

$$\frac{\partial \bar{v}}{\partial y} = A(\bar{T}) \, \overline{\tau^2} \, \overline{\tau'_{yy}} \qquad (32)$$

$$\frac{\partial \bar{u}}{\partial y} + \frac{\partial \bar{v}}{\partial x} = 2 \, A \, (\bar{T}) \, \overline{\tau^2} \, \overline{\tau'_{xy}} \qquad (33)$$

with $\overline{\tau^2} = \overline{\tau'^2_{xx}} + \overline{\tau'^2_{yy}} + \overline{\tau'_{xx}} \, \overline{\tau'_{yy}} + \overline{\tau'^2_{xy}} + \overline{\tau^2_{yz}} + \overline{\tau^2_{xz}}$

Equations (31) - (33) then constitute a nonlinear system of 3 equations in three unknowns ($\overline{\tau'_{xx}}$, $\overline{\tau'_{yy}}$, $\overline{\tau'_{xy}}$) that is solved by an iterative method. Only a few iterations appeared to be necessary to reach convergence.

This completes the brief description of the velocity field calculations, that are needed in the advective contribution in the heat transfer equation.

2.2 Thermodynamics

The heat transfer equation to be solved reads :

$$\frac{\partial T}{\partial t} = \frac{k}{\rho c_p} \nabla^2 T - \vec{v} \nabla T + \frac{\Phi}{\rho c_p} \qquad (34)$$

Here T is absolute temperature [K], t time, k thermal ice conductivity, ρ ice density, c_p specific heat capacity, v three dimensional ice velocity and Φ internal frictional heating due to deformation. Thus in the general case heat is transferred both by diffusion and advection and generated internally by deformational friction. Temperature dependence of the thermal parameters c_p and k is taken into account, whereas horizontal heat conduction is disregarded. The thermodynamic equation (34) is solved subject to boundary conditions taken as the mean annual surface temperature (conventionally taken as the 10 m ice temperature) and a given basal temperature gradient.

In some of the model runs also the thermal bed response has been treated. Since the thermal conductivity of ice is of comparable magnitude than the thermal conductivity of the bedrock below, the thermal inertia due to diffusion of the signal further down into the bed is not negligible. Ritz (1987) pointed out the importance of this in damping the basal ice temperature response. Including the bedrock thermal response has the apparent effect that the basal temperature gradient in the ice now becomes also a function of heat transfer in the rock below. In effect, this 'thermal buffer' creates a negative feedback : whenever a cold wave is conducted into the bed, temperature gradients will increase in the rock, in turn increasing the geothermal heat flux at the ice-rock interface, thereby counteracting the original cold wave. This effect has been taken care of in some of the model runs by considering flux continuity at the ice-rock interface, in the case of no basal melting and sliding :

$$k_r \left(\frac{\partial T}{\partial z} \right)_r = k_i \left(\frac{\partial T}{\partial z} \right)_i \qquad (35)$$

where the indices r and i refer to rock and ice respectively. k is the conductivity. In the more general case, where basal melting occurs and also heat is generated by basal friction, the upper boundary conditions in the rock become :

$T_r = T_{base}$ (ice) and

$$\left(\frac{\partial T}{\partial z}\right)_r = \frac{k_i}{k_r}\left(\frac{\partial T}{\partial z}\right)_i - \frac{\tau_b \vec{v}}{k_r} + \frac{1}{k_r}\int_h^{z_{melt}} \Phi \, dz \qquad (36)$$

where all surplus heat will eventually lead to a temperate ice layer between z = h and z = z_{melt}.

In the bed only heat transfer by vertical diffusion needs to be taken into account :

$$\frac{\partial T_r}{\partial t} = \frac{k_r}{\rho_r c_r}\frac{\partial^2 T_r}{\partial z^2} \qquad (37)$$

where the lower boundary condition is given by the geothermal heat flux. In the experiments discussed here, only 5 layers in the vertical are considered with a grid spacing of 400 m. As shown by Ritz (1987), a total bed thickness of 2000 m is sufficient to describe the essential features of the physical process in view at the ice-rock interface.

2.3 Bed adjustment

Large ice sheets exert considerable pressures on the underlying bed. Since the relaxation time of isostatic adjustment is comparable to the reaction of the ice sheet to changing environmental conditions, a description of the bedrock response is also included.

We consider a two layer model, consisting of rigid lithosphere resting on a viscous astenosphere. The time dependent response of the underlying viscous substratum may be described by a diffusion equation for bedrock elevation h :

$$\frac{\partial h}{\partial t} = D_a \nabla^2 (h - h_0 + w) \qquad (38)$$

where D_a is a linear diffusion coefficient, h_0 the undisturbed (without load) bedrock

topography and w the deflection.

In particular the bed deflection is a subtle process due to the relative stiffness of the bed. A local point load will bend the lithosphere, therby influencing the deflection in a wide region around. A typical value for this 'radius of relative stiffness' is 130 km (Turcotte and Shubert, 1983) with a weak forebulge situated at around 400 km.

The equation to be solved is :

$$D \nabla^4 w + \rho_m g w = q \qquad (39)$$

where D is flexural rigidity, ρ_m mantle rock density and q the load given by

$q = \rho_i g H$ for grounded ice

$q = \rho_w g (H_{sl} - h)$ in the floating ice region

The solution for (39) reads :

$$w = \frac{q \delta_x \delta_y L^2}{2 \pi D} \text{kei } x \qquad (40)$$

where L is the radius of relative stiffness, x = r/L, r being the distance to the point load and kei x Kelvin functions of zero order. More details can be found in Brotchie and Sylvester (1969).

Since lithospheric deflection is an additive process, it suffices to sum all discrete contributions in a square of 400 km to obtain the total deflection at one point. The effect is a very smoothed imprint of the local ice loading distribution.

3. DATA SETS

In order to run the model on the Antarctic Ice Sheet, data sets had to be constructed. This adresses the basic question of the resolution one is going to use. To describe processes that take place at the grounded ice boundary, a grid as fine as possible is a necessity to capture characteristics of a complicated bed topography. At the edge the ice is often chanelled in outlet glaciers and/or ice streams with a lateral spatial scale often less than 50 km. In particular, the rather subtle nature of grounding zone dynamics requires a fine grid. Ideally a computational grid with spacings around 10 ice thicknesses should be used here, as local irregularities tend to smooth out over these distances. On the other hand, this same grid in the interior parts of the East-Antarctic Ice Sheet would quite strongly contrast with typical spatial scales of variation and not in the last place, the density of measurements. Of course, the final resolution will mainly be given in by the machine one is using. Not so much memory requirements are the crucial point here, but computational times.

We opted for a 40 km grid, regarded as a fair compromise between the physical problem and the possibilities of the CRAY-2 computer (a 100000 year integration then takes around 80 minutes of CPU time). With this grid (fig.1) the model domain is covered by 141x141 = 19881 gridpoints.

Geometric data sets (bed elevation, surface elevation and ice thickness) were then generated by quadratic interpolation from a 20 km digitalisation of the SPRI maps (Drewry, 1983). In particular, the shelf areas and the grounded ice edge needed careful re- digitalisation in order to be able to reconstruct the present grounding line by using the floating criterion. These data sets are shown in figs. 2-5.

Another set of boundary conditions (accumulation rate and 10 m-ice temperature) for the present ice sheet was obtained by interpolating the raw irregularity spread original measurements of these parameters onto the same regular 40 km grid. These original data sets were also compiled at SPRI (Drewry, personal communication), and comprised around 1000 data-points each. Also a quadratic interpolation technique was adopted here, whereby data points in a radius of 500 km were weighted to their distances squared with respect to the central regular gridpoint. These basic input data are visualized in figs. 5-6.

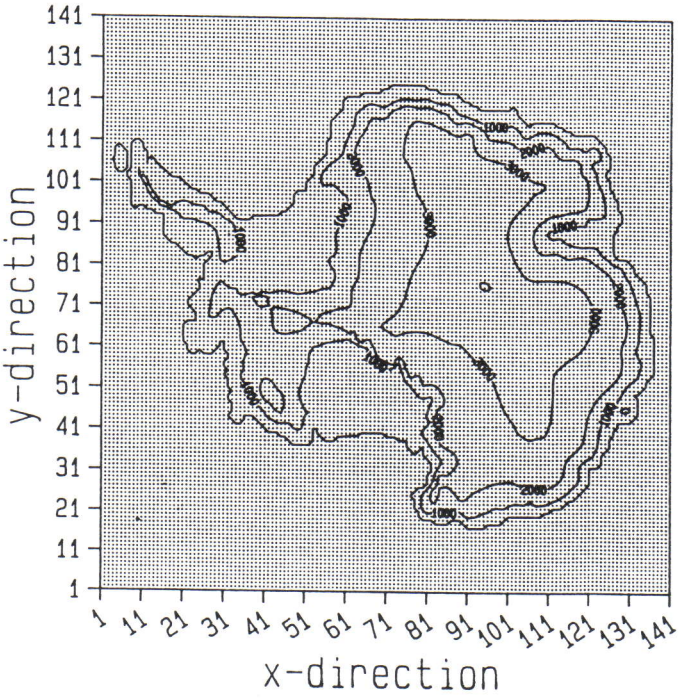

Fig.1 : Numerical grid on which the calculations take place. Every point represents a vertical, that is again subdivided into 11 layers. Contour lines are for surface elevation.

Fig.2 : Present bedrock topography as digitized on the 40 km grid. Note the high resolution, in particular in the coastal mountain ranges as e.g. the Transantarctic Mountains. The subshelf topography in the Ronne-Filchner and Ross areas have been digitized using most recent data and deviate locally from the original SPRI maps.

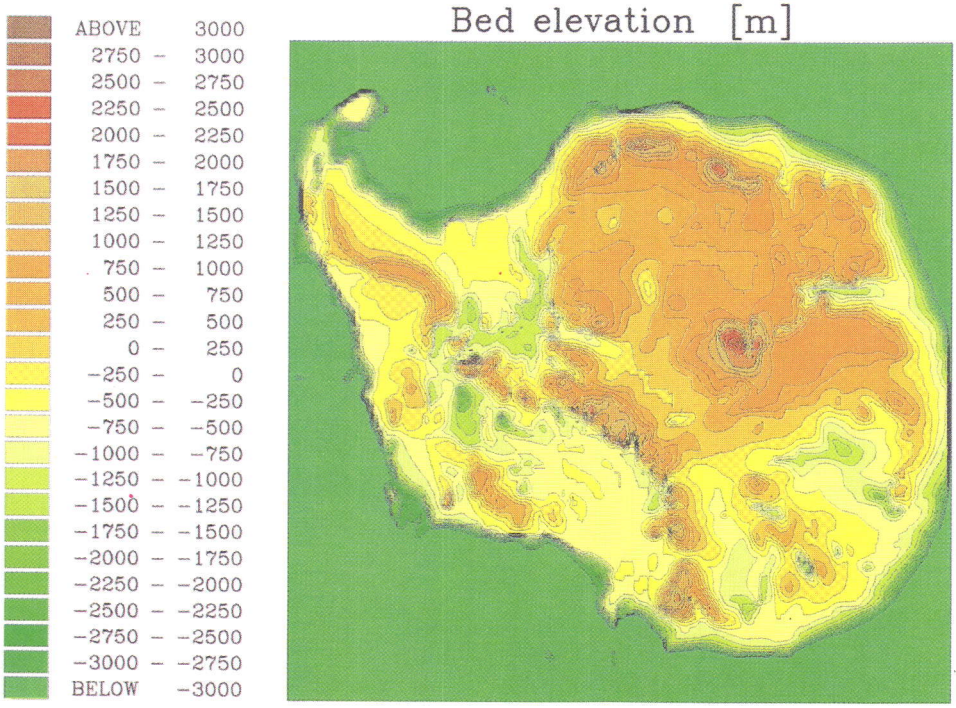

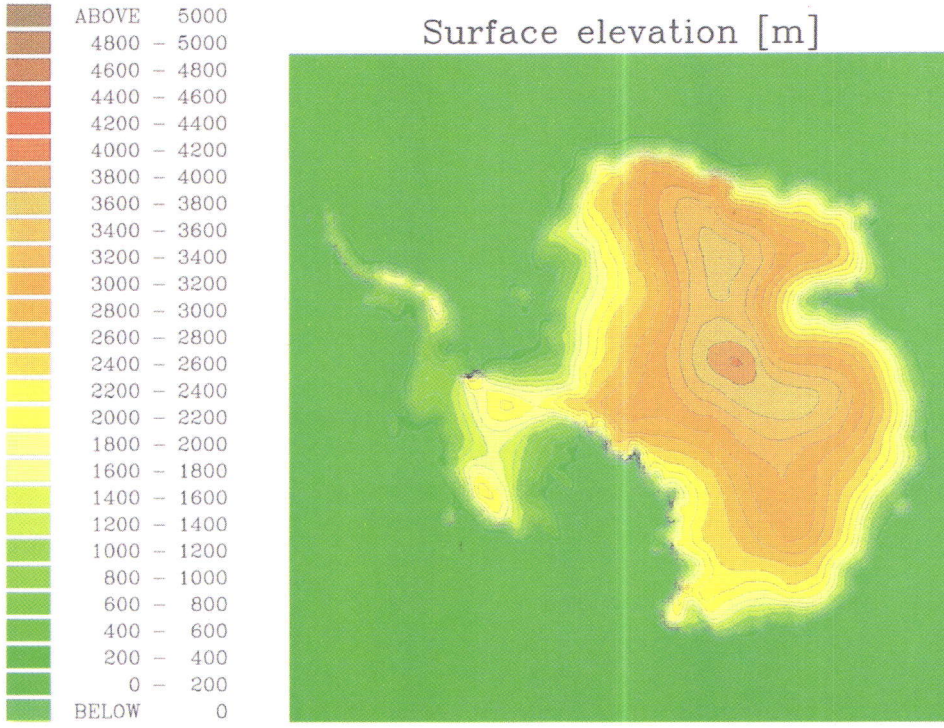

Fig.3 : Present surface elevation of the Antarctic Ice Sheet, used as input in the diagnostic model runs.

Fig.4 : Present ice thickness distribution. This data set was derived from the surface and bedrock elevation datasets, where in the ice shelf areas a constant ice density of 910 kg m^{-3} is used.

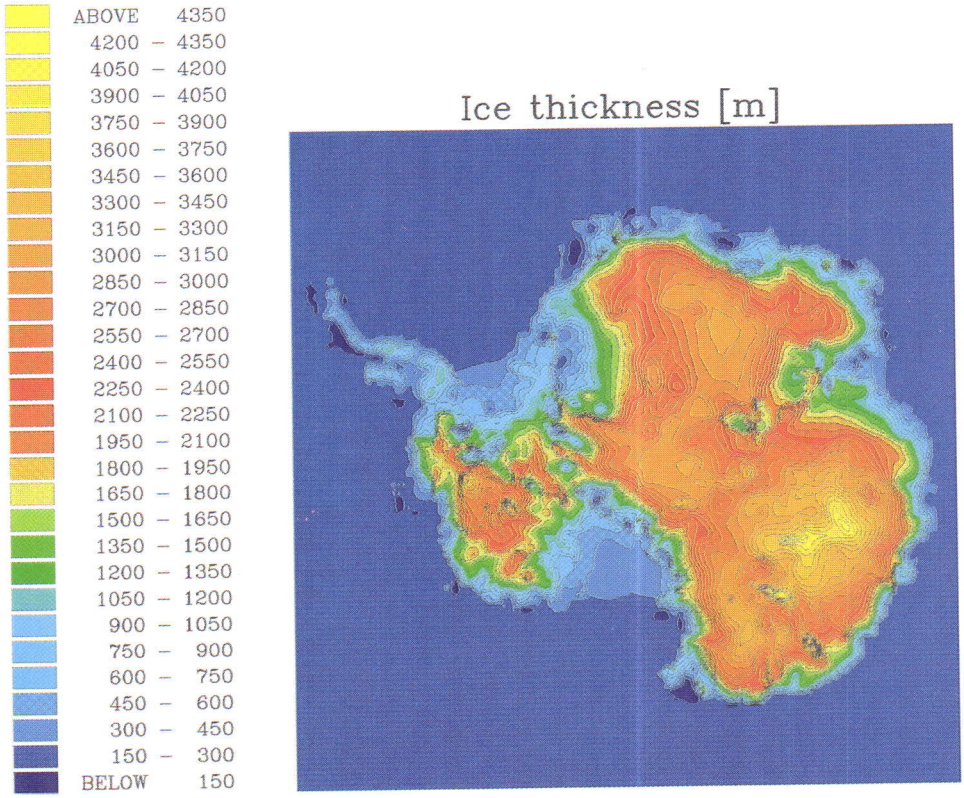

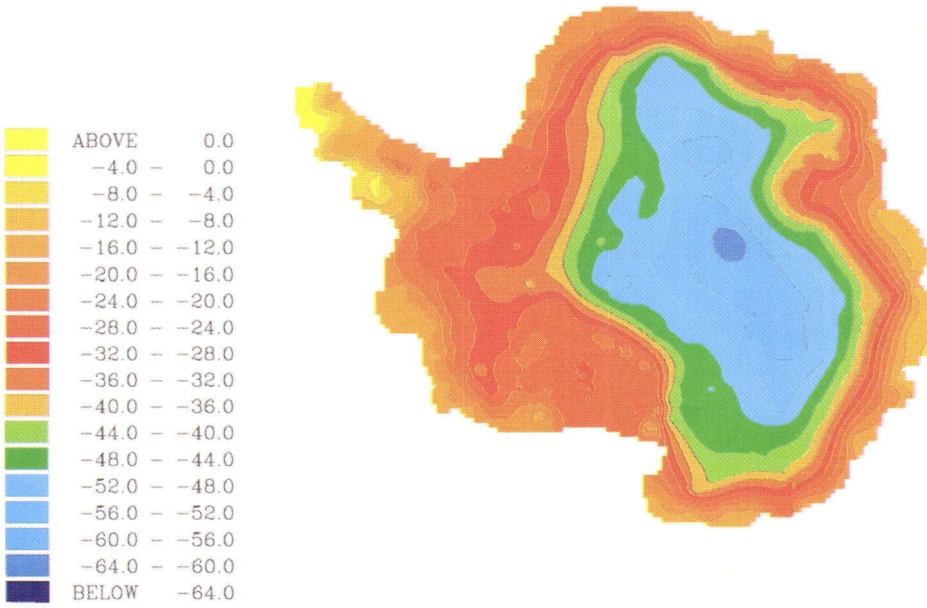

Fig.5 : Upper boundary condition for the temperature calculations. This data set was derived from an irregulary distributed 1000-point set of measurements that were interpolated on a regular 40 km grid. No large scale smoothing or cleaning up of these data was attempted, in part explaining some local irregularities.

Fig.6 : Accumulation rate data set, derived from an irregularity distributed 1000-point set of measurements that were quadratically interpolated onto the 40 km grid. Note the large scatter in places due to the absence of large scale smoothing and preliminary data cleaning. Nevertheless, some 'irregularities' represent real features, as the low accumulation rates over Siple Dome (West Antarctica) and upstream Lambert Glacier.

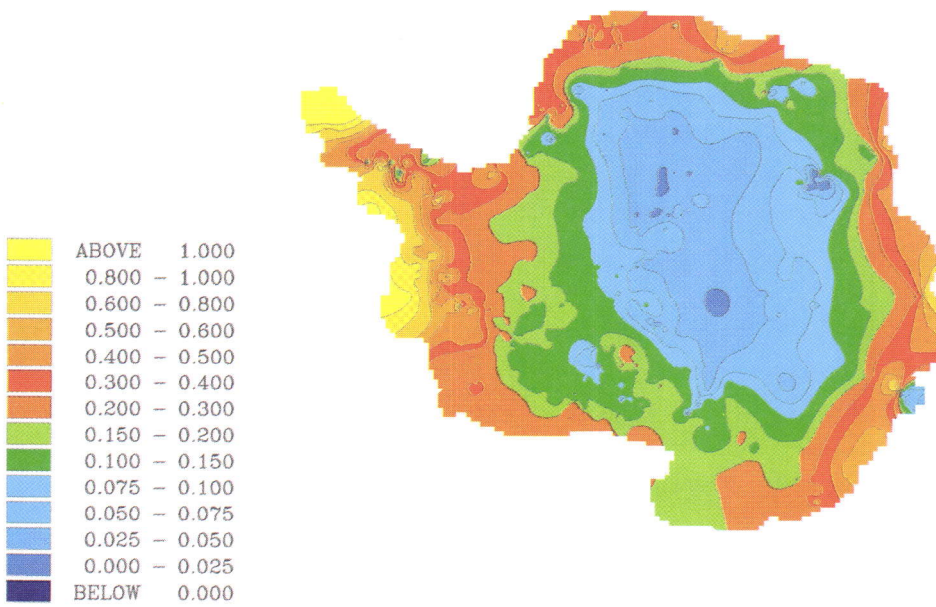

4. FIRST RESULTS : A DIAGNOSTIC SIMULATION

The first numerical experiment carried out with the model mainly aimed at finding a (quasi-) steady state temperature and flow field to be used in forthcoming experiments, where more degrees of freedom will be allowed to come into play. To this purpose, the present ice sheet geometry (bed elevation and ice thickness) was kept fixed and the coupled velocity and temperature field run 100000 years forward in time, nearing a stationary state. In the ice shelves, however, velocity - temperature coupling was not considered, and a constant flow parameter used (for -10°C). So, at this stage, interaction of the velocity field with stress conditions and the ice sheet geometry was not considered. This approach is similar with the 'dynamics velocity' approach of Budd et al. (1971) in their Derived Physical Characteristics of the Antarctic Ice Sheet.

Results for several main model variables are displayed in figs. 7-11. As a general tendency, vertically integrated velocities (fig.7) are below 1 m/year in central East Antarctica and reach typical values of about 100-200 m/years at the ice sheet / ice shelf transition zone. Main controls on this field are the mean ice temperature in basal layers, surface gradient and to a lesser extent ice thickness. It thus comes as no surprise to find high velocities where basal temperatures are high and vice versa. Suprisingly low 'diagnostic' velocities are found in Coates Land, the South Pole area and in parts of George V land. High velocities (in the 200-400 m/y bracket) show up nicely in outlet glaciers and ice streams, in particular Jutulstraumen, Shirase Glacier, Lambert Glacier, Totten Glacier, as well as the individual glaciers debouching into the ice shelves. Also the various West Antarctic regions of fast flow entering the Ross Ice Shelf, can be distinguished. In the Ross and Ronne-Filchner ice shelves velocities correspond suprisingly well with observations (MacAyeal and Thomas, 1986 ; Lange and MacAyeal, 1986), considering the fact that the pre-exponential flow-law parameter is the one for -10°C and no further tuning was attempted.

The pattern of basal temperatures relative to the pressure melting point (fig.8) appears to be quite strongly controlled by the ice thickness in central East Antarctic areas. The coolest basal ice is actually reached on the top of the Gamburtsev Subglacial Mountains, where the ice is relatively thin (1500 - 2000 m). On the other hand, where the ice is thicker, vast areas of basal melting show up, in particular Wilkes Land is characterized by a large temperate basal ice layer that is moreover extending all the way to the coast. It would be interesting to make a comparison here with radio-echo sounding records indicating the presence of basal meltwater lakes in several locations. Exept for the outlet glaciers, where substantial converging flow and dissipative heat generations takes place, coastal areas on the East Antarctic Ice Sheet are characterized by cold ice. This seems to be mainly the consequence of mountain ranges, and hence, the presence of thin ice, than a mere

thermal effect, where cold ice advection becomes dominant with respect to dissipation. Also basal melting is a dominant feature in the West Antarctic Ice Sheet.

An interesting derived quantity of the diagnostic flow field is the local ice thickness imbalance $\partial H/\partial t$ (fig.9). It is the sum of the mass flux divergence and the accumulation rate and indicates the momentaneous change in ice thickness if flow continuity would be applied. Its value is generally comprised between -0.5 and +0.5 m/y, however, with somewhat higher and more variable values in the West Antarctic Ice Sheet. Values in the ice shelf may be an indicator for basal melting (positive) or basal accretion (negative) and have been interpreted as such in several studies (e.g. MacAyeal and Thomas, 1986). With values in the 0 to 0.5 m/y bracket dominating over large areas, one may suspect velocities and/or basal temperatures be too low, altough the employed pre-exponential flow parameter is known from precursive coarse grid 3-D and 2-D studies to produce ice thicknesses close to the observed state. Of course, this positive overall imbalance may also very well be a real feature of the Antarctic Ice Sheet.

It would be most interesting at this point to speculate on possible explanations for these modelled imbalance, and the obvious discrepancies between the 'dynamics velocity' of fig.7 and the velocity pattern one would expect in more 'balanced' situations. As a matter of a fact, those thoughts are very likely to dominate our future work and model experiments.

Several explanations may be presented to explain the observed imbalances :

i) it is a real feature : the Antarctic Ice Sheet geometry is not in steady state with present-day environmental conditions, in particular with accumulation rate and/or temperature distribution.

ii) ice temperature is not the only ice property affecting ice hardness. In particular, crystal fabric (preferential crystal orientation), impurity and water content have non-negligible influences on the creep behaviour of ice.

iii) basal sliding is not taken care of well in the vertically integrated ice velocity calculations.

iv) the only free parameter for the temperature calculations, the geothermal heat flux, deviates substantially from the adopted 1.3 heat flow units and/or shows an important spatial variation.

v) the present temperature distribution is not in steady state, i.e. it is still reacting to long term climatic changes.

With respect to (iv) a few additional experiments with the present configuration were carried out with a geothermal heat flux of 1.43 heat flow units (HFU) and 1.17 HFU respectively, i.e. within the bounds found on several continents (Sclater et al., 1980). Results are shown in figs. 10 and 11. Altough the areas of basal melting appear to depend substantially on the value adopted, the influence on the pattern of the ice thickness imbalance is however rather limited (not shown).

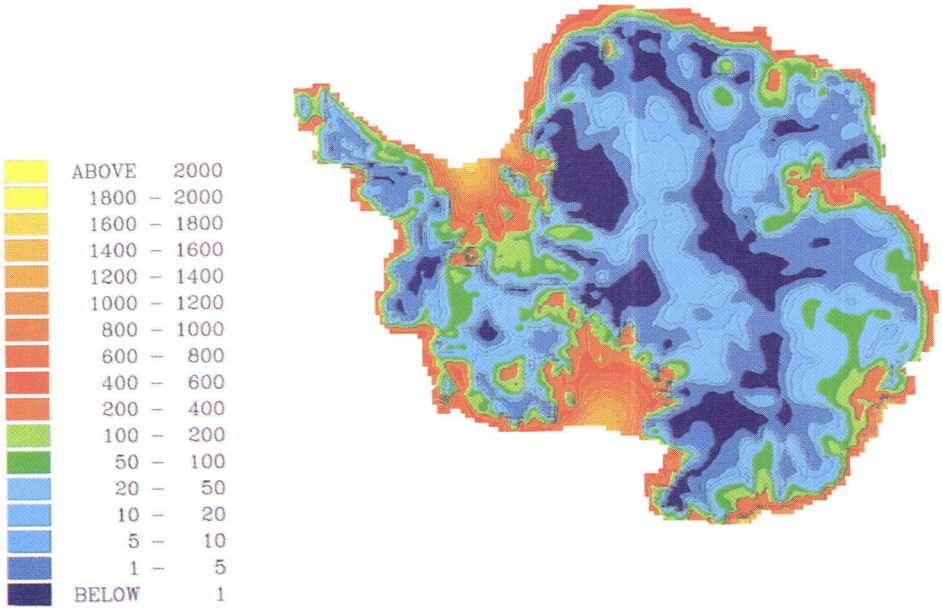

Fig.7 : Flow field in a diagnostic model run, where the geometry is kept constant, and the coupled velocity and temperature field is run 100000 years forward in time.

Fig.8 : Basal temperature field corresponding to fig.7.

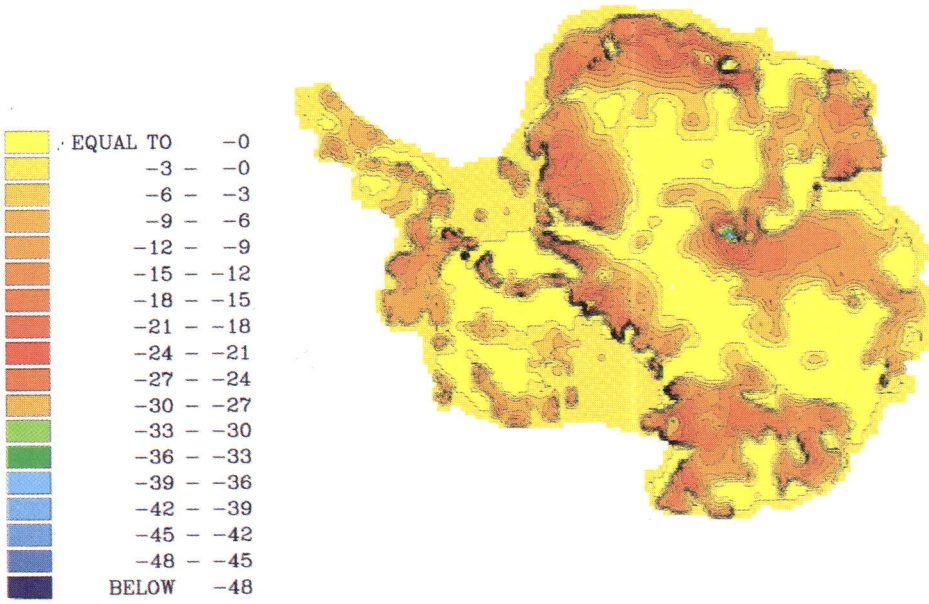

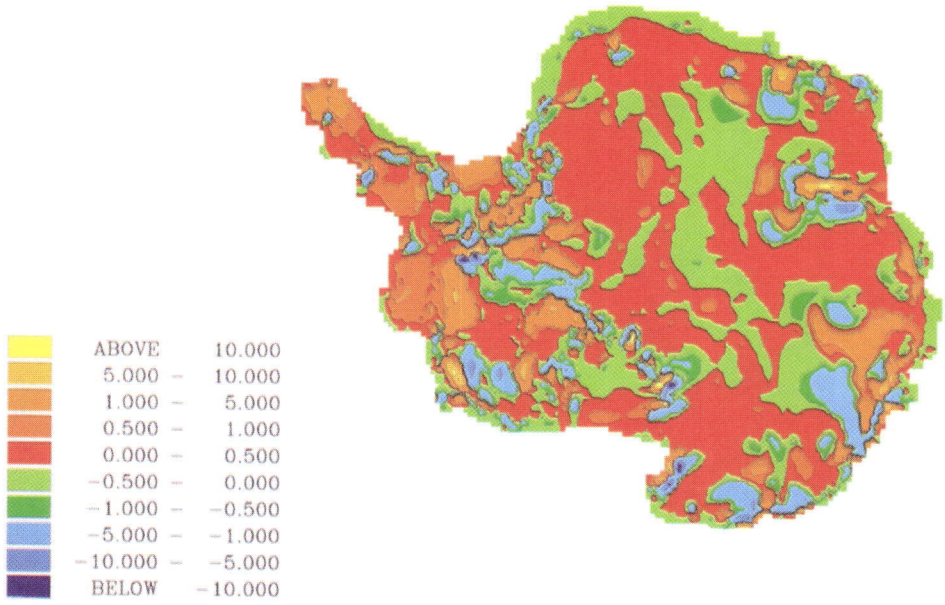

Fig.9 : Local ice thickness imbalance $\partial H/\partial t$, or the sum of the mass flux divergence and the accumulation rate. It is the momentaneous change in ice thickness if mass continuity would be applied.

Fig.10 : A comparison of the extent of grounded ice areas at basal melting in case the geothermal heat flux is lowered by 10%. The orange color refers to areas that have become frozen at the bed. Yellow areas are at the pressure melting point in both model runs.

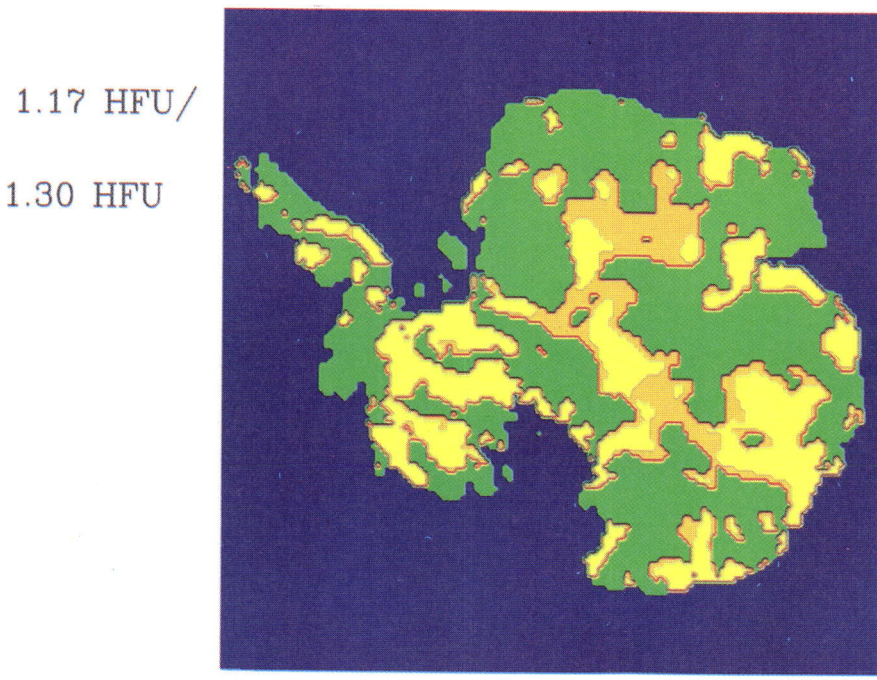

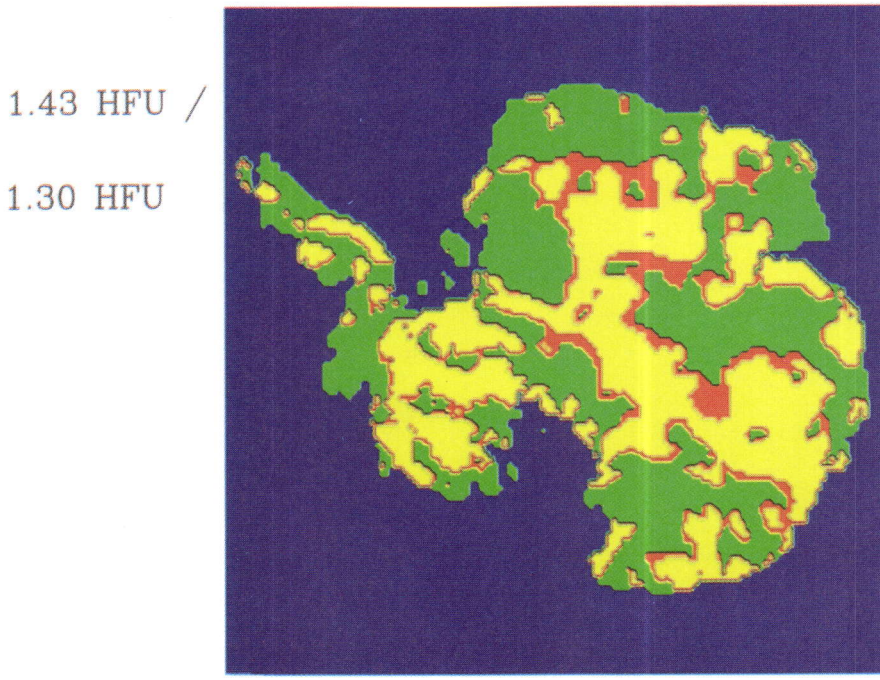

Fig.11 : A comparison of the extent of grounded ice areas at basal melting in case the geothermal heat flux is increased by 10%. The red color now characterises areas that have become wet-based. Yellow areas are at the pressure melting point in both model runs.

5. SUMMARY AND CONCLUSIONS

In this report a brief overview was presented of a numerical 3-D ice sheet - ice shelf model with geodynamics for the Antarctic Ice Sheet. This model has been developed to investigate the flow regime and the interaction of the ice sheet with changing environmental conditions. The time scale of main interest is the glacial - interglacial cycle and the essential environmental forcing is given by the accumulation rate, surface temperature and sea level stand. The model contains a maximum amount of degrees of freedom (the complete 3-D geometry, in fact) while the ice flow in the respective parts (grounded ice sheet, ice shelf and grounding zone) has been derived from basic stress relations, assuming a Glen-type flow law.

Up to now, a 2-D flowline version of the model has been extensively used to investigate the thermomechanical reaction of the East Antarctic Ice Sheet following a glacial - interglacial climatic shift. These studies (Huybrechts, 1987 ; Huybrechts and Oerlemans, 1988) have among other things, brought to light that : i) creep instability following a sudden climatic warming is unlikely to be a possible mechanism to initiate large scale surging of the East Antarctic Ice Sheet, in essence due to the stabilizing effect of horizontal heat advection. ii) this glacial - interglacial climatic shift initially leads to increased ice thickness due to enhanced accumulation, whereafter this trend is reversed due to basal warming. iii) time scales of adjustment are of the order of 10^4 years, implying that the present ice sheet has not reached steady state and iv) typical elevation changes during the glacial cycle in Central East Antarctica are of the order of 100 m, implying that the palaeotemperature signal recovered in Vostok Station is primarily of climatic origin.

At present, the high - resolution 3-D model has been implemented on a CRAY-2 super computer and first results of a diagnostic (i.e. fixed geometry) study have been obtained. In first instance, the model has proven to yield stable solutions, which is by no means a trivial result. In a recent paper (Hindmarsh and Hutter, 1988), solving the coupled thermomechanical equations for cold ice flow still appeared to lead to runaway effects, thereby preventing stationary fields to be reached. A preliminary interpretation of this diagnostic study then seems to indicate that i) the stationary flow field is dominated by temperature effects and cannot possibly be in accordance with continuity requirements. ii) West Antarctica and the Antarctic Peninsula are essentially wet - based and iii) temperate basal ice in the East Antarctic is confined to interior thick ice areas and fast-flow outlet regions at the margin, while the intermediate ring is cold, even when the principal unknown, the geothermal heat flux, is increased by 10%. iv) the ice sheet may be in overall positive balance, i.e. is still growing.

However, with respect to the burning question of the present state of the ice sheet, more

experiments, in which all degrees of freedom come into play, will have to be conducted. In particular, due to the long adjustment time scales involved, a long time integration involving the complete Vostok climatic record over 160,000 years has to be envisaged. These studies are on the way.

CHAPTER 2

ICE THICKNESS MEASUREMENTS AND ICE DYNAMICS IN THE SØR RONDANE, DRONNING MAUD LAND, ANTARCTICA

1. SPECIFIC RESEARCH GOALS

The East Antarctic Ice Sheet screens off the most of the direct glacio-geologic information on the bedrock and restricts the observations to a few isolated mountain areas. Most of the information regarding the glacial history has come from investigations in the Transantarctic Mountains (Mayewski and Goldthwait, 1985). However a large body of information can also be found on the nunataks and in some dry valleys situated in the mountain areas bordering the coast of Dronning Maud Land, Enderby Land and a few other marginal areas of the East Antarctic Ice Sheet. In contrast with the Transantarctic Mountains some of these areas are quite close to the present ice divide.

Apart from providing the necessary data on the dynamics of the ice cap, the marginal coastal mountains constrain the ice movement and create typical outlet glaciers. As such they can be said to contribute to the stability of the Antarctic Ice Sheet. The Sør Rondane Mountains provide a particular beautiful example of the damming effect of such a coastal mountain range.

The Sør Rondane were previously investigated by Belgian Antarctic Expeditions (1958,1959,1960,1964,1965 and 1966) situated 150 km south of the former Belgian Base Roi Baudouin. Geological and geomorphological investigations by Van Autenboer (1964) indicated already the present deglaciation of the range and produced evidences for more extensive glaciations in the past. Glaciological investigations by Van Autenboer and Decleir (1974,1978) put into evidence the damming effect of the Sør Rondane by distinguishing the true outlet glaciers from glaciers with a more local (or alpine) character. The same authors made an approach to estimate the total glacier discharge through the 220 km long mountain range.

In 1985 a new station, Asuka, 50 km to the north of the Sør Rondane Mountains, was established by the Japanese Antarctic Research Expedition (JARE 26). Geological and glaciological observations in this area are now being carried out by Japanese parties. During the Austrial summer 1986-87 a Belgian team was invited to join the Sør Rondane geomorphological and geological

Party of JARE 28.

This allowed a 2-man team of the University of Brussels (H.Decleir and L. De Vos) to continue the ice dynamics investigations of the Sør Rondane, started during the former Belgian Expeditions and try to situate the function of the Sør Rondane in the outflow of the ice sheet of Droning Maud Land as well as to explain the observed glacier variations, within the ice dammed mountain area.

The Belgian team boarded Ice Breaker Shirase November 28th in Fremantle, Australia, arrived in Breid Bay (Antarctica) on December 12th. By means of helicopter and Snow Tractor Transport the Sør Rondane Party reached Asuka Base on January 4th. From there, the Sør Rondane Party left for a stay of 34 days in the mountains. The Party returned to Breid Bay on February 12th. The ship reached Port Louis in Mauritius on March 15th.

2. ICE THICKNESS MEASUREMENTS, INSTRUMENTS AND METHODS

2.1. Instruments

Over the vast covered areas of continental ice sheets - remote form steep mountain ranges and nunataks - the infinite slab method to calculate ice thickness from gravity measurements has been widely used in the past. The method was particulary useful for rapid ice thickness determinations between seismic reflection stations and oversnow traverses during and following the IGY.

The method became largely obsolete when airborne radio echo sounding was introduced in the late sixties. The latter method allowed for the first time rapid and accurate measurements to be made over terrain which is characterised by difficult and dangerous access. Since that time large scale mapping of the subglacial relief became possible and was carried out both over Eastern and Western Antarctica, generally from airborne platforms (Drewry, 1984).

The usual equipment for radio echo sounding of ice have been large instruments, intended for installation in aircraft or on sledges. No commercial equipment is at present available. The Scott Polar Research Institute, which has a great deal of experience in echo sounding equipment, developed a simplified version, the "IDIOT" (Ice Depth Instrument, Operator Transportable) which can be carried out by one operator and which was thought to be valuable over steep sloping terrain and moraine covered ice.

A detailed specification of this instrument is given below. Important points to note are that it is battery powered, all solid state, light weight with a backpack harness for transport and operation, and with oscilloscope monitor and readout strapped to the operator's chest. A digital display of delay time is provided, related to a marker which the operator sets on the bottom echo. This facilitates manual or audio tape recording of thickness values. No direct recording of the instrument's output is initially provided, as the keynote is simplicity.

Specification

Transmitter:	
Type:	Switched oscillator with solid state PA
Center frequency:	160 MHz
Peak Power:	40 W
Pulse length:	250 or 500 nS, switchable
Receiver:	
Type:	TRF with log amplifier
Bandwith:	20 MHz
Log dynamic range	80 dB
Antenna:	Thick dipole,backpack mounted
Power:	Internal rechargeable sealed batteries
Physical:	
Total weight:	ca. 9 kg
Maximum dimension:	0.95 m (antenna)
Configuration:	Front and backpack mounted units, supported on operators shoulders, antenna mounted on back
Performance:	
Minimum ice thickness:	ca. 50 m
Maximum ice thickness:	dependent upon ice conditions, up to 1000 m in good conditions

The prototype equipment was acquired by the Belgian Sience Policy Office (National Programme on Antarctic Science), and has been given field trials in Switzerland before taking it to Antarctica. Unfortunately, a fault was present on this equipment which did not reveal itself during initial trials, and no succesful echo soundings of ice were made in the field. The cause of the faulty

behaviour has been located and the instrument is now being transformed possibly for both portable and sledge-mounted use.

2.2. Gravimeter-survey

Ice thicknesses were measured with a standard Worden gravimeter. 11 gravimeter traverses were carried out accross the glaciers of the central part of the Sør Rondane. As these profiles were chosen between well identificable points on rock at both sides of the glacier location and distance between the gravimeter stations would be easily determined from the mileage reader of the snow scooter. In the middle of the glacier distance between the gravity stations were generally 0.5 or 1 km. Altitudes were determined in every station by aneroid altimetry. However, near the valleysides position and altitude of the gravimeter stations, both on the glacier and the adjacent rock, were determined by theodolite tacheometry. Here the distance varied between 100 and 150 m. As most of the profiles were run back and forth altitudes and gravimeter measurements were taken as the mean of two values. This procedure eliminated drift phenomena of the instruments.

2.3. Interpretation of gravimeter ice thickness measurements

Unlike radio echo sounding the gravimetric method for ice thickness determination requires difficult modelling and is not always unambiguous. The ice thickness in a cross section of a valley glacier is calculated by an iterative procedure in which the computed gravity effect of a model cross section is compared with observed gravity values measured on the glacier surface (De Vos and Decleir, 1988).

Generally the areal integral representing the gravity effect of the two-dimensional ice mass is replaced by a line integral which is then numerically solved by a polygonal approximation of the periphery of the ice body (Talwani's method, see e.g. Telford et al, 1976). In our case the upper vertices of the polygon - which correspond with the gravimeter observation stations - are known, while the lower vertices - vertically beneath the same observation points - relate the unknown subglacial bedrock (fig.12a). It is also possible to compose the unknown ice mass by a set of rectangular vertical prisms extending from the bedrock to the ice surface. Each prism has then a

gravimeter station as boundary in the horizontal x-direction (fig.12b). It is clear that the results of both methods, which will henceforth be referred to as the polygonal and the prism method respectively, converge if the number of measuring stations becomes large.

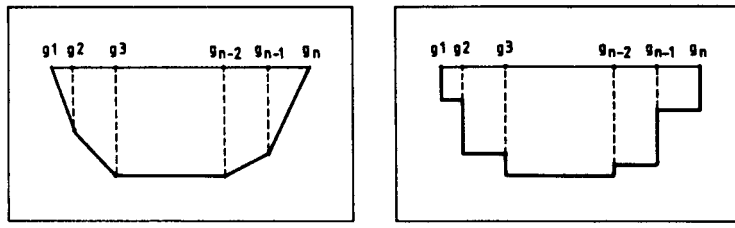

Fig.12 : Polygonal (left) and prism (right) approach of subglacial relief

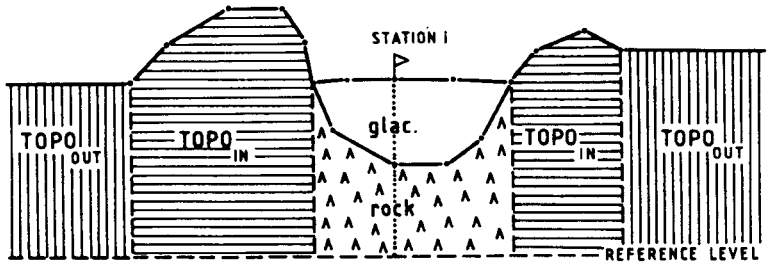

Fig.13 : Zonal subdivision of terrain for ice thickness calculations

The gravity values were first corrected for lattitude and height. To obtain a relatively fast and easy-to handle calculating model the traditional Bouguer and terrain corrections were replaced by a "zonal" algorithm (fig.13). The outer zones of the model ($Topo_{out}$) contribute a relatively minor amount to the total attraction values of the surrounding rock, therefore each outer zone can be approximated by a semi infinite slab, similar to the traditional Bouguer correction. The inner zones adjacent to the glacier ($Topo_{in}$) are much more important for the measured attraction forces. For this zone the total mass above the reference level was calculated by the Talwani method. The latter method allows the gravity effect af an arbitrary two-dimensional mass to be calculated by a polygonal approximation of the body (e.g. Telford et al.). The surface profile of this body was digitized from exsisting topographic maps.

Finally the attraction of the two masses underneath the glacier surface (g_{glac} and g_{rock}) are calculated. The first mass is the glacier mass and the second one is the mass of rock which lies

between the glacier bedrock and the reference level. The interface between these two masses is the unknown subglacial topography (De Vos and Decleir, 1988).

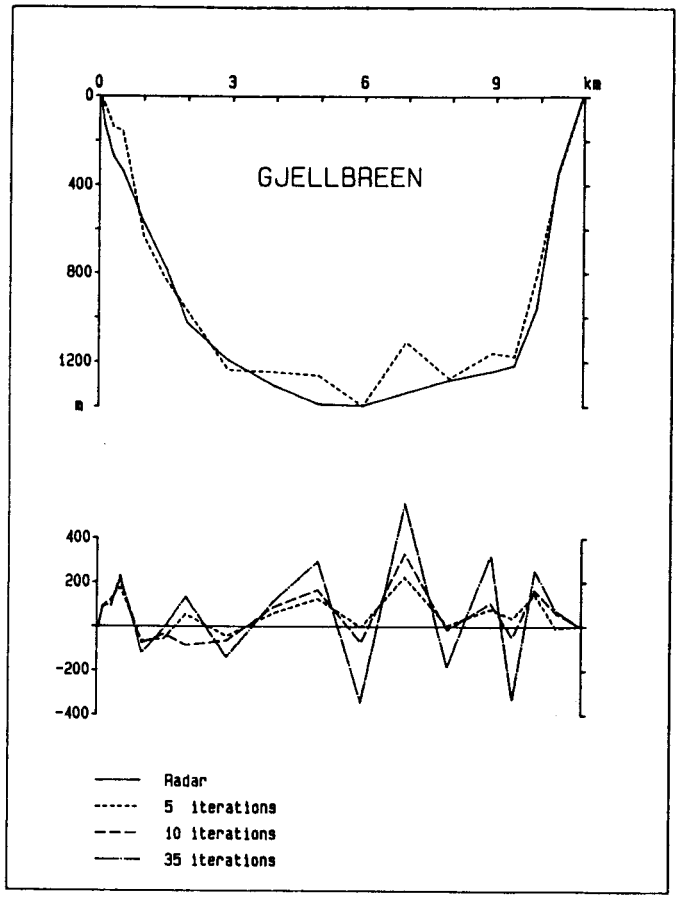

Fig.14 : Upper : comparison of radar and gravimeter ice thickness over 12 km long oversnow traverse over Gjelbreen using polygonal approach

Lower : difference between gravity and radar ice thickness

3. COMPARISON OF RADIO ECHO SOUNDING AND GRAVIMETER ICE THICKNESS RESULTS

Both airborne and oversnow radio echo sounding surveys were carried out by JARE 27 (F. Nishio and H. Ohmae). Use was made of a pulsed radar system operating at center frequency of 179 MHz, designed by the National Institute of Polar Research (NIPR) and built by Meisei Denk co, Tokyo.

Fig. 14 and 15 show the comparison of radar and gravimeter ice thickness over the 12 km long oversnow traverse over Gjelbreen (Decleir, Nishio and Ohmae, 1989). As explained above the gravimeter profile is obtained by an iteration process, where after each iteration process the computed and the observed gravity anomalies are compared. This difference diminishes rapidly during the first five iterations. Once below 1 mgal the difference decreases rather slowly. The bottom figure in fig. 14 and 15 shows the difference between gravity and radar ice thickness. It can be seen how the increasing fit between observed and computed gravity is - once below 1 mgal - accomplished by an enhanced zigzag ice thickness profile especially in the lower part of the valley floor. Fig. 14 shows the results for the polygonal method and fig. 15 for the prism method. It can be concluded that with a relatively dense series of stations the prism method gives the better results and that the iteration process should be stopped after approximately 5 iterations. More or less the same results were obtained from a comparison over a 14 km traverse over Gunnestadbreen.

The comparison allows two main conclusions : (i) when sufficient care is taken, the gravity values can give comparable results to the radio echo sounding technique (ii) an underestimate of 10% in ice thickness and ice discharge is inferred regarding the previous gravity results of Van Autenboer and Decleir (1974,1978) in their study to evaluate the total ice flux through the Sør Rondane Mountains.

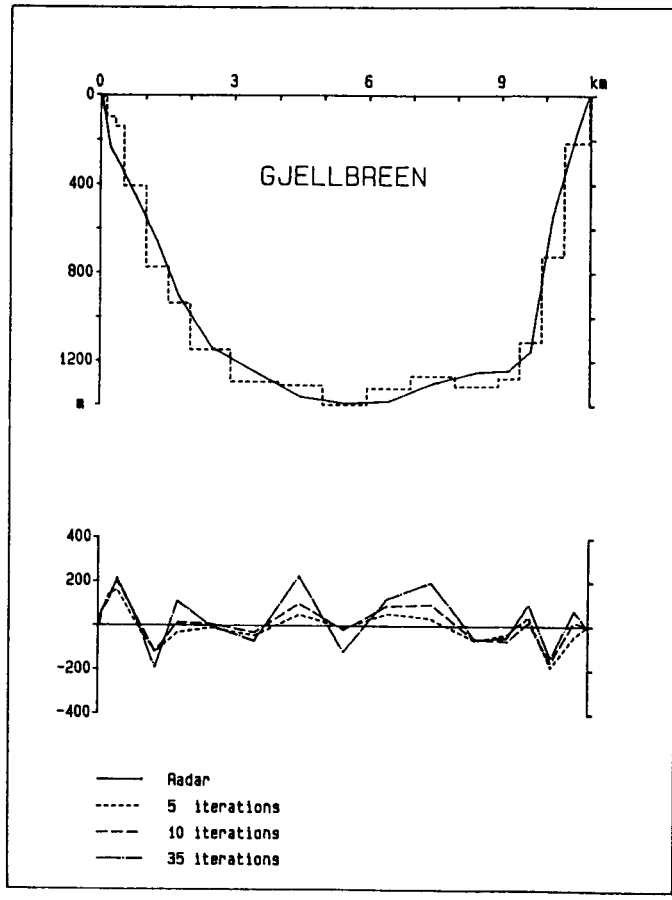

Fig. 15 : Upper : comparison of radar and gravimeter ice thickness over 12 km long oversnow traverse over Gjelbreen using prism approach

Lower : difference between gravity and radar ice thickness

4. SUBGLACIAL RELIEF IN THE SØR RONDANE

Fig. 16 shows the 11 gravimeter traverses carried out across the glaciers of the central part of the Sør Rondane. Whereas Gjelbreen can be considered as an outlet glacier (mass flux value of 0.074 $km^3 a^{-1}$), Jenningsbreen is clearly a local glacier (mass flux of 0.0025 $km^3 a^{-1}$). This is confirmed by the composition of the hillocky moraine (shear moraine?) on the eastern side of this glacier (see i.a. Souchez, 1966). This local origin of the ice was confirmed by ice samples in the moraine field whose isotopic composition revealed an origin in the snow fields just behind the mountain range (personnal communication R. Souchez). The results of all the profiles were presented in the 9th Symposium on Polar Meteorology and Glaciology (National Institute of Polar Research, Tokyo, December, 1987). Here examples are shown of Gjelbreen North (GN), Gjelbreen South (GS), Jenningsbreen Central (JC), Gjelbreen Upper (GU) and Jenningsbreen South (JS). These profiles illustrate different characteristics of the glacierization of the range and reveals fjord landscape underneath the ice cover.

The profiles in the north (e.g. Profile GN, Fig.17) demonstrate the U-shaped character of the valleys as well as the local overdeepening with the bottom floor well below sea level. The profiles Gjelbreen South (fig.18) and Jenningsbreen Central (fig.19) form more or less one traverse line and show a very similar glacier cross profile notwithstanding the different mass fluxes. The profiles Gjelbreen Upper (fig.20) and Jenningsbreen South (fig.21) situated near the upper end of the glacier clearly mark the steeply sloping valley floor, underscoring the damming effect of the Southern threshold of the range on the ice flux towards the north. In this area a clear relationship can be found between surface topography, ice depth and surface characteristics. The study of this relationship must however awaitv the image processing of Thematic Mapper and Spot scenery's, recently obtained of this area.

Profiles obtained over Mefjellbreen (not shown) contradict somewhat the apparent block faulted appearance of this part of the range (Van Autenboer, 1964). Indeed the subglacial information now available suggests the existence of a subglacial ridge connecting Mefjell and Menipa.

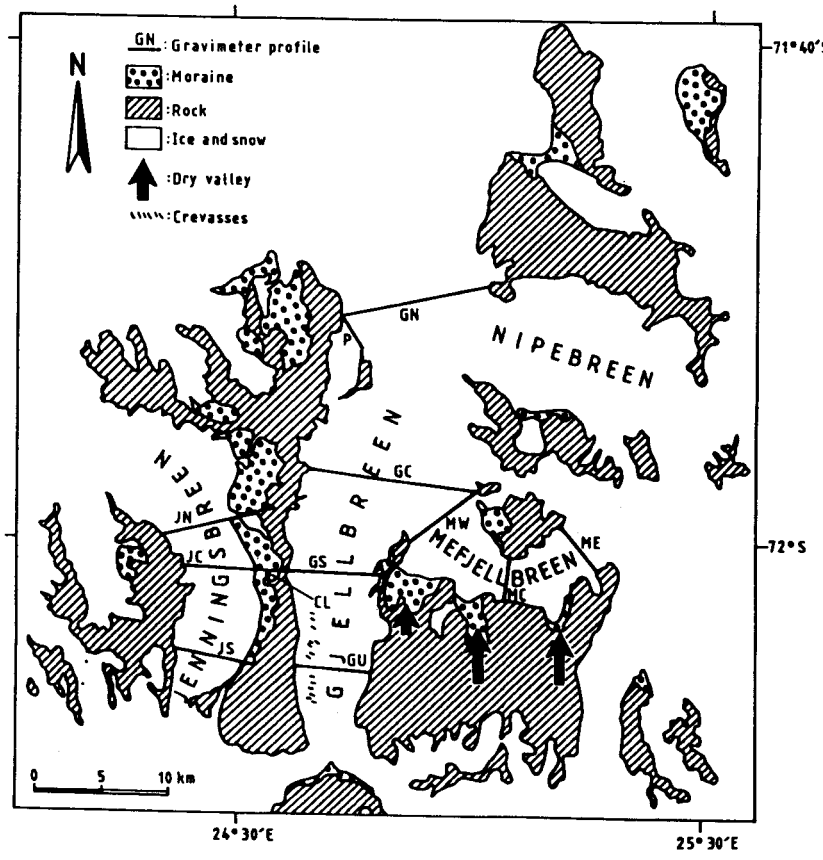

Fig.16 : Central part of the Sør Rondane and situation of the gravimeter profiles

Fig.17 : Gravity profile of Gjelbreen North (GN)

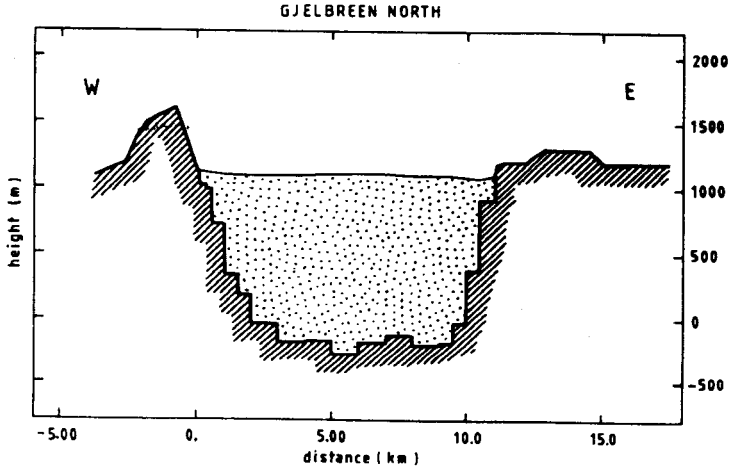

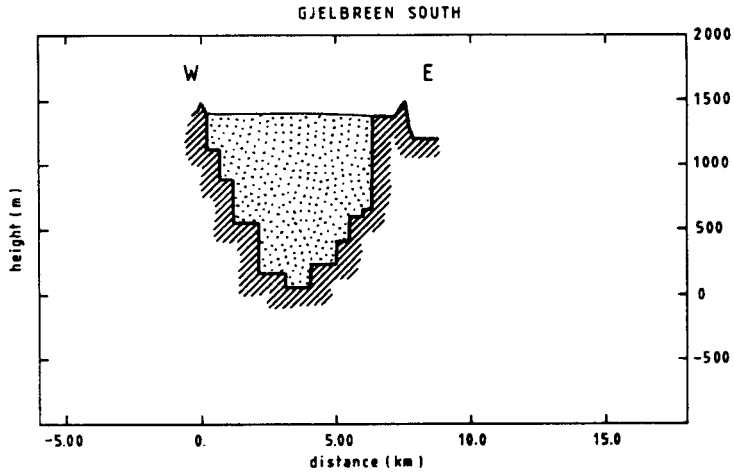

Fig.18 : Gravity profile of Gjelbreen South (GS)

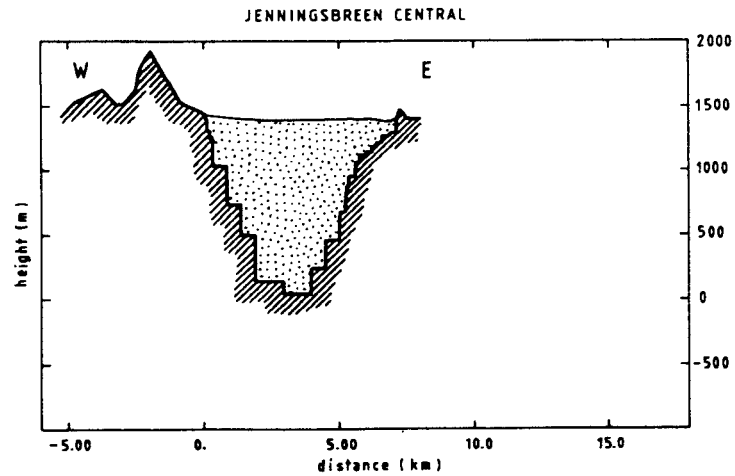

Fig.19 : Gravity profile of Jenningsbreen Central (JC)

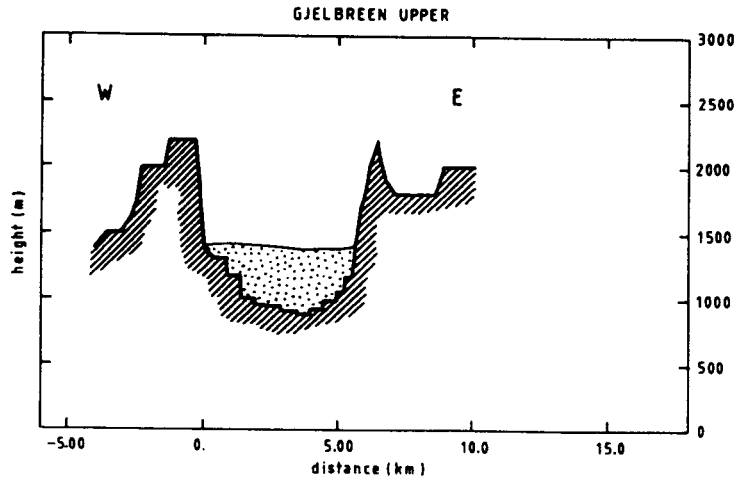

Fig. 20 : Gravity profile of Gjelbreen Upper (GU)

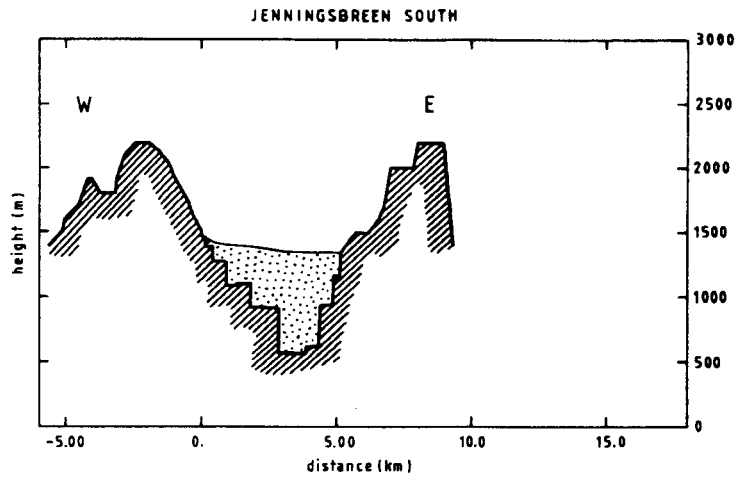

Fig.21 : Gravity profile of Jenningsbreen South (JS)

5. DYNAMICS OF THE ICE SHEET

The divergent nature of the ice flow from the Fuji Ice Divide south of the Sør Rondane is apparent on satellite images and from the stream line analysis of Van Autenboer and Decleir (1974,1978). The total ice discharge through the Sør Rondane was estimated by the same authors at 1.60 $km^3 a^{-1}$. The discharge along an equally long stretch of the coast downstream from the Sør Rondane was estimated as 3.48 $km^3 a^{-1}$, this is twice the amount flowing through the mountains (Nishio et al, 1984). From this it is concluded that if this mass deficit is not compensated by heavy snow accumulation in the area between mountains and coast, an imbalance and a lowering of the ice sheet must be inferred. Anyway, within the Sør Rondane the extensive blue ice areas and erosional features of the snow cover are signs of a glacier cover in recession.

A numerical one dimensional flow line model was developed to simulate the glacier behaviour. The model gives a description of the ice sheet dynamics, grounding line dynamics, coupling of an ice shelf and isostatic bed adjustment (cfr. Oerlemans and Van der Veen, 1984, Van der Veen, 1985). At present the model is being improved by incorporating the calculation of the temperature field, consisting of an expansion of the vertical temperature profile by means of a parabolic equation (F. Pattyn et al, in prep.). Inputs for the model are present bed elevation, surface elevation, surface temperature, mass balance, basal temperature gradient and parameters for the temperature calculation. Data were obtainedboth from the present field work and from data reports of previous Belgian investigations (Van Autenboer and Decleir, 1974). Mass balance and surface temperature needed to be parameterised in function of temperature and height, respectively.

Longitudinal profiles from ice divide to ice shelf through the mountain range were calculated for Gjelbreen, Jenningsbreen and Gunnestadbreen (figs.22, 23 and 24). The calculated longitudinal profile consists of 120 grid points, while for only a few points of them the data were available. Ice thicknesses for the other grid points were obtained by inter- and extrapolation based on the plastic ice flow theory (Paterson, 1981). At some points with extreme low surface gradient this might lead to local exaggerated ice thickness.

For Jenningsbreen, the steady state solution showed much higher velocities than those actually observed. This might be interpreted that Jenningsbreen is indeed a local glacier with its ice divide just behind the Sør Rondane as suggested by the isotope results. Gjelbreen and Gunnestadbreen on the other hand can be interpreted as true outlet glaciers.

Geomorphological and glacial-geological observations in the area indicate that the surface elevation was 500 m higher during a past glaciation (no dating). Different sensitivity experiments were carried out in order to simulate this glacial expansion : change in mass balance, change in temperature, change in sea level, and the combination of these elements. An additional simulation

was performed by shifting the ice divide by 200 km towards the interior. A 500 m ice thickness increase in the Sør Rondane can only be simulated by a shift of the grounding line towards the edge of the continental platform. The model results indicate that a shift of the ice divide cannot be held responsible for such an advance of the grounding line. It is clear that this can only be obtained by a lowering of the sea level, combined with a temperature drop of at least 10K or an increase in mass balance. Fig.25, 26 and 27 show a 500 m ice thickness increase by lowering the sea level with 150 m and a surface temperature decrease of 11K. Those conditions are typical for a large glacial stage and might help to identify the chronology of the observed glacier variations.

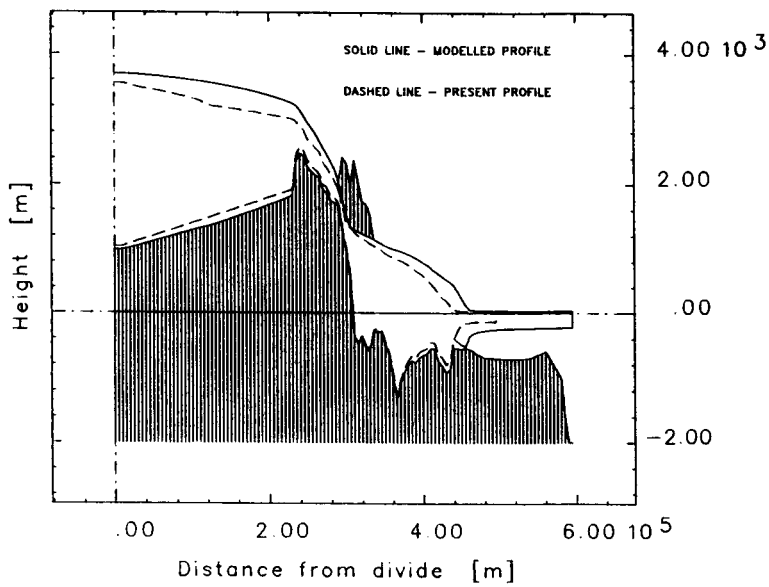

Fig.22 : Basic model run of the longitudidinal profile of Gjelbreen

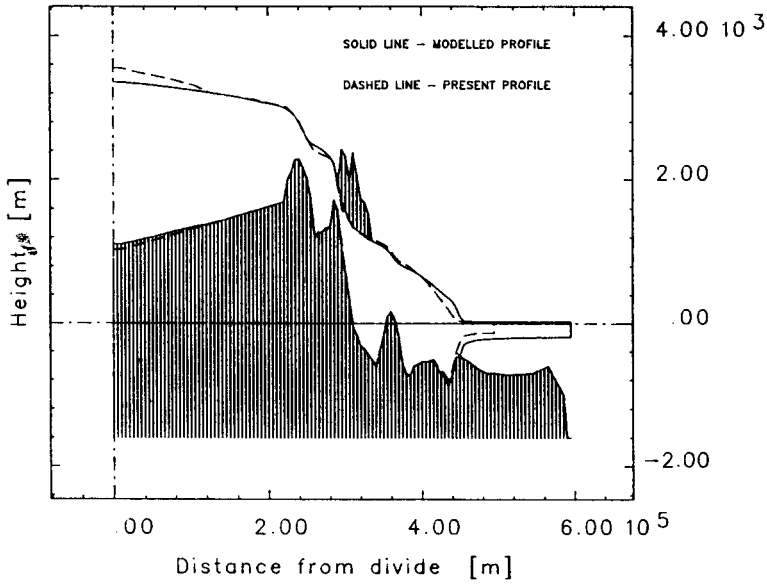

Fig.23 : Basic model run of the longitudinal profile of Jenningsbreen

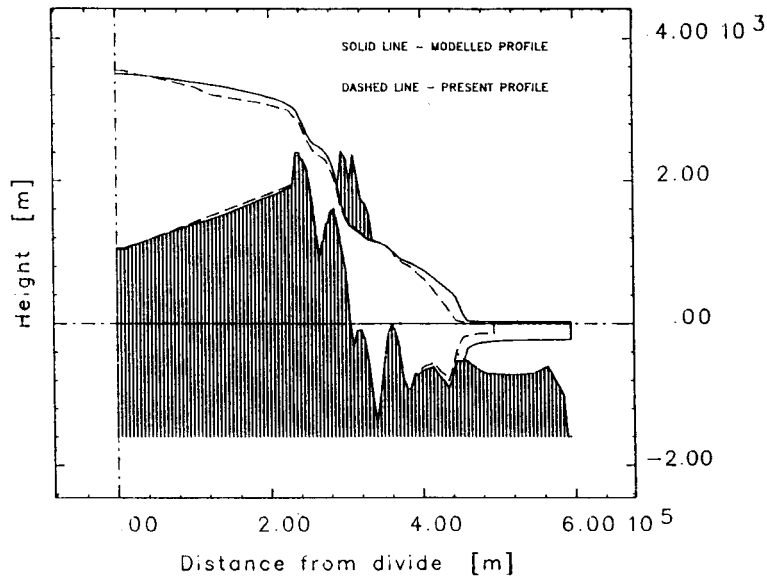

Fig.24 : Basic model run of the longitudinal profile of Gunnestadbreen

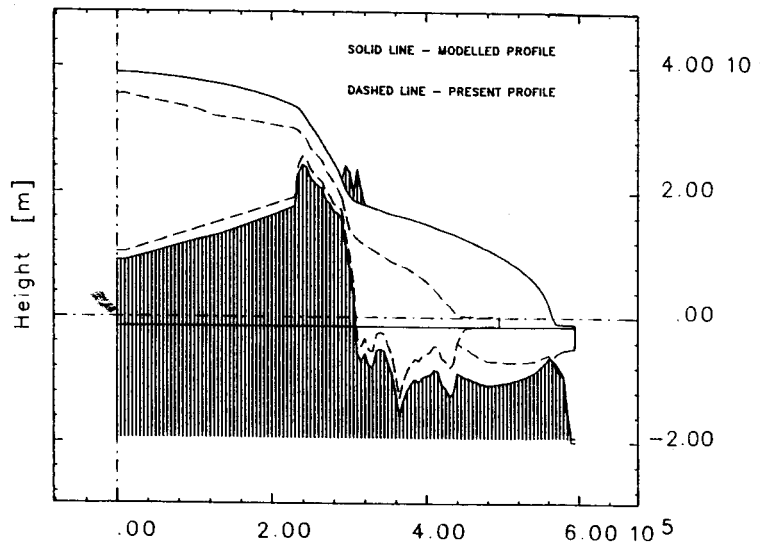

Fig.25 : Modelled steady state profile of Gjelbreen when temperature decreases with 11K and sea level lowers with 150 m

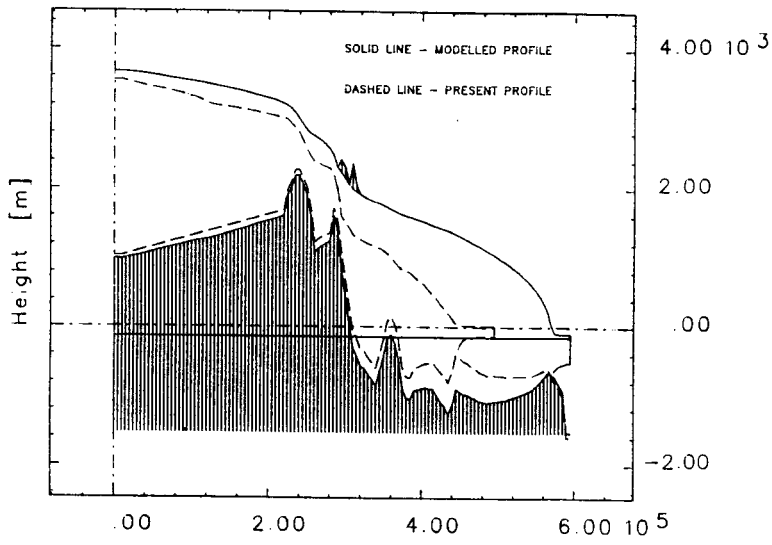

Fig.26 : Modelled steady state profile of Jenningsbreen when temperature decreases with 11K and sea level lowers with 150 m

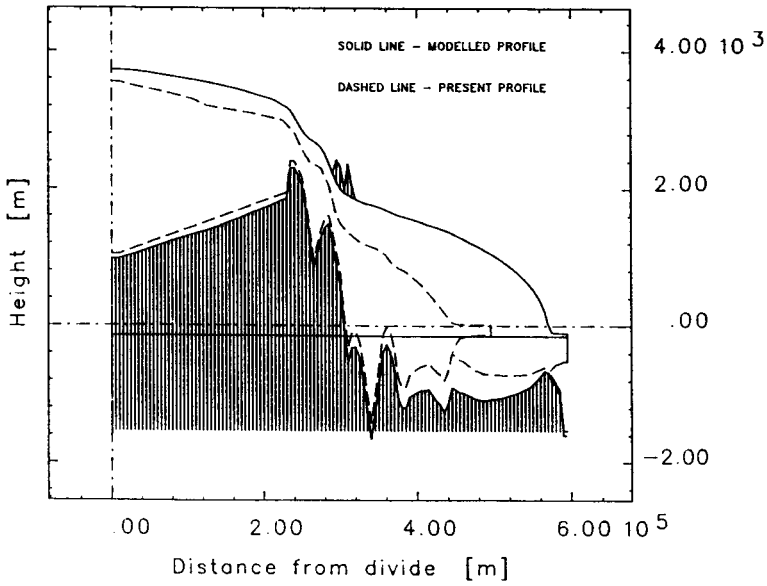

Fig.27 : Modelled steady state profile of Gunnestadbreen when temperature decreases with 11K and sea level lowers with 150 m

6. SUMMARY AND CONCLUSIONS

In this report an overview was given of the scientific work conducted within the framework of a study of the glacier behaviour in a marginal mountain area of Antarctica. During the austral summer 1986-87 a field campaign was organized in the Sør Rondane, Dronning Maud Land, in collaboration with the Japanese Antarctic Research Expedition (JARE 28). The Sør Rondane are particular interesting because there is, nowhere in Antarctica, a damming mountain range so closely situated to the main Antarctic Ice Divide. Another interesting point is that the ice dynamic studies in this area can be considered as a continuation of previous glaciological work carried out by former - purely Belgian - Antarctic Expeditions.

For this field campaign, to be carried out by a two-man team travelling by snow scooter in an area covered by bare ice and extensive moraines, a new prototype - portable radio echo sounder was developed at the Scott Polar Research Institute (Cambridge University, UK). The instrument failed however to produce good ice thicknesses in the field due to design problems. The causes of the faulty behaviour have now been located and are not considered as fundamental to the design of this new apparatus.

In fact, modifications of the instrument, expanding its power and further testing is the field is now considered as a major task, because of the universal lack of commercially available small and portable radar instruments to measure ice thickness and thus for use in the future.

In the field ice thickness measurements were carried out by gravimeter. A new algorithm was divised for calculating 2-D ice thickness profiles from gravity values. This allowed to accomplish 11 gravimeter - ice thickness profiles, extending considerably the previous Belgian data on the subglacial relief of the Sør Rondane area. This relief is characterized by very deep glacial troughs underscoring the overdeepening of these valleys at the margin of an ice sheet. An interesting comparison has been made between the superior radio echo sounding technique and gravity ice thickness values. This showed - that with careful modelling - ice thickness can be obtained within 10% of the radar results. From this it also follows that a 10% increase of ice thickness and ice transport values should be added to the results of the basic work of Van Autenboer and Decleir (1974,1978), where an estimate for the total value for the ice flux through the Sør Rondane was given.

A large body of evidence seems to indicate that a recessional phase is now taking place in the glacierization of the Sør Rondane. A one-dimensional flow line model was developed - recently with incorporation of the temperature field - and applied to the outlet glaciers of the central part of the range. It seems that some glaciers are now cut off from the main ice supply and should be considered as a local glacier in recessional phase. Experiments were also carried out to simulate

former glacial expansions and suggests that this can only be achieved through a shift of the grounding line towards the edge of the continental shelf. A possible scenario for this is a lowering of the sea level by 150 m and a temperature drop by 11K.

Finally it should be added that the recently acquired Thematic Mapper and Spot Images of the same area add much information to the observed surface features of the glacial cover and stream characteristics. Their implementation in further evaluation of data is foreseen, since besides the data also the necessary hardware and software for image processing have become available to us a few months ago.

REFERENCES

BROTCHIE, J.F. and R. SILVESTER (1969) On Crustal Flexure, Journ. Geophys. Res, 74, pp 5243 - 5252.

BUDD, W.F., D. JENSSEN and U. RADOK (1971) Derived Physical Characteristics of the Antarctic Ice Sheet, ANARE Publ. 120, 178 p. + maps

DECLEIR, H., NISHIO F. and OHMAE H. (1988) A comparison of ice thickness obtained by radio echo sounding and gravimetry in the Sør Rondane, Antarctica, Proceedings of the 9th Symposium on Polar Meteorology and Glaciology, National Institute of Polar Research, Tokyo.

DE VOS, L. and DECLEIR, H. (1988) Dynamics of the Antarctic Ice Cap, Ice thickness measurements related to the damming effect of the Sør Rondane, Dronning Maud Land, Antarctica, Proceedings of the Belgian National Colloquium on Antarctic Research, Brussels, October 20, 1987, p 214-224.

DREWRY, D.J. ed. (1984) Antarctic glaciological and geophysical folio, Cambridge, Scott Polar Research Institute.

HERTERICH, K. (1987) On the flow within the transition zone between the ice sheet and the ice shelf, in : C.J. Van der Veen and J. Oerlemans (eds) : Dynamics of the West Antarctic Ice Sheet, Dordrecht, D. Reidel, 185 - 202.

HERTERICH, K. (1988) A three-dimensional model of the Antarctic Ice Sheet, Anaals of Glaciology 11, 32-35.

HINDMARSH, R.C. and K. HUTTER (1988) Numerical fixed domain mapping solution of free-surface flows coupled with an evolving interior field, Int. Journ. Num. Anal. Meth. Geomechanics, 12, 473-459.

HUTTER, K. YAKOWITZ, S. and SZIDAROVSKY, F. (1986) A numerical study of plane ice-sheet flow, J. Glaciology 32, 139-160.

HUYBRECHTS, Ph. (1986) A three-dimensional time-dependent numerical model for polar ice sheets : some basic testing with a stable and efficient finite difference scheme, Geografisch Instituut VUB, Report 86-1, 39 p.

HUYBRECHTS, Ph. (1987) : Sensitivity experiments with a numerical ice sheet model with full thermo-mechanical coupling, Proceedings of the Belgian National Colloquium un Antarctic Research, 226-239.

HUYBRECHTS, Ph. and J. OERLEMANS (1988) A numerical study on thermo- mechanical response patterns with changing climate, Ann. Glaciology 11, in press.

JENSSEN, D. (1977) A three-dimensional polar ice sheet model, J. Glaciology 18, 373-390.

JOUZEL, J. et al. (1987) Vostok ice core : a continuous isotope temperature record over the last climatic cycle (160000 y), Nature 329, 403-408.

KVASOV, D.D. VERBITSKY, M.Ya. (1981) Causes of Antarctic Glaciation in the Cenozoic, Quaternary Research 15, 1-17.

LANGE, M.A. and D.R. MacAYEAL (1986) Finite element modelling of the Filchner- Ronne Ice Shelf, Alfred Wegener Institute for Polar Research, Filchner-Ronne Ice Shelf Program Report n3, 91-101.

MacAYEAL, D.R. and R.H. THOMAS (1986) The effects of basal melting on the present flow of the Ross Ice Shelf, Antarctica, J. Glac. 32, 72-86.

MAHAFFY, M.W. (1976) A three-dimensional model of ice sheets : tests on the Barnes Ice Cap, Northwest Territories, Journal Geophysical Research 81, 1059-1066.

MAYEWSKY, P. and GOLDTHWAIT, R.P. (1985) Glacial events in the Transantarctic Mountains : a record of the East Antarctic Ice Sheet, Paper 12 in Geol. of the Transant. Mountains, Antarctic Research series, Vol. 36, Amer. Geoph. Union, p275-324.

NISHIO, F. et al. (1984) A preliminary study of glacial geomorphology in area between Breid Bay and the Sør Rondane Mountains in Queen Maud Land, East Antarctica, Antarctic Record n.83, p 11-28.

OERLEMANS, J. (1982) A model of the Antarctic Ice Sheet, Nature 297, 550-553.

OERLEMANS, J. and VAN DER VEEN, C.J. (1984), Ice sheets and climate, D.Reidel, Dordrecht, 217 pp.

PATERSON, W.S.B. (1981) The physics of glaciers, Pergamon Press, Oxford, 380 pp.

PATTYN, F., HUYBRECHTS, Ph. and DECLEIR, H. (in prep.) A numerical ice sheet model of the glacier system in the Sør Rondane, Dronning Maud Land, Antarctica : an interpretation of observed glacier fluctuations.

RITZ, C. (1987) Time dependent boundary conditions for calculation of temperature fields in ice sheets, IAHS Publ. 170, 207-216.

SCLATER, J.G., C. JAUPART and D. GALSON (1980) The heat flow through oceanic and continental crust and the heat loss of the earth, Rev. Geophys and Space Physics 18, 289-311.

SOUCHEZ, R.M. (1966) The origin of morainic deposits and the characteristics of glacial erosion in the Western Sør Rondane, Antarctica, Journal of Glaciology, Vol.6, n.44, p 249-255.

TURCOTTE, D.L. and G. SCHUBERT (1982) Geodynamics, New York, John Wiley, 440 p.

VAN AUTENBOER, T. (1964) The geomorphology and glacial geology of the Sør Rondane, Dronning Maud Land, Antarctica, Medelingen van de Koninklijke Vlaamse Academie voor Wetenschappen, Letteren en Schone Kunsten van België, Klasse der Wetenschappen, Jaargang XXVI, nr 8, 89 pp.

VAN AUTENBOER, T. and DECLEIR, H. (1974) Mass transport measurements in the Sør Rondane, Dronning Maud Land, Antarctica, Service Geol. de Belgique, Professional paper Nr.6, 25 p, Brussels.

VAN AUTENBOER, T. and DECLEIR, H. (1978) Glacier discharge in the Sør Rondane. A contribution to the mass balance of Dronning Maud Land, Antarctica, Zeitschrift f. Gletscherk. u. Glazialgeol., Bd.14, H.1, p 1-16.

VAN DER VEEN, C.J. (1985) Response of a marine ice sheet to changes at the grounding line, Quaternary Research 24, p257-267.

VAN DER VEEN, C.J. (1987) Longitudinal stress and basal sliding : a comparative study. in : Van der Veen, C.J. and J. Oerlemans (eds), Dynamics of the West Antarctic Ice Sheet, Dordrecht, D. Reidel, 223-248.

SCIENCE POLICY OFFICE
Research contract
nr ANTAR/CVT/01

SIMULATIONS OF THE ANNUAL SEA ICE COVER IN THE WEDDELL SEA

C. Demuth and J.P. van Ypersele(*)

MANAGEMENT UNIT OF THE
MATHEMATICAL MODEL
OF THE NORTH SEA AND THE SCHELDT
ESTUARY (MUMM)
MINISTRY OF PUBLIC HEALTH AND
ENVIRONMENT
GULLEDELLE, 100
B-1200 BRUSSELS (BELGIUM)
(*)PRESENT ADDRESS:
INSTITUT D'ASTRONOMIE ET DE
GEOPHYSIQUE G. LEMAITRE,
UNIVERSITE CATHOLIQUE DE LOUVAIN,
CHEMIN DU CYCLOTRON 2,
B-1348, LOUVAIN-LA-NEUVE (BELGIUM)

BELGIAN SCIENTIFIC RESEARCH
PROGRAMME ON ANTARCTICA
SCIENTIFIC RESULTS OF PHASE ONE
(OCT 85 - JAN 89)
VOLUME III: GLACIOLOGY AND
CLIMATOLOGY

CONTENTS

1. Introduction 1
2. Sea-ice model : thermodynamic component 3
   2.1. Ice Model 3
   2.2. Parameterisation of leads 5
   2.3. Upper ocean model 6
   2.4. Convective adjustment 8
3. Sea-ice model : dynamic component 8
   3.1. Ice transport 8
   3.2. Conservation laws 9
4. Geophysical data 10
   4.1. Geographical area studied 10
   4.2. Meteorological data 10
   4.3. Oceanological data 11
   4.4. Glaciological data 12
5. Numerical aspects 12
   5.1. Grid 12
   5.2. Numerical method 12
   5.3. Time step 13
   5.4. Boundary and initial conditions 13
6. Simulations 15
   6.1. Local results 15
      a) Point inside the Weddell Sea 17
      b) Coastal point 18
   6.2. Global results 18
      a) Ice cover 18
      b) Average oceanic heat flux 19
      c) Salt conservation, relative error 19
   6.3. Choice between the configurations of the sea-ice model 20
   6.4. Two-dimensional ice cover 20
      a) Ice thickness 20
      b) Weddell Polynya 21
7. Conclusions 23
8. Applications 25
9. References 26
10. Figures 30

ABSTRACT

A model of sea-ice formation has been developed and applied to a sector of the Southern Ocean, including the Weddell Sea and the Drake Passage; it describes the annual cycle of sea-ice thickness and its spatial extent. This sea-ice model with leads consists of two parts :

- the thermodynamical component which manages the freezing and melting processes due to energy fluxes between the atmosphere, ice and ocean. This component computes also the heat and salt transfers between mixed layer and deep ocean;

- the dynamical component limited in the present version of the model to the computation of ice movement due to wind and surface current.

The surface energy budget, heat and salt exchanges and momentum transfers are modelled and/or parameterised from monthly-averaged climatological data (wind, air temperature, dew point, cloudiness and snowfall) and annually-averaged values of temperature and salinity in the ocean. These data and the results of the sea-ice model, including ice thickness, temperature, mixed-layer depth and ice extent, are presented and discussed at specific points (offshore and coastal) and for the whole area.

The sea-ice model has been applied to the Weddell Sea according to two methods : the "layer method" where the ocean depth is limited to a chosen value and the "robust-diagnostic method" where the obervations constrain the model with a short damping time. The results of both methods show good agreement with the observed amplitude for ice extent and the mean oceanic heat fluxes exchanged between ice and ocean. The sea-ice model using the robust-diagnostic method gives a smaller ice thickness than the layer method and better conserves salt and energy.

1. INTRODUCTION

The purpose of this report is to describe the research done at MUMM (Management Unit of the Mathematical Model of the North Sea and the Scheldt Estuary) within the framework of the Belgian Programme "Scientific research on the Antarctic". The main objective pursued by MUMM has been to develop a sea-ice model which would be able to reproduce the main features of the observed annual cycle of ice extent and ice thickness in an area covering on the Weddell Sea and the Drake Passage.

At the mesoscale, the sea-ice layer can be considered as a two-dimensional continuum "sandwiched" between the atmosphere and the ocean. Thermodynamical and dynamical processes at the air-sea interface constrain the ice and determine its thickness and movement. Ice growth is due to freezing of seawater and to snowfall. Its decay is associated with melting. Moreover, external and internal forces cause movement and deformation of the ice layer. These different processes must be taken into account when developing a sea-ice model. In the present study, this problem is approached in two steps. First, the thickness modifications due to the thermodynamic processes are computed. Vertically, the heat flux balances at the ice-air (or snow-air) interface and at the ice-ocean interface determine the thickness and the upper surface temperature of the ice (and snow). Horizontally, the presence of leads in the sea ice being taken into account, the heat flux balance at the surface of the leads can modify the sea-ice extent (freezing and melting). In addition, the sea-ice and the leads are connected with the deep ocean through a mixed layer. In section 2, the modelling approach followed to take into account the thermodynamic processes is presented.

Second, the dynamical processes are modelled. As discussed in section 3, one can accept that the wind stress and the ocean current stress acting on top and bottom of the sea ice are the main driving forces of the sea-ice movement. The equilibrium between these stresses results in a linear dependence of the ice velocity with the wind and to the surface current. The ice velocity field ensures the horizontal redistribution of the amount of ice available at the ocean surface. During this process, the total ice mass is conserved.

Among those sea-ice models which are coupled to an ocean model and use atmospheric conditions imposed by the climate, our model is situated between one-dimensional models which take only into account the oceanic vertical processes and the sea ice (e.g. Pease, 1975; Pollard et al., 1983; Lemke, 1987; Motoi et al., 1987; Fichefet and Gaspar, 1988) and three-dimensional models including the horizontal dispersion of heat and salinity within ocean (e.g. Toole, 1981; Hibler and Bryan, 1984 and 1987; van Ypersele, 1986; Semtner, 1987). The model belongs to the category of two-dimensional sea-ice models as developed by Parkinson and Washington (1979) and Hibler (1979). Contrarily to these authors, sea-ice rheology is not taken in consideration. Although our model adapts and extends the Fichefet and Gaspar's (1988) approach to a large extent, it is founded on the analyses and some results of the dynamic-thermodynamical model of van Ypersele (1986).

The computation of the heat transfers and the determination of the ice velocity field requires the knowledge of meteorological and oceanographical data. The data we used for the simulations are presented in section 4. In summary, the climatological data compiled by Taljaard et al. (1969), the cloudiness-function of time and space derived by Parkinson and Washington (1979), the ocean temperature and salinity given by Gordon and Baker (1982) and the upper ocean currents computed by van Ypersele (1986) are introduced in the forcing terms of the model.

A technical overview of the numerical procedure used to solve the model equations is given in section 5.

The results of the different simulations performed with the sea-ice model are presented and discussed in section 6. The analysis of the results shows that the sea-ice model based on thermodynamical and dynamical processes allows to reproduce the major features existing in the sector of the Southern Ocean including the Weddell Sea and Drake Passage.

2. SEA-ICE MODEL : THERMODYNAMIC COMPONENT

2.1. Ice model

The sea ice, assumed to be a uniform horizontal slab of ice, is caught in an "energetic trap" due to heat exchanges through the ice-air and the ice-ocean interfaces.

The energy exchanged through the air-ice interface consists of the shortwave radiation or solar radiation ($F_{sol,i}$, including the surface albedo), the non-solar heat flux ($F_{nsol,i}$) gathering the longwave radiation from the atmosphere, the longwave radiation from the surface, the sensible and latent heat flux and the conductive flux (F_c) just below the surface. The thermal equilibrium at the surface being prescribed, the balance of fluxes gives the surface temperature. If the computed temperature is above the melting point (0°C for snow, -0.1°C for ice), the surface temperature is held at that point and the excess of energy is used to melt snow or/and ice.

The snow and ice interact with the shortwave radiation, $F_{sol,i}$. Scattering and absorption attenuate the passage of the solar radiation through snow or ice. If the ice slab is overlaid by snow, the snow strongly scatters radiations and the solar radiation is completely absorbed at the surface. Without snow, the solar radiation decreases in terms of the ice depth h from a value of 0.1 m (Grenfell and Maykut, 1977) following an exponential absorption law (Beer's law) :

$$I(h) = \begin{cases} 0.17 & \text{if } h < 0.1 \text{ m} \\ 0.17 \exp(-1.5\,(h-0.1)) & \text{if } h > 0.1 \text{ m} \end{cases} \qquad (1)$$

Inside the snow-free ice, the solar radiation increases the local temperature as a function of the vertical gradient of $I(h).F_{sol,i}$. The solar radiation penetrating the ice is given by $(1 - I(h_i))$. $F_{sol,i}$. According to Semtner (1976), this energy is temporarily stored in brine pockets (a brine is a complex solution of metallic salts) located near to the top of the ice.

Brine pockets act as thermal buffers : cooling of the ice causes freezing of some brines, resulting in a release of heat and a decrease of the cooling rate, while the increase of temperature causes the ice surrounding the brine pockets to melt and subsequently a decrease of the warming rate. To model the storage of latent heat in brine pockets, Semtner introduce the concept of internal heat reservoir instead of the concept of local source in the ice model.

It should be noted that during the course of an integration, the snow accumulates on the ice. In the model, some packed snow is transformed into "white ice" when the snow weight depresses the ice below the water level, according to Pivovarov (1973) and Ledley (1985). When this transformation of snow into ice occurs, the vertical temperature profile is adjusted accordingly.

Within the ice and the snow, the temperature is governed by a one-dimensional heat diffusion equation: the physical phenomena are dominated, along the vertical, by the balance between the thermal conduction and the storage of heat in the ice medium per unit of time. To model this heat transfer, we have followed the "0-model" suggested by Semtner (1976). Briefly stated, it is assumed that no heat can be stored into ice and snow layers. The effect of the solar radiation penetrating the ice is taken into account in the surface heat flux balance by reducing the solar radiation by the factor $(1-I(h_i))$. The conductive heat flux is constant and proportional to the temperature gradient in each layer. Heat conduction at the ice-snow interface is assumed to be equal in both media.

At the base of the ice, the conductive flux within the ice must be balanced by the vertical heat flux from the deep ocean, F_b. If it is not the case, the imbalance causes ice either to grow or to melt at the bottom. In all calculations, the bottom temperature is supposed to be equal to the freezing temperature $T_f(S_m)$ which depends on the mixed-layer salinity S_m, according to Fichefet and Gaspar (1988).

2.2. Parameterisation of leads

In reality, the sea-ice field is more a discrete physical system than a continuous medium. Sea-ice is fragmented in ice floes with different thicknesses (from centimetres for young ice to a few metres for thick or multi-year ice). These floes are separated by channels of open water called "leads" (of the order of 100 square kilometers). One observes also large areas of open water surrounded by ice, called "polynyas" (up to 350000 square kilometers). The size of these "open windows" is an important parameter in the total energy budget, because of the difference between the albedo of ice (of the order of 0.8 when covered by snow) and water (0.07), and because of the large difference between ice-air and water-air in latent heat fluxes.

To take into account the presence of leads, it is assumed that the ice cover per unit area (i.e., the fractional ice cover or the "ice concentration", A) cannot exceed a maximum value of 0.98 in the Antarctic (Parkinson and Washington, 1979). The horizontal extent of the ice cover depends on the heat transfers through the lead surface. Under sea ice and leads, the mixed layer extends to depth h_m. The heat balance of a lead depends on the solar radiation absorbed at the surface $F_{sol,l}$, the non-solar flux $F_{nsol,i}$ and the heat flux F_m exchanged with the mixed layer. This exchange allows to keep the mixed-layer temperature at the freezing point $T_f(S_m)$. If the heat balance of the leads, given by

$$(1-A).\ (F_{sol,l}\cdot(1 - J(h_i)).(1-J(h_m))+ F_{nsol,l} + F_m) \qquad (2)$$

where J(h) is the fraction of the solar radiation that penetrates to the depth h, is favorable to warming, the energy available is used to melt ice laterally. If the conditions are favorable to the formation of new ice, this ice accretes onto the side of the ice already present until the ice concentration A reaches its maximum value. Beyond, the ice thickness changes accordingly in order to conserve energy.

2.3. Upper ocean model

The upper ocean layer is assumed to consist of a mixed-layer where the temperature, T_m, and the salinity, S_m, are uniform along the vertical down to depth h_m. The method we used to compute these variables is similar to Gaspar (1988).

At the upper limit, the energy due to the solar and non-solar radiations available for the mixed-layer is given by

$$F_{sol,m} = A.I(h_i).F_{sol,i} + (1-A).\ J(h_i).F_{sol,l} \qquad (3)$$

$$F_{nsol,m} = \begin{cases} 0 & \text{if } h_i > 0 \\ F_{nsol,l} & \text{if } h_i = 0 \end{cases}$$

When the mixed layer is covered by ice, salt transfers take place between ice and the mixed layer following the freezing and melting cycle. The salt exchanges are given by

$$F_{salt} = (S_m - S_i) \frac{\partial M_i}{\partial t} \qquad (4)$$

where M_i is the mass of ice per unit area (i.e. the product of the ice thickness h_i, the fractional ice cover A and the density ρ_i = 900 kg m^{-3}). The possible effect of snow-melt on the salinity of the water column are not considered in this study.

Wind and ice act on the ocean by a stress represented by means of a friction velocity u_*, equal to 0.009 ms^{-1} for ice (Lemke, 1987) and, for wind, given by a function of the surface geostrophic wind velocity. An average friction velocity, weighted by the concentration A, is chosen to define the surface dynamic effects acting on the mixed layer. The available mechanical energy flux for this layer is proportional to ρu_*^3.

Exchanges of heat, mechanical energy and salt flux represent the inputs of an oceanic mixed-layer model which is able to define the depth h_m, the temperature T_m and the salinity S_m. In order to simulate properly and rapidly these parameters, we implemented Gaspar's model (1988) in our study. This model, a mixed-layer model of Niiler and Kraus (1977) type, parameterises the turbulent dissipation rate which takes explicitly the Earth's rotation and the mixed layer stability into account. The turbulence parameterisation follows Garwood's (1977) closure technique and includes some results from Klein and Coantic (1981). The model parameters have been calibrated for higher-order turbulence models and tested on a time series of oceanological and meteorological measurements made at the station Papa (North Pacific Ocean). Fichefet and Gaspar (1988) applied the mixed-layer model to simulate the air-sea-ice interactions in the Arctic Ocean.

The analysis and choices made by Gaspar permit to define the evolution of h_m in an algebraic equation for entrainment w_e ($= \partial h_m / \partial t$) if it occurs and in another algebraic equation when h_m reduces ($w_e = 0$). The evolution of the upper ocean temperature T_m and salinity S_m, integrated over h_m, are fixed by the following conservation laws :

$$\rho c_p h_m \frac{\partial T_m}{\partial t} = (1-J(h_m)).F_{sol,m} + F_{nsol,m} - \rho c_p w_e \Delta T - c_p \rho (K_T \frac{\partial T}{\partial z})_m \quad (5)$$

$$\rho h_m \frac{\partial S_m}{\partial t} = F_{salt} - \rho w_e \Delta S - \rho (K_S \frac{\partial S}{\partial z})_m$$

where $(K_T \frac{\partial T}{\partial z})_m$ and $(K_S \frac{\partial S}{\partial z})_m$ are the heat and salt diffusion fluxes at depth h_m with the diffusivities K_T and K_S, ΔT and ΔS are the temperature and salinity jumps across the bottom of the mixed layer. In what follows, we always mean potential temperature when we refer to ocean temperature.

Below the mixed layer, temperature T and salinity S evolve according to

$$\rho c_p \frac{\partial T}{\partial t} = F_{sol,m} \frac{\partial J}{\partial z} + \rho c_p \frac{\partial}{\partial z} \left(K_T \frac{\partial T}{\partial z}\right)$$

$$\frac{\partial S}{\partial t} = \frac{\partial}{\partial z} \left(K_S \frac{\partial S}{\partial z}\right) \qquad (6)$$

All the diffusion fluxes into (6) are the product of a diffusivity fixed at the common value of 2.10^{-5} m^2 s^{-1} and the vertical gradient of the variable to conserve. In (5), this gradient is estimated according to Gaspar as the ratio between the jump ΔT or ΔS and a discontinuity depth of 15 m.

2.4. Convective adjustment

All the processes considered above do not guarantee hydrostatic stability, i.e. denser water can overlay lighter water. If this is the case, water masses of different temperature and salinity are mixed drastically, level by level, until the density profile, calculated with the Friedrich and Levitus (1972) state equation, increases with depth.

3. SEA-ICE MODEL : DYNAMIC COMPONENT

3.1. Ice transport

The sea ice is driven by wind and ocean currents. Its movement can be derived from the balance of forces acting on it. These forces are the inertial force, the wind and water drag at the air-ice or ice-water interface, the Coriolis acceleration, the gravitational force due to the sea-surface tilt, and the internal ice resistance.

A scale analysis shows that, on time scales of a few hours, the inertial term is three orders of magnitude smaller than the wind and water forces (Campbell and Rothrock cited by Parkinson and Washington, 1979) and thus can

be neglected. Moreover, Thorndike and Colony (1982) and Leppäranta and Hibler (1987) suggest to neglect the internal ice stress in a first approximation and to assume a geostrophic balance (the Coriolis acceleration is equal to the gravitational force). The ice velocity $\underline{v}_i$ is then deduced from the balance between wind and water drag and is expressed as a linear function of the geostrophic wind $\underline{V}_a$ and the ocean current $\underline{V}_w$:

$$\underline{v}_i = \alpha \exp(-i\beta)\ \underline{V}_a + \underline{V}_w \qquad (7)$$

where α is a scaling factor, β is a rotation angle.

From measurements made in the Arctic, Thorndike and Colony found that at more than 400 km from the coasts, this linear parameterisation of the ice velocity fits the observations with the parameters $\alpha = 0.008$ and $\beta = 8°$. Closer to the coasts, the ice stress term should be considered to obtain the ice motion. In the absence of similar measurements in the Antarctic, the same values will be used, except that the sign of the rotation angle has been reversed, since the area of interest is located in the Southern Hemisphere. This approach was first used in a model by van Ypersele (1986).

3.2. Conservation laws

The ice velocity (equation 7), which is not horizontally uniform, will redistribute the ice mass created at the ocean surface. During this process, the ice mass per unit area M_i must be conserved according to the equation :

$$\frac{dM_i}{dt} = \frac{\partial M_i}{\partial t} + \nabla . (\underline{v}_i M_i) = 0 \qquad (8)$$

This equation is divided into conservation laws for the ice thickness and the fractional ice cover. A similar conservation equation is obtained for snow thickness.

When the ice enters a grid cell where the temperature is higher than the freezing point, the available energy in the oceanic mixed layer is used to melt the ice layer, and the mixed-layer temperature is adjusted.

4. GEOPHYSICAL DATA

4.1. Geographical area studied

The area covered by the model extends from latitude 50° to 80° and from longitude 80°W to 30°E. It includes the southern tip of South America, the Drake Passage, the Antarctic Peninsula and the Weddell Sea. This area was chosen because it is possible to make comparisons with other modelling studies made in the region (Hibler, 1984; van Ypersele, 1986). Moreover, this sector of the Southern ocean is relatively rich in meteorological, oceanological and glaciological observations.

4.2. Meteorological data

Both the surface heat fluxes and the wind stress are computed from the climatological data compiled by Taljaard et al. (1969). These authors give monthly-averaged mean climatological values of surface air temperature, dew point, surface geostrophic wind and pressure.

Cloudiness, function of both latitude and time, modulates, like a shield, the radiative fluxes. This parameter has been derived by Parkinson and Washington (1979) from curves of van Loon (1972).

Snow is considered to fall on the ice at a prescribed rate : it is assumed to be distributed uniformly in time and space with a value of 0.2 m $year^{-1}$ (van Ypersele, 1986).

Figures 1 and 2 present, respectively, the surface temperature and surface geostrophic wind fields on Julian day 90 (March 31) and 270 (September 27). The main meteorological features are :

i) the surface temperature gradients are mostly meridional except in the Antarctic Peninsula (fig.1);

ii) the cold anticyclone over the continent produces easterly winds along the coast of Antarctic, a clockwise circulation exists in the Weddell Sea and the westerly winds are blowing hard (9 to 10 m s^{-1}) around 60°S (fig.2);

Fluxes at the surface of the ice or ocean were parameterised according to laws used by van Ypersele (1986) and Fichefet and Gaspar (1988). Similarly to these authors, we choose the solar flux parameterisation of Shine (1984); the atmospheric longwave radiation is calculated following the Marshunova (1966) formula and the latent and sensible heat fluxes are calculated from standard bulk aerodynamic formula using similar expressions as Parkinson and Washington (1979).

4.3. Oceanological data

The annual means of ocean temperature and salinity are extracted from Gordon and Baker (1982). The upper ocean currents are those computed by van Ypersele (1986) with a three-dimensional oceanic general circulation model coupled to a thermodynamic-dynamic sea-ice model.

At this stage, it is useful to comment on the vertical distribution of physical properties in the Antarctic Ocean. Gordon (1971) identified the following main water masses: the Antarctic Surface Water (AASW), the Weddell Deep Water (WDW), the Circumpolar Deep Water (CDW), and the Antarctic Bottom Water (ABW). The AASW is cold (0°C) and fresh, while the underlying CDW and WDW are warmer (0.4°C) and saltier. The cyclonic Weddell Gyre is composed mostly of WDW. The ABW, flowing close to the bottom of the ocean, is colder and fresher than deep water.

The absorption of the solar irradiance into seawater J(h) is parameterised following Paulson and Simpson (1977) with coefficients defined in Jerlov (1976). The sea albedo is given by Briegleb and Ramanathan (1982) for a clear sky; a value of 0.07 is chosen for cloudy conditions.

4.4. Glaciological data

The satellite data processed by Zwally et al. (1983) were used to validate the model results. These authors give Antarctic sea-ice cover and concentrations for the years 1973 to 1976.

Figure 3 presents the annual cycles of sea-ice cover for various ice concentrations. The maximal effective ice cover in the Weddell Sea sector is observed in 1973. The so-called Weddell Polynya appeared from 1974 to 1976, and decreased the maximal ice cover.

5. Numerical aspects

5.1 Grid

The conservation equations, written in a spherical coordinate system, are solved on a computational grid characterized by mesh sizes of 2 degrees in longitude and 1 degree in latitude (one degree in latitude is about 111 km, while two degrees in longitude represent 143 km at 50° S and 76 km at 70° S). This choice allows the use of the Gordon and Baker (1982) ocean data without interpolation.

Throughout the vertical, 12 levels are used and the centre of the grid boxes are, respectively, at depths of 30, 100, 200, 300, 500, 800, 1200, 2000, 3000, 4000, 4750, and 5250 meters. Temperature and salinity are defined at the centre of each grid box. The effective number of levels at each node of the horizontal grid depends on the bottom topography.

5.2 Numerical method

The mixed-layer model and conservation equations require the solution of dispersion equations.

The mixed-layer model conservation equations for energy and salt are solved by considering separately the effects of entrainment-retreat and surface fluxes, as in Gaspar (1988), and those of diffusion in the entire water column, following Fichefet and Gaspar (1988).

The conservation equations used for the ice dynamics are complemented with a numerical diffusion term (van Ypersele, 1986) which is a function of latitude (Blumberg et al., 1984). The divergence of the geostrophic wind $\underline{V}_a$ being not necessary equal to zero, a source/sink term is added at the right-hand side of the conservation equations. This term is equal to the product of the wind divergence by the quantity to conserve (Katada et al., 1984). The modified conservation equations are then solved with the flux-corrected method to avoid instabilities (Wang, 1985).

5.2 Time step

In a theoretical study of marginal ice zone dynamics, Røed (1984) found characteristic time scales of 2 days for the freezing of Arctic, and 6.5 days for melting. A time step of one day, compatible with numerical stability criteria, was therefore considered acceptable for the present study. This time step has also been used by Hibler (1979) to investigate the effects of ice dynamics on Artic ice thickness.

5.3 Boundary and initial conditions

No flux of matter and energy is allowed across the coasts. The northern open sea boundary is left open (actually, no ice reaches this limit neither in the observations nor in the simulations). At the western and eastern open sea boundaries, several options were possibles. The one used in the model is the "cyclic continuity" (van Ypersele, 1986): what flows out of the domain through the eastern boundary flows back into the domain through the western boundary, and vice versa. To ensure a smooth connection from one side to the other, the topography field and all the forcing data were modified by a linear interpolation over the five grid points close to the eastern boundary.

The domain is also limited in the vertical direction. We have used two different methods to introduce the deep ocean effects in the mixed-layer computation.

The first method, used by Fichefet and Gaspar (1988) and called below the "layer method", limits the vertical diffusion processes to a certain number of layers, and imposes observed temperature and salinity data at the bottom of the last layer. Various numbers of diffusive layers were used in the following computations.

The second method, used by Sarmiento and Bryan (1982) in the Atlantic Ocean and van Ypersele (1986) in the Antarctic, introduces a Newtonian forcing term in the diffusion equations (6). This forcing term is proportional to the difference between computed and observed values and inversely proportional to a characteristic "damping" time. A small damping time renders the model purely diagnostic, while a long time scale allows it to be prognostic. This method is thus called the "robust-diagnostic method". In this study, only the salinity field is constrained by the observations and its damping time has been set equal to 10 days at all levels below the mixed layer. The temperature was left fully prognostic, contrary to the two previous studies using the robust-diagnostic method, because of the dependence of the freezing point on salinity.

Each simulation is started on January 1 with temperature and salinity fields derived from the observations and processed to remove hydrostatic instabilities. It is assumed that no ice is present at the beginning of a run.

6. SIMULATIONS

In this section, the results of different simulations performed with the sea-ice model are presented and discussed.

In the first one, the model is used with the surface layer (60 m thick) only. In the second simulation, the first six layers (total thickness : 940 m) are taken into account. The third configuration introduces vertical diffusion in the complete water column. Finally, the robust-diagnostic method was used at all levels below the surface layer.

The results of these four applications are presented as follows. First the influence of the approach used to introduce the effects of the deep ocean is made clear by comparing the results obtained at two specific points of the computational grid values of selected global variables (ice extent, oceanic heat flux, error relative to the salt conservation). Afterwards, the contribution of the different components of the sea-ice model (i.e., the thermodynamic and dynamic processes) to the extent of sea-ice is discussed; information on the presence or absence of the Weddell Polynya in the simulation is given.

6.1. Local results

The sea-ice model results are presented at two points, P1 (offshore) and P2 (coastal). For both points and for each of the four sea-ice model configurations, the annual cycles of the mixed-layer depth h_m are shown in figures 4 and 9, the leads extent (1-A) in figures 5 and 10, the ice thickness h_i in figures 7 and 12 and the surface temperature figures 8 and 13. Each result shown here corresponds to the tenth year of simulation.

Table 1. Initial profiles of salinity and temperature at point P1 (28°W, 66°S) located inside the Weddell Sea.

layer	depth (m)	salinity	potential temperature (C°)	density excess ($kg\ m^{-3}$)
1	30	34.060	- 1.059	27.561
2	100	34.487	- 1.749	28.273
3	200	34.661	.044	28.811
4	300	34.685	.350	29.290
5	500	34.694	.374	30.251
6	800	34.692	.260	31.685
7	1200	34.685	.069	33.587
8	2000	34.674	- .266	37.356
9	3000	34.669	- .488	41.991
10	4000	34.657	- .682	46.544
11	4750	34.651	- .844	49.914

Table 2. Initial profiles of salinity and temperature at point P2 (46°W, 77°S) located close to Antarctica.

layer	depth (m)	salinity	potential temperature (C°)	density excess ($kg\ m^{-3}$)
1	30	34.086	- 1.345	27.593
2	100	34.415	- 1.774	28.215
3	200	34.512	- 1.918	28.786
4	300	34.592	- 1.993	29.340
5	500	34.646	- 2.157	30.360

Tables 1 and 2 provide the initial thermodynamical profiles at points P1 and P2 after a stability check (Gordon and Baker, 1982).

a) Point inside the Weddell Sea (P1).

At P1, sea ice exists during three quarters of the year (fig.6); a smooth time evolution is only observed in the sea-ice model with the first layer. The other configurations show a local melting about the 170th day (June), corresponding to a retreat of the mixed layer, followed by a deepening to 140 m. At this level, the mixed layer depths of the layer models meet the general deepening trend. They extend to the bottom between the days 238 (July - August) and 282 (September) and then, after about ten days, retire to the base of the first layer at the time of the spring melting. With the robust-diagnostic model, mixed-layer oscillations are observed during the freezing period. The absence of convection in the complete water column results from the damping term on salinity. In fig.5, the annual cycle, as computed by robust-diagnostic method, shows a fast covering of the surface by snow and ice. The surface temperature is less negative than in the layer method (fig.8).

At the end of the annual cycle, the effects of the convergence-divergence of ice due to kinematic processes results in a relatively thick layer of ice -which corresponds to the time of new-ice growth, and as light increase of the ice before complete melting. The differences between the annual cycles of ice thickness (fig.6) in function of the configurations of the sea-ice model can be related to the water mass structure (table 1) : in the sea-ice model the cold surface water induces a thick layer of ice restricted to the first layer; the warm water below the Antarctic Surface Water reduces the ice thickness to a value below the thickness of the ice taking into account all the water types. The surface temperatures (fig.8) are very sensitive to the new-ice growth from the outset of the mixed-layer deepening (fig.4). After and during the course of retreat, the surface temperatures are almost the same.

b) Coastal point (P2).

The ice and snow are present at point P2 throughout the year (see fig.11). Except for the robust-diagnostic method, the deepening to the bottom and the retreat occur very quickly. The annual cycles of the mixed-layer salinity (fig.12) and of the sea-ice thickness (fig.11) are, with the robust method, smaller than cycles computed by the layer method. Figures 10 and 13 show the annual cycle of the leads and of the surface temperature respectively. These curves follow a similar pattern in the four configurations.

6.2. Global results

a) Ice cover

Figure 14 shows the annual cycles of sea-ice cover computed with the three "layer" configurations (1, 6 and all layers) and the robust-diagnostic method.

The cycles have a common minimum of the order of 0.5 x $10^6 km^2$ close to day 50. Maxima are slightly different: the effective ice area reaches a maximum value of 7.3 x $10^6 km^2$ on day 210 with robust forcing, 7.1 x $10^6 km^2$ on day 214 with six and all layers, and 6.9 x $10^6 km^2$ on day 206 with the one-layer model. The average simulated growth period is thus 160 days, and the average decay period is 205 days. The values can be compared to the values given by Zwally et al. (1983) for the Weddell Sea sector in 1973, year where there are no polynya occurred. They found an average minimal effective ice area close to 1 x $10^6 km^2$ in mid-February and a maximum of 6 x $10^6 km^2$ in mid-September (Figure 3). The observed growth period is thus 210 days, and the decay period is 155 days. This comparison shows that the sea-ice model tends to reproduce the observed amplitude but not the phase of the seasonal cycle. There is a phase difference of about 50 days, due to absence in the model of the storage of heat in the ice (cfr.2.1.). The choice of the 3-layer version (2 ice layers + 1 snow layer) of the Semtner model would allow a better agreement with the observations (Demuth and van Ypersele (1988) for a particular study).

b) Average oceanic heat flux.

Table 3 summarizes the average oceanic heat flux over the ice-covered Weddell sector for the tenth year of simulation, as a function of the configurations of the model. The increase in layer number rises the average heat flux from 10 W m^{-2} to 19 W m^{-2}, this last value being close to the 18 W m^{-2} value obtained with the robust-diagnostic forcing. The values are in good agreement with heat flux estimates, which range from 9 to 16 W m^{-2} (Gordon et al., 1984).

Table 3 Spatio-temporal average of the heat flux over the ice-covered Weddell sector during the tenth year of simulation.

Sea-ice model Configuration	Heat flux W m^{-2}
1 layer	10
6 layers	15
all layers	19
robust-diagnostic, 10 days	18

c) Salt conservation, relative error.

During the ten years of simulation, the observed amount of salt must be conserved. The discretization of the evolution equations and the particular choice of either a damping time or a fixed number of oceanic layers may introduce an error which accumulates during the calculation. To estimate this error, we have computed the annual cycle of the relative error of salt at the tenth year of integration. The robust-diagnostic method gives the smallest values (fig.15) and thus conserves better salt than the layer method.

6.3. Choice between the configurations of the sea-ice model.

From the results presented at point P1 and P2, we note that the method which introduces the effects of the deep ocean influences the ice thickness, the salinity and depth of the mixed layer the most. The other variables (i.e., the surface temperature and the lead extent) seem to be less sensitive. The robust-diagnostic method induces a smaller ice thickness and salinity of the mixed-layer values in comparison with the layer method.

The global results show that the ice extent and oceanic heat flux values are consistent with the observations. Some differences appear when salt conservation is computed. The robust-diagnostic method better conserves salt than the layer method after the tenth year of simulation.

Taking into account the observations on the behaviours of the various configurations of the model, it seems that the robust-diagnostic method looks promising.

6.4. Two-dimensional ice cover.

a) Ice thickness

The robust-diagnostic version of the sea-ice model has been applied to the Weddell Sea area in three forcing configurations : with the thermodynamic processes only, with thermodynamics and ice kinematics forced by the wind, and finally, forced by wind and oceanic currents.

Figure 16 shows the pattern of ice thickness simulated by the thermodynamics-only-model for Julian day 270 (September 27); the positions of the northern and southern points (P1 and P2) are indicated with a star. The thickness contours follow the coast of Antarctica with an important increase up to a maximum of 16.2 m at 60°W, 74°S. This increase depends on the decrease of the oceanic heat flux from north to south. In addition, the independence between each gridpoint and the spatial variations of the oceanic heat flux introduce a few loops at the base of the Antarctica Peninsula.

The introduction of the transport parameterisation described above restructures the sea-ice field. Figures 17 and 18 show the pattern of ice thickness for day 270, respectively with wind only, and with wind and ocean current. The main differences between these results and those obtained without including any ice transport are:

i) weaker ice thickness gradients and, at point (60°W, 74°S), a maximum ice thickness of 4.3 m is observed with wind only and 3.6 m with wind and current;

ii) a cyclonic rotation of the contours under the influence of the ice velocity field;

iii) a larger amplitude of the ice extent under the influence of on ice convergence-divergence.

b) Weddell Polynya

Using data from the Nimbus-5 satellite collected during 1973 through 1976, a very large open-water area, the Weddell Polynya, was observed throughout the winters of the latter 3 years. The polynya was centered in 1974, 1975 and 1976, at about 0°W, 67°S, 15°W, 67°S and 20°W, 68°S respectively.

Many modellers have tried to reproduce this polynya. Motoi et al. (1987) showed with a vertical mixed-layer model coupled with a sea-ice linear thermodynamic model without leads, initialized with ocean data from the summer of 1974, that no sea ice was simulated for 1974 and that the mixed-layer depth reached 1600 m at point 01°14′E, 66°29′S. The high salinity in the upper ocean layers could be the reason for this deep convection in winter.

With a three-dimensional general circulation model and a dynamic-thermodynamic model of sea ice, van Ypersele (1986) succeeded in reproducing a large polynya, located approximately where the Weddell Polynya has been observed in nature. This polynya seems to be associated with the destabilization of the water column by salt rejection at the time of sea-ice growth.

In the present study, the sea-ice model has not allowed us to produce a polynya in the Weddell Sea, although we used the same forcing data and gridpoints as van Ypersele. The only interesting result in this respect comes from the "all-layers" sea-ice model without kinematics: a large open water area connected eastward with the Atlantic Ocean appears. It should be noted that this pattern offers no "resistance" to the introduction of additional physical effects, like the wind and the currents.

7. CONCLUSIONS

The goal of this study was the development of a sea-ice model based on the major thermodynamical and dynamical processes. The model was applied to an important sector of the Southern Ocean including the Weddell Sea and the Drake Passage. The atmospheric forcing was derived from climatological data, and the ocean forcing was computed with a mixed-layer model in various configurations.

The observations strongly shape the results. Contrary to the atmospheric data which are known at a level close to the sea surface, the oceanic data can be chosen along the vertical in at least two ways: i) by limiting the number of oceanic layers and by using thermodynamic information stored in the layer bordering the last used layer (the "layer" method); ii) by introducing a Newtonian forcing towards observations in each layer below the mixed layer (the robust-diagnostic method). The sea-ice model has been applied with both methods. The results show that :

a) the mixed layer tends to reach the ocean bottom in winter except when the robust-diagnostic method is used. In this case, the mixed layer depth oscillates between the depths of the first two layers, due to the forcing towards the observed salinity.

b) the ice thickness depends on the way the sea-ice model is applied : the thickest ice is produced by the sea-ice model with the first oceanic layer (60m) and the thinnest ice is produced by the sea-ice model with the robust-diagnostic forcing and with a relatively short damping time (a few days).

c) the simulation shows a seasonal cycle of effective ice cover with an amplitude which agrees well with observations of 1973, year where the Weddell Polynya has not been observed (Zwally et al., 1983). For all simulated cycles, maxima are higher than observed and minima are slightly lower. However, the phase is not well reproduced, due to the absence of the storage of heat in the ice.

d) the spatio-temporal average of the ocean heat flux exchanged between ice and mixed layer fluctuates in the 10-19 W m^{-2} range depending on the sea-ice model configuration. These values agree well with estimated values (9-16 W m^{-2}) for the Weddell Sea (Gordon et al., 1984).

e) the importance of ice transport by wind and ocean currents. The ice thickness decreases when a transport factor is added to the thermodynamics. The ice cover is characterized by weak ice thickness gradients, a cyclonic rotation in the middle of the Weddell Sea and a maximum ice thickness at the base of the Antarctic Peninsula (3.6 m with thermodynamics and ice · kinematics forced by wind and ocean currents when the robust-diagnostic method is used). The same features are given by the layer method.

The sea-ice model developed in this study is an appropriate tool for the analysis of the spatio-temporal evolution of the sea-ice in the Antarctic Ocean. Without any particular tuning -the parameters of the physical processes were fixed to their "best" values- the applications of the sea-ice model show a good agreement between the ice extent and amplitude and the observations, but the cycle phase needs improvement. The use of interannual observations would allow a refinement of the model parameters, and thus an better understanding of the air-sea interaction in the polar regions.

The sea-ice model is original because it couples in a two-dimensional approach (latitude-longitude) two components that are usually treated separately: sea ice and the ocean mixed layer. Our approach consisted in i) extending an existing one-dimensional sea-ice thermodynamical model to two dimensions, ii) improving it by including a simplified representation of ice dynamics, iii) coupling it to a state-of-the-art ocean mixed layer model, and iv) forcing it with the best atmospheric parameterisations.

Previous studies made with coupled models have either been limited to one dimension (e.g., Lemke, 1987; Fichefet and Gaspar, 1988), or have used a less detailed representation of the mixed layer (e.g., van Ypersele, 1986; Semtner 1987). The present model allows for detailed studies of the interactions between mixed-layer dynamics and sea-ice dynamics, which is not possible

with one-dimensional models.

On the other hand, the ocean circulation itself cannot be properly reproduced with a mixed-layer model, and three-dimensional studies of sea-ice/ocean interactions are only possible with a general circulation model of the ocean coupled, to a sea-ice model. Our model could also benefit from an improvement in the representation of ice dynamics, and by the use of more layers in the ice thermodynamical model. There is also a need for parameterisations of the atmospheric fluxes that are affected by the presence or absence of sea ice. This requires the coupling with a three-dimensional atmospheric model. With the collaboration of the other institutions part of the Belgian Antarctic Research Programme, these improvements will progressively be incorporated in the present model.

8. Applications

The sea-ice model developed in this study can be applied to other areas in the Southern Ocean. With the data we have, it would be feasible to extend our simulations to the full Antarctic Ocean at the same spatial and temporal scales. The simulation at the other scales, closer to navigation conditions, requires either a higher resolution data base or specific models to compensate for the absence of accurate meteorological, oceanological and ice data. In the future, a three-dimensional ocean circulation model will be developed and coupled to the sea-ice model.

In the present form, the coupled sea-ice/mixed-layer model reproduces the main elements of temporal and spatial sea-ice distribution. Studies of model sensitivity to particular parameters, like surface air temperature, wind velocity, albedo and oceanic current, would help to assess the variability of Antarctic sea-ice structure and thus to give some navigational advice.

Several ice-cover characteristics computed by the sea-ice model could be used for pollution and ecological problems. For example, they could serve as input to impact assessment studies of oil exploitation in the polar environment : ice concentration (the leads constrain the spreading of the oil), ice thickness (which limits the meteorological effects on the slick), ... Ecological processes are also affected by a cover of ice (penetration of solar radiation, f.i.).

REFERENCES

Blumberg, A.F., Kantha, L.H., Herring, H.J. and Mellor, G.L. 1984. California shelf physical oceanography circulation model. DYNALYSIS of Princeton Report, No. 88.1, 163 pp.

Briegleb, B., and V. Ramanathan, 1982 : Spectral and diurnal variations in clear sky planetary albedo. J. Appl. Meteor., 21, 1160-1171.

Davis, R.E., R. de Szoeke, D. Halpern and P. Niiler, 1981a : Variability in the upper ocean during MILE. Part I : The heat and momentum balances. Deep-Sea Res., 28A, 1427-1451.

Davis, R.E., R. de Szoeke and P.P. Niiler, 1981b : Variability in the upper ocean during MILE. Part II : Modeling the mixed layer response. Deep-Sea Res., 28A, 1453-1475.

Demuth, C. and J.P. van Ypersele de Strihou, 1988 : Sea-ice simulations in the Weddell Sea. Proceedings of the Belgian National Colloquium on Antarctic Research, Brussels, October 20, 1987, 196-212.

Fichefet, Th. and Ph. Gaspar, 1988 : A model study of upper ocean-sea ice interactions. J. Phys. Oceanogr., 18, 181-195.

Friedrich, H., and S. Levitus, 1972 : An approximation to the equation of state for sea water, suitable numerical ocean models. J. Phys. Oceanogr., 2, 514-517.

Gaspar, Ph., 1988 : Modelling the seasonal cycle of the upper ocean. J. Phys. Oceanogr., 18, 161-180.

Garwood, R.W., 1977 : An oceanic mixed layer model capable of simulating cyclic states. J. Phys. Oceanogr., 7, 455-468.

Gordon, A.L., 1971 : Oceanography of Antarctic water. Antarctic Oceanology 1, Antarctic Res. Series, Vol.15., J.L. Reid, Ed., American Geophysical Union, Washington, D.C., 169-203.

Gordon, A.L. and T.N. Baker, 1982 : Objective contouring and grid point data set. Southern Ocean Atlas, Columbia Univ. Press, New York, 11 pp., 233 plates.

Grenfell, T.C. and G.A. Maykut, 1977 : The optical properties of ice and snow in the Artic Basin. J. Glaciol., 18, 445-463.

Gordon, A.L., C.T.A. Chen and W.G. Metcalf, 1984 : Winter mixed layer entrainment of Weddell Deep Water. J. Geophys. Res., 89, 637-640.

Hibler, W.D., III, 1979 : A dynamic thermodynamic sea ice model. J. Phys. Oceanogr., 9, 815-846.

Hibler, W.D., III, and S.F. Ackley, 1983 : Numerical simulation of the Weddell Sea pack ice. J. Geophys. Res., 88, 2873-2887.

Hibler, W.D., III, 1984. The role of sea ice dynamics in modeling CO_2 increases. In Climate Processes and Climate Sensitivity. Hansen, J. and

Takahashi, T., Eds., Geophys. Mono., 29, M. Ewing, Vol.5 , 238-253.

Hibler, W.D., III, and K. Bryan, 1984 : Ocean circulation : Its effects on seasonal sea-ice simulations. Science, 224, 489-492.

Hibler, W.D., III, and K. Bryan, 1987 : A diagnostic ice-ocean model. J. Phys. Oceanogr., 17, 987-1015.

Jerlov, N.G. 1976. Marine Optics. Elsevier Oceanography Series, 14, 231 pp.

Kitada Toshihiro, Carmichael, G.R. and Peters, L.K., 1984 : Numerical simulation of the transport of chemically reactive species under land- and sea-breeze circulations. J. Climate Appl. Meteor., 23, 1153-1172.

Klein, P. and M. Coantic, 1981 : A numerical study of turbulent processes in the marine upper layers. J. Phys. oceanogr., 11, 849-863.

Ledley, T.S., 1985 : Sensitivity of a thermodynamic sea ice model with leads to time step size. J. Geophys. Res., 90, 2251-2260.

Ledley, T.S. 1985 Sea ice : Multiyear cycles and white ice. J. Geophys. Res., 90, D3 : 5676-5686.

Lemke, P., 1987 : A coupled one-dimensional sea ice ocean model. J. Geophys. Res., 92, 13164-13172.

Leppäranta, M. and W.D. Hibler, III 1987 : Mesoscale sea ice deformation in the East Greenland marginal ice zone. J. Geophys. Res., 92, C7 : 7060-7070.

Marshunova, M.S. 1966. Principal characteristics of the radiation balance of the underlying surface and the atmosphere in the Arctic. In Soviet Data on the Arctic Heat Budget and its Climatic Influence. Fletcher, J.O., Keller, B. and Olenicoff, S.M., Eds., 51-131.

Maykut, G.A., and N. Untersteiner, 1971 : Some results from a time dependent thermodynamic of sea ice. J. Geophys. Res., 76, 1550-1575.

Maykut, G.A. and D.K. Perovich, 1987 : The role of shortwave radiation in the summer decay of a sea ice cover. J. Geophys. Res. 92, C7, 7032-7044.

Millero F.J. and W.H. Leung, 1976 : The thermodynamics of seawater at one atmosphere. Amer. J. Sei., 276, 1035-1077.

Motoi Tatswo, Ono Nobuo and Wakatsuchi Masaaki, 1987 : A mechanism for the formation of the Weddell polynya in 1974. J. Phys. Oceanogr., 2241-2247.

Niiler, P.P., and E.B. Kraus, 1977 : One dimensional models of the upper ocean. Modeling and Prediction of the Upper Layers of the Ocean. E.B. Kraus (Ed.), Pergamon Press, 143-172.

Parkinson, C.L, 1983 : On the development and cause of the Weddell Polynya in a sea ice simulation. J. Phys. Oceanogr., 13, 501-511.

Parkinson, C.L. and W.M. Washington, 1979. A large-scale numerical model of sea ice. J. Geophys. Res., 84, C1, 311-337.

Paulson, C.A. and J.J. Simpson, 1977 : Irradiance measurements in the upper ocean. J. Phys. Oceanogr., 7, 952-956.

Pease, C.H., 1975 : A model for the seasonal ablation and accretion of Antarctic sea ice. AIDJEX Bull., 29, 151-172.

Pivovarov A.A., 1973. Thermal conditions in freezing lakes and reservoirs. Wiley.

Pollard, D., M.L. Batteen and Y-J. Han, 1983 : Development of a simple upper - ocean and sea-ice model. J. Phys. Oceanogr., 13, 754-768.

Røed, L.P., 1984 : A thermodynamic coupled ice-ocean model of the marginal ice zone. J. Phys. Oceanogr., 14, 1921-1929.

Sarmiento, J.L., and K. Bryan, 1982 : An ocean transport model for the North Atlantic. J. Geophys. Res., 87, 394-408.

Semtner, A.J., Jr. 1976. A model for the thermodynamic growth of sea ice in numerical investigations of climate. J. Phys. Oceanog., 6, 379-389.

Semtner, A.J. Jr., 1987 : A numerical study of sea ice and ocean circulation in the Arctic. J. Phys. Oceangr., 17, 1077-1099.

Shine, K.P. 1984. Parameterization of the shortwave flux over high albedo surfaces as a function of cloud thickness and surface albedo. Quart. J.R. Met. Soc., 110 : 747-764.

Taljaard, J.J. van Loon, H., Crutcher, H.L. and R.L. Jenne, 1969. Climate of the Upper Air, I, Southern Hemisphere, Vol. 1. Temperatures, Dew Points and Heights at Selected Pressure Levels. NAVAIR 50-1C-55, U.S. Naval Weather Service, Washington, D.C., 135 pp.

Thorndike, A.S. and R. Colony, 1982. Sea ice motion in response to geostrophic winds. J. Geophys. Res., 87 : 5845-5852.

Toole, J.M. 1981 : Sea ice, Winter convection and the temperature minimum layer in the Southern Ocean. J. Geophys. Res., 86, 8037-8047.

van Loon, H. 1972. Cloudiness and precipitation in the Southern Hemisphere. In Meteorology of Southern Hemisphere, Meteor. Monogr. 13, American Meteorological Society, Boston, Mass., 101-112.

van Ypersele de Strihou, J.P. 1986. A numerical study of the response of the Southern Ocean and its sea ice to a CO_2- induced atmospheric warming. Cooperative Thesis NCAR CT99, Université Catholique de Louvain, Belgium and National Center for Atmospheric Research, U.S.A., 135 pp.

Wang, Dong-Ping, 1985 : Numerical study of gravity currents in a channel. J. Phys. Oceanogr., 15, 299-305.

Washington, W.M. and C.L. Parkinson, 1986. An introduction to three dimensional climate modeling. University Science Books, California, 422 pp.

Zwally, H.J. Comiso, J.C. Parkinson, C.L. Campbell, W.J. Carsey, F.D. and P. Gloersen, 1983. Antarctic Sea Ice 1973-76. National Aeronautics and Space Administration (NASA), Washington, D.C., 206 pp. (Supt. of Doc., USGPO, Washington.

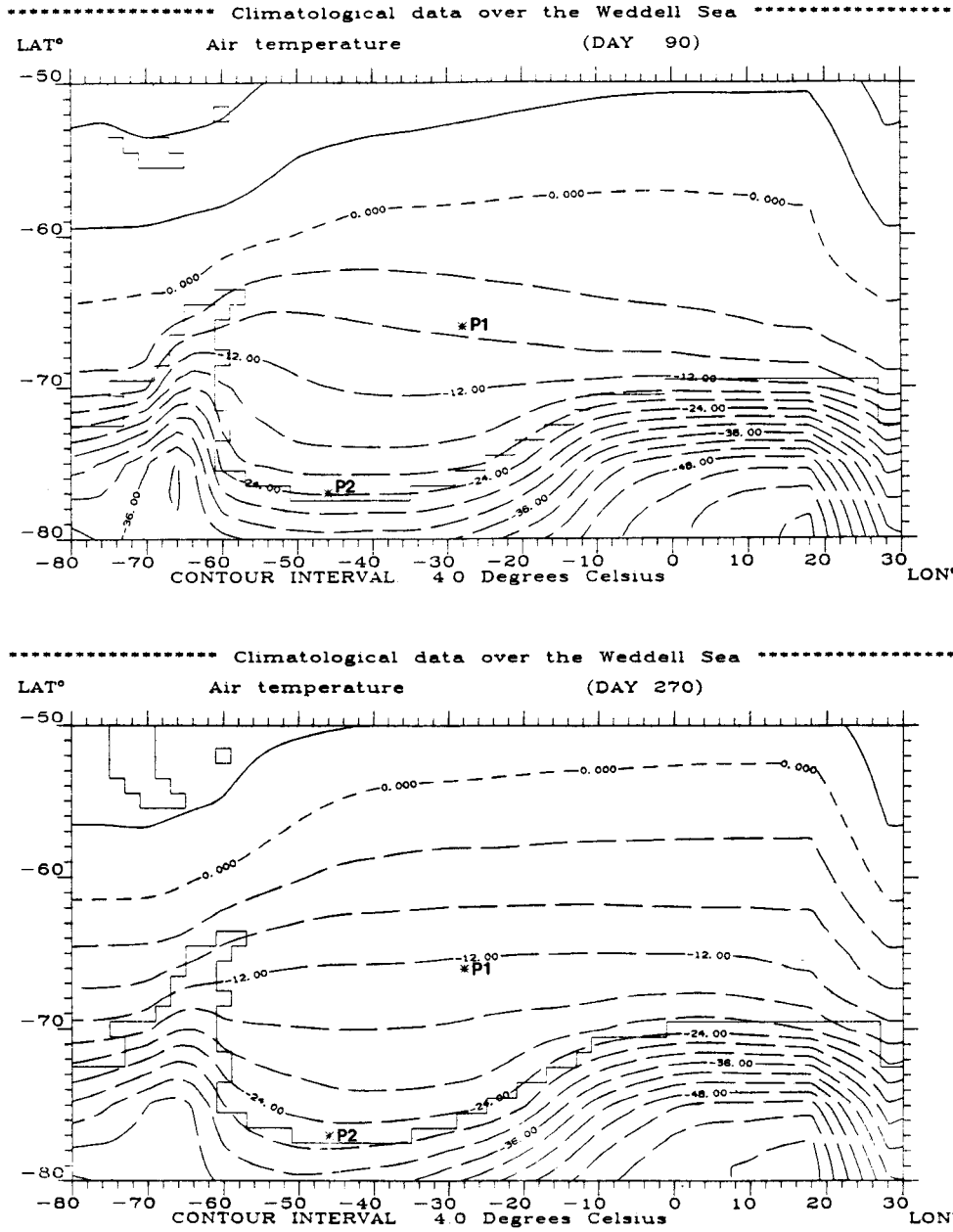

Figure 1 Surface air temperature (°C) on Julian day 90 (top) and 270 (bottom). The southern tip of South America, the Falkland Islands and the Antarctica coasts are represented by a stepwise contour in the model domain. The stars give the positions of particular points with coordinates (47° W, 77° S) and (28° W, 66° S) for which results are discussed. (From the data in Taljaard *et al., 1969).*

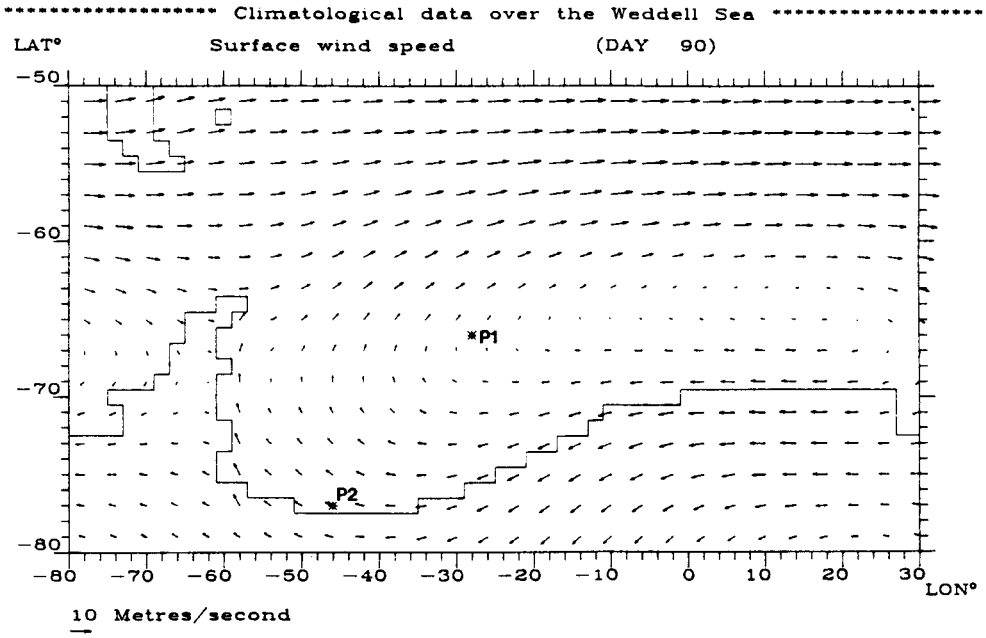

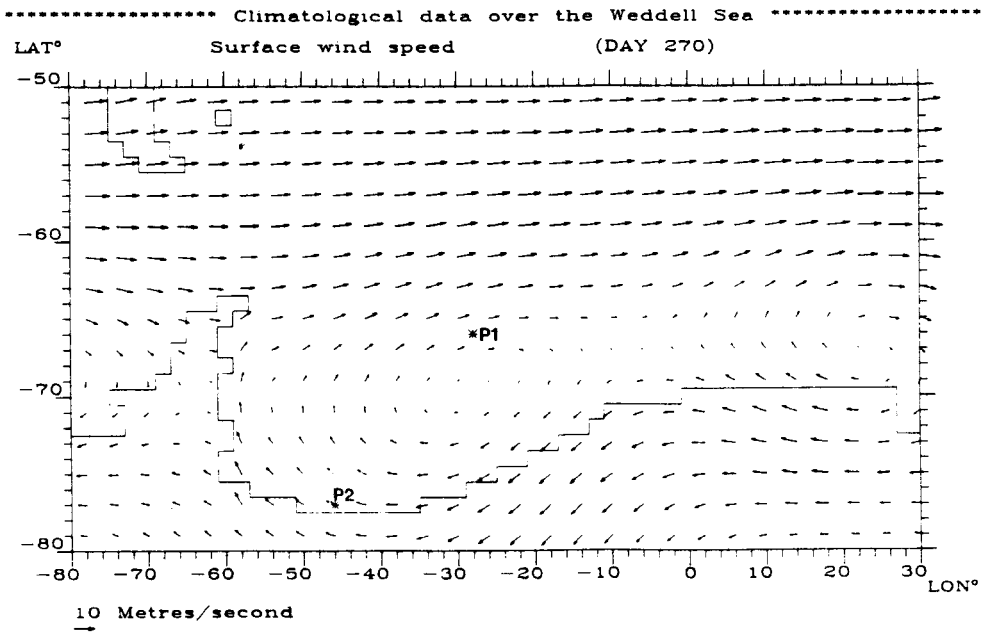

Figure 2 Surface geostrophic wind (m s^{-1}) on Julian day 90 (top) and 270 (bottom). The southern tip of South America, the Falkland Islands and the Antarctica coasts are represented by a stepwise contour in the model domain. The stars give the positions of particular points with coordinates (47° W, 77° S) and (28° W, 66° S) for which results are discussed. (From the data in Taljaard *et al.*, 1969).

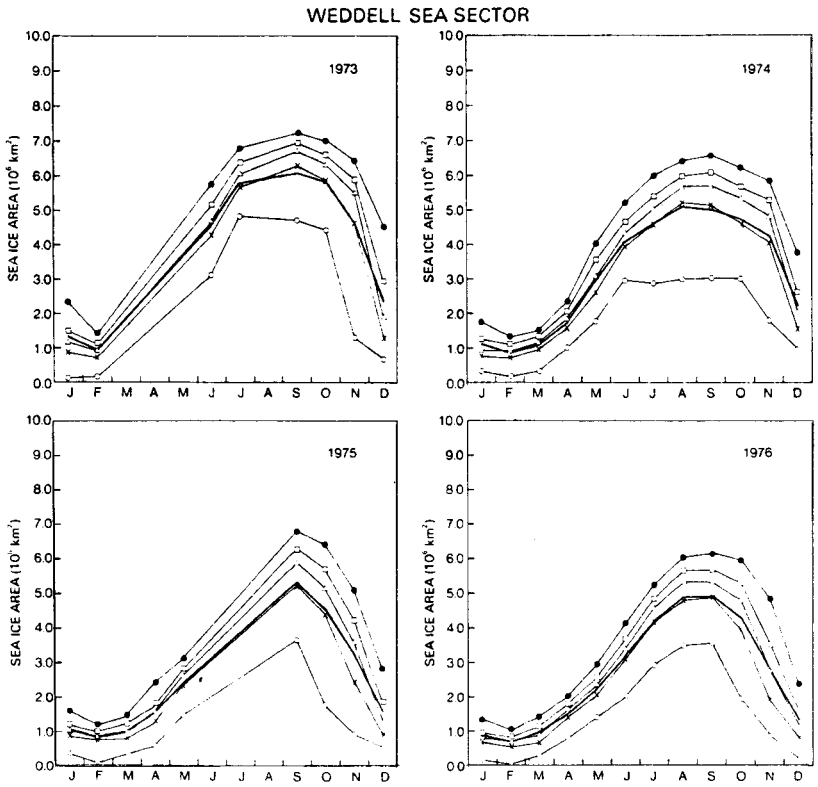

Figure 3 Yearly cycle of ice extent (total area of grid squares containing any amount of ice) and effective ice area (the total ocean surface covered by sea ice, excluding all open water) as observed in the Weddell sector between 1973 and 1976 (x $10^6 km^2$). The thick curve is for the effective ice area and the top curve for the ocean area covered by sea ice concentration higher than 0.15 (from Zwally et al.1983).

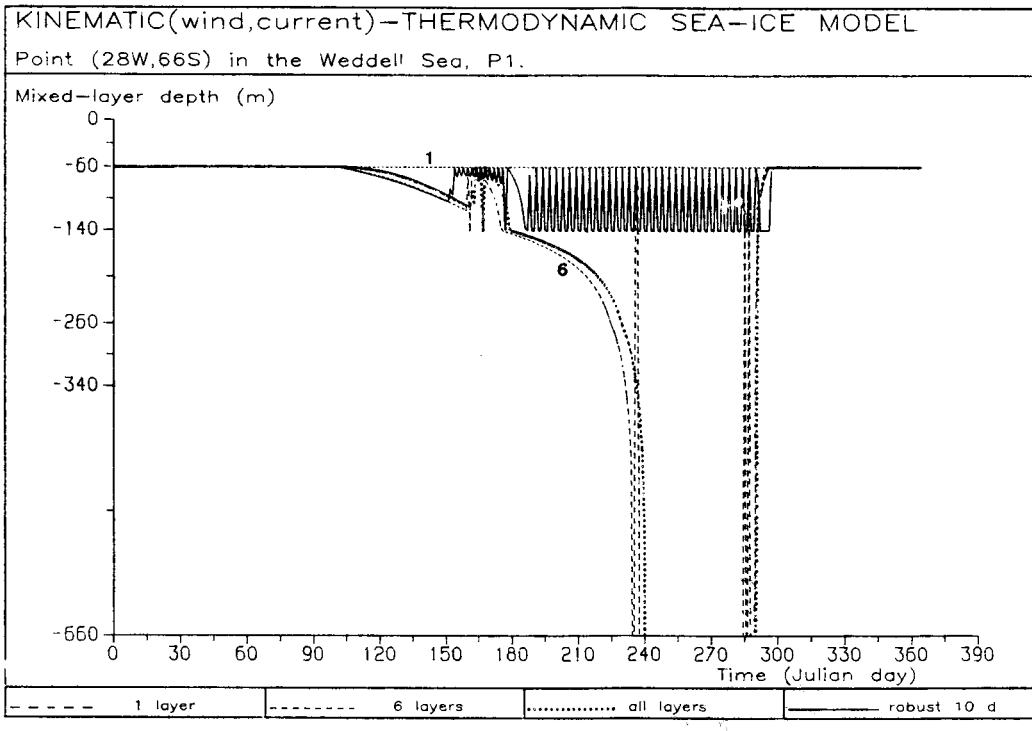

Figure 4 Comparison of annual mixed-layer depth (m) cycles at point P1 computed by the sea-ice model using the layer method (1,6 and all layers) and the robust-diagnostic method (damping time is 10 days).

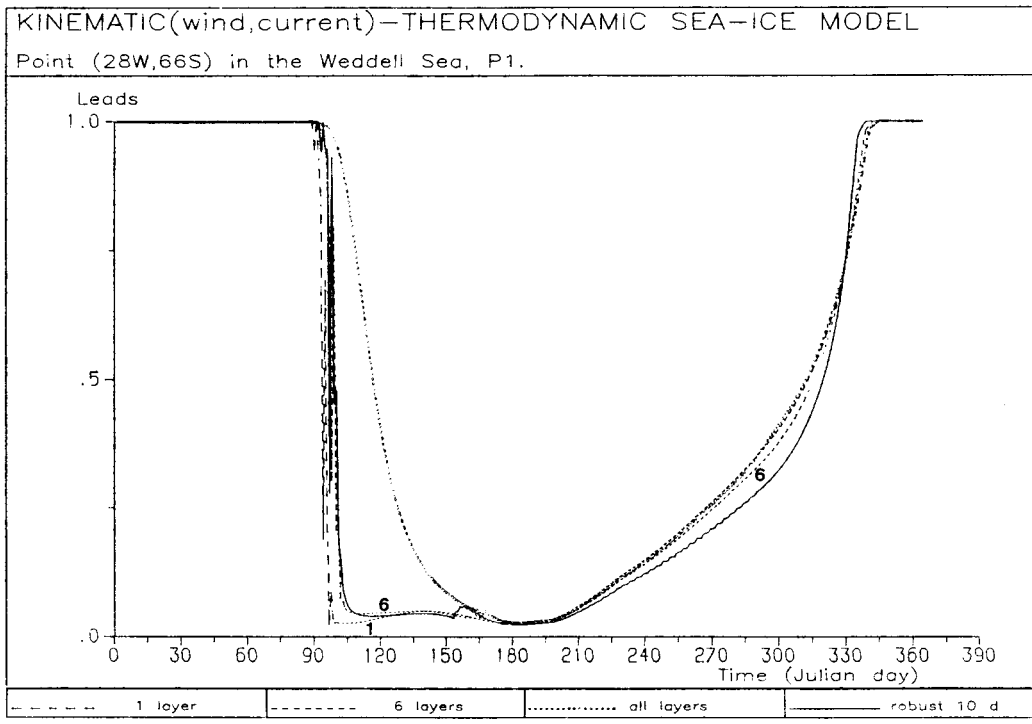

Figure 5 Comparison of annual leads cycles at point P1 computed by the sea-ice model using the layer method (1,6 and all layers) and the robust-diagnostic method (damping time is 10 days).

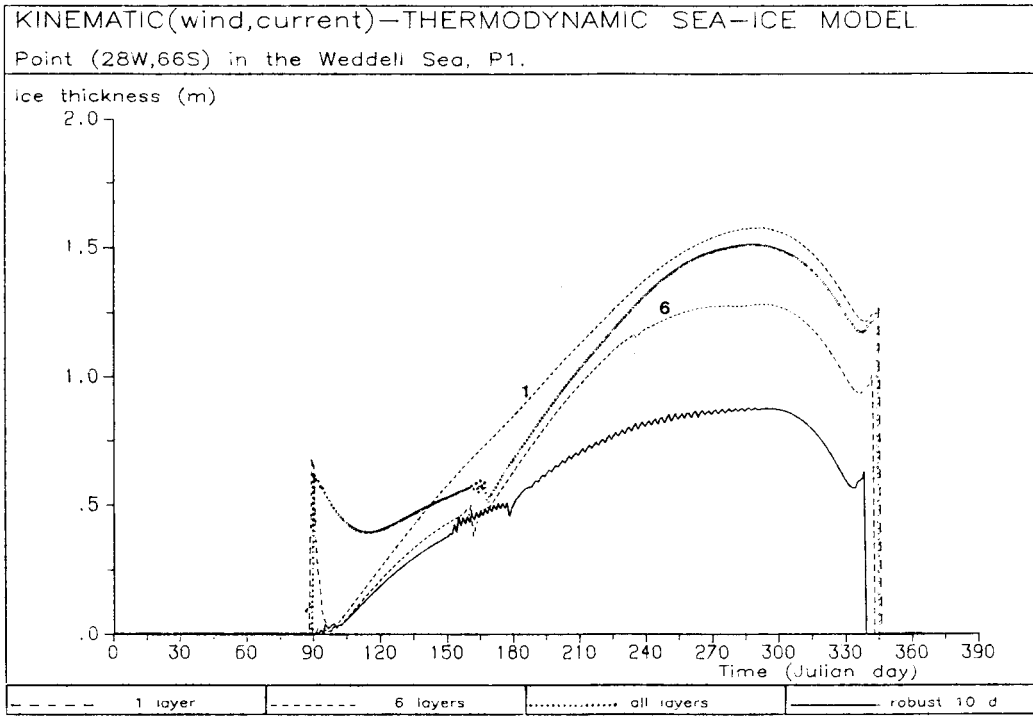

Figure 6 Comparison of annual ice thickness (m) cycles at point P1 computed by the sea-ice model using the layer method (1,6 and all layers) and the robust-diagnostic method (damping time is 10 days).

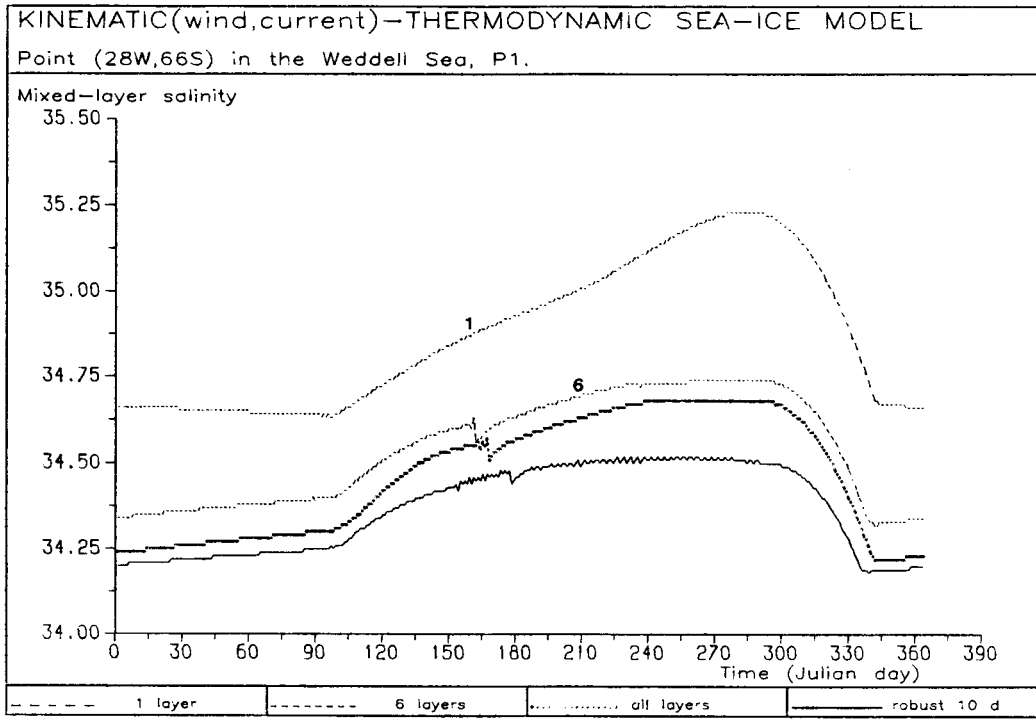

Figure 7 Comparison of annual mixed-layer salinity (x 10^{-3}) cycles at point P1 computed by the sea-ice model using the layer method (1,6 and all layers) and the robust-diagnostic method (damping time is 10 days).

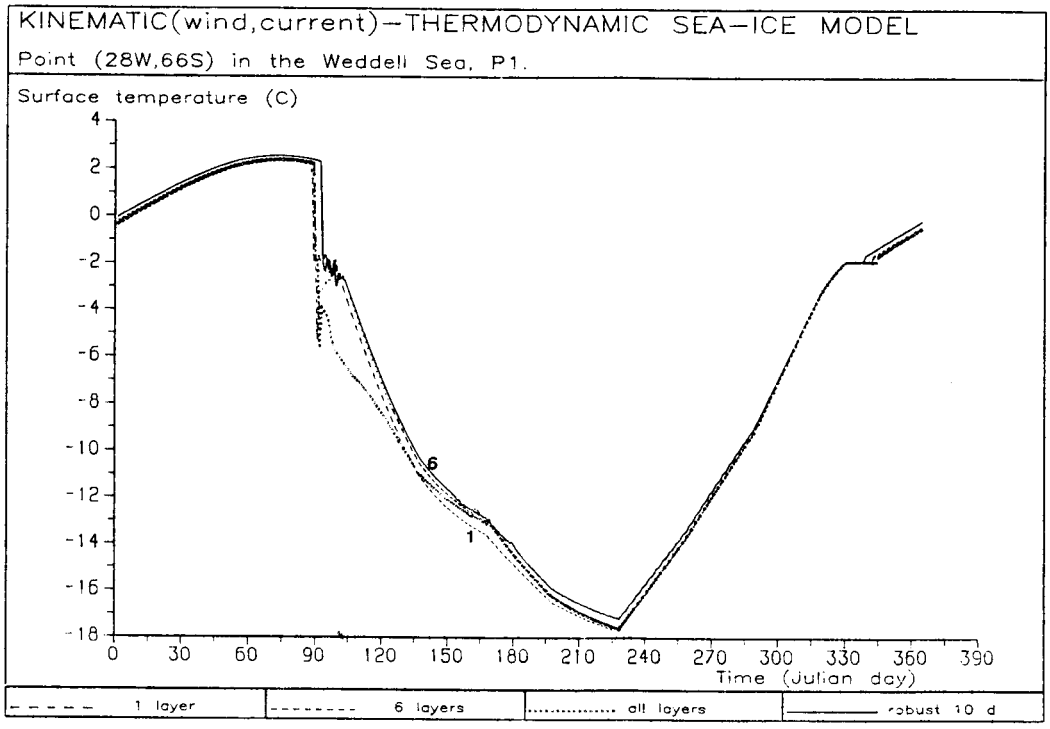

Figure 8 Comparison of annual surface temperature (degree Celsius) cycles at point P1 computed by the sea-ice model using the layer method (1,6 and all layers) and the robust-diagnostic method (damping time is 10 days).

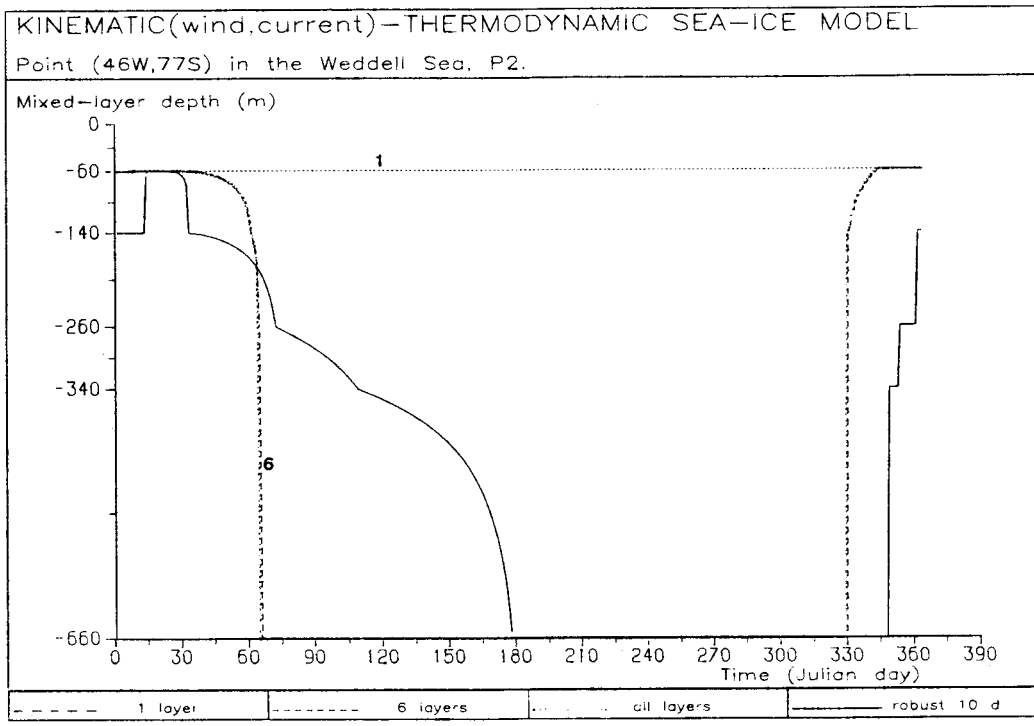

Figure 9 Comparison of annual mixed-layer depth (m) cyles computed at point P2 of the sea-ice model using the layer method (1,6 and all layers) and the robust-diagnostic method (damping time is 10 days).

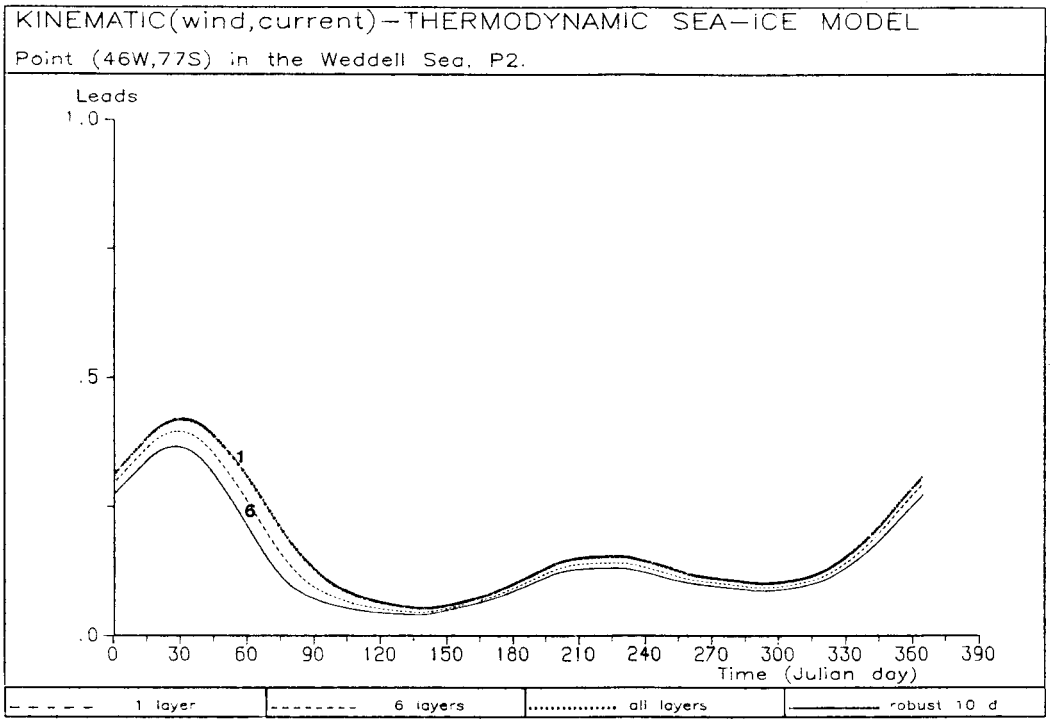

Figure 10 Comparison of annual leads cyles computed at point P2 of the sea-ice model using the layer method (1,6 and all layers) and the robust-diagnostic method (damping time is 10 days).

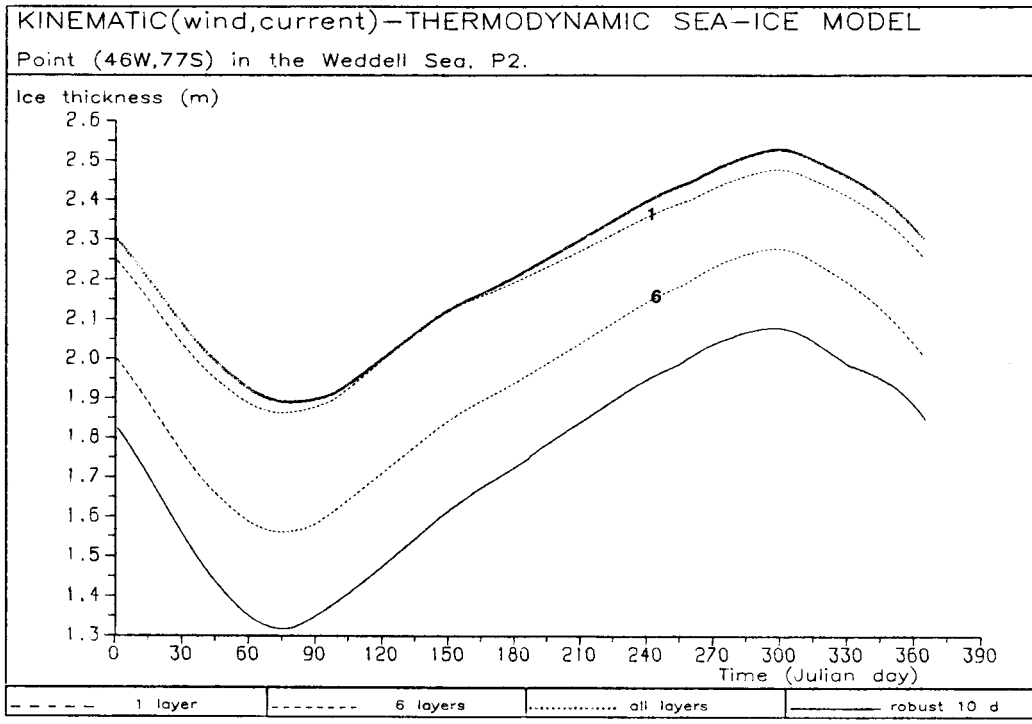

Figure 11 Comparison of annual ice thickness (m) cyles computed at point P2 of the sea-ice model using the layer method (1,6 and all layers) and the robust-diagnostic method (damping time is 10 days).

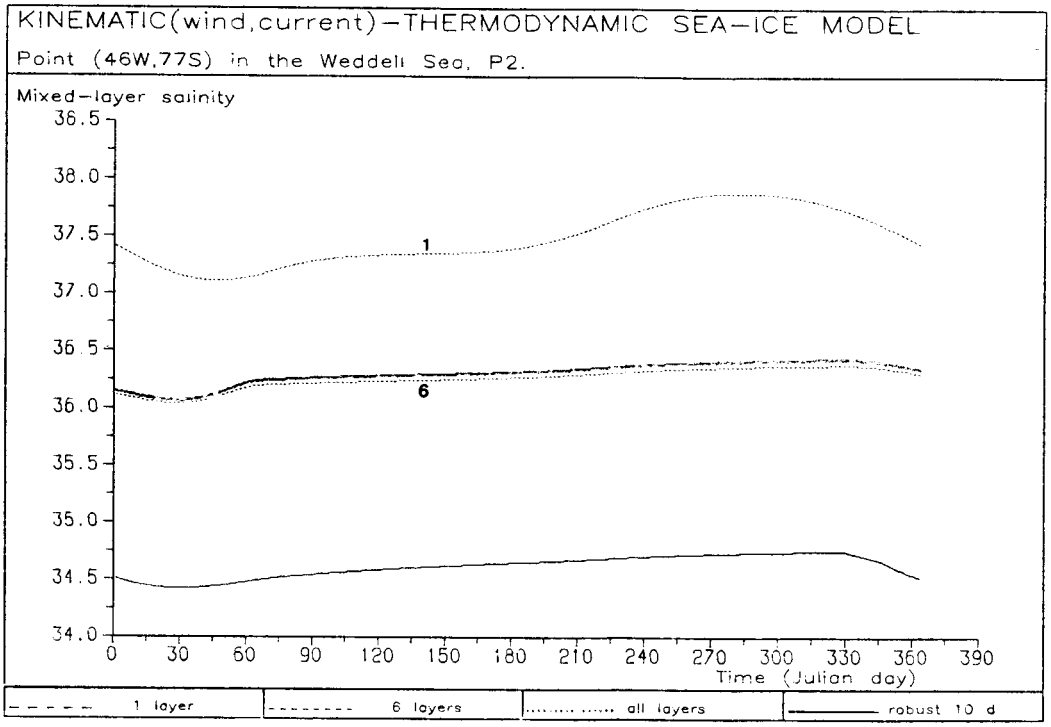

Figure 12 Comparison of annual mixed-layer salinity (x 10^{-3}) cyles computed at point P2 of the sea-ice model using the layer method (1,6 and all layers) and the robust-diagnostic method (damping time is 10 days).

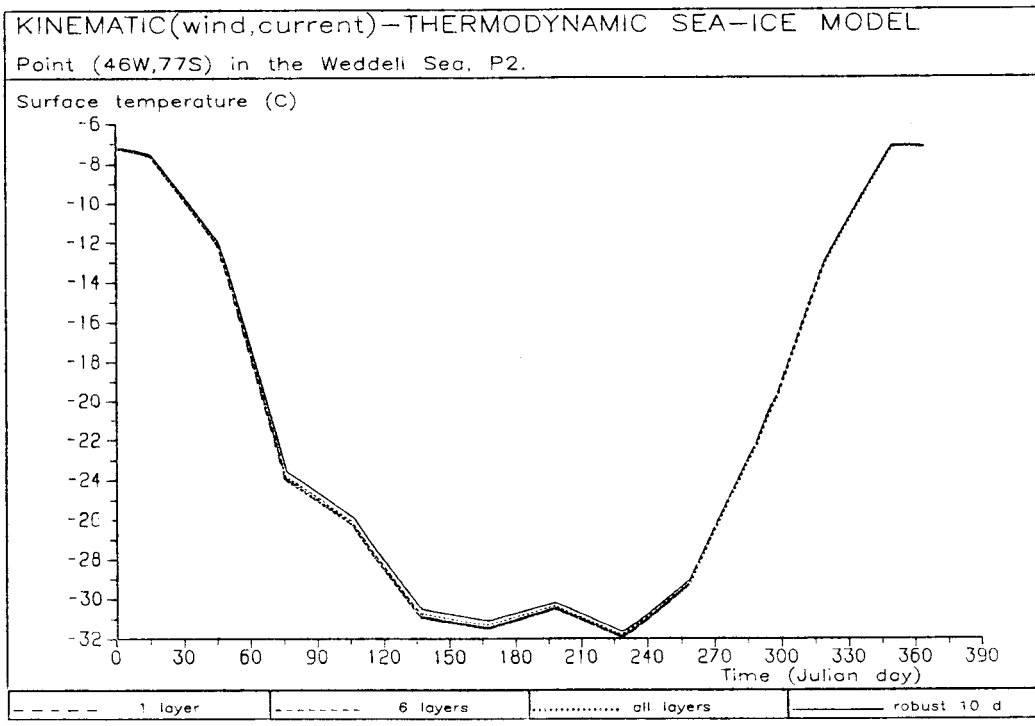

Figure 13 Comparison of annual surface temperature (degree Celsius) cyles computed at point P2 of the sea-ice model using the layer method (1,6 and all layers) and the robust-diagnostic method (damping time is 10 days).

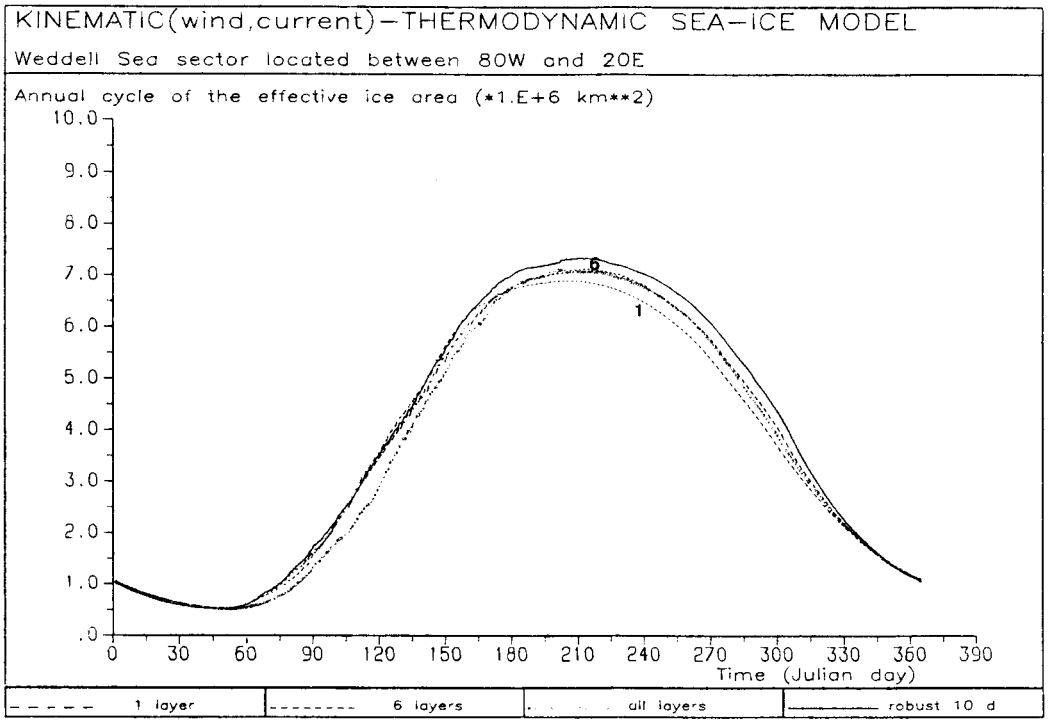

Figure 14 Comparison of annual cycles of the effective ice area computed by the sea-ice model using the layer method (1,6 and all layers) and the robust-diagnostic method (10-day damping time value).

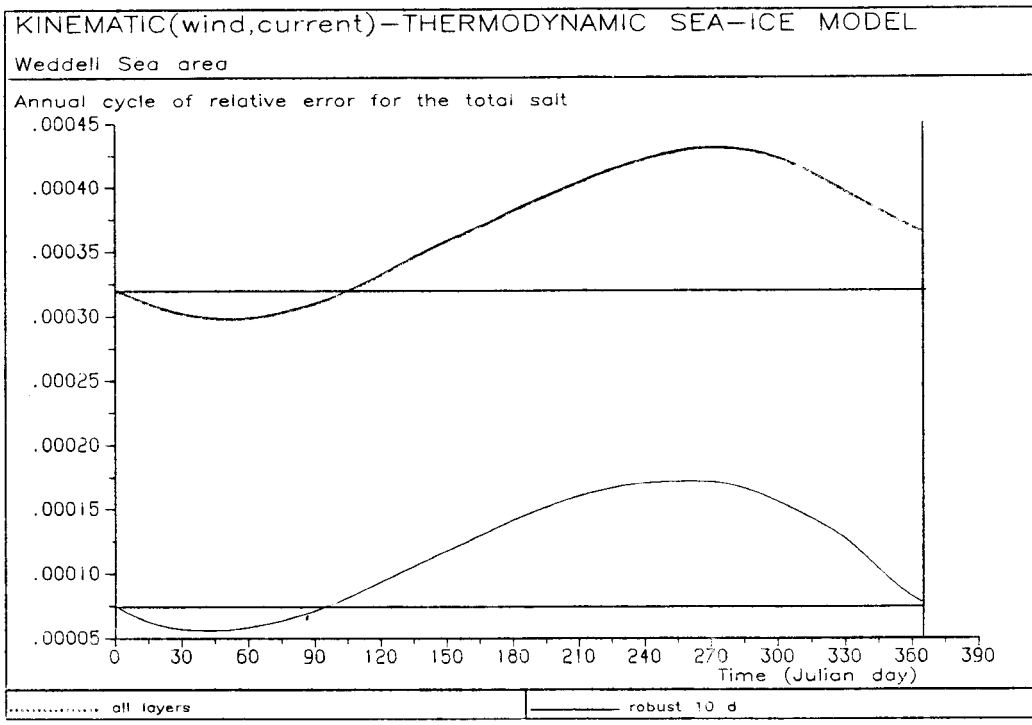

Figure 15 Yearly cycles of the relative error for the salt amount in the Weddell Sea domain computed by the sea-ice model using the layer method (all layers) and the robust-diagnostic method (10-day damping time value). The reference value corresponds to the observed salt amount in the same domain.

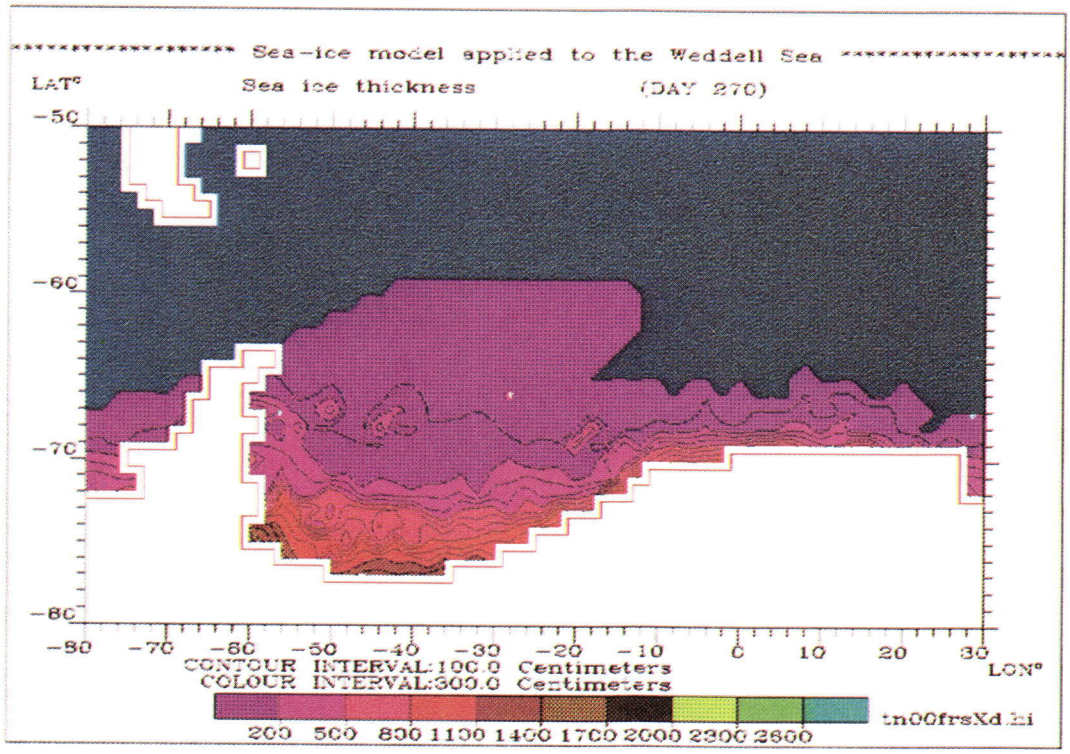

Figure 16 Ice thickness (cm) computed by the sea-ice model using the robust-diagnostic method for day 270 (September 27) of the tenth year of simulation. The model is restricted to the thermodynamic component.

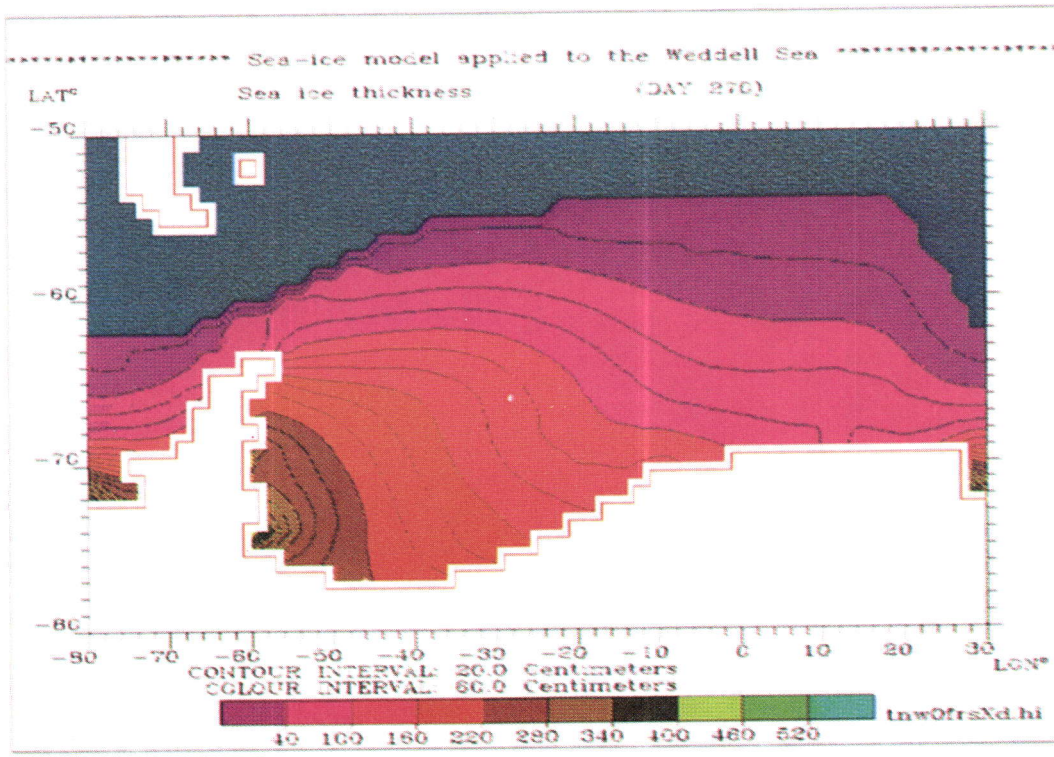

Figure 17 Ice thickness (cm) computed by the sea-ice model using the robust-diagnostic method for day 270 (September 27) of the tenth year of simulation. The model has the thermodynamic and dynamic components and the ice transport is due to wind.

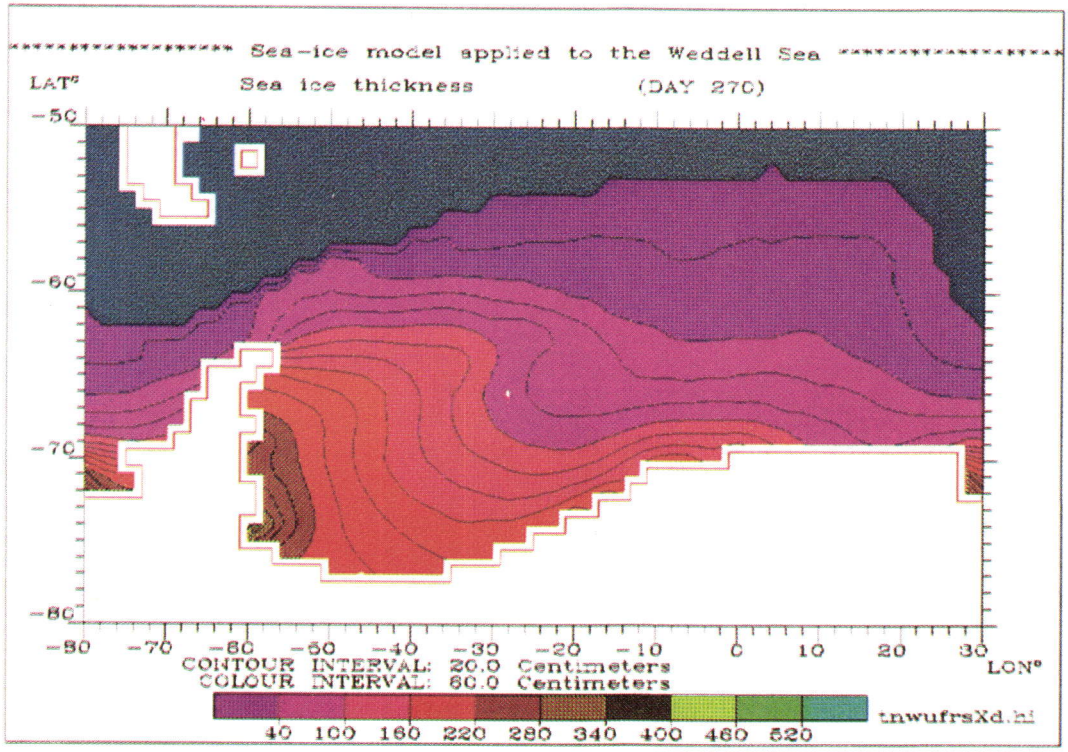

Figure 18 Ice thickness (cm) computed by the sea-ice model using the robust-diagnostic method for day 270 (September 27) of the tenth year of simulation. The model has the thermodynamic and dynamic components and the ice transport is due to wind and ocean current.